AN ABSTRACT OF THE DISSERTATION OF

Jason Frederick Kaiser for the degree of Doctor of Philosophy in Geology presented on June 4, 2014.

Title: Understanding Large Resurgent Calderas and Associated Magma Systems: The Pastos Grandes Caldera Complex, Southwest Bolivia.

Abstract approved: _____

Shanaka L. de Silva

The Pastos Grandes Caldera Complex (PGCC) in southwest Bolivia has produced two large-volume (≥800 km^3 DRE) dacite ignimbrites from a nested caldera source over a period of 5.5 Myr. In addition to the large-volume ignimbrites, a small-volume ignimbrite shield and post-climactic lavas define this composite system. Based on detailed field work and analysis of satellite imagery plus biotite $^{40}Ar/^{39}Ar$ dating, we summarize a revised stratigraphy, areal distribution and volume calculations for ignimbrites. From interpretations of stratigraphy and structures along the caldera margins, we propose an asymmetric collapse hinged along the north and western boundaries. Both the early Chuhuilla (5.45 ± 0.02 Ma), and the younger Pastos Grandes (2.89 ± 0.01 Ma) calderas share the hinge and much of the eastern collapse scarp, however the Chuhuilla caldera defines a much larger area (>1700 km^2) compared to the Pastos Grandes (870 km^2). It is proposed here that pre-existing regional tectonic weaknesses combined with influences of the magma body caused roof failure and caldera collapse. The vast majority of the ignimbrite volume lies within the Chuhuilla and Pastos Grandes calderas (92 and 75% respectively). Considerable intracaldera fill and the lack of preceding plinian deposits suggest that the caldera collapse was early and the eruptive

column was not high and was short-lived. The physical properties of the ignimbrites, the limit of their areal distribution to regional topographic lows along with paleomagnetic characteristics support the idea of dense sluggish pyroclastic flows. New volume calculations using multiple methods update previous estimates, with the Chuhuilla now at approximately1300 km^3 and the Pastos Grandes at 800 km^3.

The ignimbrite volumes and spatial pattern of vents suggest that the caldera complex mirrors the construction of a long-lived composite batholith that focused spatially with time. Eruptions from the PGCC have produced compositionally restricted, high-K dacites with volumetrically minor rhyolites. Combined with granodiorite xenoliths, each caldera cycle contains a progression of textural maturity from ignimbrite, through post-climactic lavas, to remnant pluton. The chemical signatures in the PGCC mirror those of the host Altiplano Puna Volcanic Complex (APVC) and resemble typical arc characteristics (i.e. LIL enriched magmas - Ba/Nb of 4.7-4.8 and Ba/La of 1.6-2.0). However, overprinted on the arc signature are elevated radiogenic isotopes ($^{87}Sr/^{86}Sr$ ~0.708 – 0.709), which suggest high degrees of crustal assimilation that is thought to be related to increased mantle input from melted asthenosphere. It is suggested here that a combination of assimilation and fractional crystallization from the regional mid-crustal parental source would create the magmas erupted in the PGCC. Subtle decreases in the $^{87}Sr/^{86}Sr$ from the Chuhuilla caldera cycle, to the younger Pastos Grandes cycle suggest higher amounts of crustal assimilation related to more heat flow during the peak of the flare up.

Zircon chronochemistry reveals that the climactic, caldera-forming eruptions of the PGCC punctuate the protracted magma accumulation and storage periods. The combination of in-situ zircon U-Pb ages with indicators for geochemical evolution (e.g., Zr/Hf, Yb/Gd, Eu/Eu*, Th, U) magmatic temperatures (e.g., Ti) in zircon, reveals protracted magma presence before and after the climactic 2.89 ± 0.01 Ma Pastos Grandes Ignimbrite (PGI) supereruption (~800 km^3 of magma) in southwest Bolivia. Zircons from PGI pumice and a lava dome define a pre-climactic magmatic stage of ~0.7 Myr duration prior to the climactic eruption and formation of the eponymous caldera. A further 0.4 Myr of post-climactic zircon crystallization is recorded in lava domes and cogenetic granodiorite clasts. Zircon crystallization is recorded for approximately 1.3 Myr for the Chuhuilla cycle; however the record is entirely pre-climactic. We propose a model for the Pastos Grandes cycle in which the climactic caldera-forming eruption vented the upper portions of the reservoir that were zircon saturated. Subsequently, deeper "remnant" dacite magma previously outside the zone of zircon saturation but crystallizing other major phases, rose to re-establish lithostatic equilibrium, commenced zircon crystallization anew, and drove resurgent volcanism and uplift. This ~1.1 Myr zircon crystallization history records the minimum duration of the lifetime of the PGI supereruption magma from its accumulation to post-climactic solidification. These data support >1 Myr magma lifetimes and a link between volcanic and plutonic realms in large sub-caldera magma reservoirs in the uppermost crust that feed some supereruptions.

Understanding Large Resurgent Calderas and Associated Magma Systems: The Pastos Grandes Caldera Complex, Southwest Bolivia

by
Jason Frederick Kaiser

A DISSERTATION

Submitted to
Oregon State University

in partial fulfillment of
the requirements for the
degree of

Doctor of Philosophy

Presented June 4, 2014
Commencement June 2014

Doctor of Philosophy dissertation of Jason Frederick Kaiser presented on June 4, 2014

APPROVED:

Major Professor, representing Geology

Dean of the College of Earth, Ocean, and Atmospheric Sciences

---

Dean of the Graduate School

I understand that my dissertation will become part of the permanent collection of Oregon State University libraries. My signature below authorizes release of my dissertation to any reader upon request.

Jason Frederick Kaiser, Author

ACKNOWLEDGEMENTS

If there is one thing I have learned in my academic career, it is that science cannot move forward without a community of inclusive thinkers and teachers. I have been fortunate to have been allowed to work with such bright, motivating, and inspiring people. Only in working alongside such brilliant and passionate people was I able to discover my own passion and abilities in this world. There are many who have shaped my life; as many as humanly possible are mentioned here.

First, I have to mention my parents. The most supportive, caring, and helpful people I could ever imagine having in my life. I know they would be proud of me no matter what I did with my life. It is this unfiltered love and support that has let me explore this world and make my own way. Thank you so much for introducing me to as much as possible and teaching me to think for myself. Maybe we didn't explore much of the world first-hand when I was a kid, but you sure didn't hide any of it from me. I cannot thank you enough for everything you have taught me.

I have so many teachers to thank for inspiring me from an early age. The first that comes to mind is Walter Long. The most passionate and inspiring history teacher a junior high school could ever ask for. The most important lesson I learned from Mr. Long was that there was more to life than the Mississippi River Valley and that I needed to go see and experience as much of it as I could. I am well on my way Mr. Long – Thank you. Another amazing and inspiring teacher – Mark Pfieffer – made learning more fun than I

could have ever thought. These teachers gave me a true passion for knowledge, I owe so much to them.

My life forever changed the day I met John Hogan. My first geology instructor and constant mentor taught me how to me a scientist and have fun with it. I stayed in college solely because of John, and am at this stage in my life only because of John. Whether I am in the field, in the lab, or in front of the classroom, his words are echoing in my mind. I still look to John for words of wisdom and advice, thank you Captain Contact.

My graduate career has been filled with ups and downs as anyone would expect. Sheila Seaman and Mike Williams were my first guides through this treacherous world. I cannot thank them enough for their kindness and generosity. My committee at Oregon State has been truly amazing. Anita Grunder and Andrew Meigs have given me critical instruction and guidance. Thank you for your brutal honesty and generous scientific insight along the way. I owe a special thanks to Axel Schmitt for being a surrogate advisor for a year. I will never be able to match his energy or attention to detail, but I learned more than I thought possible while trying my best to keep up. Thank you Dale and Stephanie for being with me every step of the way. I would not have survived without your help and support. Thanks for letting me crash your offices with ideas, questions, or just to vent frustration.

And finally, the biggest thanks to Shan de Silva (aka Papa Bear). I have finally learned that there is always a method to your madness. Every interaction has been a learning

opportunity and your incredibly high standards have pushed me far beyond what I thought I could be as a scientist. Thank you for your brutal honesty and unwavering motivation. I would not be the scientist or man I am today without you.

TABLE OF CONTENTS

Page

TABLE OF CONTENTS (Continued)

Page

TABLE OF CONTENTS (Continued)

Page

LIST OF FIGURES

LIST OF FIGURES (Continued)

LIST OF TABLES

Understanding Large Resurgent Calderas and Associated Magma Systems: The Pastos Grandes Caldera Complex, Southwest Bolivia.

CHAPTER 1
General Introduction

Argument

The signal of igneous activity is recorded on the Earth's surface in two fundamental ways. Plutons, which represent remnant magma systems, vary in exposed area up to hundreds of square kilometers. These plutonic bodies preserve an integrated record of their entire magmatic lifespan. Due to exhumation over long time periods, often by tectonic processes, plutonic records can be skewed. Phase assemblages reflect long histories of cooling and crystallization during piecemeal accumulation. As a result of overprinting, ages, textures, and phase chemistry represent averages of long duration processes. On the other end of the igneous spectrum, volcanic rocks represent snapshots in time, sampling single moments during magma development and evolution. Eruptions cool crystal and liquid proportions relatively abruptly, preserving mineral compositions that are in equilibrium with active magma systems. These pre-eruptive magma conditions are lost in plutonic records, however it is rarely known what proportion of the magma system is sampled in each eruption.

Since both volcanic and plutonic rocks display significant differences, there has been a tendency to view and study them as separate realms. Over recent years, attempts have been made to close the gap between these two domains (e.g. Hildreth, 1981; Grunder et al., 2006; de Silva and Gosnold, 2007; Bachmann et al., 2007; Claiborne et al., 2010). In locations where volcanic and plutonic rocks of calderas are exposed, they show striking

similarities in terms of their size, spatial associations and their geochemical and geophysical kinships (e.g. Buddington, 1959; Smith, 1960; Johnson et al., 1990; Lipman, 2007). However, in young systems which offer the best preserved and geochronologically resolvable record of volcanism, plutonic rocks are not typically exposed, and eruptions only sample an instantaneous stage of magma development and evolution. Because of these uncertainties, contrasting views of the volcano-plutonic connection have been brought forth at long-lived caldera systems. Ignimbrite formation at these caldera systems is thought to result from the partial to complete evacuation of magma chambers at shallow crustal levels, with plutons forming from the crystal-liquid residuum (Smith, 1979; Lipman, 1984; Bachmann and Bergantz, 2004, 2008a, 2008b; Hildreth, 2004; Lipman, 2007). Opposing views are that either plutonic rocks comprise crystal and liquid residua of volcanic eruptions, and are thus geochemically complementary to volcanic rocks (Hildreth, 2004; Bachmann et al., 2007; Lipman, 2007; de Silva and Gosnold, 2007), or that plutonic rocks form as unfractionated equivalents of erupted magma (Glazner et al., 2008; Tappa et al., 2011; Zimmerer et al., 2012).

The integrated volcanic record of large, multicyclic caldera complexes is thought to be mirrored in the subsurface by the construction of upper crustal batholiths of comparable size and volume (e.g., Lipman, 1984). As such, ignimbrite deposits of multicyclic caldera complexes offer an opportunity to investigate the long-term storage and evolution of some of the largest magma reservoirs on Earth, and in turn, understand how reservoir volume and emplacement conditions control eruption dynamics and ignimbrite emplacement. The factors that contribute to large-scale silicic magmatism and volcanism

must be intrinsically linked to the understanding of how continental crust grows, and stabilizes through time.

Using the volcanic stratigraphy of the Pastos Grandes Caldera Complex in the Central Andes of SW Bolivia, a detailed analysis of the volcanology is presented. The ignimbrite stratigraphy and caldera morphology are used in conjunction with detailed geochronology and geochemistry to understand the location and timing of magmatism in the shallow crust. These data are then placed into the framework of the regional magmatism and volcanism in the Central Andes.

Thesis Directions

Each of the objectives listed above are addressed in the subsequent chapters of this thesis. The second chapter of this thesis builds the stratigraphy and physical volcanology of the Pastos Grandes Caldera Complex (PGCC) in southwest Bolivia. Ignimbrite volumes and distributions were constrained with detailed field mapping and analysis of satellite imagery. New $^{40}Ar/^{39}Ar$ eruption ages supplement the initial reconnaissance study of Salisbury et al. (2011) to construct a complete chronostratigraphic framework of the complex. The third chapter explores the geochemical history of the PGCC by examining the variation in whole-rock major and trace elements as well as Sr and Nd isotopes. The fourth chapter examines the zircon history of the PGCC. Zircons from the ignimbrites and post-climactic lavas, as well as plutonic clasts were analyzed to constrain the age distribution and crystallization conditions in both pre and post-climactic conditions in the PGCC. These data combine to provide a view of caldera and magmatic evolution in a large, long-lived silicic system.

Tectonic Context of the Pastos Grandes Caldera Complex

The west coast of South America is dominated by the 7000 km long Andean arc. The arc is made of four segments that are the result of active subduction of the Nazca Plate (Figure 1.1). The central Andes stand out along the chain as the greatest orogenic volume. The contrasting segmentation along the arc reflects the fact that the Andes have been built by a variety of processes that have changed along and across strike in nature, time, and intensity (Sempere et al., 1990). A long history of subduction, and crustal shortening and thickening is recorded in the units of the central Andes (Lucassen et al., 2001). The basement block known as Arequipa-Antofalla basement was accreted during the Sunsas Orogeny at 1.05 Ga (Loewy et al., 2004). Both the northern Arequipa, and southern Antofalla domains share evidence of metamorphic and magmatic cycles associated with the subsequent Pampean (~550-500 Ma) and Famatinian (~495-400 Ma) orogenies (Loewy et al., 2004). The transition between the two domains has been identified based on Pb isotope mapping of volcanic rocks sampling the underlying crust, with the low $^{206}Pb/^{204}Pb$ of Arequipa to the north of ~20-22° S and the high $^{206}Pb/^{204}Pb$ of Antofalla to the south (McFarlane et al., 1990; Worner et al., 1992; Mamani et al., 2010) (Figure 1.2). The PGCC lies predominantly in the Antofalla domain near the transition with the Arequipa domain (Mamani et al., 2010).

Prior to the crustal thickening that created the current plateau configuration, major tectonic reorganizations occurred that resulted in extensional and transtensional regimes (Lucassen et al., 2006; Mamani et al., 2010) before shifting back to a compressional regime (Sempere et al., 2007; Mamani et al., 2010) all between the Late Paleozoic and

the Mid Cretaceous. A transition from "normal" subduction, to flat slab occurred in the Early Oligocene (James and Sacks 1999). The major period of deformation and uplift in the central Andes has been within the last 30 Myr, starting in the Late Oligocene, and is thought to have been a result of an increase in the convergence rate of the Pacific and South American plates (Isacks 1988; Coira et al. 1993; Somoza 1998). In the Late Oligocene there was an increase in subduction rates with a dominantly E-W trend (de Silva 1989; Somoza 1998; Kay et al. 1999; Riller et al. 2001). Volcanism attributed to the Oligocene and Miocene is consistent with similar slab geometry of the present day (Coira et al., 1993; Kay and Coira, 2009). Deformation in the Altiplano intensified in the Middle Miocene while slab geometry was consistent with modern dip angles, as it was in the Late Oligocene (Kay and Coira, 2009). Meanwhile Allmendinger et al. (1997) argues that the Middle Miocene was a period of uplift due to shallowing of the subducting slab. This deformation led into a period of intense crustal thickening to ~65 km in the Late Miocene (11-7 Ma) (McGlashan et al., 2008). The subduction angle steepened significantly from 7-3 Ma, resulting in delamination of the lower crust (Kay et al., 1994, Kay et al., 1999). During the period from 3 Ma to Present, steepening of the slab continued to acquire its present geometry (Kay and Coira, 2009). Surveys by Kendrick et al. (2001) and Bevis et al. (1999) provide evidence for modern back arc deformation, suggesting the central Andes continue to be shortened, although at a modest rate (~9 mm/yr).

The result of active deformation since the Proterozoic is the 300 km wide, 4 km high Central Andean Plateau (Figure 1.3), situated above a 30° E-dipping segment of the

Nazca plate (Whitman et al., 1996). Subtle differences in deformation styles in the Puna and Altiplano Plateaus leading to variations in width along the eastern fold and thrust belts are the result of variations in pre-Neogene sedimentary rocks and pre-Andean crustal structures (Allmendinger et al., 1997; Riller, et al., 2003). The product of these variations is multiple tectonic fabrics, such as the arc-parallel N-S structures and the NW-SE transversal transcurrent lineaments (Riller et al., 2001; Kay and Coira, 2009) (Figure 1.4). A close relationship seems to exist between the location of large volume Neogene volcanism of the plateaus and regional tectonic fabrics (e.g. Viramonte et al., 1984; de Silva et al., 2006; Soler et al., 2007; Folkes et al., 2011). Though, in the western APVC de Silva (1989) noted that regional structures have some influence on the volcanic centers (orientation of collapse faults and apical grabens), but regional stress fields associated with each caldera system overprint and cross-cut regional fabrics.

Magmatic Context of the CVZ

Magmatism has persisted along the western continental margin of South America since the Early Paleozoic (Coira et al., 1982). Paleozoic magmatism is characterized by strongly peraluminous granites in the eastern cordillera (Miller, 1988). According to Miller (1989) magmas show signs of an increasing role of crustal melting since the Triassic. This time period is dominated by the calc-alkaline volcanics that persist today (Atherton, 1984).

The increased convergence rate of the Late Oligocene (Isacks, 1988; Coira et al., 1993; Somoza, 1998) led to the increased magmatism that dominated the central Andes throughout Tertiary. The calc-alkaline, arc signature became prevalent in the Late

Oligocene to Early Miocene with small shoshonites in the back arc and high-K basalts to basaltic andesites of the Altiplano-Puna Plateau (Hoke and Lamb, 2007; Davidson and de Silva, 1992). Shallowing of the subducting slab in the Early to Mid Miocene led to broadening of the arc with prevalent, long-lived high-K calc-alkaline andesite to dacite volcanism (e.g. Richards and Villaneuve, 2002). Modern volcanism in the CVZ is characterized by high-K, calc-alkaline andesite, dacite and rhyolite compositions, all with high crustal affinities (Stern, 2004). CVZ magmatism is of typical arc nature with LIL enrichment and HFSE depletion (Davidson et al., 1991) (Figure 1.5).

APVC/PGCC Setting

Steepening of the subducting slab in the Late Miocene facilitated lithospheric delamination and increased melting to produce large-volume volcanism on the Altiplano and Puna Plateaus (Kay and Coira, 2009; de Silva, 1989). Onset of the ignimbrite volcanism of the APVC signified the transition from typical arc magmatism to "flare-up" conditions (de Silva 1989; de Silva et al., 2006).Large volume, ignimbrite volcanism on the Central Andean Plateau began at approximately 10 Ma with large, but regionally restricted eruptions (de Silva, 1989; Petrinovic, 1994; Ort et al., 1996; Salisbury et al., 2011). Activity in the APVC continued until Recent times but was focused into pulses at 8, 6, and 4 Ma (de Silva et al., 2006; Salisbury et al., 2011). de Silva et al. (2006) show the peak of flare-up activity to be around 4 Ma and that there is a focusing of volcanic activity with time, which is also supported by Salisbury et al.(2011). Reconnaissance work of Salisbury et al. (2011) and this thesis add data from the PGCC to support the idea of volcanic focusing in the APVC.

The dominantly dacitic ignimbrites throughout the Central Andean ignimbrite province belong to a peraluminous high-K, calc-alkaline suite (Figure 1.6a) and have chemical and isotopic characteristics that attest to subduction-related mafic magmas variably contaminated by continental crust (Figure 1.6b), the most contaminated being those in the APVC (de Silva, 1989; Ort, 1996; de Silva et al., 2006; Kay, 2009; Folkes et al., 2011). The same LIL enrichment and HFSE depletion typical of arc magmatism is present in the APVC ignimbrites. APVC magma genesis follows a three stage model with evolution attributed to assimilation of crust during ascent (de Silva and Gosnold, 2007). Trace element and isotopic models invoke (1) a lower crustal zone of melting-assimilation-storage-homogenization (MASH) where mafic magmas pond and mix with crustal rocks (de Silva, 1989; Coira, 1993; Ort, 1996; Schmitt et al., 2001; Lindsay et al., 2001). In stage (2), intermediate magmas rise from the MASH zone and accumulate at around 20 km depth in the Altiplano-Puna Magma Body (APMB). The APMB is a seismically imaged low velocity layer that has been interpreted as a zone of 20-40% partial melt (Chmielowski et al., 1999; Zandt et al., 2003; de Silva et al., 2006). The extent of the APMB closely matches that of the APVC (de Silva and Gosnold, 2007; Salisbury et al., 2011). Ultimately (stage 3), magmas of intermediate compositions rise from the APMB and accumulate in the upper crust between 4 and 8 km (e.g. Lindsay et al., 2001; Schmitt et al., 2001) from where the predominately dacite and rhyodacite crystal rich eruptions are sourced.

The PGCC is the site of activity spanning nearly 5.5 Myr (Salisbury et al., 2011; Watts et al., 1999). The Pastos Grandes Caldera Complex is the northernmost complex of the APVC. Baker (1981) first identified a 30 km elliptical resurgent caldera structure with western and northern portions buried by younger volcanic deposits. The nested complex has deposited two large-volume ignimbrites (Salisbury et al., 2011; Ort et al., 2013). The complex has erupted remarkably homogenous magmas over its 5.5 Myr history. With the exception of the relatively small volume rhyolitic Juvina Shield, the complex is dominated by high K dacites (Salisbury et al., 2011). The chronostratigraphy combined with observations of the magma longevity suggest that the PGCC is the surface manifestation of an incrementally assembled magma system in the shallow crust (de Silva et al, 2006; Salisbury et al., 2011). Influxes of magma into the sub-caldera system were processed in the mid-crustal buffering zone (identified as the APMB by Chmielowski et al., 1999). The PGCC is one of many surface representations of this regional thermal and magmatic signal (Ort et al., 1996; Lindsay et al., 2001; Schmitt et al., 2001; Soler et al., 2007; de Silva and Gosnold, 2007).

References

Allmendinger, R. W., Jordan, T. E., Kay, S. M., & Isacks, B. L. (1997). The evolution of the Altiplano-Puna plateau of the central Andes. *Annual Review of Earth and Planetary Sciences*, *25*(1), 139-174.

Atherton, M. P. (1984). The coastal batholith of Peru. In *Andean Magmatism*(pp. 168-179). Birkhäuser Boston.

Bachmann, O., Miller, C. F., & De Silva, S. L. (2007). The volcanic–plutonic connection as a stage for understanding crustal magmatism. *Journal of Volcanology and Geothermal Research*, *167*(1), 1-23.

Bachmann, O., & Bergantz, G. W. (2004). On the origin of crystal-poor rhyolites: extracted from batholithic crystal mushes. *Journal of Petrology*, *45*(8), 1565-1582.

Bachmann, O., & Bergantz, G. W. (2008). Rhyolites and their source mushes across tectonic settings. *Journal of Petrology*, *49*(12), 2277-2285.

Bachmann, O., & Bergantz, G., (2008) The magma reservoirs that feed supereruptions. *Elements*, 4(1), 17-21.

Baker, M. C. W. (1981). The nature and distribution of Upper Cenozoic ignimbrite centres in the Central Andes. *Journal of Volcanology and Geothermal Research*, *11*(2), 293-315.

Bevis, M., Kendrice, E., Smalley, R., Herring, T., Godoy, J., & Galban, F. (1999). Crustal motion north and south of the Arica Deflection: Comparing recent geodetic results from the Central Andes. *Geochemistry, Geophysics, Geosystems*, *1*.

Buddington, A. F. (1959). Granite emplacement with special reference to North America. *Geological Society of America Bulletin*, *70*, 671.

Chmielowski, J., Zandt, G., & Haberland, C. (1999). The Central Andean Altiplano-Puna magma body. *Geophysical Research Letters*, *26*(6), 783-786.

Claiborne, L. L., Miller, C. F., & Wooden, J. L. (2010). Trace element composition of igneous zircon: a thermal and compositional record of the accumulation and evolution of a large silicic batholith, Spirit Mountain, Nevada. *Contributions to Mineralogy and Petrology*, *160*(4), 511-531.

Coira, B., Davidson, J., Mpodozis, C., & Ramos, V. (1982). Tectonic and magmatic evolution of the Andes of northern Argentina and Chile. *Earth-Science Reviews*, *18*(3), 303-332.

Coira, B., Kay, S. M., & Viramonte, J. (1993). Upper Cenozoic magmatic evolution of the Argentine Puna—a model for changing subduction geometry. *International Geology Review*, *35*(8), 677- 720.

Davidson, J. P., Harmon, R. S., & Wtimer, G. (1991). The source of central Andean magmas; Some considerations. *Andean magmatism and its tectonic setting*, *265*, 233.

Davidson, J. P., & de Silva, S. L. (1992). Volcanic rocks from the Bolivian Altiplano: Insights into crustal structure, contamination, and magma genesis in the central Andes. *Geology*, *20*(12), 1127-1130.

de Silva, S. L. (1989). Altiplano-Puna volcanic complex of the central Andes. *Geology*, *17*(12),1102-1106.

de Silva, S., Zandt, G., Trumbull, R., Viramonte, J. G., Salas, G., & Jiménez, N. (2006). Large ignimbrite eruptions and volcano-tectonic depressions in the Central Andes: a thermomechanical perspective. *Geological Society, London, Special Publications*, *269*(1), 47-63.

de Silva, S. L., & Gosnold, W. D. (2007). Episodic construction of batholiths: Insights from the spatiotemporal development of an ignimbrite flare-up. *Journal of Volcanology and Geothermal Research*, *167*(1), 320-335.

Folkes, C. B., Wright, H. M., Cas, R. A., de Silva, S. L., Lesti, C., & Viramonte, J. G. (2011). A re-appraisal of the stratigraphy and volcanology of the Cerro Galán volcanic system, NW Argentina. *Bulletin of volcanology*, *73*(10), 1427-1454.

Glazner, A. F., Coleman, D. S., & Bartley, J. M. (2008). The tenuous connection between high-silica rhyolites and granodiorite plutons. *Geology*,*36*(2), 183-186.

Grunder, A. L., Klemetti, E. W., Feeley, T. C., & McKee, C. M. (2006). Eleven million years of arc volcanism at the Aucanquilcha Volcanic Cluster, northern Chilean Andes: implications for the life span and emplacement of plutons. *Earth Sciences*, *97*, 415-436.

Hildreth, W. (1981). Gradients in silicic magma chambers: implications for lithospheric magmatism. *Journal of Geophysical Research: Solid Earth (1978–2012)*, *86*(B11), 10153-10192.

Hildreth, W. (2004). Volcanological perspectives on Long Valley, Mammoth Mountain, and Mono Craters: several contiguous but discrete systems. *Journal of Volcanology and Geothermal Research*, *136*(3), 169-198.

Hoke, L., & Lamb, S. (2007). Cenozoic behind-arc volcanism in the Bolivian Andes, South America: implications for mantle melt generation and lithospheric structure. *Journal of the Geological Society*, *164*(4), 795-814.

Isacks, B. L. (1988). Uplift of the central Andean plateau and bending of the Bolivian orocline. *Journal of Geophysical Research: Solid Earth (1978–2012)*,*93*(B4), 3211-3231.

James, D. E., & Sacks, I. S. (1999). Cenozoic formation of the Central Andes: A geophysical perspective. *Geology and Ore Deposits of the Central Andes (Skinner, BJ; editor). Society of Economic Geology, Special Publication*, *7*, 1-26.

Johnson, C. M., Lipman, P. W., & Czamanske, G. K. (1990). H, O, Sr, Nd, and Pb isotope geochemistry of the Latir volcanic field and cogenetic intrusions, New Mexico, and relations between evolution of a continental magmatic center and modifications of the lithosphere. *Contributions to Mineralogy and Petrology*,*104*(1), 99-124.

Kay, S. M., Coira, B., & Viramonte, J. (1994). Young mafic back arc volcanic rocks as indicators of continental lithospheric delamination beneath the Argentine Puna plateau, central Andes. *Journal of Geophysical Research: Solid Earth (1978 –2012)*, *99*(B12), 24323-24339.

Kay, S. M., Mpodozis, C., & Coira, B. (1999). Neogene magmatism, tectonism, and mineral deposits of the Central Andes (22 to 33 S latitude). *Geology and Ore Deposits of theCentral Andes (Skinner, BJ; editor). Society of Economic Geologists, Special Publication, 7*, 27-59.

Kay, S. M., & Coira, B. L. (2009). Shallowing and steepening subduction zones, continental lithospheric loss, magmatism, and crustalflow under the Central

Andean Altiplano-PunaPlateau. *Backbone of the Americas: shallow subduction, plateau uplift, and ridge and terrane collision*, *204*, 229.

Kendrick, E., Bevis, M., Smalley, R., & Brooks, B. (2001). An integrated crustal velocity field for the central Andes. *Geochemistry, Geophysics, Geosystems*,*2*(11).

Lindsay, J. M., De Silva, S., Trumbull, R., Emmermann, R., & Wemmer, K. (2001). La Pacana caldera, N. Chile: a re-evaluation of the stratigraphy and volcanology of one of the world's largest resurgent calderas. *Journal of Volcanology and Geothermal Research*, *106*(1), 145-173.

Lipman, P. W. (2007). Incremental assembly and prolonged consolidation of Cordilleran magmachambers: Evidence from the Southern Rocky Mountain volcanic field. *Geosphere*, *3*(1), 42-70.

Lipman, P. W. (1984). The roots of ash flow calderas in western North America: Windows into the tops of granitic batholiths. *Journal of Geophysical Research: Solid Earth (1978– 2012)*, *89*(B10), 8801-8841.

Loewy, S. L., Connelly, J. N., & Dalziel, I. W. (2004). An orphaned basement block: The Arequipa-Antofalla Basement of the central Andean margin of South America. *Geological Society of America Bulletin*, *116*(1-2), 171-187.

Lucassen, F., Becchio, R., Harmon, R., Kasemann, S., Franz, G., Trumbull, R., & Dulski, P. (2001). Composition and density model of the continental crust at an active continental margin—the Central Andes between 21 and 27 S.*Tectonophysics*, *341*(1), 195-223.

Mamani, M., Wörner, G., & Sempere, T. (2010). Geochemical variations in igneous rocks of the Central Andean orocline (13 S to 18 S): tracing crustal thickening and magma generation through time and space. *Geological Society of America Bulletin*, *122*(1-2), 162-182.

Macfarlane, A. W., Marcet, P., LeHuray, A. P., & Petersen, U. (1990). Lead isotope provinces of the Central Andes inferred from ores and crustal rocks. *Economic Geology*, *85*(8), 1857-1880.

McGlashan, N., Brown, L., & Kay, S. (2008). Crustal thickness in the central Andes from teleseismically recorded depth phase precursors. *Geophysical Journal International*, *175*(3), 1013-1022.

Miller, J. F. (1988). *Granite petrogenesis in the Cordillera Real, Bolivia and crustal evolution in the Central Andes* (Doctoral dissertation, Open University).

Miller, J. F., & Harris, N. B. W. (1989). Evolution of continental crust in the Central Andes; constraints from Nd isotope systematics. *Geology*, *17*(7), 615-617.

Ort, M. H., Silva, S. L., Jiménez, C., Jicha, B. R., & Singer, B. S. (2013). Correlation of ignimbrites using characteristic remanent magnetization and anisotropy of magnetic susceptibility, Central Andes, Bolivia. *Geochemistry, Geophysics, Geosystems*, *14*(1), 141-157.

Ort, M. H., Coira, B. L., & Mazzoni, M. M. (1996). Generation of a crust-mantle magma mixture: magma sources and contamination at Cerro Panizos, central Andes. *Contributions to Mineralogy and Petrology*, *123*(3), 308-322.

Petrinovic, I. A. (1994). *Volcanismo Cenozoico asociado al lineamiento Calama–Olacapato–El Toro en el tramo comprendido entre San Antonio de los Cobres y Olacapato, provincial de Salta, Argentina* (Doctoral dissertation, Phd Thesis Universidad Nacional de Salta, Argentina. 234 p.Unpublished).

Richards, J. P., & Villeneuve, M. (2002). Characteristics of late Cenozoic volcanism along the Archibarca lineament from Cerro Llullaillaco to Corrida de Cori, northwest Argentina. *Journal of Volcanology and Geothermal Research*,*116*(3), 161-200.

Riller, U., Petrinovic, I., Ramelow, J., Strecker, M., & Oncken, O. (2001). Late Cenozoic tectonism, collapse caldera and plateau formation in the central Andes. *Earth and Planetary Science Letters*, *188*(3), 299-311.

Riller, U., Oncken, O. (2003) Growth of the Central Andean Plateau by tectonic segmentation is controlled by the gradient in crustal shortening. *Journal of Geology* 111, 367-384.

Salisbury, M. J., Jicha, B. R., de Silva, S. L., Singer, B. S., Jiménez, N. C., & Ort, M. H. (2011). $^{40}Ar/^{39}Ar$ chronostratigraphy of Altiplano-Puna volcanic complex ignimbrites reveals the development of a major magmatic province. *Geological Society of America Bulletin*, *123*(5-6), 821-840.

Schmitt, A., De Silva, S., Trumbull, R., & Emmermann, R. (2001). Magma evolution in the Purico ignimbrite complex, northern Chile: evidence for zoning of a dacitic magma by injection of rhyolitic melts following mafic recharge.*Contributions to Mineralogy and Petrology*, *140*(6), 680-700.

Sempere, T., Hérail, G., Oller, J., & Bonhomme, M. G. (1990). Late Oligocene-early Miocene major tectonic crisis and related basins in Bolivia. *Geology*,*18*(10), 946 -949.

Smith, R. L. (1960). Ash flows. *Geological Society of America Bulletin*, *71*(6), 795-841.

Smith, R. L. (1979). Ash-flow magmatism. *Ash-flow tuffs: Geological Society of America Special Paper*, *180*, 5-27.

Soler, M. M., Caffe, P. J., Coira, B. L., Onoe, A. T., & Kay, S. M. (2007). Geology of the Vilama caldera: a new interpretation of a large-scale explosive event in the Central Andean plateau during the Upper Miocene. *Journal of volcanology and geothermal research*, *164*(1), 27-53.

Somoza, R. (1998). Updated azca (Farallon)—South America relative motions during the last 40 My: implications for mountain building in the central Andean region. *Journal of South American Earth Sciences*, *11*(3), 211-215.

Stern, C. R. (2004). Active Andean volcanism: its geologic and tectonic setting. *Revista geológica de Chile*, *31*(2), 161-206.

Tappa, M. J., Coleman, D. S., Mills, R. D., & Samperton, K. M. (2011). The plutonic record of a silicic ignimbrite from the Latir volcanic field, New Mexico. *Geochemistry, Geophysics, Geosystems*, *12*(10).

Viramonte, J. G., Galliski, M. A., Saavedra, V. A., Aparicio, A., García-Cacho, G. L., & Escorza, C. M. (1984). El finivulcanismo básico de la depresión de Arizaro, provincia de Salta. *IX Cong. Geol. Arg, Actas*, *3*, 234-251.

Whitman, D., Isacks, B. L., & Kay, S. M. (1996). Lithospheric structure and along-strike segmentation of the Central Andean Plateau: seismic Q, magmatism, flexure, topography and tectonics. *Tectonophysics*, *259*(1), 29-40.

Wörner, G., Moorbath, S., & Harmon, R. S. (1992). Andean Cenozoic volcanic centers reflect basement isotopic domains. *Geology*, *20*(12), 1103-1106.

Zandt, G., Leidig, M., Chmielowski, J., Baumont, D., & Yuan, X. (2003). Seismic detection and characterization of the Altiplano-Puna magma body, central Andes. *Pure and Applied Geophysics*, *160*(3-4), 789-807.

Zimmerer, M. J., & McIntosh, W. C. (2012). The geochronology of volcanic and plutonic rocks atthe Questa caldera: Constraints on the origin of caldera-related silicic magmas. *Geological Society of America Bulletin*, *124*(7-8), 1394-1408.

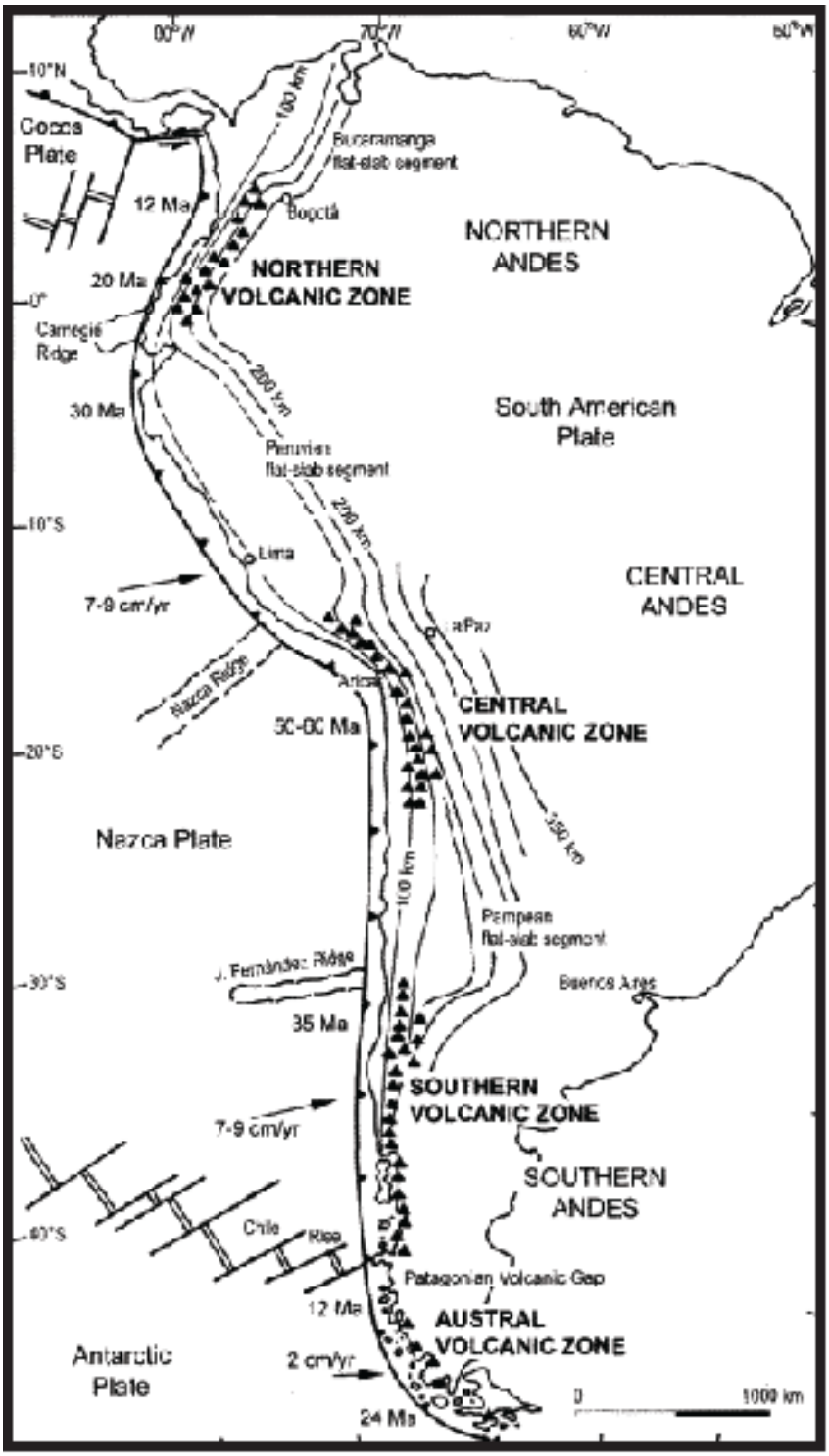

Figure1.1. The segments of the Andes are shown on the schematic map from Stern (2004). The map highlights the subducting Nazca plate and the depth to the Benioff zone, indicated with depth in kilometers. The focus of this discussion is on the Central Volcanic Zone (CVZ) which stretches from southern Peru to northern Chile/Argentina.

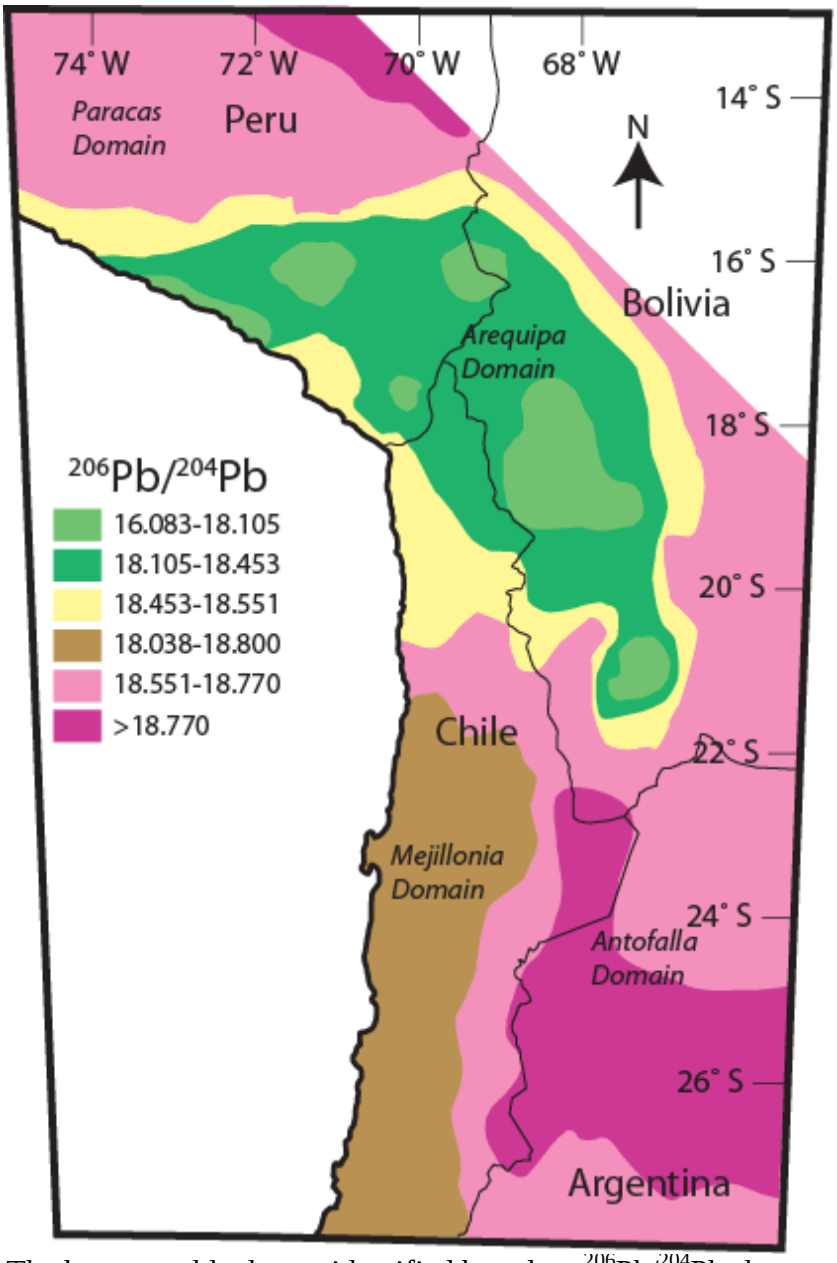

Figure1.2. The basement blocks are identified based on $^{206}Pb/^{204}Pb$ shown on the map of the CVZ modified from Mamani et al. (2010). The Arequipa and Antofalla Domains make up much of the CVZ. The margin between these two domains is located in southwestern Bolivia near the northern extent of the APVC where the PGCC is located.

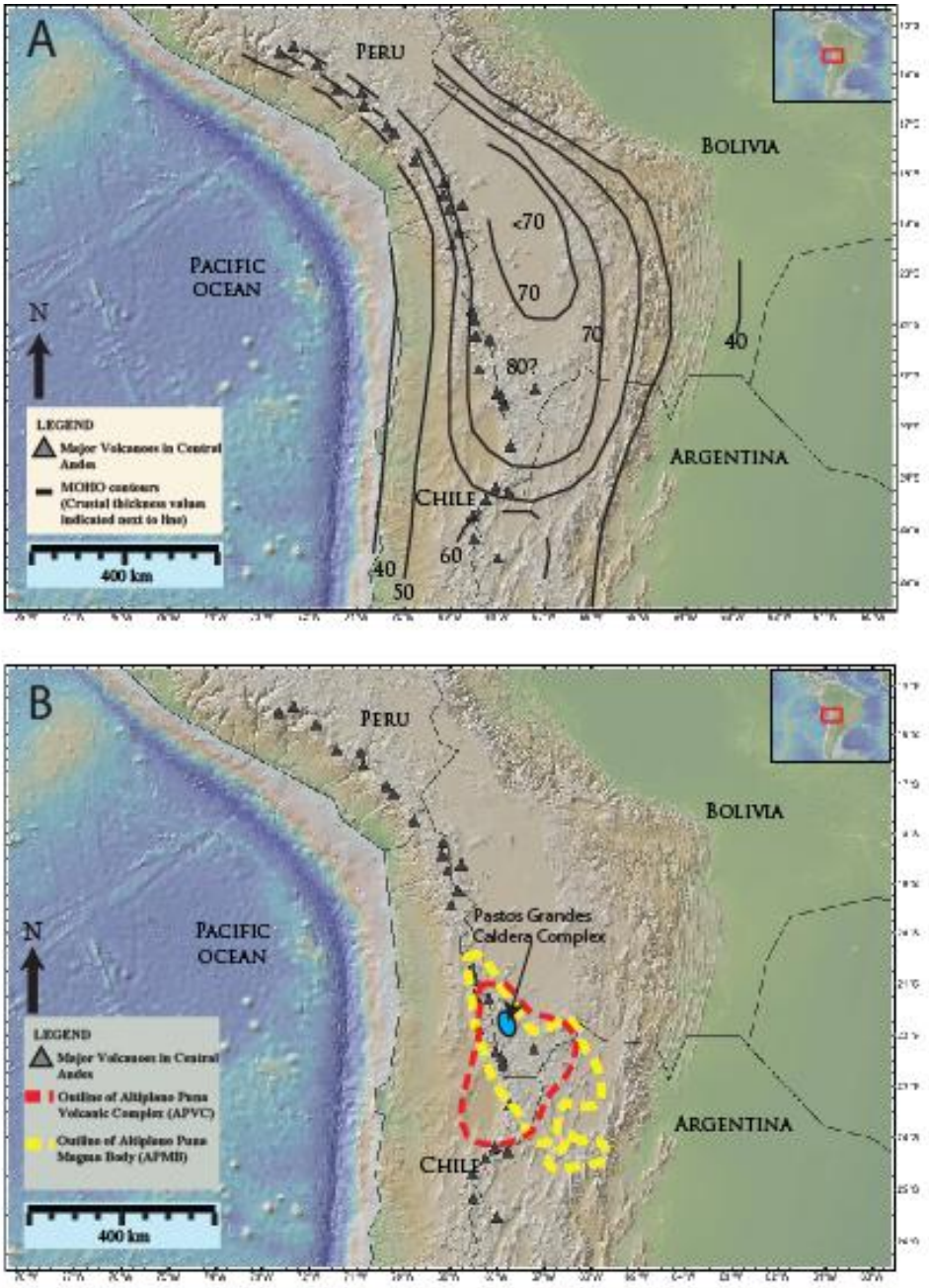

Figure1.3. Maps of the CVZ highlight the crustal variations in thickness across the arc (contours are modified from Allmendinger et al., 1997 and references therein). The crust of the CVZ is thickest in southwestern Bolivia, in the middle of the APVC (noted in Figure 1.3B). The extent of the APVC is shown in the red dotted line (taken from ignimbrite distributions of Salisbury et al., 2011; Lindsay et al., 2011, and this thesis). The low velocity zone first identified by Chmielowski et al. (1999) was interpreted to be a zone of partial melt at approximately 17-20 km depth below the APVC (Zandt et al., 2003). The extent of the zone of partial melt (the Altiplano Puna Magma Body, APMB) is shown in yellow from de Silva et al., 2006).

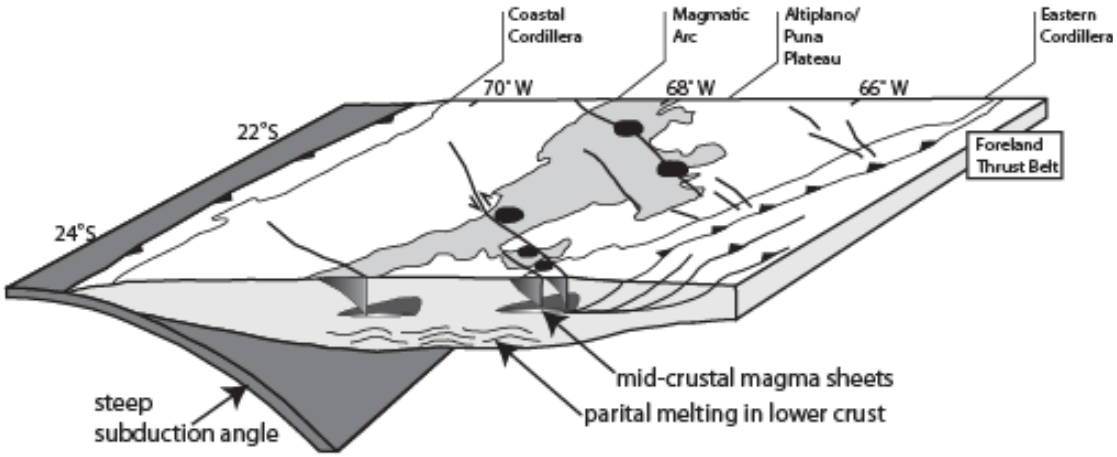

Figure 1.4. An idealized cross sectional view of the Central Andes, through the Altiplano/Puna Plateaus (modified from Riller et al., 2001). The modern magmatic arc is shown as a dark band that also encompasses the large calderas of the APVC. Many of the calderas lie along, or are influenced by regional tectonic lineaments. The steepening of the subduction angle at around 10 Ma triggered a tectonic transition to transtension and the creation of a series of NW/SE striking regional faults.

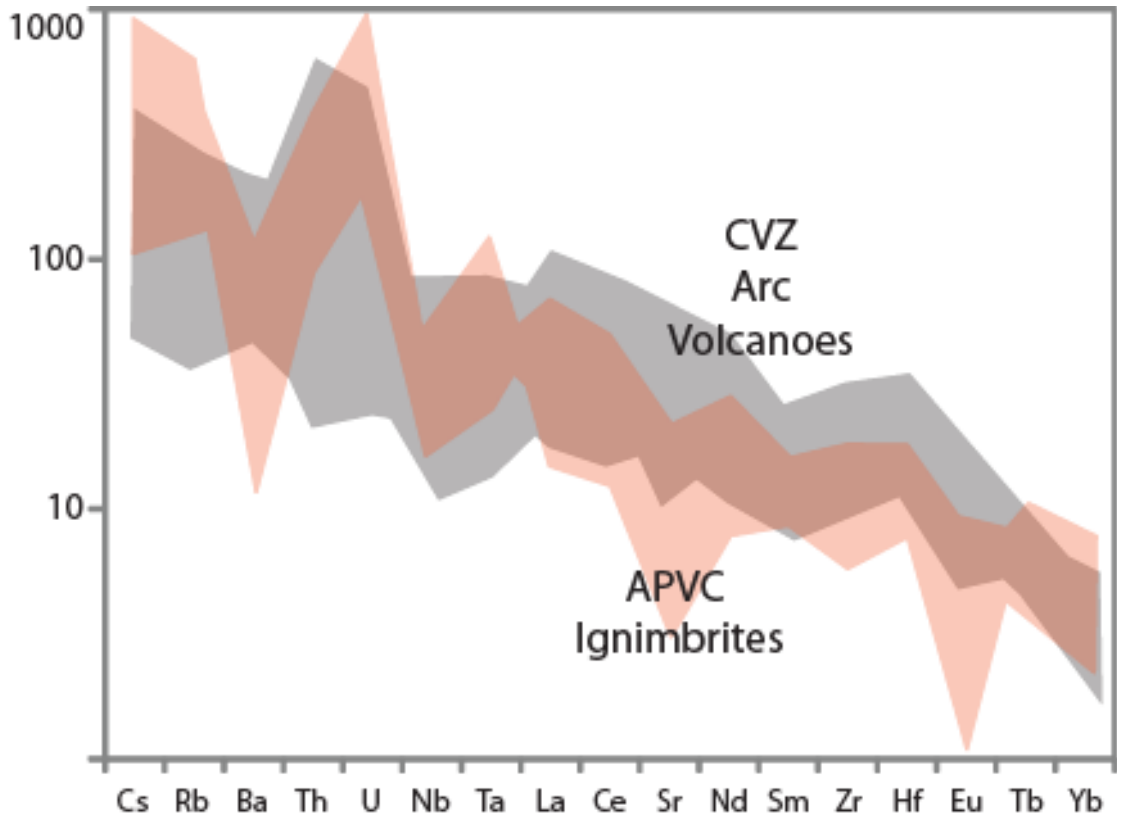

Figure 1.5. Normalized trace element spider diagrams show the arc affinity for both the CVZ (grey) and APVC (red). Elevated LIL and depleted HFSE are characteristic of both suites of samples.

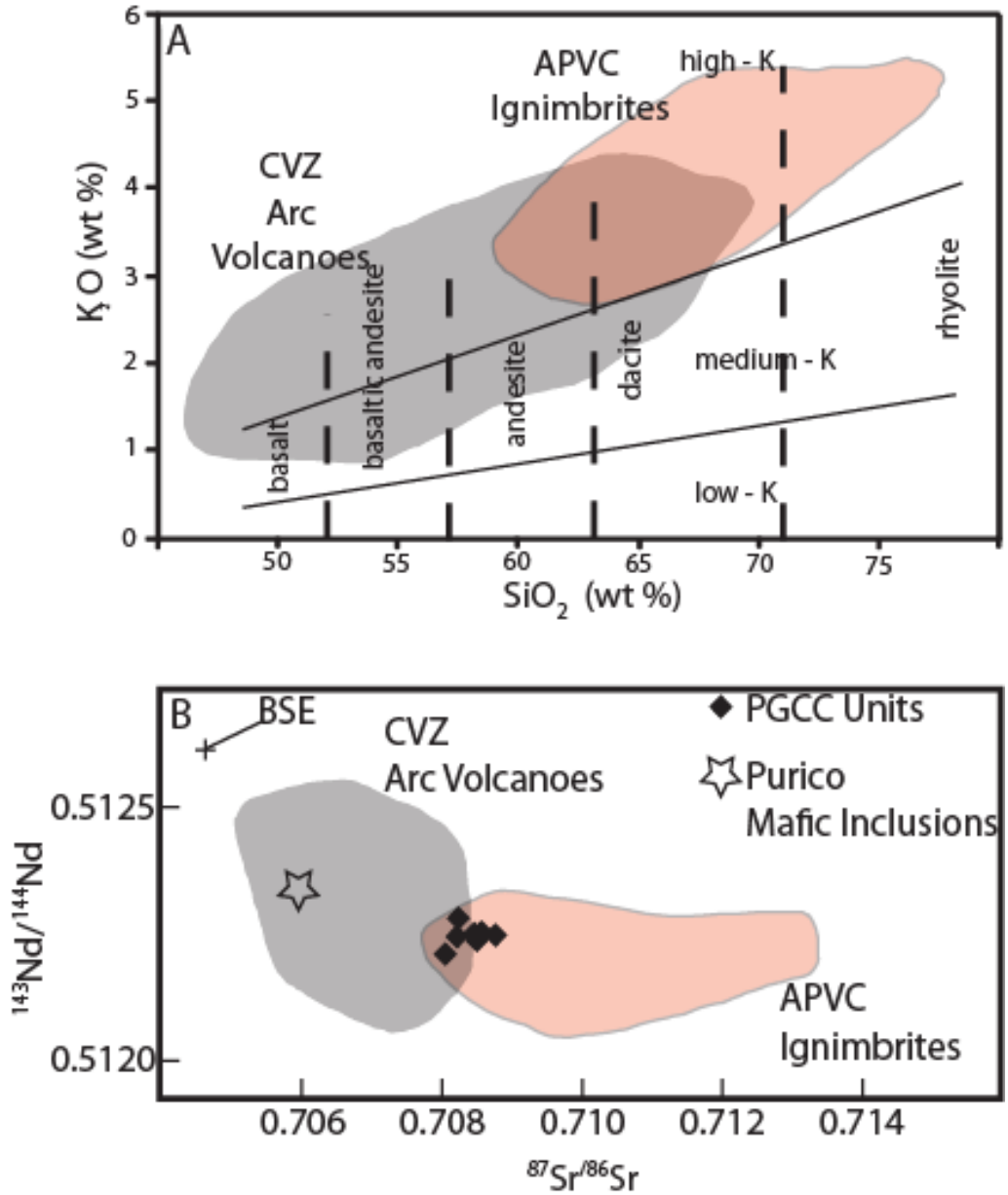

Figure 1.6. Whole rock classification diagrams show overlap of the arc and the APVC magmatism. The APVC compositions show signs of crustal contamination with higher $^{87}Sr/^{86}Sr$ leading to more evolved SiO_2 concentrations. Arc fields are from Mamani (2010) and APVC fields are a composite of de Silva et al. (2006), Lindsay et al. (2001) and this work. The composition of the Purico mafic inclusions is shown from Schmitt et al. (2001). These inclusions are thought to represent the parental source feeding the APMB.

Table 1.1. Research Plan

Objectives	Strategy	Methods
1)Understanding the Volcanology, Stratigraphy and Structures of the Pastos Grandes Caldera Complex	-Build the stratigraphic framework through field and remote mapping -Determine the temporal and spatial distributions as well as volumes of the various volcanic units -Understand the context of the Pastos Grandes caldera within the regional structures	➢ Field Mapping ➢ Remote Sensing ➢ Ar/Ar Age Dating
2)Understanding the development and evolution of the Pastos Grandes magmatic system	-Geochemically & petrologically characterize each magmatic stage -Isotopically characterize each magmatic cycle -Geochemically model the evolution of the magmatic system	➢ Petrography ➢ Whole Rock Major and Trace Element Chemistry ➢ Whole Rock Isotope Chemistry
3)Understanding the timescales of magma accumulation associated with each caldera-forming eruption	-Determine crystal residence times and inheritance for the different magmatic cycles -Compare crystal residence times to eruption ages	➢ SIMS U-Pb and trace element zircon analyses

CHAPTER 2

The Pastos Grandes Caldera Complex: Establishing the chronostratigraphy and volcanology of a nested, resurgent caldera in southwest Bolivia

Jason F. Kaiser

Shanaka de Silva

Mayel Sunagua

Abstract

We summarize a revised stratigraphy, areal distribution and volume calculations for ignimbrites of the Pastos Grandes Caldera Complex in southwest Bolivia. From interpretations of stratigraphy and structures along the caldera margins, we propose an asymmetric style collapse hinged along the north and western boundaries. Both the early Chuhuilla, and the later Pastos Grandes calderas share the hinge and much of the eastern collapse scarp, however the topographic boundary of the Chuhuilla caldera defines a much larger area (>1700 km^2) compared to the Pastos Grandes (870 km^2). Our volume calculations reveal that the vast majority of the ignimbrite volume lies within the Chuhuilla and Pastos Grandes calderas (92 and 75% respectively). New volume calculations using various different methods update previous estimates, with the Chuhuilla now at approximately1300 km^3 and the Pastos Grandes at 800 km^3 cutting previous estimates nearly in half. The physical properties of the ignimbrites, their areal distribution limited by low regional topographic elements, support paleomagnetic characteristics suggesting dense sluggish pyroclastic flows. The style of eruption that fed

these flows must have included low, short-lived columns with early caldera collapse, thought the true height and durations are not quantified here.

Introduction

The stratigraphic record of voluminous explosive eruptions can be used to shed light on the temporal evolution of the associated magmatic systems. Large, caldera-forming eruptions are capable of evacuating 10^3 km^3 of magma, providing views into the construction of large upper crustal batholiths. Understanding the time transgressive sequence of ignimbrites and lavas from a single caldera complex can provide information about the long-term magma flux rates and upper crustal magma evolution.

In the Altiplano Puna Volcanic Complex (APVC) of the central Andes (Figure 2.1), ignimbrite sequences from multiple nested caldera complexes are well exposed and preserved (de Silva, 1989; de Silva et al., 2006). While many of these ignimbrite sequences have been identified (Ort, 1993; Lindsay et al., 2001; Soler et al., 2009; Salisbury et al., 2011), detailed mapping of their distribution and source calderas has been limited by the large size of the structures, the logistically demanding terrain, and the lack of vertical exposures. A detailed understanding of the ignimbrite the stratigraphy, eruptive volumes, and caldera structures can elucidate the eruption mechanisms and emplacement of large volume ignimbrites (e.g. Lindsay et al, 2001; Folkes et al., 2011). Understanding the volcanic stratigraphy can help to constrain the temporal evolution of long-lived silicic magmatic systems that fed the ignimbrite flare-up of the APVC (Schmitt et al., 2001; Lindsay et al., 2001)

In this paper we focus on the stratigraphy of the ignimbrite succession and the structures associated with the Pastos Grandes Caldera Complex (PGCC) (Figure 2.2). The Pastos Grandes Caldera, which lies at the northern extent of the APVC, shares many traits, such as scale and morphology with classic long-lived silicic systems (Folkes et al., 2012; Mason et al., 2004; Lindsay et al., 2001; Lipman, 1997). The PGCC produced eruptions of the same order of magnitude as the Fish Canyon Tuff, Cerro Galan Ignimbrite, Atana Ignimbrite, Toba Tuff and others of the APVC, which are all considered to be the largest explosive eruption on Earth (Lipman, 1997; Folkes et al., 2011; Lindsay et al., 2001; Chesner, 2011). With new field mapping and updated geochronology we present a complete stratigraphy and a more accurate estimation of exposed aerial extents and volumes for each ignimbrite. These volumes can have a large effect on models of eruption dynamics as well as magma flux calculations. In the APVC, these magma flux calculations play a large role in understanding the thermal history of the crust during the ignimbrite flare-up. A summary of caldera collapse structures is also presented. Altogether, these data provide key information on the evolution of the PGCC and its magmatic system, allowing the PGCC to be put into context with the rest of the APVC and other large silicic magmatic systems.

Previous Work/Geologic Background

The Altiplano-Puna Volcanic Complex (APVC), which hosts the PGCC has been the site of numerous large-volume silicic ignimbrite eruptions since 10 Ma (de Silva et al., 1989; de Silva et al., 2006; Salisbury et al., 2011). These deposits are dominated by crystal-rich dacite ignimbrites with very minor volumes of rhyolite and andesite distributed over

70,000 km^2 in Argentina, Chile, and Bolivia. A total magma equivalent volume exceeding 13,000 km^3 has been estimated to have been erupted during the flare-up. Eruptions are organized into pulses of activity that punctuate the 10 Ma history of the APVC (de Silva and Gosnold, 2007; Salisbury et al., 2011). During the eruptive pulses magma supply rates were high, allowing for the growth of large-volume silicic magma chambers over the course of hundreds of thousands to millions of years (de Silva and Gosnold, 2007; Chapter 4 of thesis).

The Pastos Grandes Caldera Complex is the northernmost complex of the APVC. Baker (1981) first identified a 30 km elliptical resurgent caldera structure with western and northern portions buried by younger volcanic deposits. This was named the Pastos Grandes caldera after the eponymous salar that occupied much of the northern moat of the caldera. Baker and Francis (1978) assigned a K-Ar biotite age of 5.9 ± 0.3 Ma (Table S2.1) to the Chuhuilla ignimbrite the lowest in the sequence around the caldera. Mapping by the Bolivian Geological Survey identified two younger ignimbrites on the flanks, the Alota and Pastos Grandes Ignimbrites (Carrasco, 1978). de Silva and Francis (1989, 1991) identified two ignimbrites from the caldera; an unnamed 3.2 Ma unit and the 5.6 Ma Chuhuilla ignimbrite. They also suggested a third older unit, the 8.1 Ma Sifon ignimbrite found close to the southwestern flank of the caldera in Chile may have been erupted from the vicinity of the PGC. Pacheco and Ramirez (1997) mapped what they referred to as the Juvina tuffs around Cerro Juvina and obtained a K-Ar age of 6.5 ± 0.3 Ma. Pacheco and Ramirez (1997) also mapped what they referred to as the Chatola tuffs

east of the caldera and attributed the thickness and high degree of induration to a proximal source at the Pastos Grandes Caldera.

Modern studies have refined the ages and the general stratigraphy (e.g., Watts et al., 1999; Salisbury et al., 2011, Ort et al., 2013) and confirmed that the PGCC was the site of two major ignimbrite-forming supereruptions; the Chuhuilla ignimbrite at 5.45 ± 0.02 Ma, and the Pastos Grandes ignimbrite (now including the Chatola Tuffs) at 2.89 ± 0.01 Ma. These ignimbrite eruptions produced a nested resurgent caldera. The Juvina Tuffs (or Artola ignimbrite) are now known to have been erupted from the rhyolitic, Juvina ignimbrite shield at 5.23 ± 0.01 Ma. Characteristic remanent magnetization (ChRM) and anisotropy of magnetic susceptibility (AMS) positively correlate the extents of the major outflow facies as well as link them to the Pastos Grandes caldera (Ort et al., 2013). The Sifon ignimbrite is now known to have been erupted from another close-by structure but is not associated with the PGCC. All lava domes within the complex are coeval with, or post-date the ignimbrite eruptions representing post-caldera activity. The youngest activity is the Late Pleistocene, 0.94 to 0.84 Ma Chascon-Runtu Jarita dome complex (Watts et al., 1999). This chain of blocky lava domes formed along the southwest margin of the caldera and represents the latest episode of activity in the PGCC and the APVC as a whole. This general stratigraphic framework is the basis for the detailed study presented here.

Methods

The stratigraphic section was built from field mapping, which included correlation and section logging of specific stratigraphic sections combined with previous age data (see Table 2.1 and S2.1) and paleomagnetic correlation (Ort et al, 2013). Field

reconnaissance of all safely accessible sections (such as the Río Chaira Waykho drainage between Cerro Chuhuilla and the Alota Ignimbrite Shield in Figure 2.2) was done to build stratigraphic sections. Analysis of satellite imagery (Landsat TM and Google Earth) was used to capture the full distribution of the deposits over the ~6000 km^2 area.

$^{40}Ar/^{39}Ar$ Geochronology

We collected and analyzed five samples of lavas flows along the Serrania Khenwal and post-climactic domes to supplement the regional dataset (Table S2.1) (Salisbury et al., 2011). As sanidine was not observed in the lavas, biotite was separated by crushing sieving, and heavy liquid separation. Only the freshest, black, euhedral, unaltered biotites with no adhering glass were selected. Aliquots of ~ 50 mg were irradiated at the Oregon State University (OSU) TRIGA research reactor. Incremental heating $^{40}Ar/^{39}Ar$ age determinations were performed on the CO_2 laserprobe and MAP-215/50 mass spectrometer at OSU. Samples were heated in 50-100° C increments, from 500°C to total fusion in 13 steps. One exception, a Cerro Chuhuilla lava flow, was analyzed in multiple total fusion aliquots to check for age heterogeneity within the separated biotites. The plateau ages and argon isochron ages were calculated using the ArArCALC v2.2 software (Koppers, 2002) and are presented in Figure 2.3. Both the previously published $^{40}Ar/^{39}Ar$ sanidine ages and the new $^{40}Ar/^{39}Ar$ biotite ages are shown in Tables 2.1 and S2.

Whole rock analysis of the Pastos Grandes units was done via X-Ray Fluorescence (XRF) and Inductively Coupled Plasma – Mass Spectrometry (ICP-MS) at the Washington State University GeoAnalytical Lab. Sample aliquots were crushed and powdered for analysis at Washington State University. For major element analyses using

XRF (ThermoARL), powders were added to the dilithium tetraborate flux and fused following the methods of Johnson et al. (1999).

The Pastos Grandes Caldera Complex

Two major caldera-forming ignimbrite eruptions, associated lavas, and satellite ignimbrite shield and a young dike-related dome complex defines the Pastos Grandes Caldera Complex (PGCC). The complex covers 7000 km^2, elevation averages ~4500 m and is dominated by a nested pair of calderas, the shared topographic margins of which are defined by the arcuate line of lavas extending south from Cerro Chuhuilla (Serrania Khenwal) and by a subtle topographic rise to the West (Figure 2.4). The distinct resurgent dome is associated with the younger Pastos Grandes caldera. Both the Chuhuilla and Pastos Grandes calderas are thought to share the western margin of the caldera. The Alota-Juvina ignimbrite shield is to the east, outside the collapsed caldera depression. Cross sections show the collapse relationship between the lavas and ignimbrites (Figure 2.5).

Available age data and our new stratigraphic framework define a volcanic history extending from 5.6 Ma to 0.082 Ma, a time period of ~5.5 Myr. The following description refers to Figure 2.6.

Eruptive cycle 1 – *Chuhuilla Caldera*; the earliest activity is recorded in the Chuhuilla ignimbrite (5.45 ± 0.02 Ma; Table 2.1b, Salisbury et al., 2011). Associated lavas immediately overlying these are found in the Cerro Chuhuilla and Serrania Khenwhal. While two biotite Ar-Ar ages (6.10 ± 0.09 Ma, and 6.63 ± 0.09 Ma) from these lavas are

older than the sanidine and biotite ages of the Chuhuilla ignimbrite (5.45±0.02 Ma), stratigraphic relations clearly show these are younger (see below for further discussion) and represent post Chuhuilla ring fracture volcanism. Resurgence of this caldera is recorded by the Cerro Kapina welded ignimbrite and lava massif and the Quebrada Honda dome. The Chuhuilla ignimbrite, Cerro Kapina, and Q. Honda dome, Cerro Chuhuilla and the lavas of the Serrania Khenwal centers are all included in the Chuhuilla caldera cycle.

Eruptive cycle 2 – Alota – Juvina Ignimbrite Shield. At 5.23 ± 0.01 Ma (Table 2.1b, Salisbury et al., 2011) activity the locus of volcanism shift to 10 km the east resulting in a sequence of phreatomagmatic deposits, the single thick Alota ignimbrite and a final effusion of the Juvina domes that overly the pyroclastic deposits. No collapse caldera is seen.

Eruptive cycle 3 – Pastos Grandes Caldera. At 2.89 ± 0.01 Ma (Table 2.1a & b, Salisbury et al., 2011) activity shifted back into the main caldera depression and eruption of the Pastos Grandes ignimbrite resulted in a second collapse and resurgence. A group of post-caldera domes surround the resurgent center and collectively called the central dome complex. These have ages ranging from within error of the PGI eruption to 2.20 ± 0.04 Ma.

Eruptive cycle 4 – Chascon-Runtu Jarita dome complex. A linear group of coherent dike fed andesite-rhyolite composite domes with ages (~85 ka, Watts et al., 1999). Since this

has been described in detail by Watts et al., 1999, it will not be further detailed, with the exception of emplacement relative to regional structures in the discussion.

As a group, the pumice and lavas of the PGCC belong to the high – K calc alkaline suite (Figure 2.7). Chuhuilla crystal-rich pumice ranges from andesite to dacite with 61 – 69 wt% SiO_2. Pastos Grandes crystal-rich pumice is very similar to that of Chuhuilla, but more restricted with 64 – 68 wt% SiO_2. In contrast, pumice samples of the Alota ignimbrite are high silica rhyolites with 74 – 77 wt% SiO_2. Banded pumice does exist in the Pastos Grandes and Chuhuilla ignimbrites but is rare. Whole rock major element compositions are shown in Table S2.2.

Fresh lava samples from flows along the eastern collapse scarp (Serrania Khenwal), Cerro Chuhuilla, and the Post-Climactic Domes, as well as the Cerro Juvina Ignimbrite Shield, have a similar composition range to the respective ignimbrites (Figure 2.7). Serrania Khenwal and Cerro Chuhuilla have a combined compositional range of 61-65 wt% SiO_2. Post-climactic lava domes have a compositional range of 64-69 wt% SiO_2. Lavas of the Cerro Juvina Ignimbrite Shield match the compositions of the Alota Ignimbrite with 74 – 77 wt % SiO_2. The lavas along the scarp and among the central domes share a compositional range with the large volume ignimbrites (64 -68 wt% SiO_2).

Stratigraphy and Unit Descriptions

The stratigraphy around the PGCC is shown in Figure 2.8. The stratigraphy of the outflow facies of the ignimbrites is preserved exceptionally well in the Rio Chaira Waykho area to the northeast of the caldera (Figure 2.9). The Pastos Grandes Ignimbrite

buries much of the stratigraphy surrounding the caldera, with the exception of distal outcrops of the Chuhuilla Ignimbrite to the North and South of the complex. Modern arc-related volcanoes are built directly on the Pastos Grandes Ignimbrite to the West and north obscuring the ignimbrites most distal extent. The Alota Ignimbrite is not extensive but is demonstrably limited to the Alota basin on the eastern flank of the caldera. Field photos supporting the stratigraphy discussion are shown in Figure 2.10.

Unit Descriptions

Chuhuilla Ignimbrite

The oldest unit of the PGCC is the Chuhuilla ignimbrite (5.45 ±0.02 Ma $^{40}Ar/^{39}Ar$ in Sanidine age). It is positively distinguished from the stratigraphically co-located Alota and Pastos Grandes ignimbrites by ChRM (169° and 179° angular separation respectively, Ort et al., 2013). The Chuhuilla ignimbrite is exposed over an aerial distribution of approximately 6400 km^2. The distribution is restricted to the East by Paleozoic strata and to the West by a topographic rise that makes up the base of the modern arc (Geologic Map of Figure 2.2). These bounding features extend the distribution North and South of the caldera (Figure S2.1).

The outflow facies of the ignimbrite is poorly sorted, pumice and lithic-poor, crystal-rich and matrix supported. The proximal exposures are massive and highly indurated while distal outcrops are only moderately indurated. Maximum thicknesses of over 70 m were observed as much as 20 km from the caldera; however typical exposed thicknesses nearer to the caldera are between 20 and 30 m. The base of the section was never observed.

Pumice and lithic concentration varies throughout the unit. Lithic content is estimated at 5% however lithics are larger and more concentrated near the lower portions of the exposures. Pumice is typically small (1-2 cm), and concentrated closer to the top of the section. Chuhuilla pumice is crystal rich (45%) with phenocrysts of plagioclase (40%), quartz (25%), biotite (15%), sanidine (15%), and amphibole (<5%). Analyzed pumice blocks contain 68-69 wt % SiO_2. Dense, crystal rich enclaves (first noted in de Silva, 1989) with plagioclase, quartz, biotite, and amphibole are common in the pumice of the unit.

Cerro Chuhuilla and Scarp Lavas

Overlying the Chuhuilla ignimbrite are the multiple lava flows make up the eastern collapse scarp (Serrania Khenwal) and Cerro Chuhuilla along the eastern margin of the caldera. The total length of the suite that makes up Serrania Khenwal is over 48 km from the northern margin of Cerro Chuhuilla to the southern extent of the scarp. The scarp is very narrow with short, thick flows of lava; however, some of the flows can be traced to 6-10 km away from their source. The andesite to dacite lavas show variable degrees of alteration, but are typically dark and glassy with phenocrysts of plagioclase (80%), biotite (15%), and quartz (5%), with trace amphibole. Phenocrysts are typically small (1-3 mm) and euhedral. Six analyzed samples contain 61-64 wt% SiO_2. Discrepancies between the $^{40}Ar/^{39}Ar$ ages and the field stratigraphic relationships arise around the Cerro Chuhuilla Lava dome on the northeastern flank of the caldera. Along the margins of the Cerro Chuhuilla volcano the lavas are seen capping the Chuhuilla Ignimbrite (Figure 2.11). This stratigraphic relationship disagrees with the $^{40}Ar/^{39}Ar$ biotite age for the Cerro Chuhuilla Lavas (6.63 ± 0.09 Ma), which suggests that the lavas are older than the

Chuhuilla Ignimbrite. Though the Cerro Chuhuilla sample did not yield a smooth plateau age, the same discrepancy exists along the collapse scarp of the caldera where lavas along the Serrania Khenwal overlay the Chuhuilla ignimbrite (Figure 2.12); however the $^{40}Ar/^{39}Ar$ biotite age (6.10 ± 0.09 Ma) indicates that they are also older than the ignimbrite. Since the stratigraphic relationship cannot be argued, this discrepancy points to an issue with combining $^{40}Ar/^{39}Ar$ biotite and sanidine ages.

Alota Ignimbrite and Juvina Dome complex

Overlying a thick sequence of lake sediments and aeolian deposits above the Chuhuilla ignimbrite is the rhyolitic Alota Ignimbrite (5.23 ± 0.01 Ma $^{40}Ar/^{39}Ar$ in Sanidine age). The Alota ignimbrite is restricted to an area of approximately 200 km^2 around the Juvina dome in the Alota Basin. This unit defines a shallow shield capped by the rhyolitic Juvina domes. Dissection in the summit area reveals rhyolitic phreatomagmatic deposits underneath the domes that mark the footprint of the vent area. The bedded phreatomagmatic deposits transition distally and stratigraphically upward into a single thick rhyolitic ignimbrite that dominates the Alota basin. No signs of collapse are found in the vent area now capped by domes. The Alota ignimbrite and Juvina dome complex define a classic ignimbrite shield (Baker, 1978; de Silva and Francis, 1991). The ignimbrite and lavas are constrained to the Alota basin. The most distal extent of the Alota Ignimbrite is 12 km from the summit of the shield in the Rio Chaira Waykho valley. In this valley the ignimbrite is 10 m thick, however the Alota ignimbrite is approximately 55 m thick just under the summit lavas to the east of the shield. The Alota and the co-located Pastos Grandes ignimbrite have ChRM directions that are statistically indistinguishable (angular separation is 9° and their combined error is 9°, Ort et al.,

2013), but they are different enough in age to be identified by stratigraphic position. They are also distinguished by petrologic characteristics.

The Alota ignimbrite is poorly indurated throughout its distribution. It is massive, crystal rich, lithic rich (~10%), and pumice poor, with pumice rich zones at the top of the section. There is a fine grained, pumice rich layer at the base of the observed Alota section, just above the lacustrine deposits. This pumice-rich layer grades and thickens by meters laterally into phreatomagmatic tuffs. Juvenile blocks of the Alota Ignimbrite are both highly-expanded pumice (low-density) and poorly expanded rhyolite. Both types are petrographically identical among the most silicic in the APVC (75 wt % SiO_2). These juvenile blocks are crystal rich (40%) with phenocrysts of quartz, sanidine, biotite and amphibole.

Pastos Grandes Ignimbrite

Outflow of the Pastos Grandes Ignimbrite (2.89 ± 0.01 Ma $^{40}Ar/^{39}Ar$ in Sanidine age) is exposed to the North, East, and West of the caldera in an area nearly 6000 km^2 (Figure S2.1). The Pastos Grandes ignimbrite overrides the stratigraphy surrounding the caldera, though it has been eroded away from the caldera along the eastern outflow portions, exposing the older ignimbrite stratigraphy below. The ChRM direction of the Pastos Grandes is distinguishable from the Chuhuilla but within error of the Alota ignimbrite (Ort et al., 2013). Schematic stratigraphic columns around Cerro Chuhuilla and Serrania Khenwal highlight the ignimbrite stratigraphy.

Outflow thicknesses vary dramatically, especially in areas of pronounced topography. Exposures reach >90 m in thickness East of the caldera; however, the thickness varies greatly in this area, as the outflow disappears approximately 11 km from the source. To the North, the Pastos Grandes averages approximately 20 m in thickness, but reaches 60 m in valleys closer to the caldera. The most distal outcrop was found east of the Chilean border, where it is 50 m thick, as it was funneled into a small valley prior to being covered by an Arc-related lava succession related to Inacaliri.

The outflow facies of the PGI is massive, crystal-rich and pumice and lithic poor. Proximal exposures are more massive and highly indurated, while many of the observed distal extents were well sorted and weakly layered with only minor induration. Few outcrops contain thin basal surge deposits that are pumice rich with cross bedding parallel to outflow directions. Lithic content is estimated at 5-10%, however lithics are larger and more concentrated near the base of the unit. Pumice is rare except when concentrated in zones in distal exposures. Pumice of the Pastos Grandes Ignimbrite is crystal rich (40%) with phenocrysts of plagioclase (40%), quartz (25%), biotite (15%), sanidine (15%), and amphibole (<5%). Pumice contains 65-68 wt% SiO_2. The texture and mineralogy is remarkably similar to those observed in the Chuhuilla ignimbrite.

The intracaldera section is exposed in the central depression of the resurgent dome. The prominent resurgent dome covers approximately 200 km^2 of the Pastos Grandes caldera. The dome is circular with gently sloping margins and radiating drainages (Figure 2.13). The resurgent dome itself is not fault bounded on any side; however faults that parallel

the margin of resurgent uplift cut the southern post-climactic domes (Cerro Arenal and Cerro Sombrero) indicating the extent of uplift above the caldera moat. The resurgent dome has a maximum height of 1.3 km above the caldera moat. A central depression dissects the dome, exposing nearly 1 km of the Pastos Grandes intracaldera facies. This central depression has an ESE trend (110°), similar to the trends of grabens along the Cerro del Azufre chain (124°) that are manifest themselves as a part of the regional Lipez Lineaments.

The exposed section is nearly 900 m thick, however, the resurgent dome has a total relief of 1.3 km from caldera moat to dome summit (Figure 2.14). The base of the section consists of welded Pastos Grandes ignimbrite that has been reworked by drainages. It is granular and lithic rich (>20%) with no fiamme present. The majority of the section is densely welded and massive, lithic and fiamme poor, with abundant xenoliths. Fiamme rich layers are present approximately 250 – 300 m up from the base of the section. The top of the section consists of massive, crystal rich, welded ignimbrite that is lithic (~20%) and enclave rich and fiamme poor.

Post-Pastos Grandes Domes

These consist of Cerro Arenal and Cerro Sombrero that overlie the flanks of the resurgent dome itself, while the northern post-climactic domes (Cerro Aguas Calientes, Cerro Cachi Laguna, and Cerro Pabellon Cachi Laguna) cap the intracaldera sequence to the north. Together these domes make up the central dome complex.

The central dome complex of the Pastos Grandes caldera consists of a string of dacite lava domes surrounding the resurgent dome (Figure 2.13 A-E). Much of the dome complex stands more than one kilometer above the caldera moat. The northern domes (Cerro Aguas Calientes, Cerro Cachi Laguna, and Cerro Pabellon Cachi Laguna) are not in contact with the resurgent structure and have $^{40}Ar/^{39}Ar$ biotite ages that range from 2.20 – 2.43 ± 0.04 Ma. The southern domes (Cerro Arenal and Cerro Sombrero) are older and deformed by the resurgent center. The Cerro Sombrero dome (2.83 ± 0.02 Ma; sanidine Salisbury et al., 2011) is similar in age to Cerro Arenal, which yielded a biotite $^{40}Ar/^{39}Ar$ age of 3.01 ± 0.07. The domes are dense and microlitic with phenocrysts of plagioclase (40%), quartz (25%), amphibole (25%), biotite (10%), and rare sanidine. These domes contain 65 – 67 wt% SiO_2. Thus, the suite shares general mineralogic and chemical properties with a trend of increasing textural coarseness (maturity) from pumice to lava.

Discussion

Age Discrepancies

Some of the biotite $^{40}Ar/^{39}Ar$ ages disagree with the stratigraphy in the PGCC. For example, the lavas of Serrania Khenwal and Cerro Chuhuilla along the eastern collapse scarp overlie the Chuhuilla ignimbrite, yet they yielded ages much older (6.10 ± 0.09 and 6.63 ± 0.09 Ma respectively) than the sanidine age of the Chuhuilla ignimbrite (5.45 Ma ± 0.02). Also, the southern-most post-climactic dome (Cerro Arenal) yielded a biotite $^{40}Ar/^{39}Ar$ age of 3.01 ± 0.07 compared to the stratigraphically older Pastos Grandes Ignimbrite with a sanidine age of 2.89 ± 0.01 Ma. The biotites used in the analyses were quite large (typically 3-4mm and more than 200 μm thick) so the issue of ^{39}Ar recoil loss

(e.g. Paine et al., 2006) is assumed to be negated. Samples were unaltered and the Altiplano has been among the most arid climates on Earth since the Middle Miocene ruling out isotope redistribution by weathering (Gaupp et al., 1999; Roberts et al., 2001). Furthermore, microscopic analyses during the picking process revealed little to no alteration phases as inclusions (e.g. Smith et al., 2008). As shown in Figure 2.3, the plateaus and isochrons of each sample (with the exception of Cerro Chuhuilla) are relatively flat (i.e. no excess Ar saddle spectra; Lanphere and Dalrymple, 1976). That is not to say that the analyses were perfect. As shown in Table 2.1a, the radiogenic yield is quite low for each sample (30-40%). Overall however, the $^{40}Ar/^{39}Ar$ biotite ages yielded seemingly precise, yet inaccurate ages. Even with the removal of the Cerro Chuhuilla sample due to a poorly constrained plateau, it seems a geologic reason is needed to explain the systematic discrepancy within the $^{40}Ar/^{39}Ar$ system (biotite vs sanidine) and compared to the stratigraphy.

Due to the lack of sanidine in the samples, biotite $^{40}Ar/^{39}Ar$ ages were performed on lavas that erupted immediately following the large-volume ignimbrite eruptions. As is shown in Figure S2.2, the post-climactic lavas of Serrania Khenwal and Cerro Chuhuilla along the eastern scarp and the southern-most post-climactic dome (Cerro Arenal) contain disequilibrium textures and microlites, the latter indicating high degrees of undercooling in the remnant magma systems. It is proposed here that the remnant magmas continue cooling following the climactic eruption, however, due to the high closer temperature of biotite in the Ar system, the daughter nuclide retention would reflect pre-climactic conditions and ages. These ages would even be offset compared to the sanidine eruption

age in the ignimbrites following the inherent $^{40}Ar/^{39}Ar$ assumption that sanidine passes through its closure temperature and is fully retentive of Ar following the eruption. According to Hora et al., (2010), a similar process of pre-eruption cooling leads to addition additional partitioned ^{40}Ar in biotite yielding older ages. These data support the notion proposed by Hora et al., (2010) that the age discrepancies are not analytical, rather instrument precision is recording subtle systematic differences in the magmatic phases.

Tectonic Controls on Caldera Location and Formation

We note a close relationship between the volcanism of the PGCC and the regional tectonic structures (both N-S arc parallel and the WNW-ESE transversal, transcurrent lineaments noted on Figure 5) (e.g. Richards et al., 2002; Riller et al., 2001; Kay et al., 1999). The complex as a whole is bound by major tectonic and morphologic features, as the deposits are predominantly aligned in a WNW-ESE orientation. The northeastern margin of both the Chuhuilla and Pastos Grandes calderas is cross cut by the WNW-ESE Lipez structures, while the southeastern margin of both calderas parallels the N-S structures. Though the western margin of the calderas appears to be sub parallel to the N-S structures, much of the regional influence is manifested along the eastern collapse scarp. The greater influence to the east is suggested here as the driving force behind the asymmetric collapse of the caldera to the east. The regional influences can be seen in features that post-date the caldera as well. The bounding transtensional faults of the Lipez lineaments are proposed here to not only to result in the elongation of the caldera itself, but to create local extension in the central depression of the resurgent dome (Figure 2.4b). Alignment of the central depression of the resurgent dome and even portions of

the Runtu-Jarita dome complex indicate that the regional stresses continued to influence magmatism and volcanism long after the caldera activity ended.

The location of the caldera complex is a reflection of the location of the magma system in the shallow crust (e.g. Lipman, 1984). In this holistic view of the volcano-pluton connection, any tectonic controls interpreted to influence location of the caldera, apply to the shallow magma system as well. It is suggested here, that the tectonic features act as funnels to discretize magma in the shallow crust sourced from the regional magma system known as the APMB (first identified by Chmielowski et al., 1999, and discussed in detail in Chapter 3). Whereas the regional structures are thought to control the general location of the magma system and caldera, it is noted that the arcuate nature of the caldera between tectonic intersections reflects the outline of the magma system. This relationship suggests that local magmatic stresses and regional tectonic stresses combine to control the morphology of the calderas.

Complex, large-scale collapse structures (often resurgent and piecemeal or trapdoor style) influenced by regional tectonic fabrics have been cited around the APVC (Baker and Francis, 1978; Baker, 1981; de Silva and Francis, 1989; de Silva et al., 2006) and all over the world (e.g. van Bemmelen, 1939; Lipman, 1983; Hildreth and Mahood, 1986, Spinks et al., 2005; Kennedy et al., 2012). The commonality of these volcanic centers brings to light the importance of the volcano-tectonic depression (VTD) as introduced by van Bemmelen (1939). These features inform the style of caldera collapse discussed below.

Caldera Collapse Characteristics

In both the Chuhuilla and Pastos Grandes calderas, lavas along the eastern arcuate margin define the topographic and structural margin of the caldera complex. No such boundary is observed to the West of the caldera. Instead, there is a subtle N-S trending rise to the west of the resurgent dome and post-climactic dome complex. We suggest collapse was asymmetric trapdoor style, hinged to the West of the current resurgent dome. This interpretation is also supported by the lower elevation of the eastern moat compared to the West, a difference of nearly 200m (Figures 2.4 & 2.5). This interpretation places the PGCC in a growing group of studies classifying systems with asymmetric collapse (e.g. Pantelleria, Mahood and Hildreth, 1983; Calabozos, Hildreth et al., 1984; La Pacana, Lindsay et al., 2001; Cerro Galan, Folkes et al., 2011)

We envisage a scenario where collapse of the Chuhuilla and Pastos Grandes calderas was initiated along the northeast margin where the regional lineaments are seen to intersect the arcuate normal faults of Serrania Khenwal. The calderas then unzipped, outlining the eastern edge of the magma system. We determined the location of the collapse of the Pastos Grandes caldera from a topographic boundary along the preexisting Chuhuilla scarp to the East. In fact, there is no exposed faulting associated with the collapse of the Pastos Grandes caldera. We believe that the Pastos Grandes Caldera formed by reactivating the Chuhuilla collapse scarp and subsequently buried any associated collapse features with intracaldera fill. The western hinge line of the calderas represents the least amount of collapse along the western outline of the magma system. Ignimbrite outflow patterns are largely similar for both the Chuhuilla and Pastos Grandes ignimbrite,

suggesting that caldera geometry, collapse styles, and eruption dynamics were largely similar.

The eruption trigger itself cannot be determined from the observations made from the PGCC alone. However, data collected from the PGCC seem to fit into the VTD paradigm originally created by van Bemmelen (1939). The large volumes in the sub-caldera magma system likely led to local tumescence. These local stresses, combined with the regional extensional stress associated with plateau uplift led to mechanical failure of roof rock, aided by regional strike slip movements along the Lipez Lineaments. This scenario is supported by previous models of the geothermal gradient and the viscoelastic response of the crust to large magma volumes in the upper crust (de Silva et al., 2006; Gregg et al., 2012). This roof-triggered collapse would have occurred early, creating a basin to collect the large intracaldera volume observed in the Pastos Grandes caldera.

Revised Volume Estimations

Accurate volume estimations of large silicic pyroclastic eruptions are often made difficult by the lack of preservation or exposure. In older systems, erosion of the outflow units and burial by subsequent flows present major contributions to the uncertainties in volume calculations (Best et al., 1989) In these older systems, extrapolation from existing exposures to the original deposited volume has become the norm (e.g. Lipman, 1997). In younger systems, a lack of dissection through the outflow and particularly the caldera itself has created the need for inferences and correction factors associated with the volume calculations (Lindsay et al., 2001; Folkes et al., 2011). Here we compare our

methods and assumptions with those cited for systems of similar size and volume (La Garita, Toba, La Pacana, Oruanui, Cerro Galan; Lipman, 1984; Rose and Chesner, 1987; Lindsay et al., 2001; Wilson, 2001; Folkes et al., 2011) to build a comprehensive volume calculation procedure for the Pastos Grandes Caldera Complex. A detailed discussion of the volume calculations is presented in the supplement.

Ignimbrite distributions and volumes for the Pastos Grandes Caldera Complex were first reported by de Silva and Francis (1991) and subsequently updated by Salisbury et al. (2011). Taking into consideration the assumptions and correction factors used in previous studies of eruptions of comparable scale, we present volume constraints for the Pastos Grandes and Chuhuilla ignimbrites based on new deposit maps and field observations. Detailed field work and analysis of satellite imagery has led to revisions of the ignimbrite outflow distributions and thicknesses.

Based on observed areal extents, correction factors, and intracaldera fill constraints, we calculated new bulk volume estimates with uncertainties for the large volume ignimbrites of the Pastos Grandes Caldera Complex (Table 2.2). Our volumes are shown as bulk values and converted to dense rock equivalent (DRE) using a density of 2450 kg/m^3. The revised volume of the Pastos Grandes and Chuhuilla ignimbrites are approximately 800 and 1300 km^3 respectively. The Chuhuilla has a much larger uncertainty associated with its volume calculation (± 100s km^3) based on lack of exposure in the outflow and major assumptions made about possible intracaldera fill scenarios. The Alota ignimbrite is recalculated to a volume of 8 km^3. The volumes calculated here are smaller than

previously calculated by Salisbury et al., (2011) (down from 1500 km^3 for the PGI and nearly equal for the Chuhuilla ignimbrite). This is in large part due to the fact that we see evidence for trapdoor style collapse of the caldera and therefore use a wedge volume for the intracaldera effectively cutting the previous estimates in half. In addition, outflow distributions and thicknesses have been better constrained due to more detailed mapping.

Inherent assumptions regarding loss of material due to erosion and lack of exposure of the caldera fill have commonly been used to estimate volumes in systems such as La Garita, Toba, Oruanui, La Pacana, and Cerro Galan (Lipman, 1984; Rose and Chesner, 1987; Lindsay et al., 2001; Wilson, 2001; Folkes et al., 2011). Lipman (1984) first used an approximate 1:1:1 relationship for the intracaldera fill, outflow, and ash fall portions of the Fish Canyon Tuff deposit to extrapolate the volume to 5000 km^3 from minimal exposure. This subequal approximation has since been used at Toba and Oruanui to estimate volumes of 2800 km^3 and 1170 km^3 respectively (Rose and Chesner, 1987, and Wilson, 2001). In cases where the source calderas are not exposed at all, the outflow volume is assumed to be subequal to the intracaldera volume (Ellis et al., 2012). The lack of sufficient alternatives has forced similar assumptions in many studies around the globe (Mason et al., 2004). Recent work in the APVC at La Pacana (Lindsay et al., 2001) and Vilama (Soler, et al., 2007) and in the southern Central Volcanic Zone at Cerro Galan (Folkes et al., 2011) have shown that intracaldera volumes do not match the outflow volumes in all systems. The lack of plinian fall deposits, high degrees of induration, and pumice poor – lithic rich nature of many monotonous intermediates has been used as evidence to suggest that caldera collapse occurs early, hindering of the formation of a

sustained eruption columns (Sparks et al., 1985; Ort et al., 1993, Lindsay et al., 2001). This phenomenon would result in a higher ratio of intracaldera to outflow, up to 3:1 (Lindsay et al., 2001). Salisbury et al. (2011) and Folkes et al. (2011) agree with this idea. As with the findings of Lindsay et al. (2001), Soler et al. (2007) and Folkes et al. (2011), our calculations show variability that disagrees with the 1:1 approach (e.g. Lipman (1984), Rose and Chesner (1987), and Wilson (2001)). Our calculations show that much of the erupted volume lies within the caldera. Intracaldera:outflow ratios for the Pastos Grandes Caldera Complex are 3:1 for the Pastos Grandes Ignimbrite and much higher (~12:1) for the Chuhuilla ignimbrite).

Ignimbrite Emplacement Dynamics of the Pastos Grandes System

The ignimbrites of the PGCC share many physical properties with other large-volume ignimbrites. Here we place the ignimbrites of the PGCC in the context of other silicic systems of the APVC and globally by discussing their depositional characteristics, lithic and pumice size/proportions and crystallinity. Hildreth (1981), de Silva (1989), Ort (1993), and Folkes (2011) describe crystal-rich, large-volume ignimbrites that lack initial plinian deposits, and are massive with widely dispersed, highly indurated outflows. These characteristics are common to the Chuhuilla and Pastos Grandes ignimbrites and suggest that they required high eruption rates, accomplished through foundering of the roof of the magma chamber into the magma reservoir, causing eruption along the extensive eastern ring fault. This is similar to the scenario suggested by Sparks et al. (1985) for Cerro Galan, as well as de Silva et al. (2006) and Ort (1993) for other large APVC ignimbrites.

The Pastos Grandes Ignimbrite varies from a single massive depositional unit to multiple smaller depositional units in some distal localities. No field evidence was observed to indicate significant time breaks between distal depositional units. The vast majority of the ignimbrite is a single massive unit up to 90 m thick, with horizontal to sub horizontal AMS fabrics (Ort et al., 2013) indicating constant rates of deposition (e.g. Branney and Kokelaar, 2002) as opposed to several discrete flows or unsteady flow conditions. Multiple depositional units appear only where pre-existing topography was pronounced, suggesting the transition from steady to unsteady flow conditions upon interaction between the pyroclastic flow and paleotopography. Figure S2.3 shows a lobe of the PGI above a massive basal unit of the PGI to the north of Cerro Chuhuilla. These stacked flows indicate that the PGI encountered the topography created by Cerro Chuhuilla and was broken into multiple flows to the north. The toes of these flow lobes are rich in pumice. These pumice concentration zones represent low energy portions of the flow that allowed pumice to rise buoyantly (Branney and Kokelar, 2002).

The dense, massive, and homogenous flows require deposition that fed from a source at constant rates. We agree with the model proposed by de Silva et al. (2006) that the physical properties of the ignimbrites in the PGCC are best explained in a model with emplacement during eruptions of high mass eruption rates that led to column collapse soon after the initiation of the eruption. This style of eruption would explain the pumice poor, fine grained, highly indurated nature of the dense ignimbrites. Just as with many of

the ignimbrites of the APVC, we suggest that the absence of a plinian fall deposit requires a low and/or short-lived eruption column (i.e. de Silva 2006).

Though lithic contents were observed as moderately high in some outcrops, overall the ignimbrites are lithic poor (5-10%). The Pastos Grandes ignimbrite is more lithic rich than the older Chuhuilla ignimbrite (up to 10% for PGI, 5% for the Chuhuilla). The majority of the lithics are assumed to be accidental clasts, eroded and entrained from the Paleozoic basement and pre-existing volcanic deposits. Over the entire volume of these deposits the lithic concentration is likely lower than what is observed at the outcrop scale. Lithic content in ignimbrites of the APVC and the central Andes is variable (Ort, 1993; Lindsay et al., 2001; Folkes et al., 2011). The lower lithic contents in the Chuhuilla are likely due to the erosion being limited by caldera widening, forming the much larger Chuhuilla caldera. However, in the 2.5 Myr between caldera-forming eruptions, collar erosion could have provided ample accidental lithics to be incorporated into the younger, Pastos Grandes ignimbrite, regardless of eruption rate.

Implications for the Sub-Caldera Magma System

Eruptions over the ~5.5 Myr. lifespan of the PGCC tap long lived, crystal rich, compositionally limited magma. The pattern of volcanic activity on the surface reflects a focusing of viable melt from the larger system with peripheral activity during the Chuhuilla and Alota stages to the smaller Pastos Grandes and subsequent post-climactic stages. The magmatic and volcanic activity in the Pastos Grandes Caldera Complex coincides with the peak of the APVC flare-up that resulted in the thermomechanical evolution of the crust to a state that promoted the accumulation of larger bodies of dacite

magma in the upper crust (de Silva and Gosnold, 2007). The magma volumes in the PGCC were greatest during the peak of the regional flare up (Chuhuilla Ignimbrite) and decrease during the waning stages (Pastos Grandes Ignimbrite) coinciding with the focusing of volcanic activity in the confocal PGCC.

The Chuhuilla, Pastos Grandes, and Alota ignimbrites, like many APVC ignimbrites, are crystal rich (>45% crystals) (Lindsay et al., 2001; Salisbury et al., 2011). High crystal content in the ignimbrites has been attributed to storage and growth in shallow magma chambers (Folkes et al., 2011). As the only vestiges of the plutonic realm exist as xenoliths, determining the appropriate plutonic-volcanic ratio is a first order approximation at best. Previous estimates have included 3:1 to 10:1 ratios (Lipman, 1984; Smith, 1979). These ratios would lead to plutonic volumes between 2500 and 10000 km^3 for the Pastos Grandes system for instance. These volumes fit with the roof dimensions of the Pastos Grandes caldera (~1000 km^2) and a pluton thickness of ~2.5 – 10 km, a value within the range of previous estimates for large silicic systems (McNulty et al., 2000; Fliedner and Ruppert, 1996).

Bachmann and Bergantz (2004) proposed that these crystal rich, homogenous ignimbrites are the result of long-lived, non-zoned magma chambers, an idea supported by zircon chronochemistry of the Pastos Grandes magmatic system (Chapter 4 of thesis). Constant recharge of chemically similar magma into the shallow crustal reservoir and efficient mixing of the new and existing magmas are needed to build large accumulations of homogenized magma that source the large-volume ignimbrites (Bachmann and Bergantz,

2008). This model explains the consistent trace element signatures in zircons from magmas over the entire timespan of magma storage under the Pastos Grandes Caldera Complex (Chapter 4 of thesis). These constant injections create residence times of more than 10^5 years (Bachmann and Bergantz, 2004, Chapter 4 of thesis). Ubiquitous but volumetrically insignificant andesite inclusions and bands in pumice are rare, but are the only sign of the andesite parent and deeper mafic roots of the upper crustal silicic systems that create the mafic downward sequence of Hildreth (1981).

Conclusions

The Pastos Grandes Caldera Complex consists of a 52 x 32 elliptical, nested caldera structure and peripheral ignimbrite shield. In addition to the large volume dacite ignimbrite eruptions, the complex has produced a smaller volume rhyolite ignimbrite and effusive dacite domes and lava flows. The physical properties of the volcanic structures and products are similar to others in the APVC as well as Cerro Galan, Long Valley, Toba, Yellowstone, and the Taupo Volcanic Zone (Lindsay et al., 2001; Folkes et al., 2011; Chesner, 2011; Christiansen, 2001; Wilson et al., 2001). Key additions to the geologic framework of the PGCC are as follows:

-The extents of the Chuhuilla and Pastos Grandes ignimbrites have been redefined to the North of the caldera. Previously misidentified units have been identified and remapped, altering the distribution of the Pastos Grandes relative to the Chuhuilla ignimbrite. The newly defined distribution has led to updated and more accurate volume estimates.

-Field mapping and interpretation of satellite imagery of the caldera margins supports previous claims of trap-door style collapse to the East. We propose that collapse was initiated along the northeast margin of the caldera where the scarp is controlled by the

location of the regional tectonic lineaments. Collapse was almost entirely accommodated along the eastern margin, as no faulting was identified along the western margin.

-Biotite $^{40}Ar/^{39}Ar$ ages reveal that lavas along the eastern arcuate scarp of the caldera are related to the older, Chuhuilla pulse of volcanism (6.10 ± 0.09 Ma and 5.45 ± 0.02 Ma sanidine age respectively). Based on field relations, it is thought that the Pastos Grandes collapse was accommodated inward of the Chuhuilla collapse scarp, with all structural features buried by the intracaldera ignimbrite.

-Revised volume calculations do not change the magnitude of the major ignimbrite eruptions, but do provide a more quantitative approach with realistic errors associated with each estimate. Assumptions leading to the intracaldera volume estimates are made from the previously described collapse model and thickness constraints made from the resurgent dome.

-A long-term chemical homogeneity is observed in the upper crustal magma system of the PGCC. Homogeneity of the system from one eruption to the next is consistent with previous models proposing repeated injections of chemically identical magma into large, long-lived dacite reservoirs in the upper crust.

-The PGCC was the site of significant volcanic activity over a 5 Myr period. Evidence for multiple large volume eruptions, as well as numerous lava flows, and silicic dome extrusions suggest magmatic and volcanic activity was continuous from ~6 Ma, through the Late Pleistocene.

References

Bachmann, O., & Bergantz, G. W. (2008). Deciphering magma chamber dynamics from styles of compositional zoning in large silicic ash flow sheets.*Reviews in Mineralogy and Geochemistry*, *69*(1), 651-674.

Baker, M. C. W., & Francis, P. W. (1978). Upper Cenozoic volcanism in the Central Andes—ages and volumes. *Earth and Planetary Science Letters*, *41*(2), 175-187.

Baker, M. C. W. (1981). The nature and distribution of Upper Cenozoic ignimbrite centres in the Central Andes. *Journal of Volcanology and Geothermal Research*, *11*(2), 293-315.

Best, M. G., Christiansen, E. H., & Blank, R. H. (1989). Oligocene caldera complex and calc-alkaline tuffs and lavas of the Indian Peak volcanic field, Nevada and Utah. *Geological Society of America Bulletin*, *101*(8), 1076-1090.

Branney, M. J., & Kokelaar, B. P. (2002). Pyroclastic density currents and the sedimentation of ignimbrites. Geological Society of London.

Breitkreuz, C., de Silva, S. L., Wilke, H. G., Pfänder, J. A., & Renno, A. D. (2014). Neogene to Quaternary ash deposits in the Coastal Cordillera in northern Chile: Distal ashes from supereruptions in the Central Andes. *Journal of Volcanology and Geothermal Research*, *269*, 68-82.

Chesner, C. A. (2012). The Toba caldera complex. *Quaternary International*,*258*, 5-18.

Chmielowski, J., Zandt, G., & Haberland, C. (1999). The Central Andean Altiplano-Puna magma body. *Geophysical Research Letters*, *26*(6), 783-786.

Christiansen, R. L. (2001). The Quaternary and pliocene Yellowstone plateau volcanic field of Wyoming, Idaho, and Montana. Professional Paper 729 – G.

de Silva, S. L. (1989). Altiplano-Puna volcanic complex of the central Andes.*Geology*, *17*(12),1102-1106.

de Silva, S. L., & Francis, P. W. (1989). Correlation of large ignimbrites—two case studies from the Central Andes of Northern Chile. *Journal of volcanology and geothermal research*, *37*(2), 133-149.

de Silva, S. L., & Francis, P. W. (1991). *Volcanoes of the central Andes*. Springer.

de Silva, S., Zandt, G., Trumbull, R., Viramonte, J. G., Salas, G., & Jiménez, N. (2006). Large ignimbrite eruptions and volcano-tectonic depressions in the Central Andes: a thermomechanical perspective. *Geological Society, London, Special Publications*, *269*(1), 47-63.

de Silva, S. L., & Gosnold, W. D. (2007). Episodic construction of batholiths: Insights from the spatiotemporal development of an ignimbrite flare-up. *Journal of Volcanology and Geothermal Research*, *167*(1), 320-335.

Ellis, B. S., Branney, M. J., Barry, T. L., Barfod, D., Bindeman, I., Wolff, J. A., & Bonnichsen, B. (2012). Geochemical correlation of three large-volume ignimbrites from the Yellowstone hotspot track, Idaho, USA. *Bulletin of volcanology*, *74*(1), 261-277.

Fliedner, M. M., Ruppert, S., & Southern Sierra Nevada Continental Dynamics Working Group. (1996). Three-dimensional crustal structure of the southern Sierra Nevada from seismic fan profiles and gravity modeling. *Geology*, *24*(4), 367-370.

Folkes, C. B., Wright, H. M., Cas, R. A., de Silva, S. L., Lesti, C., & Viramonte, J. G. (2011). A re-appraisal of the stratigraphy and volcanology of the Cerro Galán volcanic system, NW Argentina. *Bulletin of volcanology,73*(10), 1427-1454.

Gaupp, R., Kött, A., & Wörner, G. (1999). Palaeoclimatic implications of Mio–Pliocene sedimentation in the high-altitude intra-arc Lauca Basin of northern Chile. *Palaeogeography, Palaeoclimatology, Palaeoecology*, *151*(1), 79-100.

Gregg, P. M., De Silva, S. L., Grosfils, E. B., & Parmigiani, J. P. (2012). Catastrophic caldera-forming eruptions: Thermomechanics and implications for eruption triggering and maximum caldera dimensions on Earth. *Journal of Volcanology and Geothermal Research*, *241*, 1-12.

Hildreth, W. (1981). Gradients in silicic magma chambers: implications for lithospheric magmatism. *Journal of Geophysical Research: Solid Earth (1978–012)*, *86*(B11), 10153-10192.

Hildreth, W., & Mahood, G. A. (1986). Ring-fracture eruption of the Bishop Tuff.*Geological Society of America Bulletin*, *97*(4), 396-403.

Hora, J. M., Singer, B. S., Jicha, B. R., Beard, B. L., Johnson, C. M., de Silva, S., & Salisbury, M. (2010). Volcanic biotite-sanidine 40Ar/39Ar age discordances reflect Ar partitioning and pre-eruption closure in biotite. *Geology,38*(10), 923-926.

Kay, S. M., Mpodozis, C., & Coira, B. (1999). Neogene magmatism, tectonism, and mineral deposits of the Central Andes (22 to 33 S latitude). *Geology and Ore Deposits of theCentral Andes (Skinner, BJ; editor). Society of Economic Geologists, Special Publication*, *7*, 27-59.

Kennedy, B., Wilcock, J., & Stix, J. (2012). Caldera resurgence during magma replenishmentand rejuvenation at Valles and Lake City calderas. *Bulletin of volcanology*, *74*(8), 1833-1847.

Koppers, A. A. (2002). ArArCALC—software for $^{40}Ar/^{39}Ar$ age calculations. *Computers & Geosciences*, *28*(5), 605-619.

Lanphere, M. A., & Dalrymple, G.B. (1976). Identification of excess ^{40}Ar by the $^{40}Ar/^{39}Ar$ age spectrum technique. *Earth and Planetary Science Letters*, *32*(2), 141-148.

Lindsay, J. M., Schmitt, A. K., Trumbull, R. B., De Silva, S. L., Siebel, W., & Emmermann, R. (2001a). Magmatic evolution of the La Pacana caldera system, Central Andes, Chile: compositional variation of two cogenetic, large-volume felsic ignimbrites. *Journal of Petrology*, *42*(3), 459-486.

Lindsay, J. M., de Silva, S., Trumbull, R., Emmermann, R., & Wemmer, K. (2001b). La Pacana caldera, N. Chile: a re-evaluation of the stratigraphy and volcanology of one of the world's largest resurgent calderas. *Journal of Volcanology and Geothermal Research*, *106*(1), 145-173.

Lipman, P. W. (1983). The Miocene Questa caldera, northern New Mexico: relation to batholith emplacement and associated molybdenum mineralization. In *The genesis of Rocky Mountain ore deposits: changes with time and tectonics. Proc Denver Region Explor Geol Soc Symp* (pp. 133-147).

Lipman, P. W. (1984). The roots of ash flow calderas in western North America: Windows into the tops of granitic batholiths. *Journal of Geophysical Research: Solid Earth (1978–2012)*, *89*(B10), 8801-8841.

Lipman, P. W. (1997). Subsidence of ash-flow calderas: relation to caldera size and magma-chamber geometry. *Bulletin of Volcanology*, *59*(3), 198-218.

Mason, B. G., Pyle, D. M., & Oppenheimer, C. (2004). The size and frequency of the largest explosive eruptions on Earth. *Bulletin of Volcanology*, *66*(8), 735-748.

McNulty, B. A., Tobisch, O. T., Cruden, A. R., & Gilder, S. (2000). Multistage emplacement of the Mount Givens pluton, central Sierra Nevada batholith, California. *Geological Society of America Bulletin*, *112*(1), 119-135.

Ninkovich, D., Sparks, R. S. J., & Ledbetter, M. T. (1978). The exceptional magnitude and intensity of the Toba eruption, Sumatra: an example of the use of deep-sea tephra layers as a geological tool. *Bulletin Volcanologique*, *41*(3), 286-298.

Ort, M. H. (1993). Eruptive processes and caldera formation in a nested downsag collapse caldera: Cerro Panizos, central Andes Mountains. *Journal of Volcanology and Geothermal Research*, *56*(3), 221-252.

Ort, M. H., Silva, S. L., Jiménez, C., Jicha, B. R., & Singer, B. S. (2013). Correlation of ignimbrites using characteristic remanent magnetization and anisotropy of magnetic susceptibility, Central Andes, Bolivia. *Geochemistry, Geophysics, Geosystems*, *14*(1), 141-157.

Pacheco, J., and Ramírez, V., 1997a, Hoja Geológica Cañapa/ Alota 5929/6029: Servicio Nacional de Geológica y Mineria Carta Geológica de Bolivia Publicacíon SGM Serie I–CGB-45, scale 1:100,000, 1 sheet.

Paine, J. H., Nomade, S., & Renne, P. R. (2006). Quantification of ^{39}Ar recoil ejection from GA1550 biotite during neutron irradiation as a function of grain dimensions. *Geochimica et Cosmochimica Acta*, *70*(6), 1507-1517.

Richards, J. P., & Villeneuve, M. (2002). Characteristics of late Cenozoic volcanism along the Archibarca lineament from Cerro Llullaillaco to Corrida de Cori, northwest Argentina. *Journal of Volcanology and Geothermal Research*,*116*(3), 161-200.

Riller, U., Petrinovic, I., Ramelow, J., Strecker, M., & Oncken, O. (2001). Late Cenozoic tectonism, collapse caldera and plateau formation in the central Andes. *Earth and Planetary Science Letters*, *188*(3), 299-311.

Roberts, H. J., Kelley, S. P., & Dahl, P. S. (2001). Obtaining geologically meaningful ^{40}Ar/^{39}Ar ages from altered biotite.*Chemical Geology*, *172*(3), 277-290.

Rose, W. I., & Chesner, C. A. (1987). Dispersal of ash in the great Toba eruption, 75 ka. *Geology*, *15*(10), 913-917.

Salisbury, M. J., Jicha, B. R., de Silva, S. L., Singer, B. S., Jiménez, N. C., & Ort, M. H. (2011). ^{40}Ar/^{39}Ar chronostratigraphy of Altiplano-Puna volcanic complex ignimbrites reveals the development of a major magmatic province. *Geological Society of America Bulletin*, *123*(5-6), 821-840.

Schmitt, A., de Silva, S., Trumbull, R., & Emmermann, R. (2001). Magma evolution in the Purico ignimbrite complex, northern Chile: evidence for zoning of a dacitic magma by injection of rhyolitic melts following mafic recharge. *Contributions to Mineralogy and Petrology*, *140*(6), 680-700.

Sigurdsson, H., & Carey, S. (1989). Plinian and co-ignimbrite tephra fall from the 1815 eruption of Tambora volacano. *Bulletin of Volcanology*, *51*(4), 243-270.

Smith, R. L. (1979). Ash-flow magmatism. *Ash-flow tuffs: Geological Society of America Special Paper*, *180*, 5-27.

Smith, M. E., Singer, B. S., Carroll, A. R., & Fournelle, J. H. (2008). Precise dating of biotite in distal volcanic ash: Isolating subtle alteration using $^{40}Ar/^{39}Ar$ laser incremental heating and electron microprobe techniques. *American Mineralogist*, *93*(5-6), 784-795.

Soler, M. M., Caffe, P. J., Coira, B. L., Onoe, A. T., & Kay, S. M. (2007). Geology of the Vilama caldera: a new interpretation of a large-scale explosive event in the Central Andean plateau during the Upper Miocene. *Journal of volcanology and geothermal research*, *164*(1), 27-53.

Sparks, R. S. J., Francis, P. W., Hamer, R. D., Pankhurst, R. J., O'callaghan, L. O., Thorpe, R. S., & Page, R. (1985). Ignimbrites of the Cerro Galan Caldera, NW Argentina. *Journal of Volcanology and Geothermal Research*, *24*(3), 205-248.

Sparks, R. S. J., Bursik, M. I., Carey, S. N., Gilbert, J., Glaze, L. S., Sigurdsson, H., & Woods, A. W. (1997). *Volcanic plumes*. Wiley.

Spinks, K. D., Acocella, V., Cole, J. W., & Bassett, K. N. (2005). Structural control of volcanism and caldera development in the transtensional Taupo Volcanic Zone, New Zealand. *Journal of Volcanology and Geothermal Research*, *144*(1), 7-22.

Strecker, M. R., Alonso, R. N., Bookhagen, B., Carrapa, B., Hilley, G. E., Sobel, E. R., & Trauth, M. H. (2007). Tectonics and climate of the southern central Andes. *Annu. Rev. Earth Planet. Sci.*, *35*, 747-787.

Van Bemmelen, R. V. (1939). The volcano-tectonic origin of Lake Toba (North Sumatra). *Ing. Ned. Ind*, *6*(9), 126-140.

Watanabe, K., Ono, K., Sakaguchi, K., Takada, A., & Hoshizumi, H. (1999). Co -ignimbrite ash-fall deposits of the 1991 eruptions of Fugen-dake, Unzen Volcano, Japan. *Journal of volcanology and geothermal research*, *89*(1), 95-112.

Watts, R. B., de Silva, S. L., de Rios, G. J., & Croudace, I. (1999). Effusive eruption of viscous silicic magma triggered and driven by recharge: a case study of the Cerro Chascon-Runtu Jarita Dome Complex in Southwest Bolivia.*Bulletin of volcanology*, *61*(4), 241-264.

Wilson, C. J. N. (2001). The 26.5 ka Oruanui eruption, New Zealand: an introduction and overview. *Journal of Volcanology and Geothermal Research*, *112*(1), 133-174.

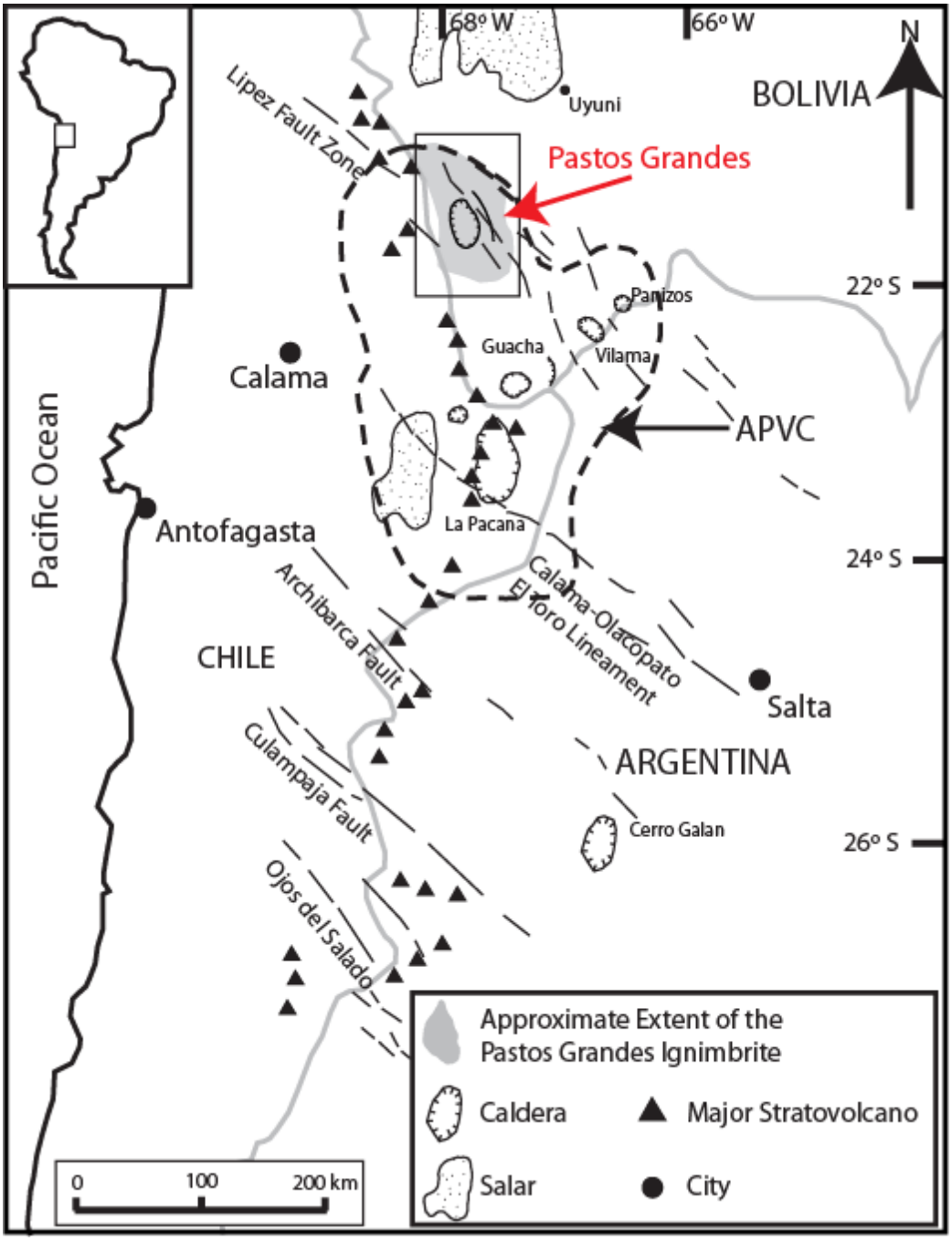

Figure 2.1. Regional setting of the Pastos Grandes Calder Complex (PGCC) in the Altiplano-Puna Volcanic Complex of the Central Andes of Bolivia, Chile, and Argentina. Modern arc volcanoes, regional strike-slip lineaments and the extent of Fig. 2 are also shown.

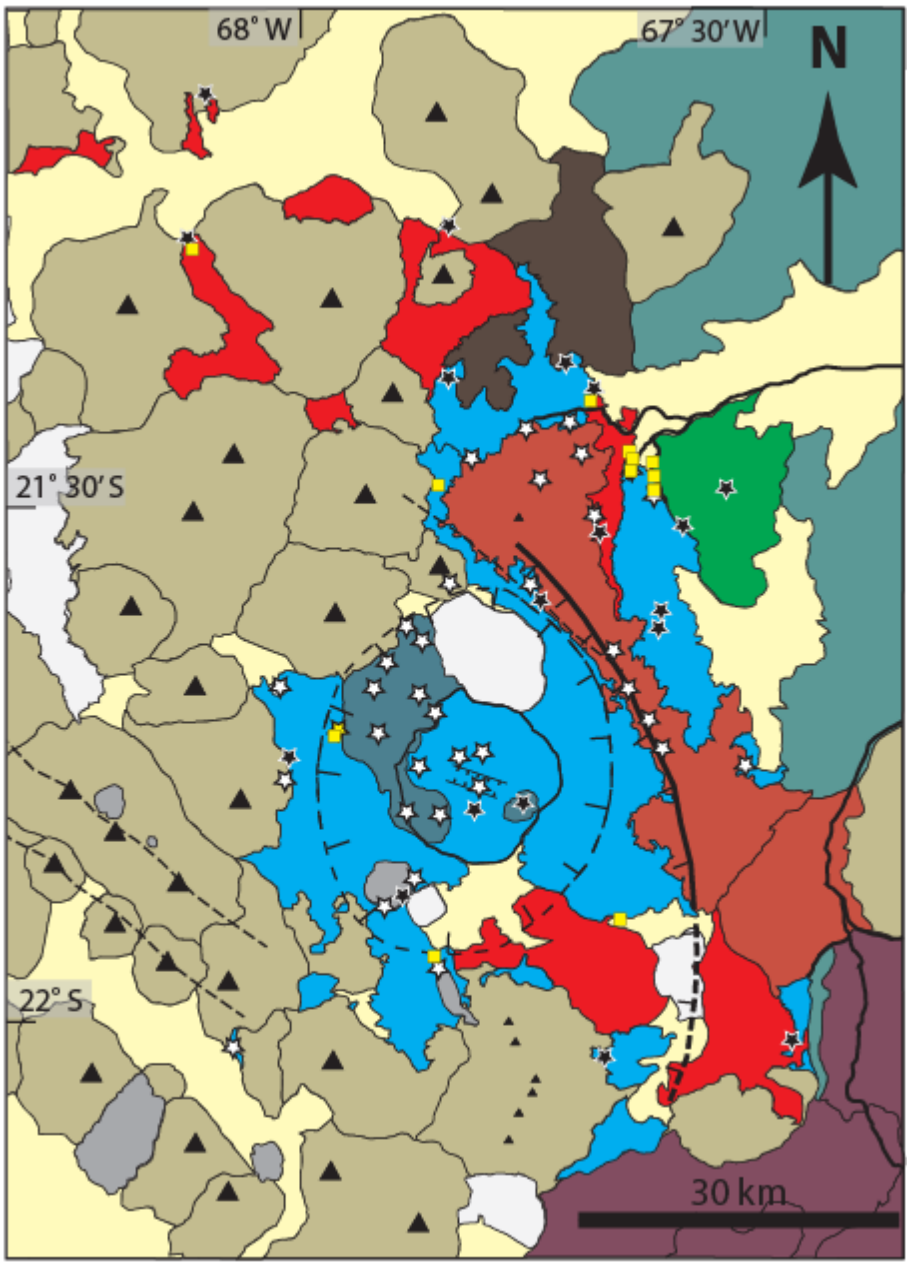

Figure 2.2a. Geologic map of the Pastos Grandes Caldera Complex.

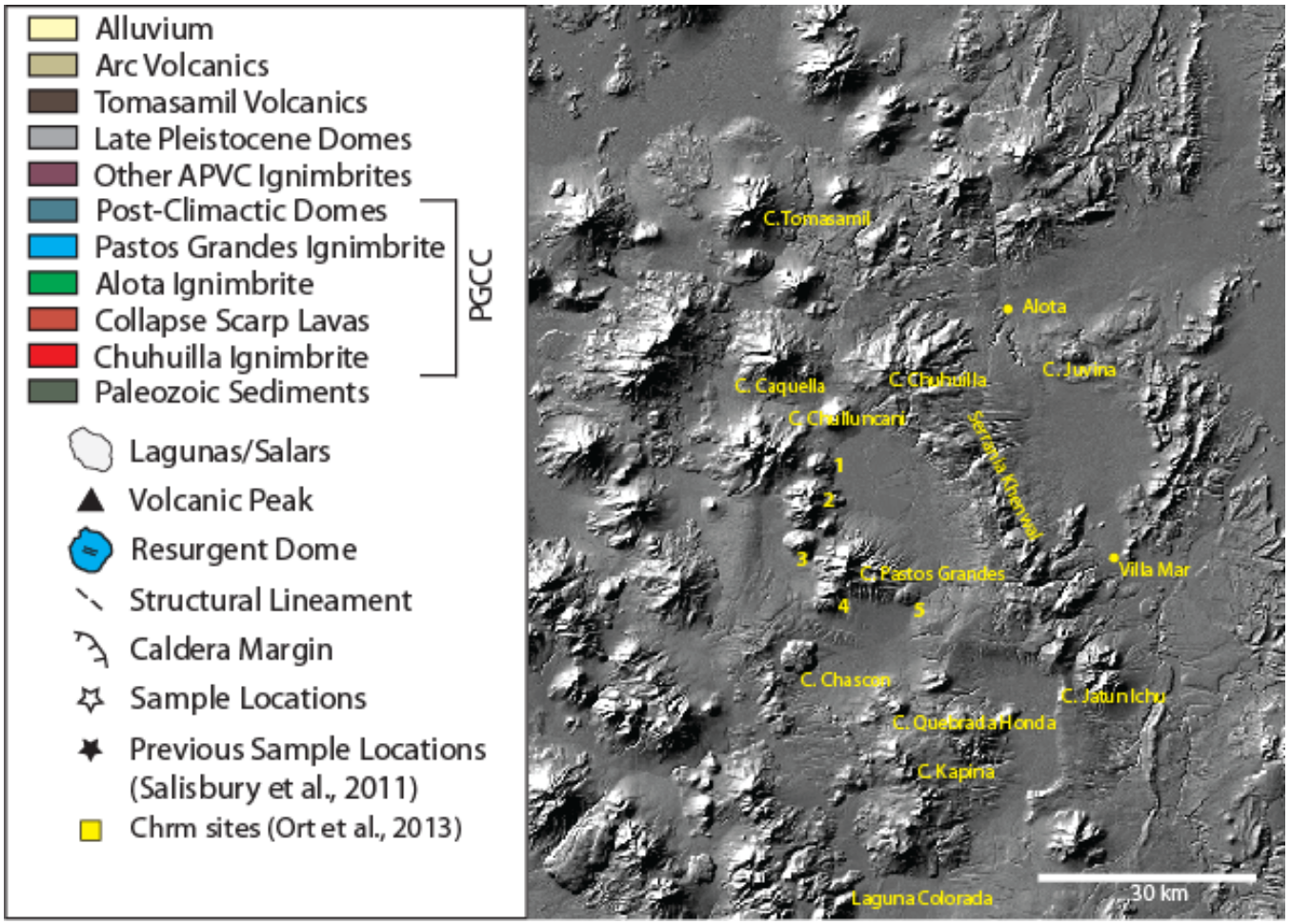

Figure 2.2b. A hillshade image is shown with the geologic map to highlight prominent topographic and geographic features. 1) C. Aguas Calientes, 2) C. Cachi Laguna, 3) C. Pabellon Cachi Laguna, 4) C. Arenal, 5) C. Sombrero. The legend follows the symbols of the geologic map.

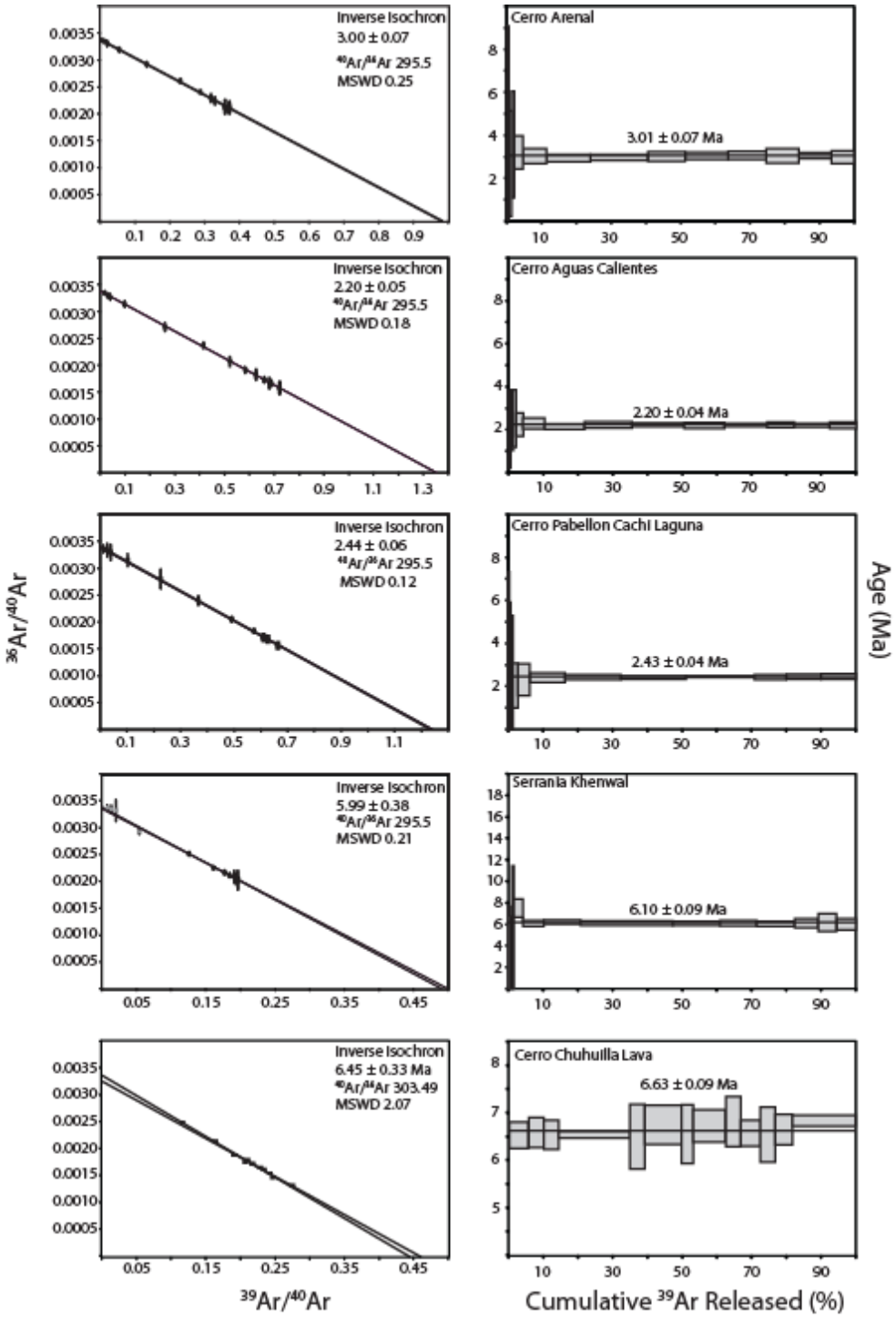

Figure 2.3. Age plateaus and inverse isochrons for lava samples of the Pastos Grandes Caldera Complex. Biotite $^{40}Ar/^{39}Ar$ ages calculated using the weighted plateau function of the ArArCALC v2.2 (Koppers, 2002). Each data point with the associated 2 sigma error is shown. Grey boxes represent plateau steps. The samples exhibit generally flat, undisturbed spectra with higher variation at the low temperature steps.

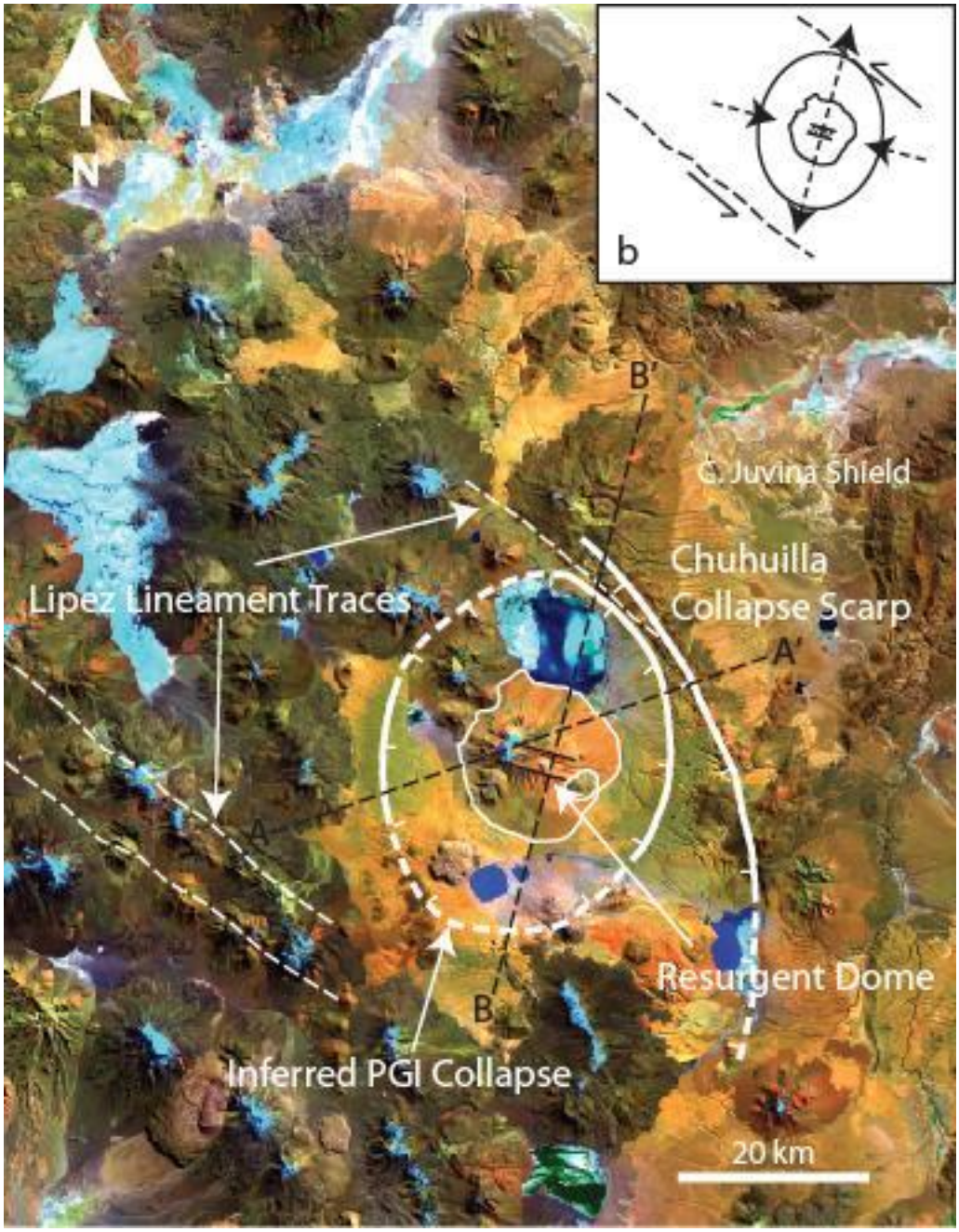

Figure 2.4. Landsat image of the Pastos Grandes Caldera Complex. Major structural features such as the caldera collapses, resurgent dome, and the regional lineaments are marked. The location of cross sections from Figure 6 are also shown. B) After de Silva et al. (2006) a schematic drawing of the Pastos Grandes caldera and Lipez Lineaments showing the regional trancurrent faulting result in elongation of the caldera and local extension in the central depression of the resurgent dome.

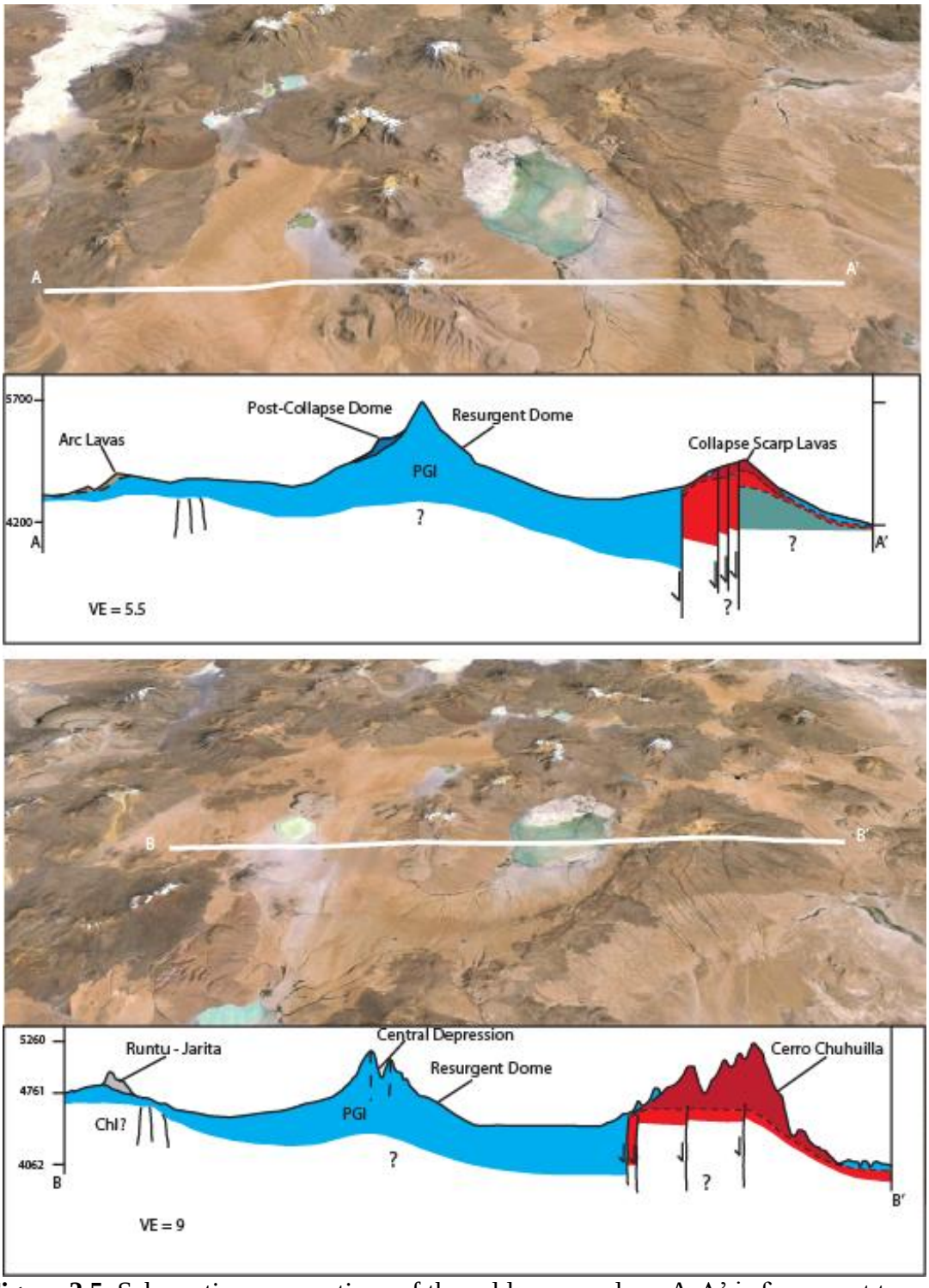

Figure 2.5. Schematic cross sections of the caldera complex. A-A' is from west to east parallel to the collapse asymmetry. B-B' is from north to south perpendicular to the graben of the resurgent dome. In both cases, the wedge structure is visible with the asymmetric collapse towards the east.

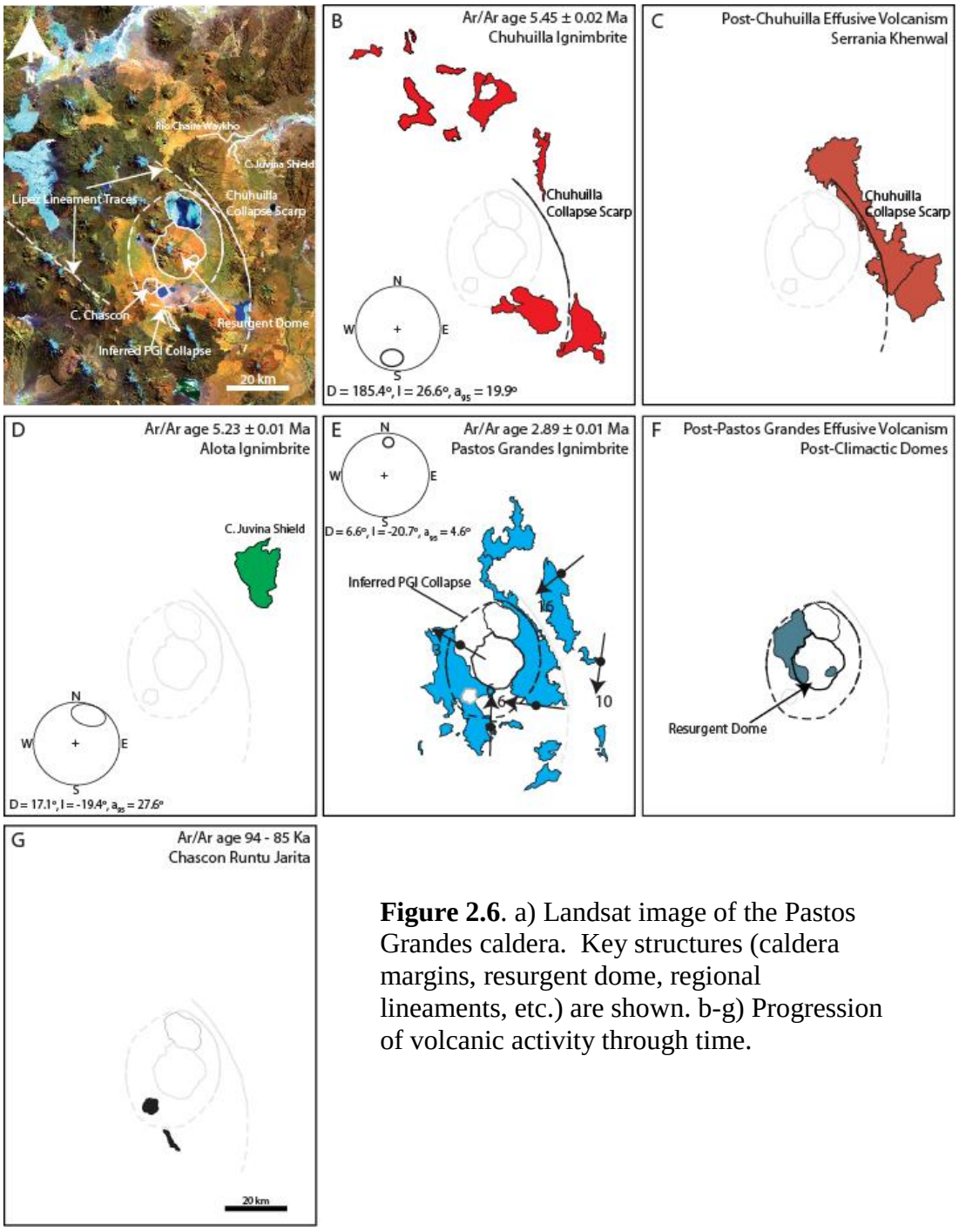

Figure 2.6. a) Landsat image of the Pastos Grandes caldera. Key structures (caldera margins, resurgent dome, regional lineaments, etc.) are shown. b-g) Progression of volcanic activity through time.

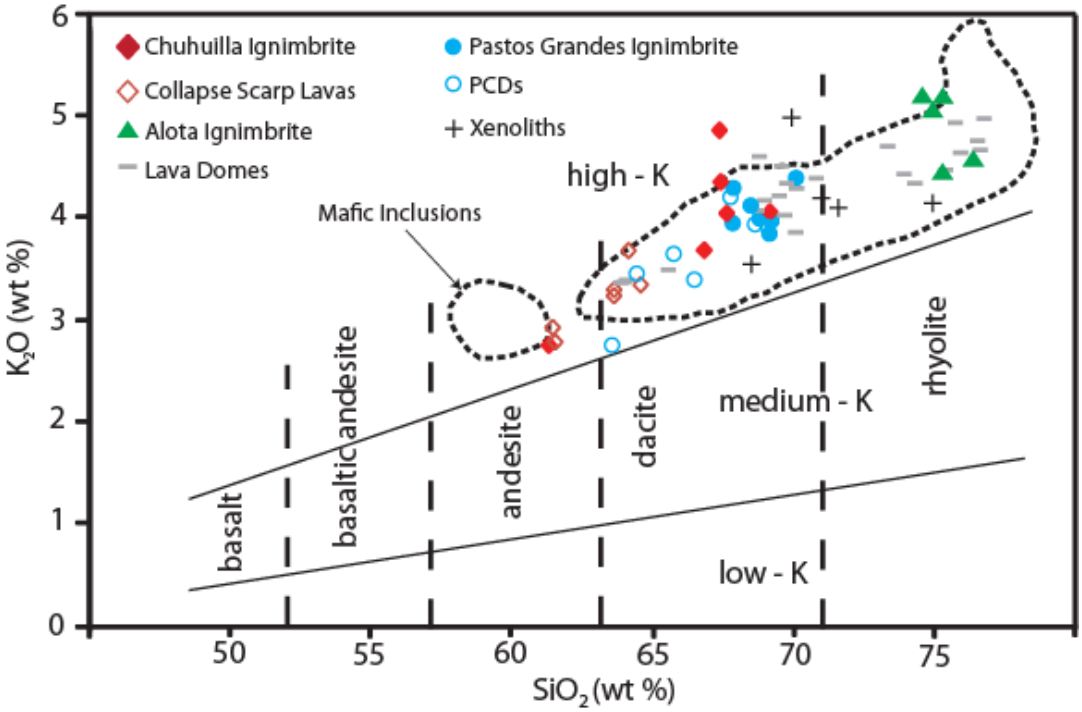

Figure 2.7. Whole rock SiO_2 vs K_2O classification diagram. Volcanic and plutonic samples of the PGCC are predominantly high K dacites with lesser amounts of andesite and rhyolite. The Juvina Shield and Alota Ignimbrite make up all of the rhyolite in the complex.

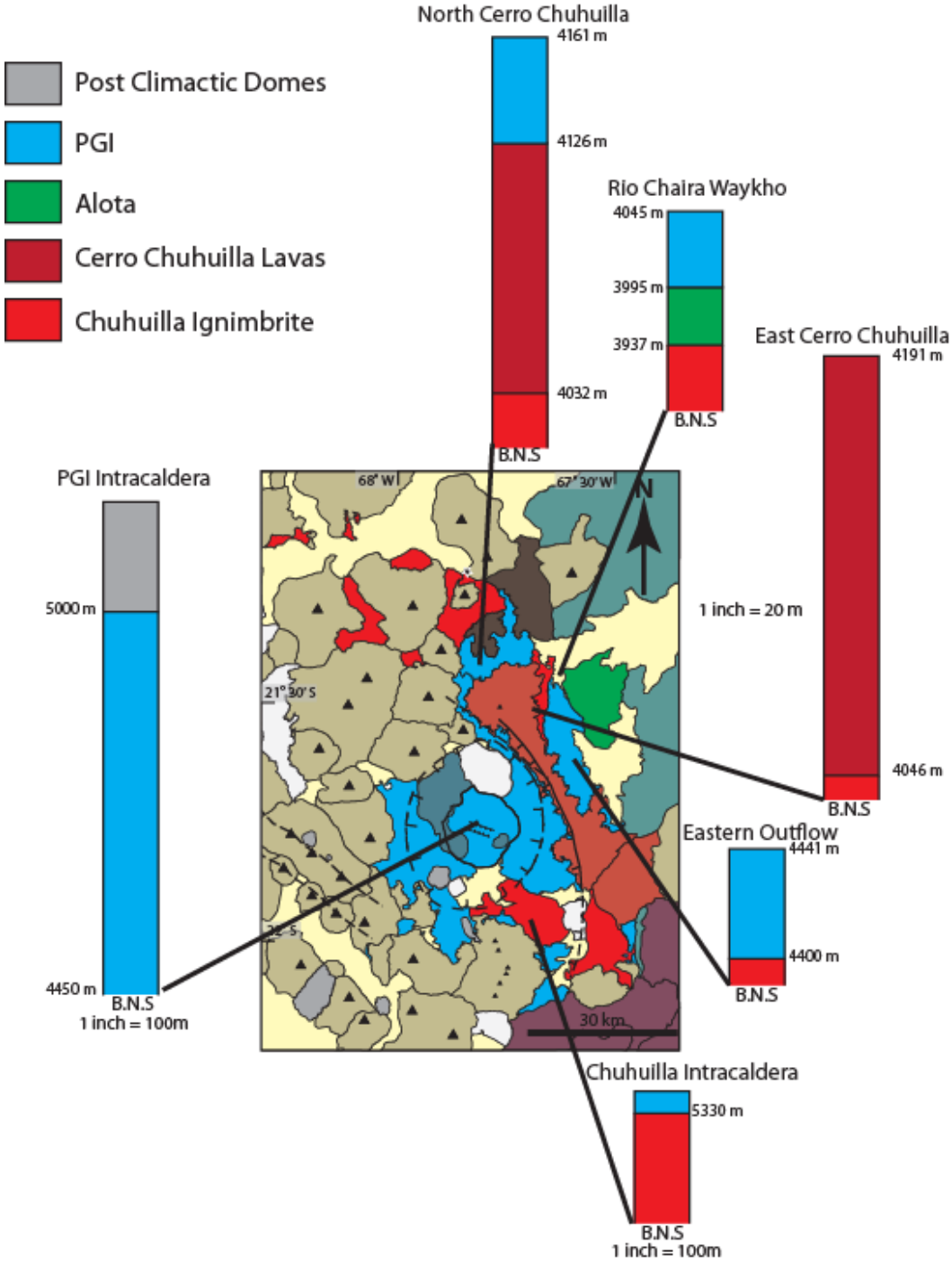

Figure 2.8. General stratigraphy of outflow sequences surrounding the Pastos Grandes and Chuhuilla calderas.

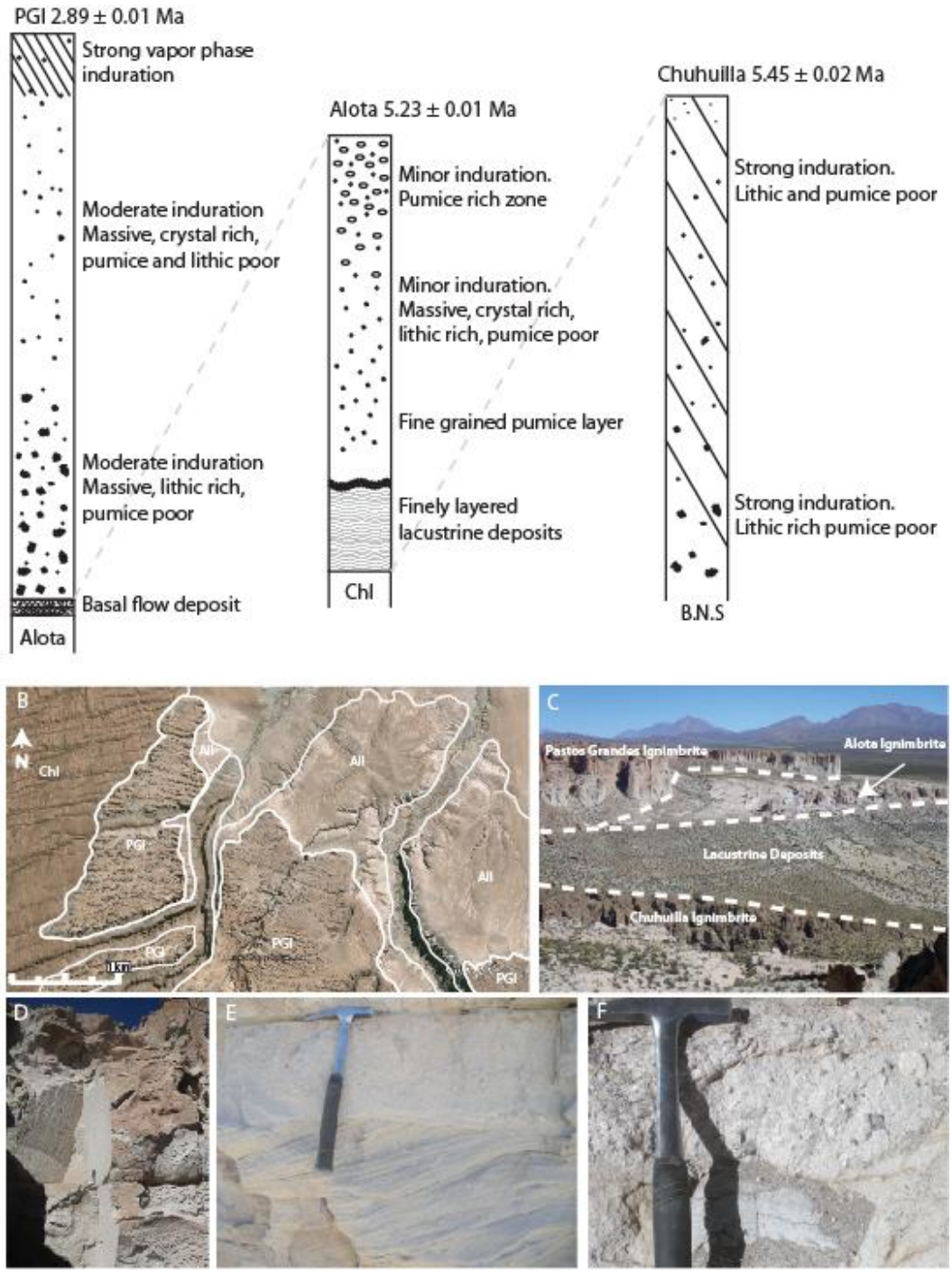

Figure 2.9. Idealized ignimbrite outflow stratigraphic sections. A) Schematic stratigraphic sections of the Pastos Grandes, Alota, and Chuhuilla ignimbrites. Each section shows the transition from relative lithic rich to pumice rich portions of the sequence. B) Google Earth image of the Rio Chaira Waykho drainage where the three ignimbrites are well exposed. C) Field photo of the drainage. D) Outcrop photos of the Pastos Grandes ignimbrite highlighting the upper indurated portion. E) The basal flow unit of the PGI. F) The general outcrop appearance of the Alota ignimbrite.

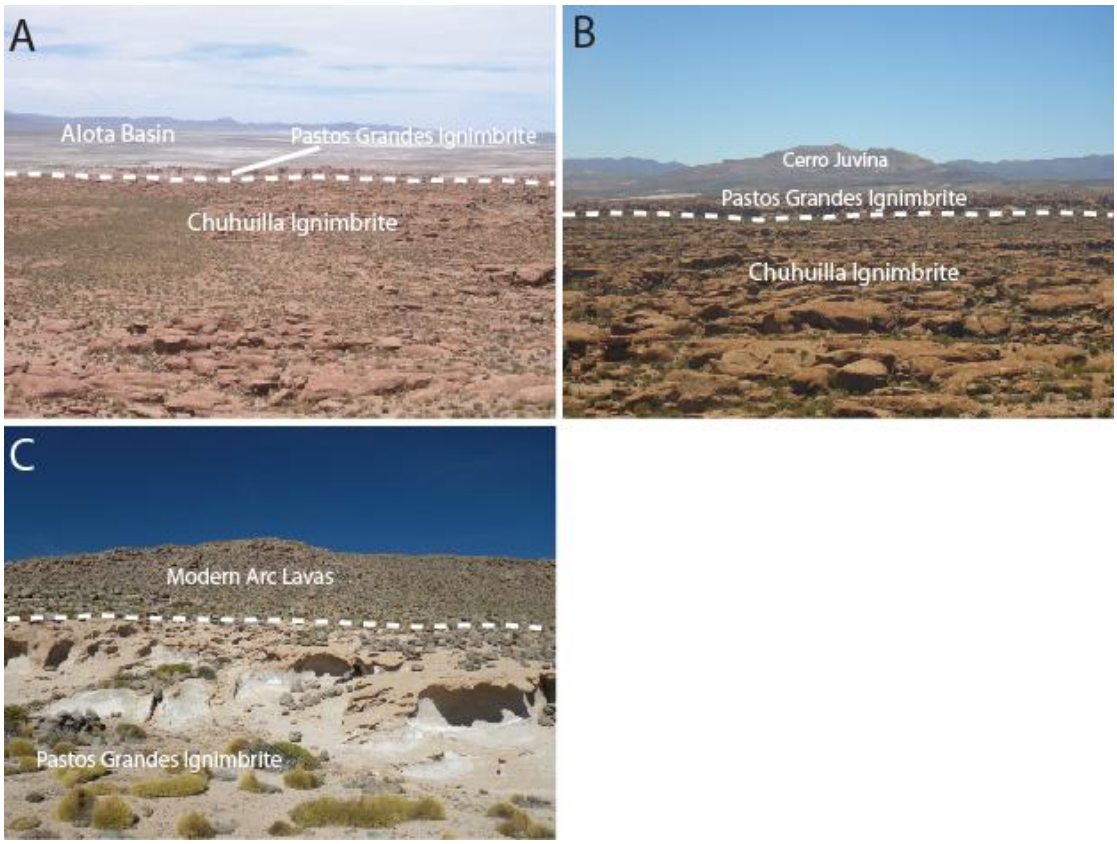

Figure 2.10. Field photos of eastern and western outflow facies of the Chuhuilla and Pastos Grandes ignimbrites. A and B are views of the Alota Basin. A) A view to the southeast into the basin with the Pastos Grandes overriding the Chuhuilla ignimbrite. B) A view to the east towards Cerro Juvina. The Pastos Grandes ignimbrite can be seen on top of the Chuhuilla ignimbrite in the foreground. C) Looking west along the western outflow sequence with the Pastos Grandes below the modern Arc-related lavas.

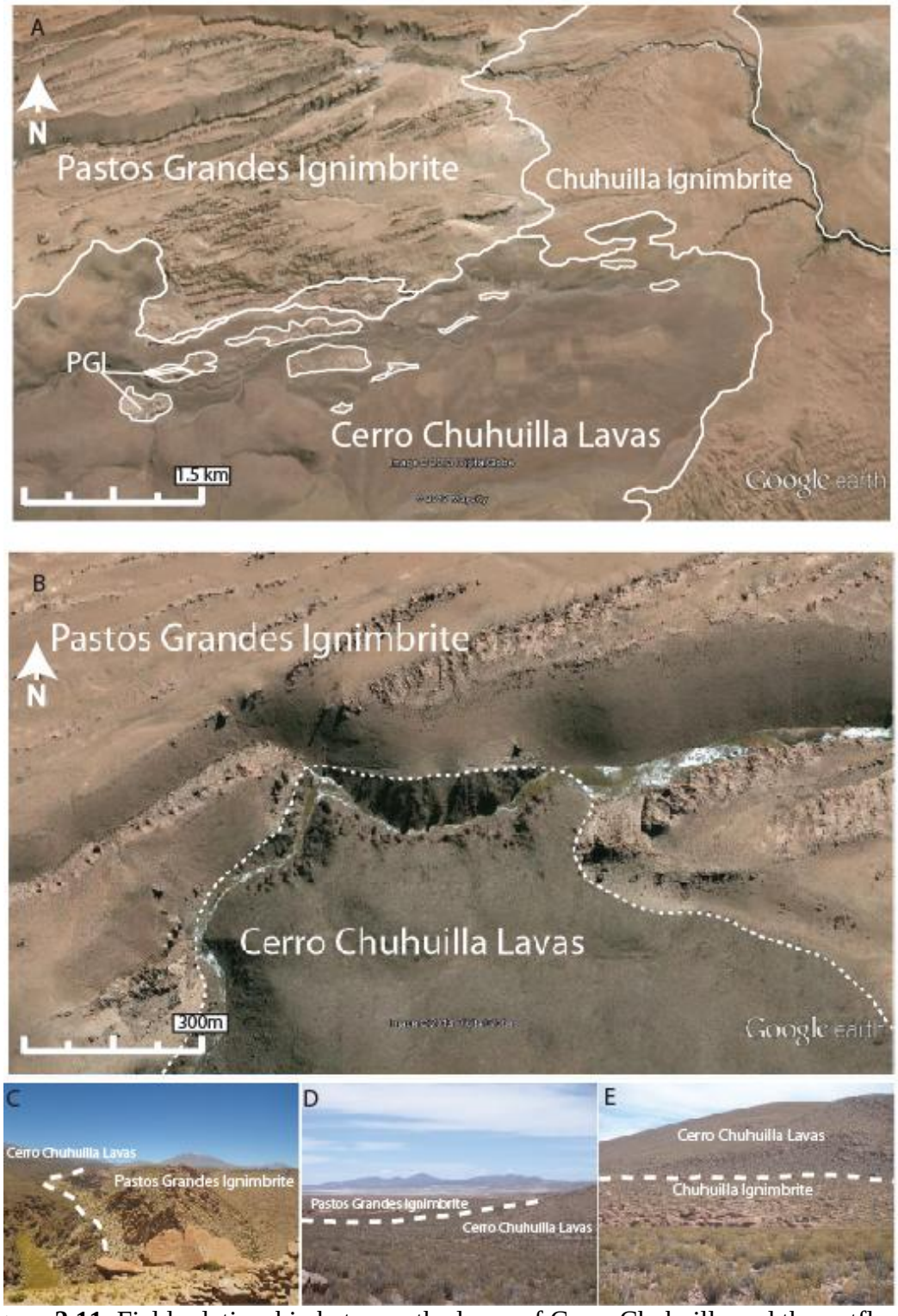

Figure 2.11. Field relationship between the lavas of Cerro Chuhuilla and the outflow facies of the Chuhuilla and Pastos Grandes ignimbrites. A) The northeastern margin of Cerro Chuhuilla, where the lavas lie stratigraphically between the Chuhuilla (below) and the Pastos Grandes (above).

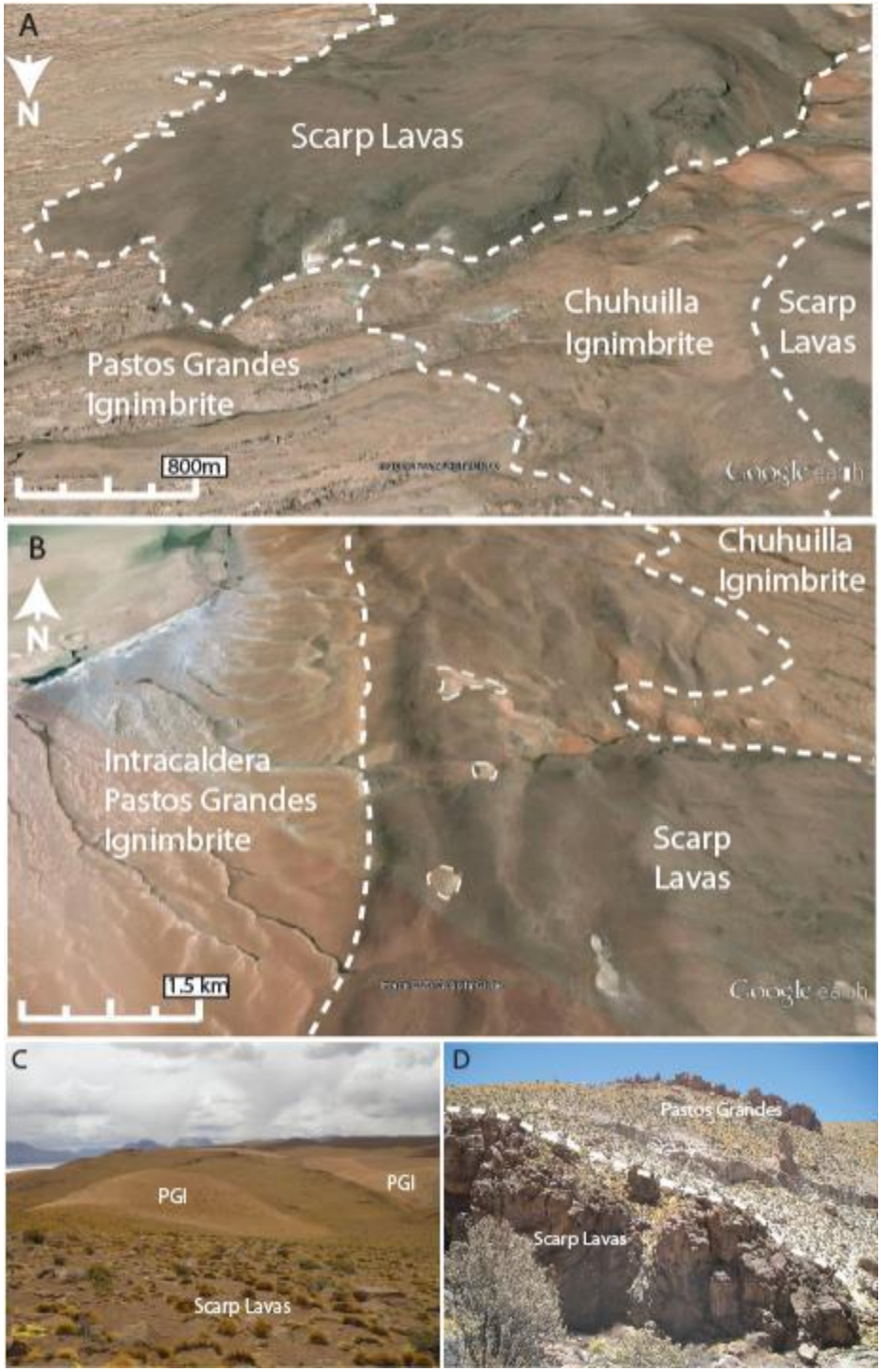

Figure 2.12. Field relationship between the lavas along the eastern caldera scarp and the Chuhuilla and Pastos Grandes ignimbrites. A and B are Google Earth images of the outflow facies and the intracaldera facies as they relate to the scarp lavas respectively. C) Remnants of the PGI on top of the scarp lavas that connect the intracaldera to the outflow. D) The PGI outflow overriding the scarp lavas.

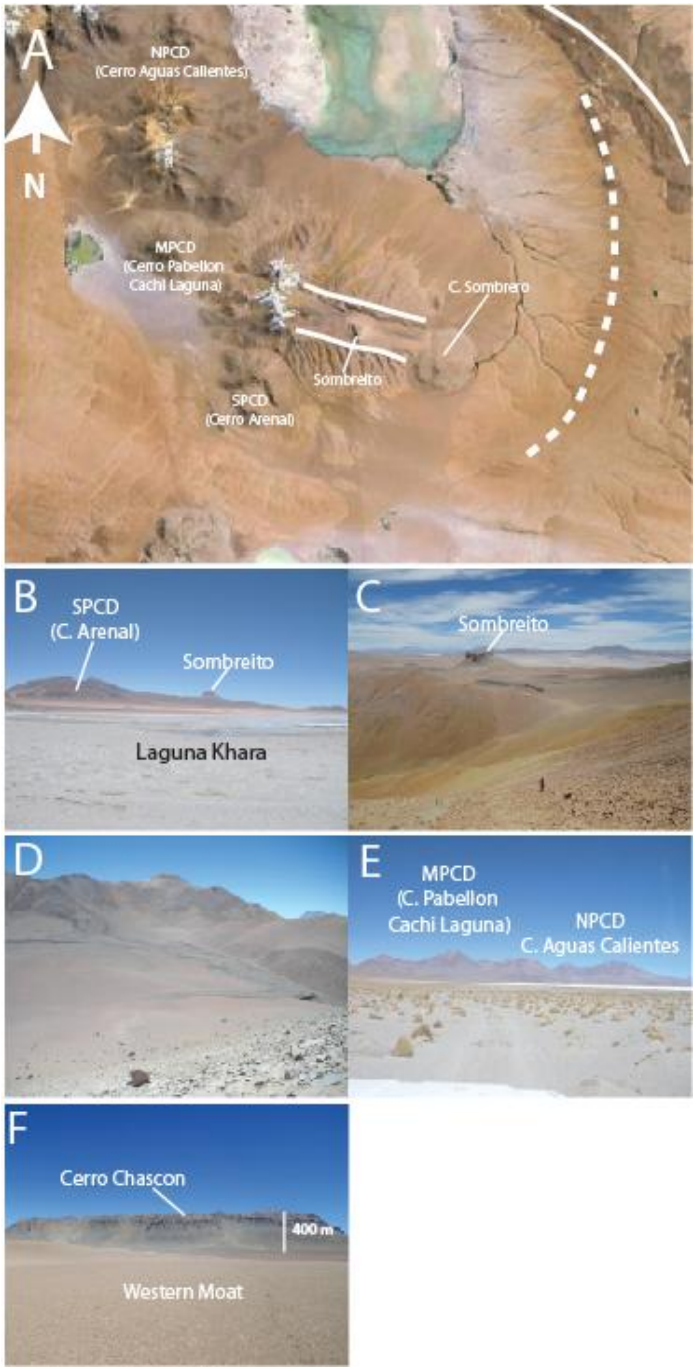

Figure 2.13. Field photos of the post-climactic and resurgent domes of the Pastos Grandes Caldera. A) Google Earth image of the resurgent center surrounded by the post-climactic lava domes. B) Looking north towards the resurgent dome from the southern margin of the Pastos Grandes caldera. C and D) Looking into the central depression of the resurgent dome from the northwest flank and southern flank respectively. E) Looking west towards the post-climactic dome complex from the eastern margin of the caldera. F) Looking south towards Cerro Chascon from the western moat of the caldera.

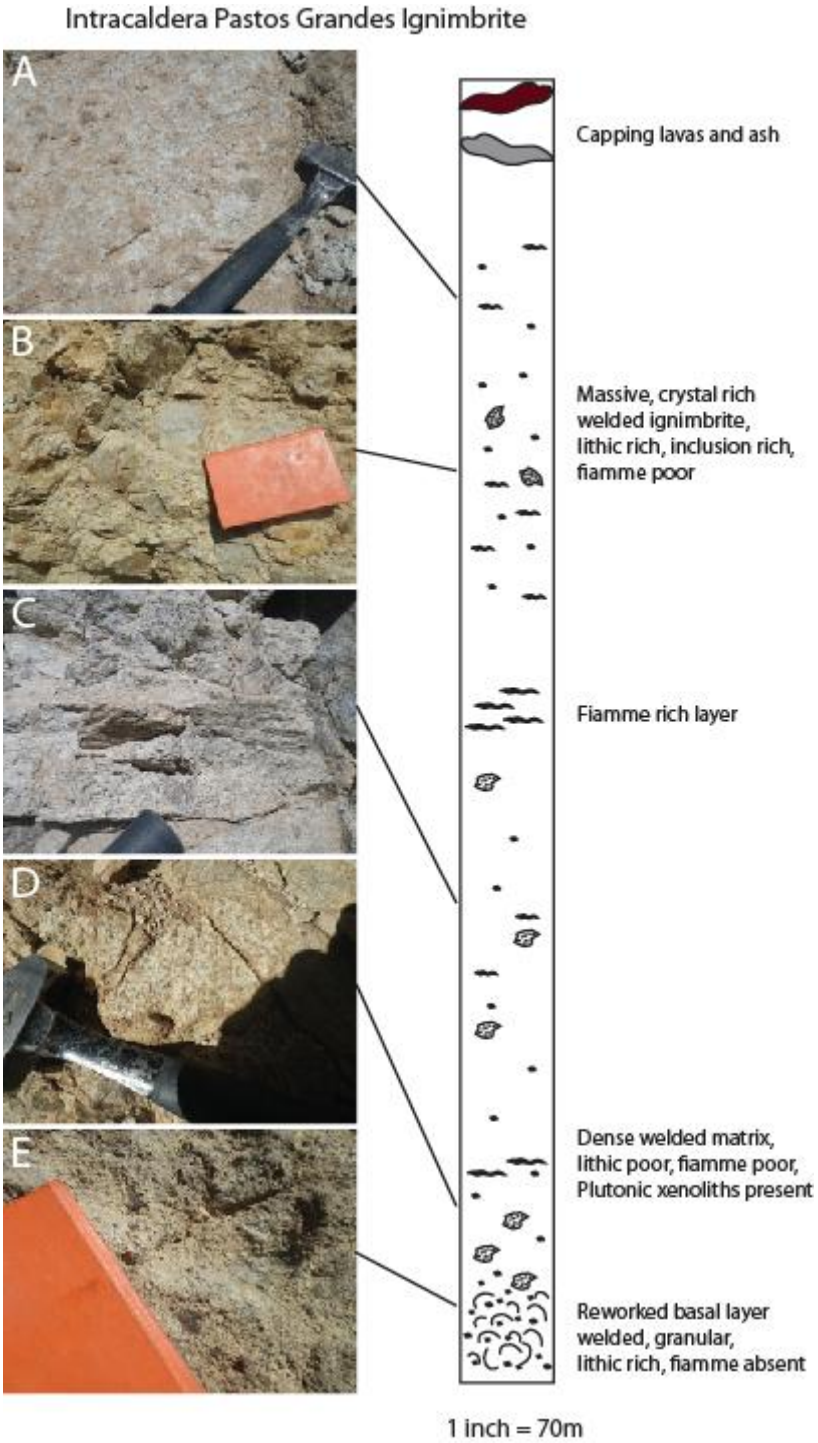

Figure 2.14. Idealized intracaldera stratigraphic sequence for the PGI. Field photos (A-E) show examples of the sequence from the lowest exposed to the top.

Table 2.1a. New chronologic data for the PGCC. All analyses were done on biotite separates. The locations are discussed in the text. Coordinates are as follows: Cerro Chuhuilla (21°27'01.3"S, 67°41'46.4"W), Serrania Khenwal (21° 46'07.4", 67°31'46.6") Northern post-climactic dome (Cerro Aguas Calientes; 21°37'4.80"S, 67°53'21.20"W), Middle post-climactic dome (Cerro Pabellon Cachi Laguna; 21°42'59.20"S, 67°54'37.20"W), Southern post-climactic dome lava (Cerro Arenal; 21°49'6.20"S, 67°53'2.70"W).

Unit/Sample #	Min	$^{40}Ar/^{36}Ar$	$^{40}Ar(\%)$	Isochron age (Ma)	Age (Ma)	2σ (Ma)	MSWD
Serrania Khenwal							
JFKBOL10-006	bio	295.5 ± 10.6	37.0	5.99 ± 0.38	6.10	0.09	0.22
Cerro Chuhuilla							
JFKBOL10-009	bio	295.5 ± 10.6	47.7	6.46 ± 0.32	6.63	0.09	2.12
Northern PCD (Cerro Aguas Calientes)							
JFKBOL10-011	bio	295.5 ± 10.6	45.3	2.44 ± 0.06	2.43	0.04	0.17
Middle PCD (Cerro Pabellon Cachi Laguna)							
JFKBOL10-013	bio	295.5 ± 10.6	42.5	2.20 ± 0.05	2.20	0.04	0.17
Southern PCD (Cerro Arenal)							
JFKBOL10-014	bio	295.5 ± 10.6	33.4	3.00 ± 0.07	3.01	0.07	0.25

Table 2.1b. Preferred ages from Salisbury et al. (2011). Ages discussed in the text refer to sanidine ages. Biotite ages from Salisbury et al. as well as ages from all previous studies are provided in the supplement (Table S2.1).

Unit/Sample #	Min	$^{40}Ar/^{36}Ar$	Isochron age (Ma)	Age (Ma)	2σ (Ma)	MSWD
Pastos Grandes						
B06-056	san	293.0 ± 18.0	2.89 ± 0.02	2.88	0.01	0.65
B06-058	san	294.0 ± 37.0	2.88 ± 0.02	2.88	0.01	0.44
B06-036	san	292.1 ± 06.2	2.95 ± 0.03	2.88	0.01	0.75
B06-045	san	293.0 ± 15.0	2.91 ± 0.02	2.91	0.02	0.77
				2.89	**0.01**	**0.78**
Sombrero Dome						
B06-057	bio	296.6 ± 03.9	2.98 ± 0.06	3.00	0.01	0.93
B06-057	san	402.0 ± 280.0	2.98 ± 0.09	**2.83**	**0.02**	**0.75**
Alota Ignimbrite						
B06-063	bio	247.0 ± 34.0	5.78 ± 0.13	5.63	0.04	0.91
B06-063	san	294.3 ± 02.5	5.25 ± 0.07	5.24	0.02	0.4
ALI-189	san	301.5 ± 13.0	5.22 ± 0.03	5.23	0.02	1.56
				5.23	**0.01**	**0.49**
Alota Dome						
92CJ018	bio	298.3 ± 4.9	5.46 ± 0.06	5.49	0.02	0.79
92CJ018	san	290.9 ± 7.1	5.23 ± 0.04	**5.22**	**0.02**	**0.60**
Chuhuilla						
89019	san	296.4 ± 06.4	5.45 ± 0.04	**5.45**	**0.02**	**0.46**

Table 2.2. PGCC Ignimbrite Volumes

Unit	Exposed Outflow Area (A)	Exposed Outflow Volume (B)	Factor A (exposure) (C)	Factor B (erosion) (D)	Corrected Outflow Volume (E)	Extrap. Outflow Area (F)	Extrap. Outflow Volume (G)	Intracaldera Area (H)	Intra-caldera Thickness (I)	Intra-caldera Volume (J)	Adjusted Intracaldera Volume (K)	Total Bulk Volume (L)	Total Volume (DRE) (M)	Intra-caldera x 3 (N)	Intra-caldera x 2 (O)
Pastos Grandes	1027	44	4	1.33	233	5852	327	868	1.4	1215	608	877	809	1823	1215
Chuhuilla	563	21	6	1.33	111	6370	191	1737	1.4	2432	1216	1327	1299	3648	2432
Alota	226	5			NA	NA	NA		0.2	4	NA	9	8	NA	NA

Supplementary Volume Calculation Information

All discussion refers to Table S2.3

Column A Exposed Outflow Area

Aerial extent of identifiable outcrops of Pastos Grandes ignimbrite – refer to calculations tab.

Column B Exposed Outflow Volume

A minimum constraint on the ignimbrite outflow volume is made based on the exposed outcrops of the Pastos Grandes ignimbrite. Outcrop volumes are calculated based on aerial extent (Column A) and average thickness. Thicknesses are calculated based on vertical exposures in drainages or by distal toes of the outflows. The average thicknesses for each area of outcrop in the calculations tab vary by as much as 50 m. On this basis, the total exposed outflow volume of the PGI is approximately 40 km^3 (Column B in Table S2.3). These minimum volumes are the basis for the extrapolated and corrected volumes discussed below.

Column C Correction Factor A

Much of the northern and western distribution of the PGI is obscured by burial by younger deposits. Folkes et al. (2011) describe a correction factor to account for the underestimation of preserved deposits due to burial by younger deposits. A correction factor of 1 indicates that all preserved material is exposed and observed. The Pastos Grandes ignimbrite is well exposed to the North and East of the caldera. However, modern arc related volcanism covers the outflow in most of the western hemisphere (Figure 2.2 of text). Rare exposures of PGI were found under modern arc lavas along the western margin of the complex in Chile and in other surrounding areas. Around the

caldera area 4x that exposed is thought to be covered by younger deposits, so a correction factor of 4 is applied to the Pastos Grandes volume.

Column D Correction Factor B

A second correction factor is used to account for loss of the deposits due to erosion. A correction factor of 1 indicates that there has been no post-depositional erosion (Folkes et al., 2011). Steep cliffs at the distal extent of the Pastos Grandes ignimbrite to the East and deep incision from drainage indicate moderate erosion on even the youngest of the ignimbrites in the complex. We assume that the ignimbrites did not travel great distances from the caldera due to topographic boundaries such as the Paleozoic sediments in the Alota Basin, as well as to the north of the complex (Figure 2.2 of text). These barriers would have impeded the outflow and constrained the aerial extent. Distal outcrops of the PGI have been observed in the Alota Basin in the form of pumice rafts. These accumulation zones are typically five meters thick. Even in areas where pre-existing topography forced ponding of the ignimbrite, the original distal thicknesses were likely less than the 15-20 m observed for the PGI in the Alota Basin and the nearly 40 m north of the caldera, implying headward erosion along the margins of the ignimbrite. Using satellite images and elevation data, we estimate that as much as 30% of the Pastos Grandes Ignimbrite north of the caldera and 20% east of the caldera (area the Alota Basin) has been lost to post-depositional erosion, thus a correction factor B of 1.33 is applied (Column D in Table S3).

Column E – Corrected outflow volume

This is the Exposed Volume (Column B) to which the correction factors have been applied.

Column F Extrapolated outflow area

The outflow distributions can be extrapolated to cover the area surrounding the caldera out to the maximum exposed outcrop in each direction. The extrapolated outflow area for the Pastos Grandes ignimbrite is 5900 km^2 (Column F in Table 3 of text). As with the Chuhuilla ignimbrite, the largest run-out distance was to the north (~40 km). Run-out distances of approximately 20 km surround the caldera to the east, south, and west. Ambiguity associated with the western run-out distance is due to the subsequent lava flows of the modern arc. To the north, east, and south the outflow was constrained by topography among the Paleozoic sediments and pre-existing APVC volcanic successions. The 5900 km^2 comes from the total area created by connecting all of the distal outcrops after subtracting the included caldera area. Cell C19 in calculations.

Column G Extrapolated Outflow Volume

This is the extrapolated area in Column F multiplied by the average thickness and Factor B. 327 km^3 Cell C20 in calculations.

Comments

Both the correction factors and the extrapolation based on outcrops involve ambiguity and uncertainties. The two different methods give 211 and 327 km^3 respectively. These methods give a good constraint on minimum the outflow volumes and we combine the two methods by taking an average 269 km^3. We use 270 km^3 as the minimum volume of outflow Pastos Grandes ignimbrite.

Intracaldera Volume

Previous constraints on intracaldera volume involved using the caldera area and height of the resurgent dome to calculate minimum volumes (Salisbury et al., 2011). These calculations do not account for the true thickness of the dipping intracaldera sequence nor the possible asymmetric collapse style of the caldera.

Column H - Intracaldera area.

The area contained within the Pastos Grandes Caldera is approximately 900 km^2 (Column H in Table S2.3).

Column I – Intracaldera thickness

Geometrically corrected minimum thickness of the intra caldera calculated according to Figure S4.

Column J – Intracaldera volume

The maximum height of the resurgent dome is 1.1 km above the caldera moat. We constrain the intracaldera volume based on the surface area of the caldera, and the true thickness of the dipping intracaldera facies exposed in the apical graben of the resurgent dome. A NW-SE trending apical graben dissects the resurgent dome exposing over 1 km of the intracaldera facies of the Pastos Grandes ignimbrite. (Figure S4) Based on the geometry of the exposed facies, a minimum thickness of 1.4 km (Column I in Table 3 of text) was calculated for the intracaldera fill (Figure S4). As the base of the ignimbrite is not exposed in the central depression or in any of the drainages flanking the dome this calculation represents a minimum volume. As stated by Lindsay et al. (2001) the intracaldera fill may be thicker than the height of the resurgent block, so our intracaldera thickness is a minimum. These parameters lead to an intracaldera volume of 1215 km^3

(Column J in Table S3). Fill is assumed to be thicker on the East side of the caldera following trap-door style collapse, hinged on the West. Following the approach of Lindsay et al. (2001) we take only half of the calculated volume for the intracaldera wedge volume (~600 km ^{3}) (Column K in Table S3). Collapse breccias along the margin of the caldera were not observed; therefore no correction is applied to the intracaldera volume (i.e. Lipman, 1997).

Column K Adjusted Intracaldera Volume

Since the evidence suggests an asymmetric collapse hinged on the West, the intracaldera fill is assumed to be thicker on the east side of the caldera. Following the approach of Lindsay et al. (2001) we take only half of the calculated volume for the intracaldera volume giving an estimate of ~600 km ^{3}.

Columns L & M Total Bulk Volumes

The total bulk volume (Column L) is calculated by adding the adjusted intracaldera volume (Column K) and the average outflow volume of 267 km^3 that combines the extrapolated and corrected outflow volumes in an average. The total bulk volume of the PGI was calculated to be roughly 800 km^3.

Columns M DRE volumes

Based on bulk outflow ignimbrite densities of 1.8-2.2 g/cm^3 (Salisbury et al., 2011), outflow volumes are adjusted by 75% to give dense rock equivalent (DRE) or magma equivalent volumes. No adjustment is made for the intracaldera because the densities are in the 2.4 to 2.6 g/cm^3 and are magma equivalent. A DRE volume of 809 km^3 for the PGI (Column M) is achieved by adding Column K (intracaldera volume) to 75% of Column E

(outflow volume). As the outflow accounts for such a small percentage of the total volume, the bulk volume and the DRE volume are relatively close in value.

Chuhuilla Ignimbrite

The volume of the Chuhuilla Ignimbrite was calculated using the same methods as the PGI. The proximal outcrops of the Chuhuilla Ignimbrite are buried beneath the Pastos Grandes Ignimbrite in all directions surrounding the caldera. Distal outcrops were mapped to the North and South of the caldera. The total exposed outflow volume is calculated in exactly the same way as for the PGI. The exposed outflow volume of the Chuhuilla ignimbrite is approximately 21 km^3.

The same correction factors used in the PGI calculation are used for the Chuhuilla Ignimbrite. The base of the Chuhuilla Ignimbrite is never observed and much of the outflow to the North and East of the caldera is buried under the Pastos Grandes Ignimbrite (Figure 2 of text). It is assumed that the Chuhuilla ignimbrite has a similar distribution to the Pastos Grandes ignimbrite (Figure S5); therefore a correction factor of 6 is applied to the Chuhuilla volume to account for the lack of exposure. It is difficult to constrain the Chuhuilla outflow volume lost to erosion. It is thought that the climate has remained relatively constant in the region over the duration of activity in the PGCC (Strecker et al., 2007; Guapp et al., 1999); therefore it is valid to assume that erosion of the Chuhuilla ignimbrite would be on the same scale as that of the PGI.

The extrapolated outflow volume is based on the distal outcrop pattern surrounding the larger Chuhuilla caldera. For the Chuhuilla ignimbrite, the total extrapolated outflow

area is 6300 km^2. This area comes from a large run-out to the north of the caldera (~ 60 km), a range of 15-20 km east and west of the caldera and minimal run-out to the South.

A similar approach was taken for the Chuhuilla caldera. The area is assumed by continuing the line of arcuate lava flows and using the same hinge geometry to yield an area of 1700 km^2. Assuming the Chuhuilla caldera experienced the same magnitude of resurgence, the minimum intracaldera thickness would also have been on the order of 1.4 km. Thus, the intracaldera volume would have been 1200 km^3, taking into account the same wedge geometry.

Column N and O Extrapolated volumes

While assumptions have been made regarding the exposure of outflow volume as well as the intracaldera thickness, we believe that our approach has been to minimize the errors and constrain minimum volumes accurately. In particular we have minimized intracaldera volumes by taking collapse geometry into account. We have not followed the typical practice of assuming a piston caldera collapse and equivalent volumes of intracaldera to outflow. We have also not included any extrapolation for co-ignimbrite ash plumes that can deposit material well beyond the extent of the ignimbrite. Due to the nature of this poorly consolidated ash, it is likely quickly eroded and re-deposited elsewhere, obscuring its existence from the stratigraphic record (Sparks et al., 1997). As much as 30-50% of the total volume of the eruption has been reported in the co-ignimbrite ash fall deposits for Toba, Unzen, and Tambora (Ninkovich et al. 1978; Rose and Chesner 1987; Watanabe et al. 1999; Sigurdsson and Carey 1989). Accounting for this volume requires a large amount of extrapolation and inference that can nearly double the total volumes.

While the style of eruption envisaged for the Pastos Grandes and Chuhuilla ignimbrites calls for a low column, distal ash deposits have been found in the Chilean coastal range hundreds of km away (Breitkreuz et al., 2012). Here, we avoid any attempt to reconcile volumes of co-ignimbrite ash due to lack of contiguous preservation of ashfall deposits, making extrapolations and correction factors ambiguous.

If we adopted the practice if 1:1:1 with our data could obtain volumes of 1800 to 3600 km^3 for the PGI and 3600 to 7200 km^3 for the Chuhuilla Ignimbrite for wedge and disc shaped intracaldera respectively. These would bring these and other Andean eruptions in alignment with some of the largest known eruptions in the geological record. True volumes for the PGI and Chuhuilla are likely to be much greater than the total DRE values calculated here.

References

Breitkreuz, C., de Silva, S. L., Wilke, H. G., Pfänder, J. A., & Renno, A. D. (2014). Neogene to Quaternary ash deposits in the Coastal Cordillera in northern Chile: Distal ashes from supereruptions in the Central Andes. *Journal of Volcanology and Geothermal Research*, *269*, 68-82.

Folkes, C. B., Wright, H. M., Cas, R. A., de Silva, S. L., Lesti, C., & Viramonte, J. G. (2011). A re-appraisal of the stratigraphy and volcanology of the Cerro Galán volcanic system, NW Argentina. *Bulletin of volcanology*, *73*(10), 1427-1454.

Gaupp, R., Kött, A., & Wörner, G. (1999). Palaeoclimatic implications of Mio–Pliocene sedimentation in the high-altitude intra-arc Lauca Basin of northern Chile. *Palaeogeography, Palaeoclimatology, Palaeoecology*, *151*(1), 79-100.

Lindsay, J. M., De Silva, S., Trumbull, R., Emmermann, R., & Wemmer, K. (2001). La Pacana caldera, N. Chile: a re-evaluation of the stratigraphy and volcanology of one of the world's largest resurgent calderas. *Journal of Volcanology and Geothermal Research*, *106*(1), 145-173.

Lipman, P. W. (1997). Subsidence of ash-flow calderas: relation to caldera size and magma-chamber geometry. *Bulletin of Volcanology*, *59*(3), 198-218.

Ninkovich, D., Sparks, R. S. J., & Ledbetter, M. T. (1978). The exceptional magnitude and intensity of the Toba eruption, Sumatra: an example of the use of deep-sea tephra layers as a geological tool. *Bulletin Volcanologique*, *41*(3), 286-298.

Rose, W. I., & Chesner, C. A. (1987). Dispersal of ash in the great Toba eruption, 75 ka. *Geology*, *15*(10), 913-917.

Salisbury, M. J., Jicha, B. R., de Silva, S. L., Singer, B. S., Jiménez, N. C., & Ort, M. H. (2011). $^{40}Ar/^{39}Ar$ chronostratigraphy of Altiplano-Puna volcanic complex ignimbrites reveals the development of a major magmatic province. *Geological Society of America Bulletin*, *123*(5-6), 821-840.

Sigurdsson, H., & Carey, S. (1989). Plinian and co-ignimbrite tephra fall from the 1815 eruption of Tambora volacano. *Bulletin of Volcanology*, *51*(4), 243-270.

Strecker, M. R., Alonso, R. N., Bookhagen, B., Carrapa, B., Hilley, G. E., Sobel, E. R., & Trauth, M. H. (2007). Tectonics and climate of the southern central Andes. *Annu. Rev. Earth Planet. Sci.*, *35*, 747-787.

Watanabe, K., Ono, K., Sakaguchi, K., Takada, A., & Hoshizumi, H. (1999). Co -ignimbrite ash-fall deposits of the 1991 eruptions of Fugen-dake, Unzen Volcano, Japan. *Journal of volcanology and geothermal research*, *89*(1), 95-112.

Watts, R. B., de Silva, S. L., de Rios, G. J., & Croudace, I. (1999). Effusive eruption of viscous silicic magma triggered and driven by recharge: a case study of the Cerro Chascon-Runtu Jarita Dome Complex in Southwest Bolivia.*Bulletin of volcanology*, *61*(4), 241-264.

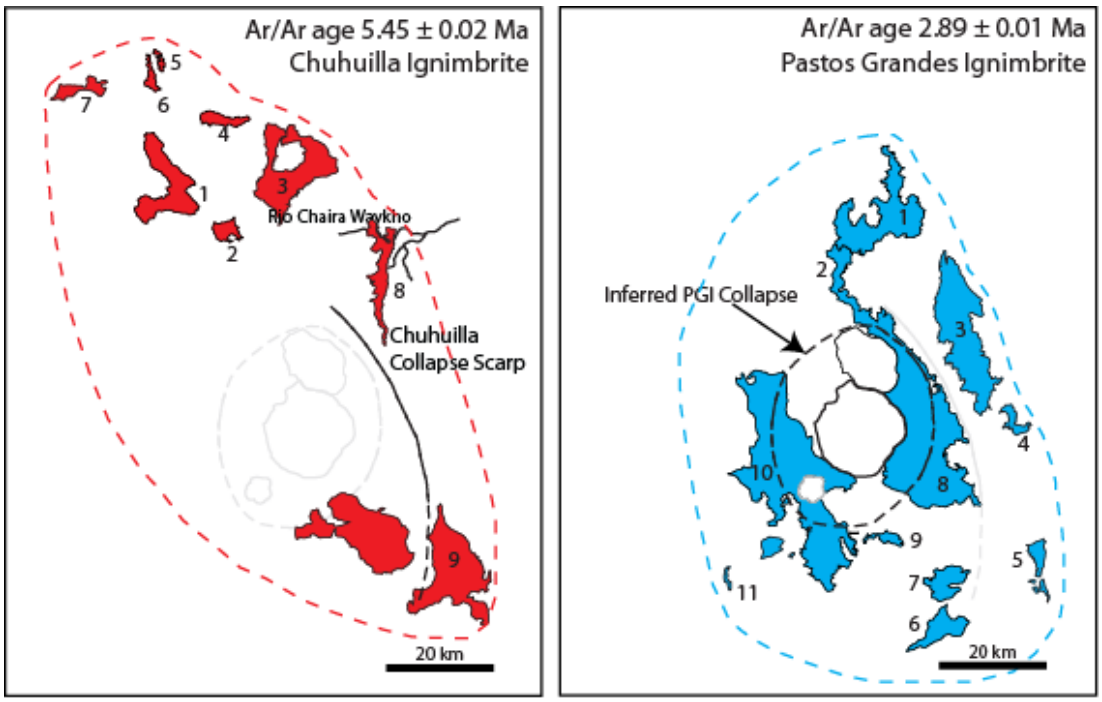

Figure S2.1. The assumed maximum distribution of the Chuhuilla and Pastos Grandes ignmibrites. Numbers refer to the outcrop discussed in the volume table. Each outcrop volume was calculated individually and added to create the total exposed outflow volume. Note that outcrops in the caldera are not part of this calculation as they create part of the intracaldera volume calculated separately.

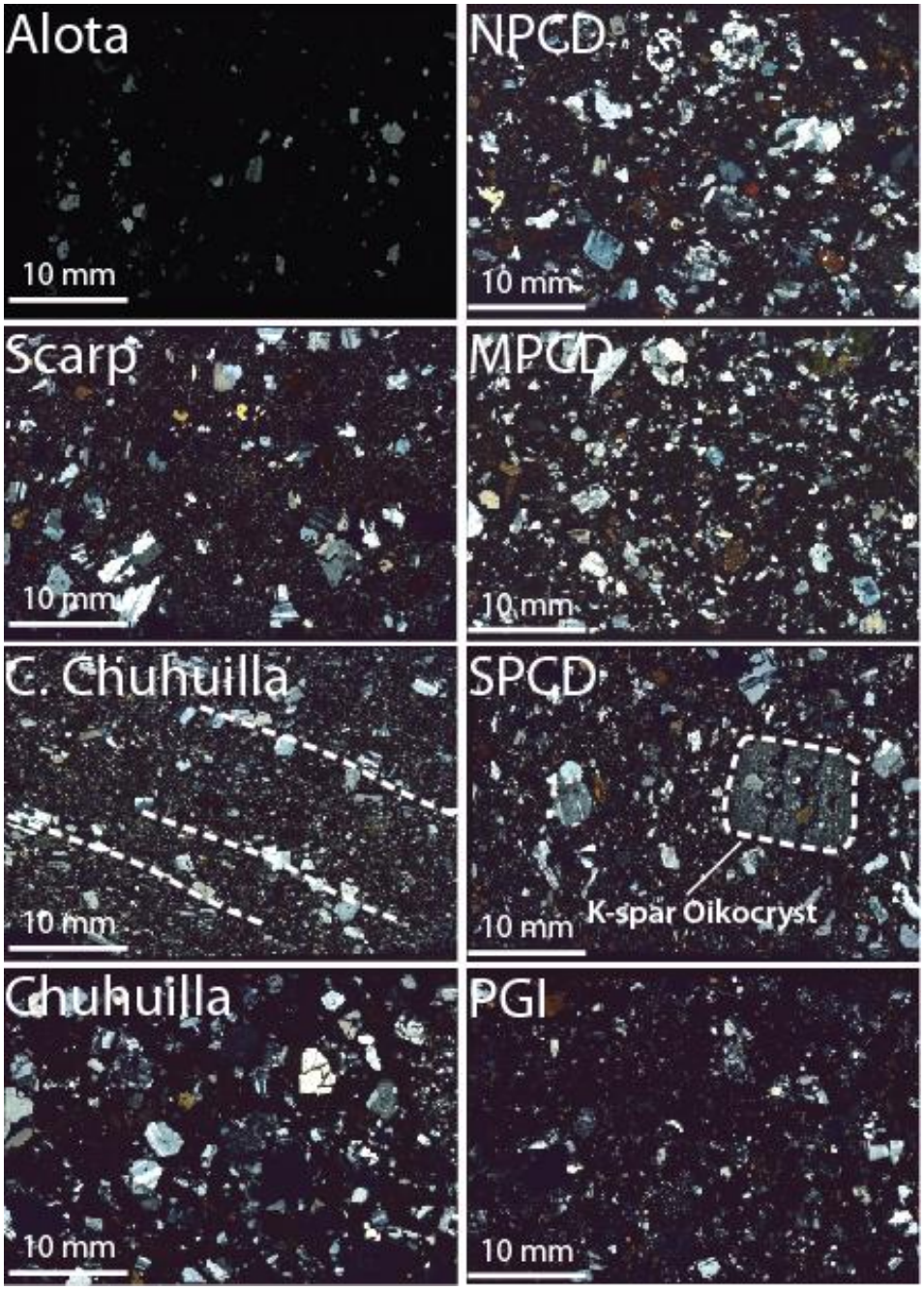

Figure S2.2. Thin section scans (cross polarized) of each unit described in the text. While Alota seems to show fewer crystals in the scanned image, the crystallinity of the unit is similar to that of the larger-volume ignimbrites. Phenocrysts of the ignimbrites are typically broken. Microlites are more common in the post-caldera lavas (PCDs as well as the scarp lavas and C. Chuhuilla) than in the ignimbrites. The PCDs are almost identical with the exception of the K-spar oikocrysts of the SPCD (Cerro Arenal). The oikocrysts contain inclusions of quartz, biotite, and other feldspars. Alignment of phenocrysts is only faintly present in C. Chuhuilla (indicated by dotted lines).

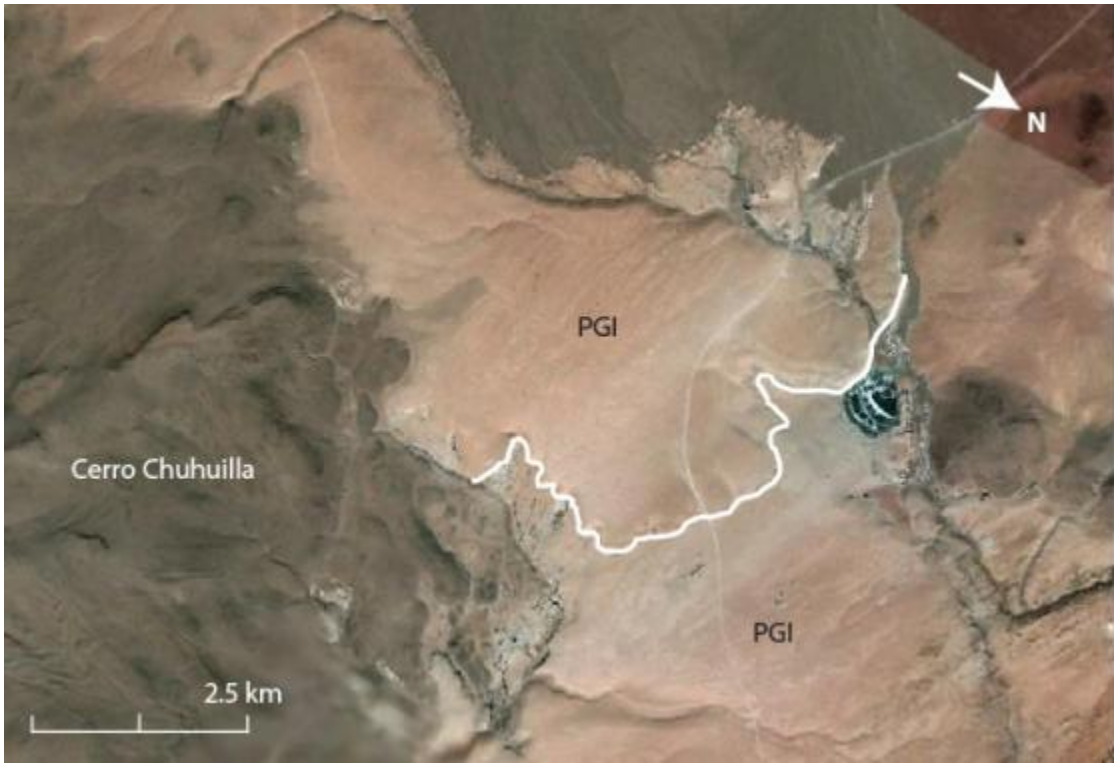

Figure S2.3. Image of a Pastos Grandes lobe that overrides previous pulses of the PGI that were broken up by the topographic boundary created by Cerro Chuhuilla.

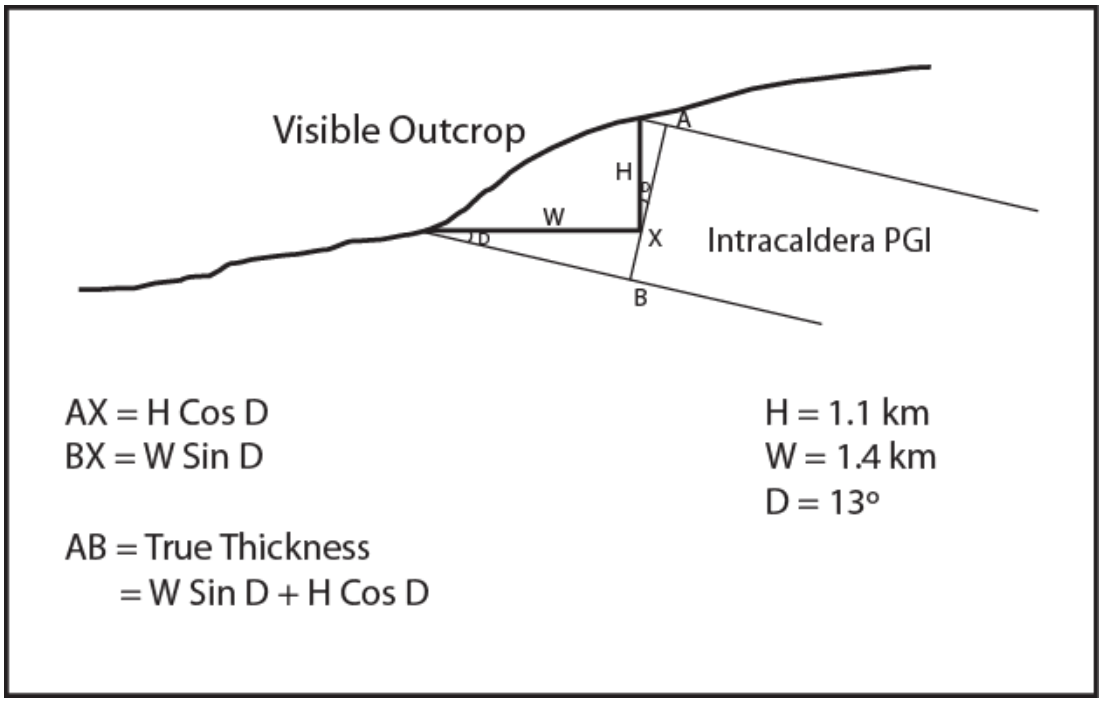

Figure S2.4. Welded tuff corresponding to the Pastos Grandes ignimbrite located in the central depression of the resurgent dome. "True" thickness (~1.4 km) of the welded tuffs is calculated using height difference (1.1 km), horizontal outcrop distance (1.4 km) and dip of the layers (13˚).

Table S2.1. Previously Reported Ages for the PGCC. A compilation of both Ar/Ar and K/Ar analyses from four decades of work in the APVC. The analyses from Salisbury et al. (2011) are biotite ages that supplement the sanidine ages reported in Table 2.1b.

Ignimbrite and Correlated Tuffs	Age (Ma)	2σ (Ma)	Analysis	Reference
Pastos Grandes Ignimbrite				
PGI	2.91	0.03	Ar/Ar	Salisbury et al. (2011)
PGI	2.93	0.01	Ar/Ar	Salisbury et al. (2011)
PGI	2.96	0.02	Ar/Ar	Salisbury et al. (2011)
PGI	2.97	0.02	Ar/Ar	Salisbury et al. (2011)
PGI	3.20	0.3	K/Ar	Lema and Ramos (1996)
PGI	3.20	0.4	K/Ar	From Baker and Francis (1978)
PGI	3.50	0.3	K/Ar	Pacheco and Ramirez (1997)
Chatola Tuffs	3.60	0.5	K/Ar	Pacheco and Ramirez (1996)
Chatola Tuffs	3.20	0.2	K/Ar	From Baker and Francis (1977)
Alota Ignimbrite				
Alota Ignimbrite	5.70	0.03	Ar/Ar	Salisbury et al. (2011)
Alota Ignimbrite	5.50	0.03	Ar/Ar	Salisbury et al. (2011)
Alota Ignimbrite	5.54	0.03	Ar/Ar	Salisbury et al. (2011)
Juvina Tuffs	6.40	0.3	K/Ar	From Baker and Francis (1978)
Chuhuilla Ignimbrite				
Chuhuilla Ignimbrite	5.70	0.03	Ar/Ar	Salisbury et al. (2011)
Chuhuilla Ignimbrite	5.51	0.03	Ar/Ar	Salisbury et al. (2011)
Chuhuilla Ignimbrite	5.54	0.03	Ar/Ar	Salisbury et al. (2011)
Chuhuilla Ignimbrite	5.90	0.3	K/Ar	From Baker and Francis (1978)
Tomasamil Tuffs	6.00	0.5	K/Ar	Almendras and Baldellon (1997)
Tomasamil Tuffs	6.20	0.7	K/Ar	Almendras and Baldellon (1997)
Tomasamil Tuffs	6.30	0.8	K/Ar	Pacheco and Ramirez (1997)
Tomasamil Tuffs	6.70	0.6	K/Ar	Almendras and Baldellon (1997)
Thiumayu Tuffs	7.40	0.8	K/Ar	Pacheco and Ramirez (1997)

Table S2.2. Whole Rock Chemistry.

Sample ID	Sample Number	SiO_2	TiO_2	Al_2O_3	FeO*	MnO	MgO	CaO	Na_2O	K_2O	P_2O_5
Chuhuilla	JFKBOL10 -010	67.34	0.523	15.07	3.57	0.070	1.65	3.70	2.57	5.00	0.501
Chuhuilla	CRT 07 - BOL25C*	61.26	0.954	16.78	6.26	0.100	2.99	5.20	3.36	2.87	0.229
Chuhuilla	SALB06 - 050*	67.59	0.544	14.93	3.50	0.066	1.80	3.47	3.78	4.17	0.136
Chuhuilla	SALB06 -054*	69.13	0.510	15.12	2.84	0.055	1.72	3.30	3.01	4.19	0.128
Chuhuilla	JFKBOL12 -003	67.38	0.547	15.28	3.61	0.063	1.96	3.64	2.91	4.48	0.123
Chuhuilla	JFKBOL12 -006	66.79	0.610	15.79	4.05	0.071	1.83	3.93	2.96	3.81	0.159
Scarp Lava	JFKBOL10-006	64.10	0.876	15.73	5.22	0.080	2.67	4.33	2.98	3.80	0.209
Scarp Lava	JFKBOL12 -021	63.58	0.852	16.04	5.87	0.082	2.41	4.50	3.11	3.36	0.199
Scarp Lava	JFKBOL12 -020	64.53	0.756	15.90	5.42	0.075	2.03	4.36	3.29	3.47	0.186
Scarp Lava	JFKBOL12 -022	63.59	0.823	15.83	6.54	0.083	2.00	4.35	3.17	3.42	0.198
Scarp Lava	JFKBOL10 -008	61.40	0.944	16.22	6.03	0.104	3.30	5.67	3.08	3.04	0.212
Scarp Lava	JFKBOL10 -009	61.49	0.940	17.05	5.95	0.099	2.91	5.10	3.36	2.90	0.218
Alota	SALB06 -063*	74.93	0.061	14.68	0.98	0.125	0.11	0.61	3.16	5.18	0.171
Alota	CRT 92 -CJ002*	75.27	0.113	14.41	1.20	0.072	0.20	0.84	3.24	4.58	0.068
Alota	CRT 92 -CJ005*	76.37	0.103	13.05	1.22	0.089	0.23	0.88	3.28	4.70	0.064
Alota	CRT 92 -CJ0012*	74.55	0.077	14.63	0.97	0.113	0.15	1.03	3.07	5.32	0.096
Alota	CRT 92 -CJ015*	75.28	0.112	13.85	1.20	0.069	0.20	0.84	2.97	5.33	0.156
PGI	JFKBOL10-003	70.05	0.516	14.32	3.25	0.061	1.43	2.98	2.71	4.53	0.152
PGI	SALB06 -037*	68.77	0.501	14.83	3.00	0.060	1.38	3.92	2.91	4.12	0.521
PGI	CRT 07 -BOL27*	68.44	0.543	15.35	3.41	0.062	1.51	3.35	2.93	4.25	0.144
PGI	JFKBOL12 -002	67.83	0.519	15.05	3.19	0.065	1.45	3.54	3.81	4.43	0.118
PGI	JFKBOL12 -008	69.18	0.504	15.17	3.13	0.056	1.32	3.35	3.07	4.10	0.121
PGI	JFKBOL12 -009	69.11	0.517	14.79	3.33	0.056	1.47	3.45	3.17	3.98	0.124
PGI	JFKBOL12 -023	67.81	0.549	15.61	3.42	0.062	1.63	3.67	3.04	4.08	0.127
Post Collapse Lavas	JFKBOL10 -011	65.69	0.669	15.91	4.38	0.085	2.08	3.99	3.26	3.77	0.155
Post Collapse Lavas	JFKBOL10 -013	66.44	0.620	16.19	3.89	0.068	1.76	3.95	3.42	3.51	0.151
Post Collapse Lavas	JFKBOL10 -014	67.71	0.637	15.33	3.73	0.062	1.63	3.16	3.24	4.34	0.153
Post Collapse Lavas	JFKBOL10 -015	64.40	0.807	16.37	4.71	0.071	1.96	4.45	3.44	3.58	0.218
Post Collapse Lavas	JFKBOL12 -015	69.03	0.495	15.33	3.43	0.050	1.03	3.14	3.34	4.04	0.108
Post Collapse Lavas	JFKBOL12 -016	68.62	0.495	15.18	3.67	0.063	1.32	3.05	3.42	4.07	0.123
Post Collapse Lavas	JFKBOL10 -016	63.47	0.576	17.01	4.96	0.108	2.69	5.18	3.06	2.79	0.142

* Sampled from previous studies

CHAPTER 3
The Upper Crustal Magma System of the Pastos Grandes Caldera Complex: Sources and Processes

Jason F. Kaiser
Shanaka de Silva

Abstract

Eruptions from the Pastos Grandes Caldera Complex (PGCC) have produced compositionally restricted, high-K dacites with volumetrically minor rhyolites. The large-volume ignimbrites as well as the post-climactic lavas of each caldera cycle are dense and crystal rich. Combined with granodiorite xenoliths, each caldera cycle contains a progression of textural maturity from ignimbrite, through post-climactic lavas, to remnant pluton. The chemical signatures in the PGCC mirror those of the host Altiplano Puna Volcanic Complex (APVC) and resemble typical arc characteristics. The peraluminous, large ion lithophile element (LILE) enriched magmas (Ba/Nb of 4.7-4.8 and Ba/La of 1.6-2.0) certainly have an arc affinity; however, radiogenic isotopes ($^{87}Sr/^{86}Sr$ ~0.708 – 0.709) suggest high degrees of crustal assimilation related to increased mantle input from melted asthenosphere. It is suggested here that a combination of assimilation and fractional crystallization from the regional parental source would create the magmas erupted in the PGCC. Decreases in the $^{87}Sr/^{86}Sr$ from the Chuhuilla caldera cycle, to the younger Pastos Grandes cycle suggest higher amounts of crustal assimilation related to more heat flow during the peak of the flare up. Meanwhile, shallow crustal magma processing manifests itself as steep and increasing normalized La/Yb ratios (11-23) as well as increasing Eu/Eu* over time. These differentiation processes were enough to lead to a similar AFC style scenario that

produced a small rhyolite magma body that was sourced from the caldera-related dacites. Overall, these episodes of a largely homogenous magmatism in the shallow crust built a composite batholith that is a small part of the regional batholith under the APVC.

Introduction

Eruptions of nested caldera systems record geologic instants of batholith scale magma evolution. The volcanic successions combined with the remnant plutons provide records of batholith accumulation and solidification. Many studies have commented on the degree of chemical homogeneity of crystal-rich, calc-alkaline, high-K dacite to rhyodacite ignimbrites (Hildreth et al. 1991; Chesner 1998; Lindsay et al. 2001; Bachmann et al. 2002; Mason et al. 2004). It is recognized that these magmas have high crystal contents (up to 50% based on pumice samples) resulting in very high bulk viscosities. Accumulation and eruption of 1,000's of km^3 of these viscous magmas requires a unique thermal and mechanical environment in the upper crust. These systems require a thermally primed crust where the behavior of chamber wall rocks promotes the growth of large magma bodies over eruption (Jellinek and DePaolo 2003; de Silva and Gosnold, 2007), while receiving periodic inputs from a mid crustal processing zone (Chmielowski et al. 1999; Zandt et al., 2003). Clarifying the development and history of upper crustal magmatic systems is important for understanding not only the conditions leading to supervolcanic eruptions, but also to the growth of granite batholiths and the evolution of the continental crust.

The Pastos Grandes Caldera in SW Bolivia is an ideal case study to examine the long-term evolution of a large silicic magma chamber, as it has produced a series of dacitic

ignimbrites and lavas over a long time period (~5.5 Myr), with a relatively restricted compositional range. These deposits offer the rare opportunity to explore the long term evolution of a batholith-scale system in a series of volcanic eruptions. Here, a petrologic and geochemical record of the volcanic and plutonic units is reported that builds on previous reconnaissance studies (Watts et al., 1999, Salisbury et al., 2011). With a clear understanding of the chronostratigraphy as a framework, we can compare geochemical signatures of volcanic and plutonic counterparts to elucidate the upper crustal development and evolution of the Pastos Grandes magmatic system. The pre-eruptive magmatic conditions and history are then compared to other systems of the APVC and the Central Volcanic Zone (CVZ) to show similar records of repeated accumulation and evolution of large volumes of remarkably similar magma in the upper crust on the million-year timescale.

Geology of the PGCC

The Pastos Grandes Caldera Complex is located in the Central Volcanic Zone of the Andean Arc (Figure 3.1). The caldera is one of many within the Altiplano Puna Volcanic Complex (APVC) (de Silva, 1989). The APVC spans over 70,000 km^2 of the Altiplano and Puna plateaus. This region experienced crustal shortening and subsequent thickening starting at 25 Ma (Allmendinger et al., 1997). It is estimated that the average crustal thickness in the region of the APVC is 60-80 km (Zandt et al., 2003). The combination of over-thickened crust and an increased input from the mantle resulted in an ignimbrite flare-up from >10 Ma to Present (de Silva, 1989; de Silva, et al., 2006). The peak of this flare up was between 6 and 4 Ma and has been waning since (de Silva, et al., 2006, de Silva and Gosnold, 2007; Salisbury et al., 2011).

As outlined in Chapter 1, the chemical signatures of the arc and APVC magmas require large amounts of crustal modification to the mantle derived magmas as they ascend through the Central Andean crust (LILE enriched – Ba/Nb of 4.7-4.8 and Ba/La of 1.6-2.0 and $^{87}Sr/^{86}Sr$ ~0.708-0.713). Decompression melting of the asthenosphere producing basaltic melts (e.g. Kay and Kay, 1993; Kay et al., 1994) leads to intermediate magma generation through melting, and assimilation (Hildreth, 1981; Hildreth and Moorbath, 1988). As mantle input increased, melting and mixing would have become more prevalent (e.g. Huppert and Sparks, 1988). de Silva et al. (2006) suggest a zone of intermediate magma generation in the mid crust as a result of prolonged input of mafic magma from the deep crust. The Altiplano Puna Magma Body (APMB) was seismically imaged (Chmielowski et al., 1999) and is thought to be the remainder of the source of shallow crustal magmatism during the formation of the APVC (de Silva et al., 2006; de Silva and Gosnold, 2007). Silicic magmas are suggested to have risen from the APMB to the shallow crust where further differentiation produced homogenous high-K dacites throughout the region (Lindsay et al., 2001; Schmitt et al., 2001; Kay et al., 2010; Folkes et al., 2011; Muir et al., 2014).

Baker (1981) first identified the Pastos Grandes caldera (PGCC) as a 30 km elliptical structure with western and northern portions buried by younger volcanic deposits. Subsequent investigations confirmed the PGCC as the source of the Chuhuilla, Alota and the Pastos Grandes Ignimbrites (Salisbury et al., 2011; Ort et al., 2013). The total

cumulative volume of magma erupted from the PGCC is estimated to be more than 2000 km^3 (Kaiser et al., In Prep).

The volcanic succession of the PGCC consists of three ignimbrites that erupted in phases spanning nearly 5.5 Myr of activity and small-volume lava flows and domes associated with each caldera cycle (Figure 3.1). Activity started at roughly 5.5 Ma with formation of the Chuhuilla caldera and ignimbrite. The Chuhuilla ignimbrite (ChI) is poorly exposed due to the deposition of younger ignimbrites and lavas. The total volume is estimated to be ~ 1300 km^3DRE. A suite of lavas formed along Serrania Khenwal, the eastern collapse scarp of the Chuhuilla caldera. The suite of lavas stretches more than 60 km along an arcuate line and terminates with the Cerro Chuhuilla volcano on the northeastern margin of the caldera. At 5.23 Ma, the Alota ignimbrite was formed from the Cerro Juvina Ignimbrite Shield. This ignimbrite is confined to the Alota Basin and accounts for less than 10 km^3. Following a hiatus of nearly 2.5 Myr, the Pastos Grandes ignimbrite (PGI) was formed from the Pastos Grandes Caldera. This caldera is nested within the older, Chuhuilla caldera. The PGI is well exposed in the caldera itself as well as in outflow sheets to the North and East. The total volume of the PGI is estimated to be ~800 km^3 DRE. Following the collapse of the Pastos Grandes caldera was the formation of a complex of post-collapse domes. These domes fill the center of the caldera and surround the structural, resurgent center. The last stage of volcanic activity in the PGCC as well as the APVC is a series of Late Pleistocene domes (Tierney, 2012). The Chascon Runtu Jarita dome complex is part of the regional series and formed inside the margins of the Pastos Grandes Caldera (Watts et al., 1999). Granodiorite xenoliths have been recovered from both the Chascon dome and the resurgent dome of the Pastos Grandes

Caldera. In total, eight units represent multiple stages of caldera, dome, and shield activity in the complex, spanning nearly 5.5 Myr.

Sample Descriptions

Ignimbrites

Ignimbrites of the PGCC (Chuhuilla, Alota, and Pastos Grandes) are dense and crystal rich, each with limited compositional variability (Figure 3.2). The caldera-related ignimbrites (Chuhuilla and Pastos Grandes) are dominated by plagioclase, quartz, biotite, sanidine, and amphibole (modal abundances in Table 3.1). The Alota ignimbrite is unique in the PGCC, offset to higher SiO_2. Pumice of the Alota ignimbrite is dominated by quartz, sanidine, and to a lesser extent, plagioclase and biotite (Table 3.1).

Phenocrysts of the large-volume ignimbrite pumice are typically subhedral to euhedral and many are fractured (Figure 3.3). Plagioclase is common to all three ignimbrites, though it is much larger and better formed in the Chuhuilla ignimbrite. Plagioclase often has oscillatory zoning and equilibrium textures. Biotite is seriate (2-5 mm) and commonly well formed. Amphibole is typically small (1-2 mm) and euhedral in the caldera-related ignimbrites. Sanidine occurs as aggregate crystals, filled with inclusions. The Alota ignimbrite phenocryst assemblage is different from the caldera-related samples. Pumice samples are dominated by sanidine and quartz with less dominant biotite and amphibole. The phenocrysts are more commonly euhedral and less fractured. Trace phases such as zircon and oxides were not observed.

Post-Climactic Lavas

Post-climactic lavas are compositionally more diverse than their ignimbrite counterparts. The post-caldera lavas are more crystal rich than the preceding ignimbrites. Lavas along the eastern scarp of Serrania Khenwal and Cerro Chuhuilla are dense and crystal rich with phenocrysts of plagioclase, biotite, amphibole and small amounts of quartz (Table 3.1). Similarly, the post-climactic dome complex of the Pastos Grandes caldera (C. Aguas Calientes, C. Pabellon Cachi Laguna, C. Arenal) are dense and crystal rich with phenocrysts of plagioclase, biotite, amphibole, and quartz. Sanidine is present as oikocrysts in the southern dome (C. Arenal).

The phenocrysts of each of the post-climactic units are set in glassy matrices with varying amounts of microphenocrysts. Plagioclase microphenocrysts (≤ 1mm) dominate the matrices of lavas along Serrania Khenwal and Cerro Chuhuilla (Figure 3.4). Plagioclase phenocrysts (seriate from 3-6 mm) are sieved to varying degrees with oscillatory zoning and undulose extinction. Biotite and amphibole vary in size from 1-4 mm occurring both individually and in clusters. Both of these phases are corroded to various degrees, to the point of being relict phases in some flows of Cerro Chuhuilla. Reaction rims were observed on biotite, but are extremely rare. Quartz is typically small (1-3 mm) and anhedral to subhedral. These textures are nearly identical to those seen in the post-climactic dome complex of the Pastos Grandes caldera. The only unique feature is the sanidine oikocrysts of Cerro Arenal. These oikocrysts are euhedral and average 1 cm in size. Inclusions in the oikocrysts include biotite as well as smaller sanidine crystals. No reaction textures have been observed in the oikocrysts.

The Chascon dome is similar in crystallinity and texture to the post-collapse domes (Watts et al., 1999). According the Watts et al. (1999), the Chascon dome is crystal-rich (45-48 vol. %) with phenocrysts of plagioclase, quartz, biotite, amphibole, and sanidine. The plagioclase is typically seriate textured exhibiting undulose extinction. The quartz and sanidine show corroded rims with the quartz showing embayments unlike anything seen in the older units of the PGCC. Biotite shows reaction rims, and generally aligned with the flow texture of the groundmass. Amphibole is commonly associated with biotite clusters and is rarely completely altered. The groundmass consists of microlites of abundant plagioclase and minor biotite lathes in a vesicular glass.

Plutonic Clasts

Plutonic clasts were recovered that are holocrystalline counterparts to the pumice and lavas of the volcanic succession. Mineralogy of clasts found in both the resurgent dome and Cerro Chascon have mineralogy similar to the caldera-related ignimbrites (Figure 3.5). The clasts are phaneritic with interlocking plagioclase, K-feldspar, quartz, biotite, and hornblende (Table 3.1). Plagioclase crystals are euhedral to subhedral and are seriate between 2 and 6mm. K-feldspar crystals are typically subhedral and are seriate between 3 and 5mm. Quartz is anhedral to subhedral and 1-5mm. Both biotite and amphibole are euhedral and 1-mm.

Trace phases such as zircon, allanite, titanite, and apatite and Fe-Ti oxides are ubiquitous in both the volcanic and plutonic rocks of the complex with the exception of the Alota ignimbrite. The phases are observed petrographically and in mineral separates, but

abundance, occurrence, and size are difficult to constrain due to their scarcity. Their effect on the trace element trends can be seen in the discussion below.

Textural Maturity

Textural maturity (coarseness) increases from pumice of each of the caldera-forming ignimbrites, through the post-climcatic lavas, to the plutonic clasts (Figure 3.6). Pumice of the caldera-related ignimbrites is vesicular with 40-45% phenocrysts of plagioclase, quartz, biotite, sanidine, and amphibole. Crystallinity increases to roughly 50% in the dense lavas of the post-climactic terrains along the Chuhuilla-related Serrania Khenwal/Cerro Chuhuilla suite and the post-climactic dome complex of the Pastos Grandes caldera. The grey ashy matrix is poorly vesicular and contains phenocrysts of plagioclase, amphibole, biotite, and quartz just as in the ignimbrites. Modal abundances are relatively constant across the volcanic progression with the exception of the addition of plagioclase microphenocrysts in the post-climactic lavas. The plutonic clasts are at the end of the textural progression with their holocrystalline texture.

Methods

Sampling

Sampling in 2010 and 2012 from each unit was done to gain an array of spatial and temporal data. Samples were taken of the pumice in the ignimbrites or of the primary lava from flows and domes. Fresh rocks were collected; altered or weathered surfaces were avoided. Bulk matrix samples of the ignimbrite were excluded due to the likelihood of mechanical fractionation or contamination during eruption and transport. These samples supplement an already extensive collection obtained from past studies (Watts et al., 1999; Salisbury et al., 2011).

Whole Rock Major and Trace Element Analyses

Whole rock analysis of the Pastos Grandes units was done via X-Ray Fluorescence (XRF) and Inductively Coupled Plasma – Mass Spectrometry (ICP-MS) at the Washington State University GeoAnalytical Lab. Sample aliquots were crushed and powdered for analysis at Washington State University. For major element analyses using XRF (ThermoARL), powders were added to the dilithium tetraborate flux and fused following the methods of Johnson et al. (1999). For trace element analyses using ICP-MS (Agilent 7700, quadrupole mass spectrometer), sample preparation followed the low-dilution fusion with dilithium tetraborate followed by an open-vial mixed HF acid digestion method of the geoanalytical lab at WSU. Whole rock chemical results are summarized in Table 3.2.

Radiogenic Sr and Nd Isotope Analyses

Whole rock powders were dissolved in various acids following the standard procedures of New Mexico State University. Sr, Nd, isotopic suites were separated using cation exchange columns. Samples were pipetted onto cation exchange resin in quartz columns with elution medium of 2.5 N hydrochloric acid. Samples were then loaded onto rhenium filaments and analyzed with a VG Sector 30 Thermal Ionization Mass Spectrometer (TIMS).

Zircon Oxygen Isotopes

Zircon was separated from a subset of samples representing the Pastos Grandes eruption sequence using heavy liquids. Zircons were mounted and polished in 1 inch epoxy rounds. Zircons were analyzed via Secondary Ion Mass Spectrometry (SIMS) at UCLA. Secondary oxygen ions were collected after sputtering zircon crystals with a primary

cesium source beam. The instrumental mass fractionation corrected data is presented in Table 3.3.

Whole-Rock Composition

Major Elements

The samples of the PGCC define a high-K calc-alkaline trend typical of the APVC (Figure 3.2). The compositional range in SiO_2 spans 61-76 wt%. The total range is extended by the occurrence of mafic inclusions and a small volume rhyolite center. The ignimbrites however, represent 97% of the magma erupted from the PGCC and fall within 67-70 wt % SiO_2. The rhyolitic Juvina Shield and associated Alota Ignimbrite fall are high-Si rhyolites (74-77 wt% SiO_2). Lava flows and domes along the collapse scarp as well as among the central post-collapse complex encompass a larger, more dacitic, range (64-69 wt% SiO_2). Late Pleistocene domes of the Chascon-Runtu Jarita Complex have the widest range of SiO_2 (63-76 wt% SiO_2) (Watts et al., 1999). Xenoliths recovered from the Chascon dome as well as the resurgent dome of the Pastos Grandes Caldera, fall within the SiO_2 range of the pumice (68-72 wt %), with the exception of one analysis that contains 75 wt% SiO_2.

Variations in whole rock major elements define regular, generally negative correlations with SiO_2 with the exception of K_2O which increases and Na_2O which has no correlation (Figure 3.7). Lavas along the scarp define the most primitive endmember and the Alota ignimbrite defines the most evolved. Caldera-related lavas such as the scarp lavas and the post-collapse domes are lower in SiO_2 and K_2O, and higher in all other major

elements with the exception of Na_2O, which has similar concentrations. In all cases, the plutonic clasts overlap in composition with the pumice from each of the ignimbrites. The subsequent effusive volcanic activity (lavas of Cerro Chuhuilla and Serrania Khenwal as well as the post-climactic dome complex) that followed each caldera-forming eruption represents slightly less evolved magma (67 wt% to 63 wt% SiO_2 for the Chuhuilla cycle and 69 wt% to 66 wt% SiO_2 for the Pastos Grandes cycle). While there is a slight offset between the explosive and effusive stages of each caldera cycle, the variation is only on the order of 3-4 wt% SiO_2. Samples from Cerro Chascon-Runtu Jarita span nearly the entire range of compositions in the complex from 63-76 wt% SiO_2.

Samples of the Alota ignimbrite and Juvina dome define trends that conflict with those of the caldera-related samples. The SiO_2 concentration is higher in the Juvina lavas than in the Alota ignimbrite pumice. This increase in SiO_2 is associated with increases in TiO_2, FeO, MgO, and CaO. The suite overlaps in Al_2O_3, MnO, and P_2O_5 over a wide range compared to that of the caldera-related samples. The Alota pumice and Juvina lavas overlap in K_2O and Na_2O with the caldera-related samples.

Trace Elements

As with the major element oxides, the trace element concentrations of the ignimbrites and lavas of the PGCC cluster in variation diagrams (Figure 3.8). Trace element trends such as those of Figure 3.8 are generally linear, but far more diffuse than in the major elements. With respect to trace element variation, low SiO_2 dacites mirror the more evolved rhyolite samples in that increasing Rb correlates with decreasing Sr, Zr, Eu, and Ba.

As with the major element trends, the PGI and ChI are nearly indistinguishable in terms of trace element concentrations. The two large volume ignimbrites occupy the middle of the compositional range of the PGCC. The xenoliths overlap with the ignimbrite compositions and extend to represent the most evolved of the main population (excluding the Alota samples). The Scarp lavas and post-collapse lavas are enriched in Sr, Zr, Eu, Ba, and depleted in Rb relative to the rest of the PGCC (Figure 3.8).

Similar to the major element trends, the Alota and Juvina samples do not fit the trends defined by the caldera-related samples. The Juvina-Alota samples cluster in two distinct rhyolite endmember populations. The diffuse trend created by these endmembers differs in slope from the caldera-related samples. The Juvina lavas are closer in trace element composition to the caldera-related samples than the Alota pumice. Samples from the Alota ignimbrite pumice are enriched in Rb, and depleted in Sr, Zr, and Ba relative to the other units of the PGCC.

Rare Earth Elements

Chondrite normalized rare earth element (REE) patterns of the PGCC show relative LREE enrichment and HREE depletion typical of magmas with an arc affinity (Figure 3.9a & b). Only the Alota/Juvina samples have pronounced negative Eu anomalies (Figure 3.9a). The Juvina-Alota samples have the flattest overall REE trend with the lowest LREE and highest HREE concentrations. The Chuhuilla and Pastos Grandes samples have nearly identical REE trends. La/Yb_n ratios generally increase from the older to the younger caldera-related samples (13.6 to 16.9) (Figure 3.9c). The Alota

samples have the lowest La/Yb_n ratio (3.2). Dy/Yb_n ratios are nearly identical for the Chuhuilla and Pastos Grandes samples (1.45 and 1.41 respectively) (Figure 3.9d). Alota is still lower (1.2). Eu/Eu^*_n decreases only slightly (0.73 to 0.69) from Chuhuilla to Pastos Grandes (Figure 3.9e). Alota is much lower (0.28).

Isotopes

Though compositionally restricted overall, each cycle of the PGCC has distinct whole rock radiogenic isotope ratios (Figure 3.10a). The earlier, Chuhuilla caldera cycle varies between 0.70845 and 0.70876. The Chuhuilla pumice samples lie in the middle of the range defined by the lavas of Serrania Khenwal and the plutonic clasts. The younger, Pastos Grandes caldera cycle varies between 0.70804 - 0.70824. The post-collapse dome, Sombrero, and the plutonic clasts have higher $^{87}Sr/^{86}Sr$ values than the Pastos Grandes ignimbrite. The $^{143}Nd/^{144}Nd$ ratios are even more restricted overall (0.512223-0.512293). The Chuhuilla cycle is extremely restricted (0.512257-0.512264) while the Pastos Grandes cycle is relatively more variable (0.512223-0.512293), though much of the variability is due to one PGI analysis (Figure 3.10c). Table 3.2 summarizes all of the whole rock chemical data.

Oxygen isotopes

A reconnaissance study of oxygen isotopes in zircons from the Pastos Grandes ignimbrite, Cerro Aguas Clientes, Cerro Pabellon Cachi Laguna, and granodiorite clasts recovered from Cerro Chascon reveal remarkable homogeneity in the system. The $\delta^{18}O$ varies over less than 1‰ (all but two of the 78 analyses fall between 6-7‰) Figure 3.11. These values are both homogenous and elevated.

Discussion

Regional Context of the PGCC Magmas

The ignimbrites of the PGCC reflect many characteristics of the host APVC. The ignimbrites are typical of large-volume "monotonous intermediates" (Hildreth, 1981) being crystal-rich calc-alkaline high-K, dacites. Subordinate volumes of rhyolite and andesite are present in the PGCC, but the majority of samples by volume fall within 67-70 wt% SiO_2 (Figure 3.12). These characteristics are common to many of the large-volume systems of the APVC (e.g. La Pacana, Panizos, Vilama; Lindsay et al., 2001; Ort, 1993; Soler et al., 2007; Folkes et al., 2011) as well as volcanic centers across the Puna (e.g. Cerro Galan, Aguas Calientes, and Cerro Blanco among others, Folkes et al., 2011; Petrinovic et al., 2010; Kay et al., 2006; Kay et al., 2010). The resemblance extends to trace elements, for instance, chondrite normalized REE patterns are close to the other western APVC deposits of de Silva et al. (2006) (La/Yb 15-20). This restricted chemical variability is seen in the PGCC as well as the APVC as a whole suggest a strong family resemblance with a common magmatic source (de Silva et al., 2006).

The volcanic deposits of the PGCC and the APVC as a whole share the subduction-related chemical signatures typical of the volcanic arc. Trace element trends of LILE enrichment and HFSE depletion are common to both the arc and the PGCC deposits (elevated Ba/Nb of 4.7-4.8 and Ba/La of 1.6-2.0). This is similar to the trace element relationship cited by de Silva et al. (2006) and Kay et al. (2010) for the APVC and Puna deposits. PGCC and APVC samples share a high peraluminous signature that is less variable than the CVZ magmas (Al/K+Na+Ca of ~1.4 and range of 1.0-1.5 respectively).

The same limited variability is true of the radiogenic isotope ratios ($^{87}Sr/^{86}Sr$ and $^{143}Nd/^{144}Nd$) when compared to the CVZ (i.e. $^{87}Sr/^{86}Sr$ of ~0.708 for the PGCC and 0.704-0.708 for the arc; Hawkesworth et al., 1982). Details of the magma processing that led to the shallow crustal PGCC magmas are discussed below.

PGCC Magma Genesis

Major element chemical signatures suggest continuous fractionation of the PGCC magmas along a liquid line of descent. The variations in major elements with increasing SiO_2 (decreasing FeO, CaO, TiO_2, MgO, MnO, and increasing K_2O) (Figure 3.7) are consistent with progressive fractionation of the observed phenocryst phases: plagioclase, biotite, and amphibole. The overlapping patterns for both caldera cycles, suggests that the major fractionation processes were taking place for protracted timescales in the magma system.

Trace element patterns support continuous fractionation in the caldera-related dacite magmas. For example, the variation trends of Sr and Rb for all of the caldera-related volcanic deposits share a similar slope (Figure 3.8a). This pattern suggests that fractionation was governed by similar bulk melt-mineral distribution coefficients over the life span of each caldera cycle. The slight, albeit diffuse, depletion in Ba over the span of caldera-related magmas indicates that they were saturated in biotite and, to a lesser extent, K-feldspar. The consistent depletion in Eu and Zr with increasing Rb (index of fractionation) (Figure 3.8b-d) suggests saturation of plagioclase and zircon, respectively in the caldera-related magmas, the latter a condition previously proven for the PGI cycle (Chapter 4 of thesis).

Whole rock chemistry suggests a common origin for the caldera-related dacites of the PGCC. The majority of the eruptive volume in the complex was deposited in the Chuhuilla and Pastos Grandes ignimbrites, which were sourced from nearly indistinguishable rhyodacite magmas suggestive of a compositionally restricted magma chamber. Whole rock major and trace elements along with radiogenic isotope compositions suggest a combination of crystal fractionation and assimilation was needed to form the upper crustal dacites from the parental APMB compositions. To test this hypothesis, Assimilation/Fractional Crystallization (AFC) models were run using "parental" compositions ($^{87}Sr/^{86}Sr$ = .706; Sr = 360ppm; Rb = 115ppm) of the mafic enclaves of the Purico Complex (Schmitt et al., 2001) representing the upper crustal APMB source. A crustal contaminant was chosen that best fit the PGCC data ($^{87}Sr/^{86}Sr$ = .713; Sr = 300ppm; Rb = 85ppm) and that matches compositions previously reported for basement compositions in the region (Lucassen et al., 2001; Kay et al., 2010). The ratio of assimilation to fractionation was held constant at r = 0.8. This modeling shows that the suite of dacite to rhyodacite PGCC magmas can be explained by AFC processes (5-10% AFC) (Figure 12a). These processes support the long history of investigations constraining the amount of assimilation and fractionation in Central Andean magmas (Francis et al., 1989; Hawkesworth et al., 1982; Hildreth et al., 2004; Kay et al., 2010; Grocke et al., submitted). Similar chemical restrictions have been noted throughout the APVC and CVZ (Schmitt et al., 2001; Lindsay et al., 2001; Soler et al., 2007; Kay et al., 2010; Folkes et al., 2011). As a result of this regional homogeneity, the APMB (discussed in Chapter 1) was suggested as a chemical "buffer" zone in the mid crust

which stored and homogenized magmas prior to their ascent to the upper crust (Lindsay et al., 2001; Schmitt et al., 2001; de Silva et al., 2006).

Though not specifically placed in the petrogenetic model here, it should be noted that the Chascon Runtu Jarita (CRJ) samples also lie along the chemical trends established by the PGCC magmas. The CRJ suite is interpreted to share the same liquid line of decent and thus a similar evolutionary history as the caldera-related dacite magmas. As the CRJ is much younger (~85 ka) and much smaller (~5 km^3) than the PGCC eruptions, these magmas likely represent the late-stage pulses of a waning regional system.

The Petrogenetic Relationship between the Large Volume Dacites and the Rhyolites

The negative slopes associated with Sr, and Ba versus Rb change from the dacites to the rhyolites (Figure 3.8), suggesting that the fractionation process was governed by different distribution coefficients and differing amounts of assimilation/mixing relative to fractionation. In addition, incompatible trace elements such as Th and U, which we would expect to be enriched in the rhyolites relative to the dacites, are depleted (Th/U ~2 in dacites compared to ~1.5 in Juvina and 0.5-0.7 in Alota). Furthermore, the flattening of the REE pattern from the dacite to the rhyolite (e.g. La/Yb ~ 12 in Chuhuilla and ~3 in Juvina/Alota) (Figure 3.9c) is inconsistent with both rhyolites being a direct continuation of the dacite trend through pure crystal fractionation.

Trace element trends suggest that similar AFC process that produced the dacites could account for the Alota compositions as they lie along the same trend; however the Juvina rhyolites define a population offset from this primary trend. The genesis of the rhyolite magma is modeled here in a two stage method due to the differing compositions of the

Juvina and Alota rhyolites relative to the dacites. First, as the Juvina lavas are close in composition to the dacite magmas, Rayleigh fractionation is used with the Chuhuilla ignimbrite composition as the parent (Rb = 200ppm; Sr = 322ppm). It is shown in Figure 3.13b that 60-70% fractionation is required to create the Juvina lavas from the source magma of the Chuhuilla. Fractionation from the dacite parent cannot account for the extremely high Rb concentrations (e.g. Rb 360-380 ppm) in the Alota pumice. It is shown here that fractionation from the Juvina rhyolite parent would produce the Alota compositions (an additional 40% fractionation) (Figure 3.13c).

Evidence for Shallow Crustal Magma Processes at the PGCC

Though thermobarometry is lacking for the magmas of the PGCC, the phase assemblage and whole rock chemistry suggest that upper crustal processes dominated the chemical evolution of the magma system. While the PGCC shows restricted textural and compositional variability over its 5.5 Myr lifespan, subtle heterogeneities are observed that suggest changing crustal upper crustal conditions within each caldera cycle and from one cycle to the next. These heterogeneities are recorded in changing REE abundances and radiogenic isotope compositions with time and suggest evolving shallow crustal conditions that correlate with the evolution of the APVC ignimbrite flare-up. On a shorter timescale, whole rock major and trace elements show that the large-volume ignimbrites along with the plutonic clasts represent the most evolved samples of each cycle while the post-caldera volcanism represents slightly less evolved magma. Mineral textures in the pumice show mineral-melt equilibrium leading up to the ignimbrite-forming eruptions. Disequilibrium textures and microlites in post-climactic units (Figure 3.3 & 3.4) suggest rapid decompression either during eruption or as a result of magma

movement following of caldera collapse. These textures coincide with minor compositional variations that show chemical and physical evolution of the magma system leading up to, and immediately following the large caldera-forming eruptions.

Chondrite normalized REE abundance patterns are moderately steep for all caldera related magmas and vary over a large range (La/Yb = 11-23) (Figure 3.9c). La/Yb ratios increase from the Chuhuilla to the Pastos Grandes caldera cycle and correlate with only a minute increase in the negative Eu anomaly (Eu* ~0.73 in Chuhuilla and 0.68 in Pastos Grandes). There is a consistent HREE concentration, but a lack of a strong depletion signature which is consistent with magma sources in the shallow crust above garnet stability. Increasing LREE concentrations and Eu anomalies also point to the magmas having similar sources in the shallow crust with increasing amounts of plagioclase fractionation in the shallow crust, where plagioclase is stable over time. It is possible that limited evolution was enough to produce subtle chemical zoning in the magma chamber leading to the more evolved ignimbrite eruptions preceding slightly more primitive, post-caldera lava flows and domes. However, given the relative volumes of each of the eruptions, it is likely that the subtle compositional variations seen in from each ignimbrite to the small-volume, post-climactic eruptions are simply characteristics of the large volume eruptions mixing huge portions of the magma system at a given time.

The radiogenic isotope ratios in the caldera-related magmas are indicative of crustal assimilation. Models for the peak and waning stages of the ignimbrite flare-up (de Silva et al., 2006; de Silva and Gosnold, 2007), suggest that higher amounts of crustal

assimilation occur during the peak of magmatic activity. The Chuhuilla cycle records slightly higher $^{87}Sr/^{86}Sr$ ratios (0.70845-0.70875) (Figure 3.10b) suggesting higher amounts of crustal input (i.e. the range of basement compositions described by Lucassen et al., 2001) coinciding with the peak of the APVC flare-up and maximum geothermal gradient (de Silva et al., 2006). In each caldera cycle, the post-caldera volcanic deposits are more radiogenic than the ignimbrite ($^{87}Sr/^{86}Sr$ of 0.7087 compared to 0.7085 in the Chuhuilla cycle and 0.7082 compared to 0.7081 in the Pastos Grandes cycle). The increase in $^{87}Sr/^{86}Sr$ radiogenic isotopic composition within each caldera cycle needs to be supported by more data in order to distinguish between roof/side wall assimilation of the surrounding country rock following caldera collapse, or simply eruptive mixing of the large volume system homogenizing the magma over the small volume eruptions. The subtle yet significant decrease in $^{87}Sr/^{86}Sr$ from the initial Chuhuilla cycle to the younger Pastos Grandes cycle suggests that upper crustal assimilation was more prevalent during the early stages of magma accumulation that coincides with the peak of the APVC flare-up and higher geothermal gradients (de Silva et al., 2006).

A reconnaissance study of $\delta^{18}O$ in zircon reveals homogenous and elevated signatures over the course of the Pastos Grandes volcanic progression. The $\delta^{18}O$ values of +6-7‰ are elevated relative to the typical mantle values of +5.5‰ (Valley, 2003). Bindeman et al. (2001) illustrate zircon-quartz $\delta^{18}O$ fractionation of 2.19 ± 0.07 ‰. This fractionation value would correspond to $\delta^{18}O$ in quartz values of ~8-9 ‰. $\delta^{18}O$ in quartz studies of other large systems in the region propose similar values (Folkes, 2010). The results here,

combined with evidence from other large systems of the CVZ suggest magmas contain a large crustal component in their genesis from mantle-derived melts.

The presence of granodiorite and granitic plutonic clasts combined with the chemical signals of the volcanic deposits provide views into the upper crustal batholith that grew during the lifespan of the PGCC. Granodiorite clasts largely overlap in composition with each associated ignimbrite-forming eruption. This implies that much of the batholith must be granodiorite in composition. Small rhyolite eruptions (Alota and Juvina) suggest that small portions of the remnant batholith are of granitic composition. The long-lived nature of the volcanic complex and the upper crustal geochemical signatures discussed above suggest that the batholith grew episodically by repeated injections from a mid- to upper-crustal processing center. The ignimbrite compositions overlap with other centers of the APVC (Ort et al., 1996; Lindsay et al., 2001; Schmitt et al., 2001; Soler et al., 2007) and add to the model of a regional composite batholith that grew by the accumulation of successively larger magma injections into the shallow crust (de Silva and Gosnold, 2007). This compositional restriction, seen at multiple spatial scales, speaks to the importance of the APMB as a magma processing center during the construction of the APVC ignimbrite flare-up.

Concluding Remarks

The Pastos Grandes Caldera Complex produced high-K dacites with restricted chemical variability typical of the APVC. The PGCC and host APVC each reflect crustal signatures in their source magmas. Upper crustal geochemical signatures and restricted compositional variability point to a magma processing zone in the upper crust. This

processing center periodically gave rise to shallow magma systems that fed the voluminous eruptions on the surface. As is the case for many of the ignimbrites of the APVC, the APMB generated the fundamental chemical signatures of the PGCC before minor chemical variations were applied to the accumulated magma in the sub-caldera magma chambers.

The PGCC spans the peak and waning stages of magmatic and volcanic activity in the APVC. The PGCC records subtle isotopic tracers that coincide with the stages of the regional flare-up and suggest higher amounts of crustal assimilation during the height of activity in the region. The waning stage also manifests itself as chemical heterogeneity in the Late Pleistocene, Cerro Chascon dome. Overall, the large-volume volcanic activity at the PGCC reflects the episodic construction of a largely homogenous composite batholith in the shallow crust. This batholith is a small part of the regional magmatic system that built the composite batholith under the APVC.

References

Allmendinger, R. W., Jordan, T. E., Kay, S. M., & Isacks, B. L. (1997). The evolution of the Altiplano-Puna plateau of the central Andes. *Annual Review of Earth and Planetary Sciences*, *25*(1), 139-174.

Bachmann, O., Dungan, M. A., & Lipman, P. W. (2002). The Fish Canyon magma body, San Juan volcanic field, Colorado: rejuvenation and eruption of an upper-crustal batholith. *Journal of Petrology*, *43*(8), 1469-1503.

Baker, M. C. W. (1981). The nature and distribution of Upper Cenozoic ignimbrite centres in the Central Andes. *Journal of Volcanology and Geothermal Research*, *11*(2), 293-315.

Bindeman, I. N., & Valley, J. W. (2001). Low-δ18O rhyolites from Yellowstone: Magmatic evolution based on analyses of zircons and individual phenocrysts. *Journal of Petrology*, *42*(8), 1491-1517.

Chesner, C. A. (1998). Petrogenesis of the Toba Tuffs, Sumatra, Indonesia.*Journal of Petrology*, *39*(3), 397-438.

Chmielowski, J., Zandt, G., & Haberland, C. (1999). The Central Andean Altiplano-Puna magma body. *Geophysical Research Letters*, *26*(6), 783-786.

Coira, B., Kay, S. M., & Viramonte, J. (1993). Upper Cenozoic magmatic evolution of the Argentine Puna—a model for changing subduction geometry.*International Geology Review*, *35*(8), 677- 720.

de Silva, S. L. (1989). Altiplano-Puna volcanic complex of the central Andes. *Geology*, *17*(12), 1102-1106.

de Silva, S., Zandt, G., Trumbull, R., Viramonte, J. G., Salas, G., & Jiménez, N. (2006). Large ignimbrite eruptions and volcano-tectonic depressions in the Central Andes: a thermomechanical perspective. *Geological Society, London, Special Publications*, *269*(1), 47-63.

de Silva, S. L., & Gosnold, W. D. (2007). Episodic construction of batholiths: Insights from the spatiotemporal development of an ignimbrite flare-up. *Journal of Volcanology and Geothermal Research*, *167*(1), 320-335.

Folkes, C. B., de Silva, S. L., Wright, H. M., & Cas, R. A. (2011). Geochemical homogeneity of a long-lived, large silicic system; evidence from the Cerro Galán caldera, NW Argentina. *Bulletin of volcanology*, *73*(10), 1455-1486.

Grocke, S. B; de Silva, S. L; Lindsay, J. M., Iriarte, R., Cottrell, E; Andrews, B. J., Magma Evolution and Dynamics of the 3.49 Ma Tara Supereruption, Guacha Caldera, SW Bolivia. Manuscript Submitted for Publication.

Hildreth, W. (1981). Gradients in silicic magma chambers: implications for lithospheric magmatism. *Journal of Geophysical Research: Solid Earth (1978–012)*, *86*(B11), 10153-10192.

Hildreth, W., & Moorbath, S. (1988). Crustal contributions to arc magmatism in the Andes of central Chile. *Contributions to Mineralogy and Petrology*, *98*(4), 455 -489.

Hildreth, W. E. S., Halliday, A. N., & Christiansen, R. L. (1991). Isotopic and chemical evidence concerning the genesis and contamination of basaltic and rhyolitic magma beneath the Yellowstone Plateau volcanic field. *Journal of Petrology*, *32*(1), 63-138.

Huppert, H. E., & Sparks, R. S. J. (1988). The generation of granitic magmas by intrusion of basalt into continental crust. *Journal of Petrology*,*29*(3), 599-624.

Jellinek, A. M., & DePaolo, D. J. (2003). A model for the origin of large silicic magma chambers: precursors of caldera-forming eruptions. *Bulletin of Volcanology*, *65*(5), 363-381.

Johnson, D. M., Hooper, P. R., & Conrey, R. M. (1999). XRF analysis of rocks and minerals for major and trace elements on a single low dilution Li-tetraborate fused bead. *Advances in X-ray Analysis*, *41*, 843-867.

Kay, R. W., & Mahlburg Kay, S. (1993). Delamination and delamination magmatism. *Tectonophysics, 219* (1), 177-189.

Kay, S. M., Coira, B., & Viramonte, J. (1994). Young mafic back arc volcanic rocks as indicators of continental lithospheric delamination beneath the Argentine Puna plateau, central Andes. *Journal of Geophysical Research: Solid Earth (1978–2012)*, *99*(B12), 24323-24339.

Kay, S. M., Coira, B. L., Caffe, P. J., & Chen, C. H. (2010). Regional chemical diversity, crustal and mantle sources and evolution of central Andean Puna plateau ignimbrites. *Journal of Volcanology and Geothermal Research*, *198*(1), 81-111.

Lindsay, J. M., Schmitt, A. K., Trumbull, R. B., De Silva, S. L., Siebel, W., & Emmermann, R. (2001). Magmatic evolution of the La Pacana caldera system, Central Andes, Chile: compositional variation of two cogenetic, large-volume felsic ignimbrites. *Journal of Petrology*, *42*(3), 459-486.

Lucassen, F., Becchio, R., Harmon, R., Kasemann, S., Franz, G., Trumbull, R., & Dulski, P. (2001). Composition and density model of the continental crust at an active continental margin—the Central Andes between 21 and 27 *Tectonophysics*, *341*(1), 195-223.

Mason, B. G., Pyle, D. M., & Oppenheimer, C. (2004). The size and frequency of the largest explosive eruptions on Earth. *Bulletin of Volcanology*, *66*(8), 735-748.

Muir, D. D., Blundy, J. D., Rust, A. C., & Hickey, J. (2014). Experimental constraints on dacite pre-eruptive magma storage conditions beneath Uturuncu volcano. *Journal of Petrology*, *55*(4), 749-767.

Ort, M. H. (1993). Eruptive processes and caldera formation in a nested downsag collapse caldera: Cerro Panizos, central Andes Mountains. *Journal of Volcanology and Geothermal Research*, *56*(3), 221-252.

Ort, M. H., Coira, B. L., & Mazzoni, M. M. (1996). Generation of a crust-mantle magma mixture: magma sources and contamination at Cerro Panizos, central Andes. *Contributions to Mineralogy and Petrology*, *123*(3), 308-322.

Ort, M. H., Silva, S. L., Jiménez, C., Jicha, B. R., & Singer, B. S. (2013). Correlation of ignimbrites using characteristic remanent magnetization and anisotropy of magnetic susceptibility, Central Andes, Bolivia. *Geochemistry, Geophysics, Geosystems*, *14*(1), 141-157.

Salisbury, M. J., Jicha, B. R., de Silva, S. L., Singer, B. S., Jiménez, N. C., & Ort, M. H. (2011). $^{40}Ar/^{39}Ar$ chronostratigraphy of Altiplano-Puna volcanic complex ignimbrites reveals the development of a major magmatic province. *Geological Society of America Bulletin*, *123*(5-6), 821-840.

Schmitt, A., De Silva, S., Trumbull, R., & Emmermann, R. (2001). Magma evolution in the Purico ignimbrite complex, northern Chile: evidence for zoning of a dacitic magma by injection of rhyolitic melts following mafic recharge.*Contributions to Mineralogy and Petrology*, *140*(6), 680-700.

Soler, M. M., Caffe, P. J., Coira, B. L., Onoe, A. T., & Kay, S. M. (2007). Geology of the Vilama caldera: a new interpretation of a large-scale explosive event in the Central Andean plateau during the Upper Miocene. *Journal of volcanology and geothermal research*, *164*(1), 27-53.

Tierney, C.R., (2011) Timescales of large silicic magma systems: implications from accessory minerals in Pleistocene lavas of the Altiplano-Puna Volcanic Complex, central Andes (Master's Thesis) Oregon State University, Corvallis OR.

Valley, J. W. (2003). Oxygen isotopes in zircon. *Reviews in mineralogy and geochemistry*, *53*(1), 343-385.

Watts, R. B., de Silva, S. L., de Rios, G. J., & Croudace, I. (1999). Effusive eruption of viscous silicic magma triggered and driven by recharge: a case study of the Cerro Chascon-Runtu Jarita Dome Complex in Southwest Bolivia.*Bulletin of volcanology*, *61*(4), 241-264.

Zandt, G., Leidig, M., Chmielowski, J., Baumont, D., & Yuan, X. (2003). Seismic detection and characterization of the Altiplano-Puna magma body, central Andes. *Pure and Applied Geophysics, 160*(3-4), 789-807.

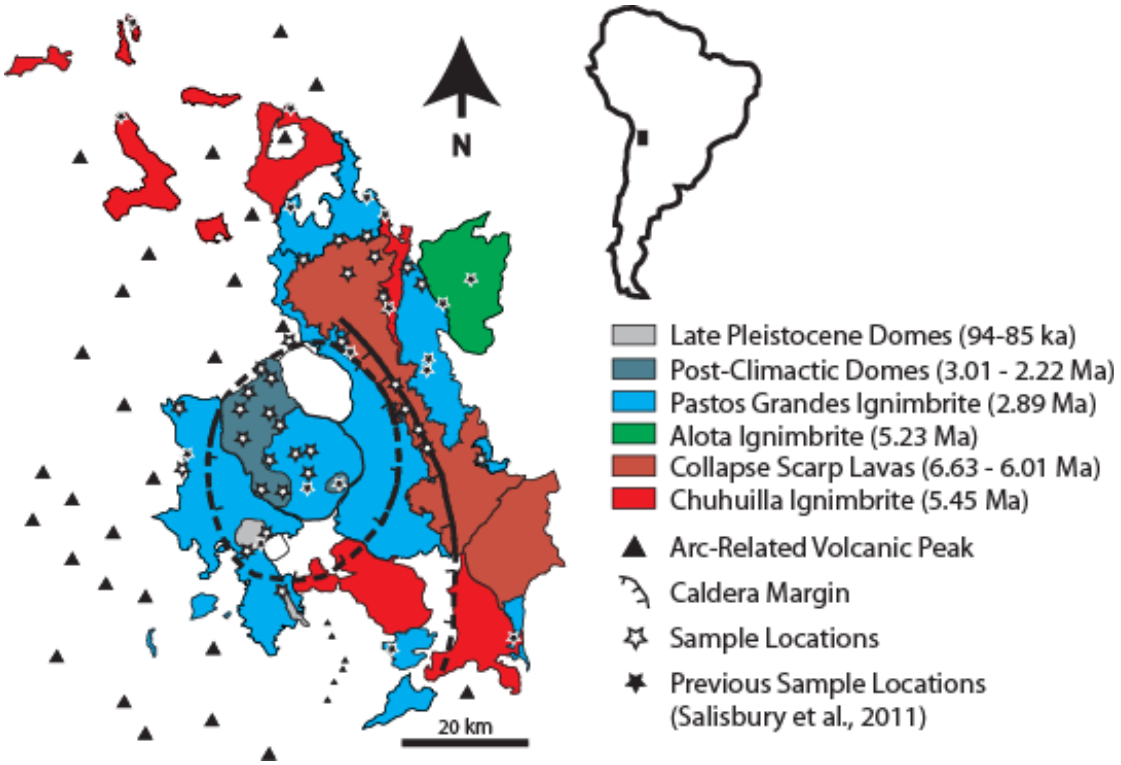

Figure 3.1. Geologic map of the Pastos Grandes Caldera Complex. The distribution of the deposits are largely obscured by Arc-related volcanic activity to the West and bounded by Paleozoic sediments and metasediment ranges to the East. Sample locations from this and previous studies are shown.

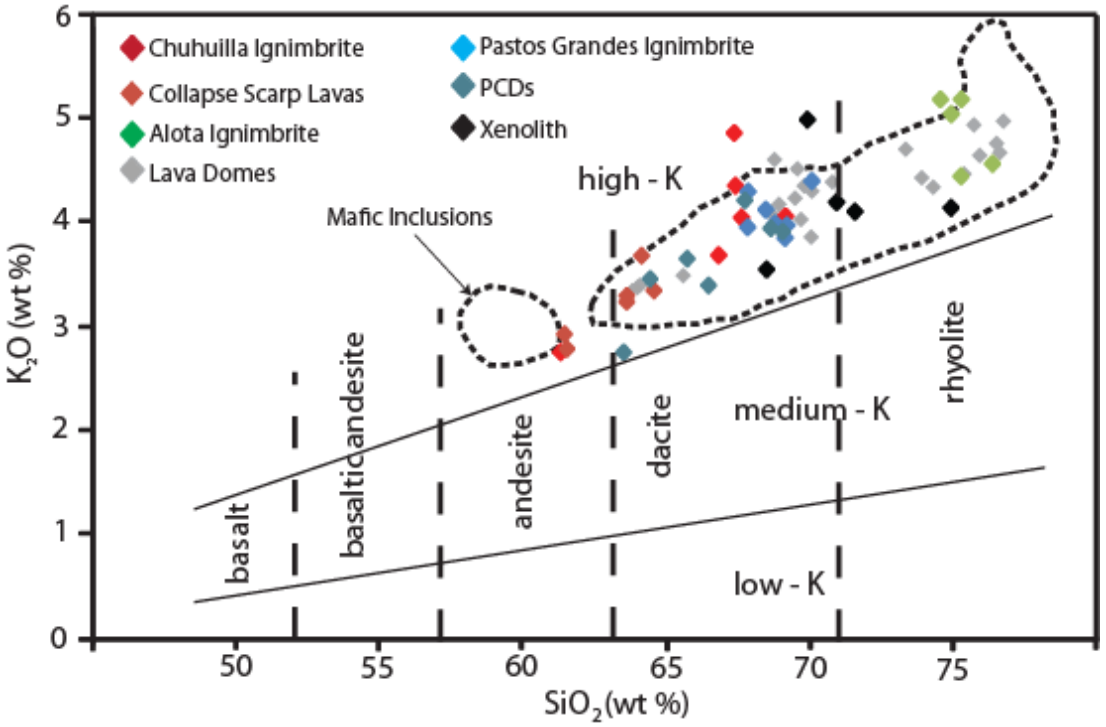

Figure 3.2. The whole rock K_2O vs SiO_2 classification diagram for the PGCC shows a progression of high-K dacites and rhyolites. The large-volume ignimbrites are each compositionally restricted while the post-climactic lavas show more diversity. The Late-Pleistocene, Chascon dome contains samples with the most compositional diversity.

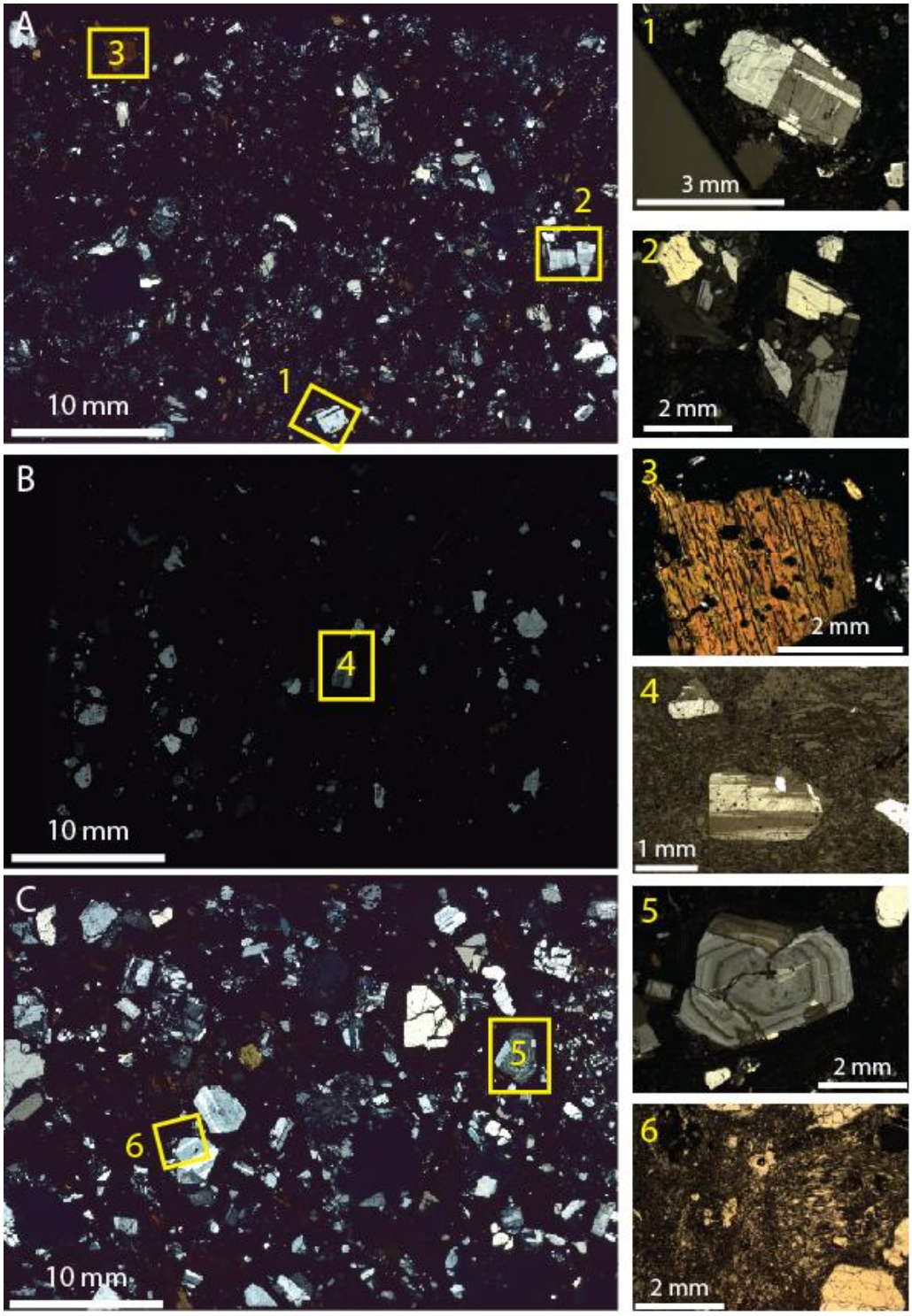

Figure 3.3. Scans of thin sections of pumice from each ignimbrite show relative crystallinities (greatest in the large volume ignimbrites). The photomicrographs show phenocrysts that are in equilibrium with the host melt. (1, 2, 4, & 5 show euhedral plagioclase; 3 shows euhedral biotite filled with inclusions; 6 shows the groundmass texture typical of the pumice).

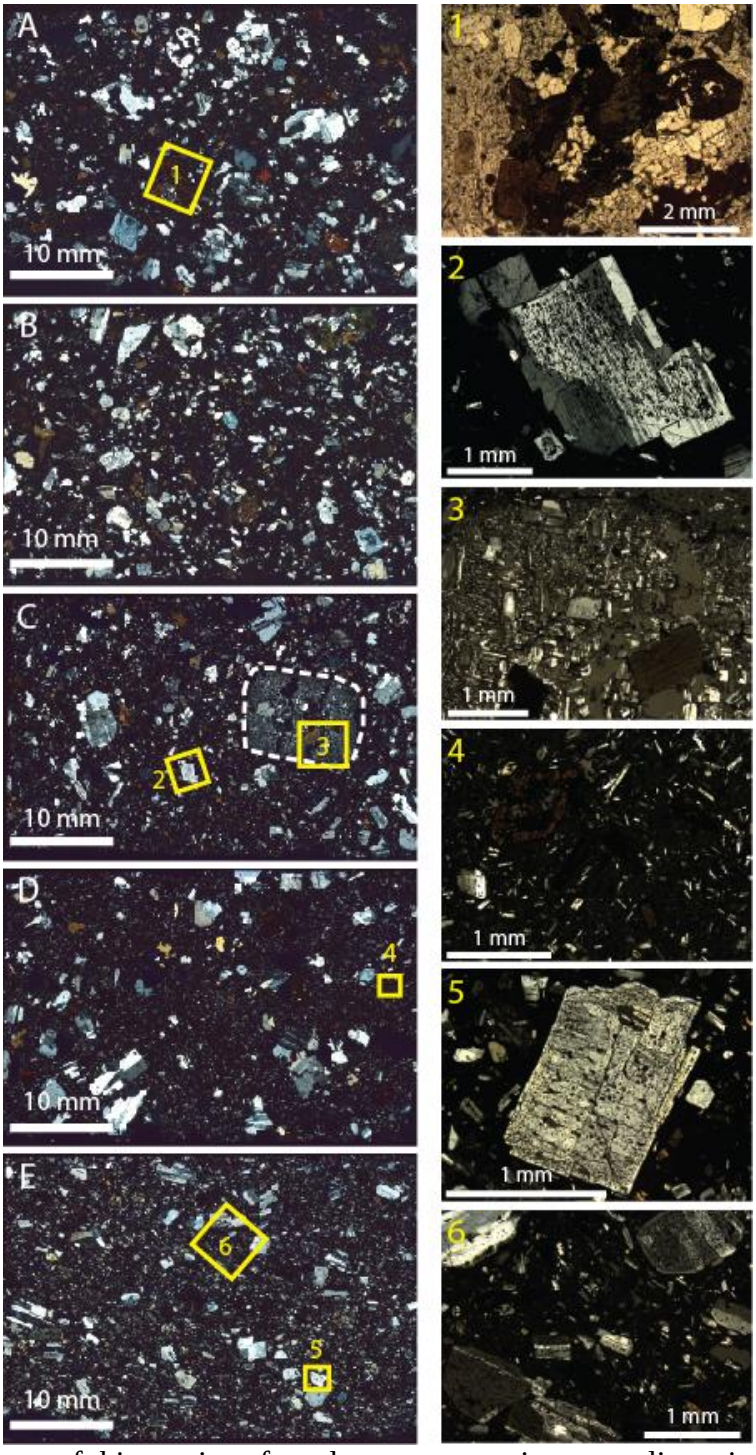

Figure 3.4. Scans of thin sections from lavas representing post-climactic activity following each ignimbrite eruption show an increase in crystallinity from the ignimbrites. Disequilibrium textures are common among the phenocryst phases (shown in the photomicrographs). Microphenocrysts are also common to the post-climactic lavas. Sanidine oikocrysts are present in Cerro Arenal. These oikocrysts contain inclusions of other phases such as biotite and plagioclase (photo 3).

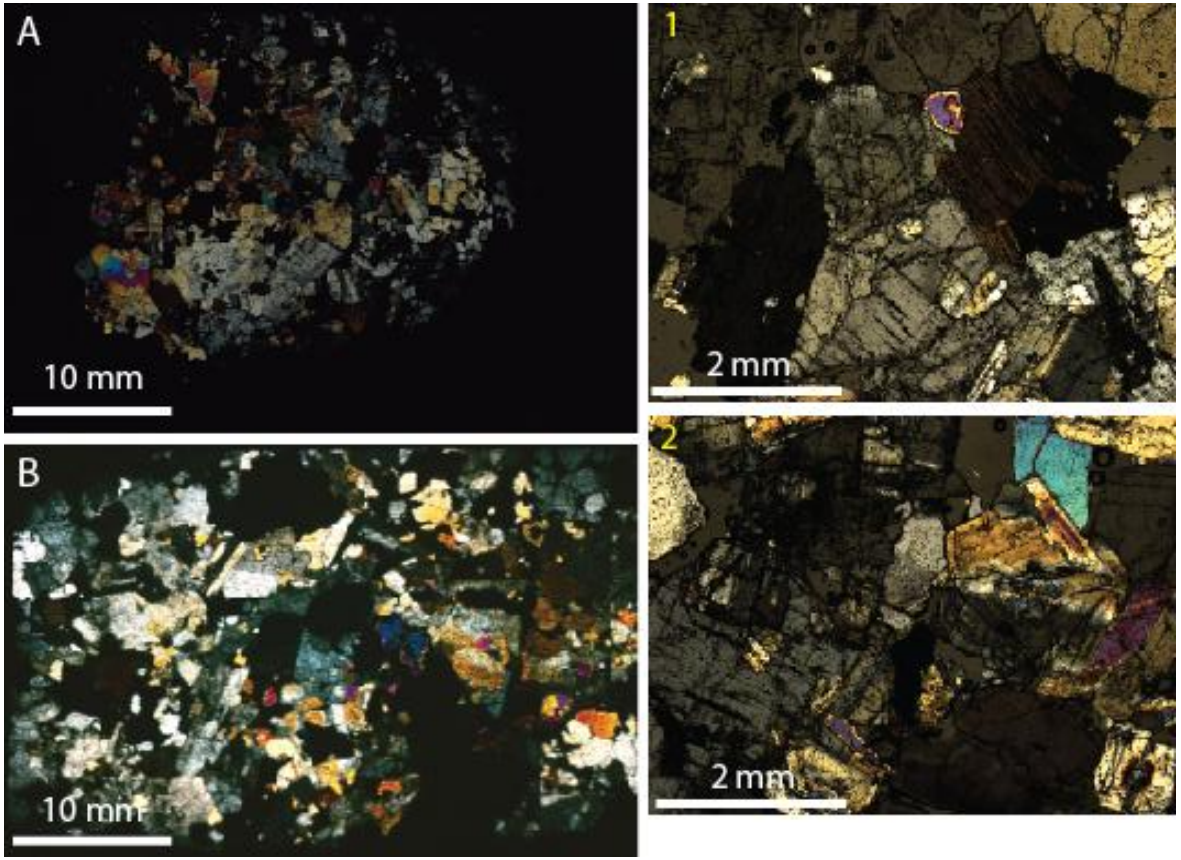

Figure 3.5. Scans of thin sections from the plutonic clasts show holocrystalline counterparts to the volcanic succession. The thin sections are thicker than normal so interference colors are skewed. The scans and photomicrographs show phaneritic textures of mineralogy identical to that of the ignimbrite pumice and lavas.

Figure 3.6. Examples from the PGI pumice, Cerro Aguas Calientes, and clasts found in lavas of Cerro Chascon show increasing textural maturity with time.

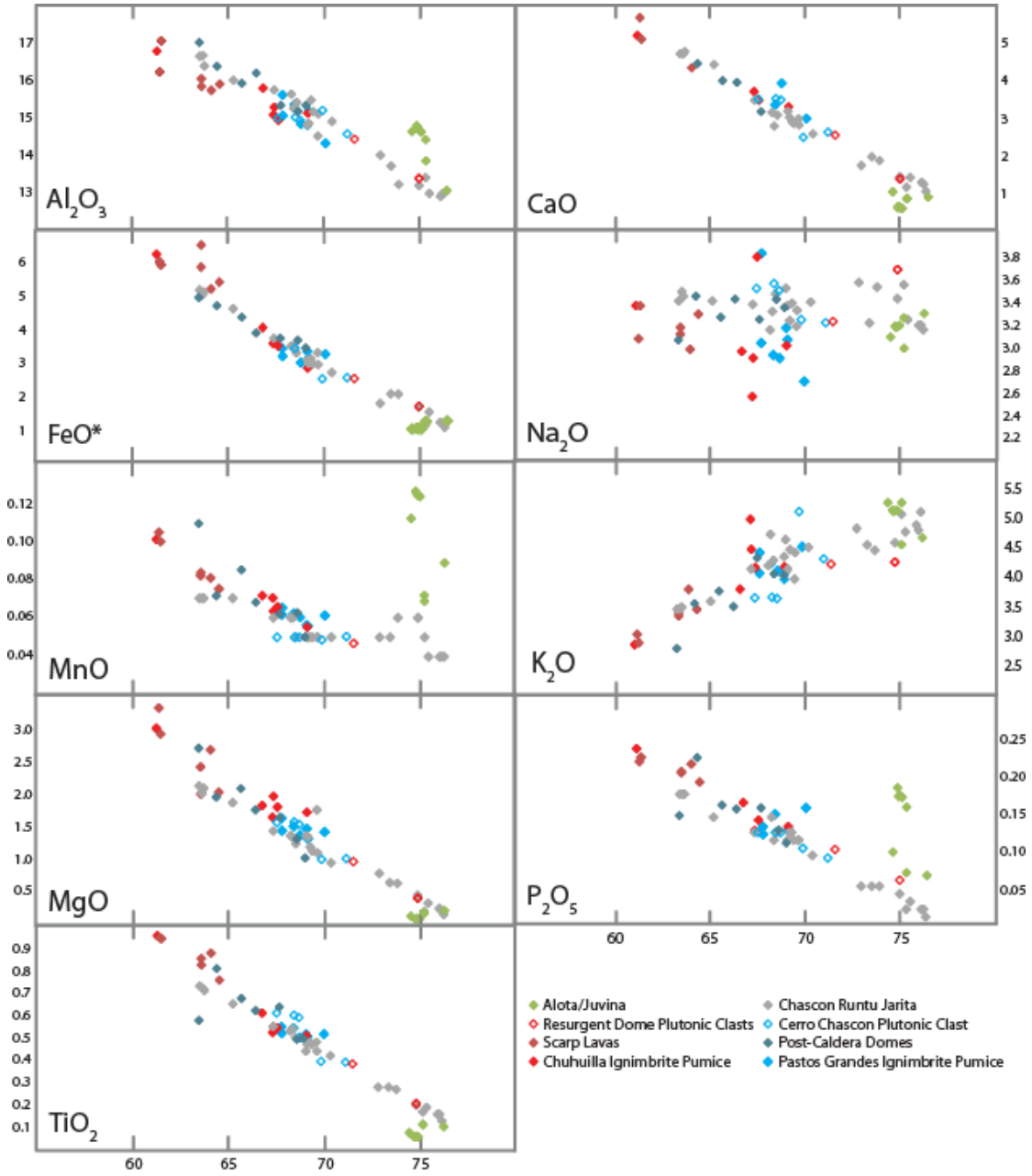

Figure 3.7. Harker variation diagrams show decreasing trends with increasing SiO_2 for all major elements with the exception of K_2O which shows an increasing trend, and Na_2O which has no correlation with SiO_2. The Alota Ignimbrite has a larger variation in Al_2O_3, MnO, and P_2O_5 than any other unit in the complex.

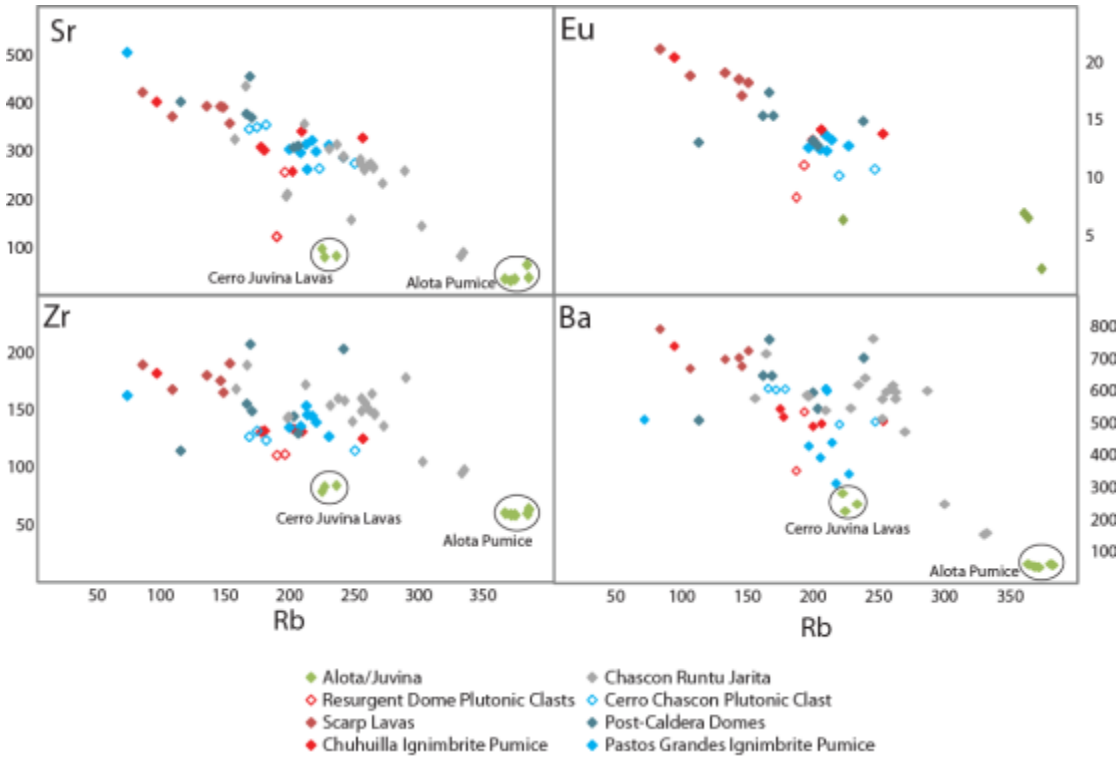

Figure 3.8. The trace element variations within each sample and among the complex as a whole, define diffuse but consistent collinear trends. Lavas of along the scarp and of the PCDs are enriched in Sr, Zr, Eu, Ce, Ba, and U and depleted in Rb relative to the ignimbrites of the PGCC. The samples of the Juvina-Alota suite define a separate trend with the Alota pumice offset to much higher Rb values.

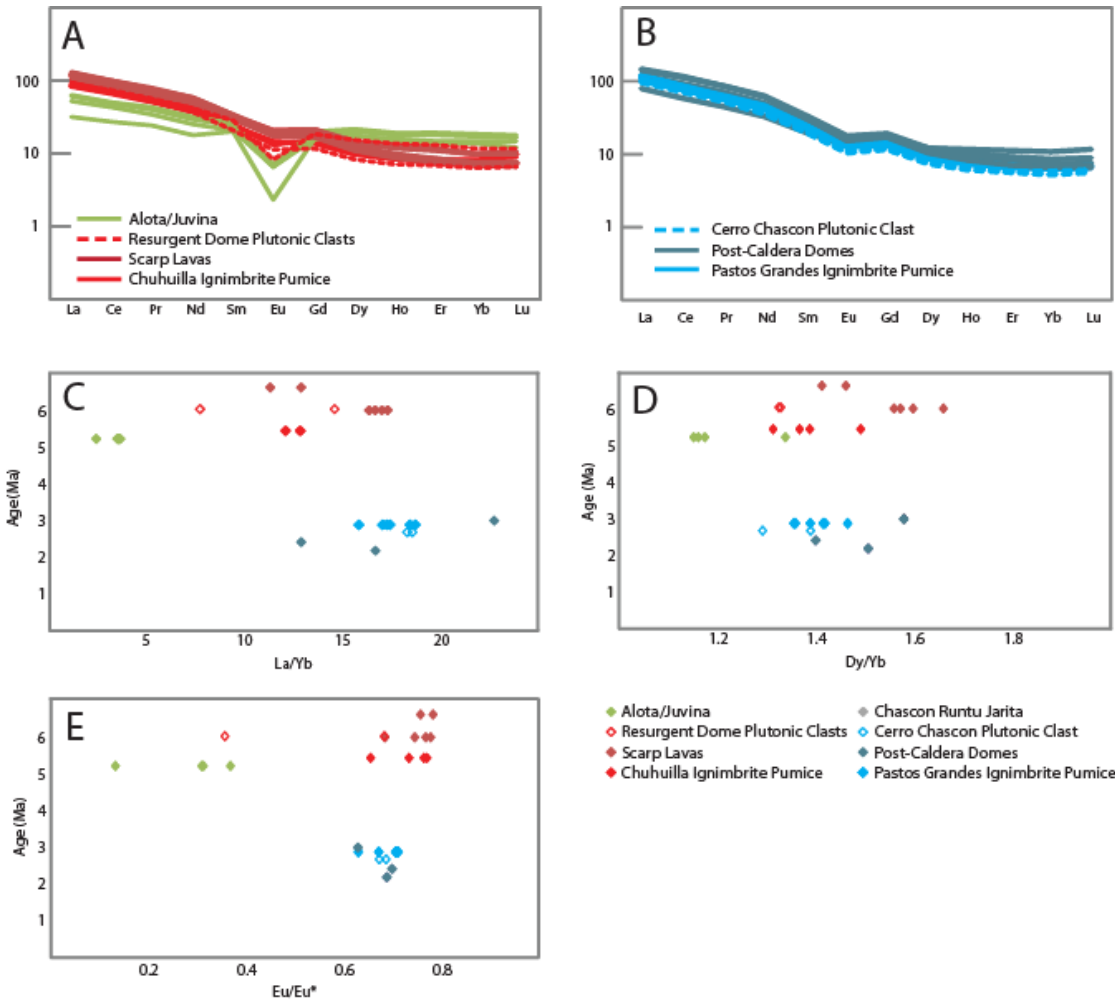

Figure 3.9. Rare Earth Element concentration diagrams. Chrondrite normalized rare earth element patterns of the Chuhuilla and Pastos Grandes cycles (A & B respectively) show relative LREE enrichment and HREE depletion typical of magmas with an arc affinity. La/Yb (C) increases over the lifespan of the complex while Dy/Yb and Eu/Eu* are relatively constant (D & E).

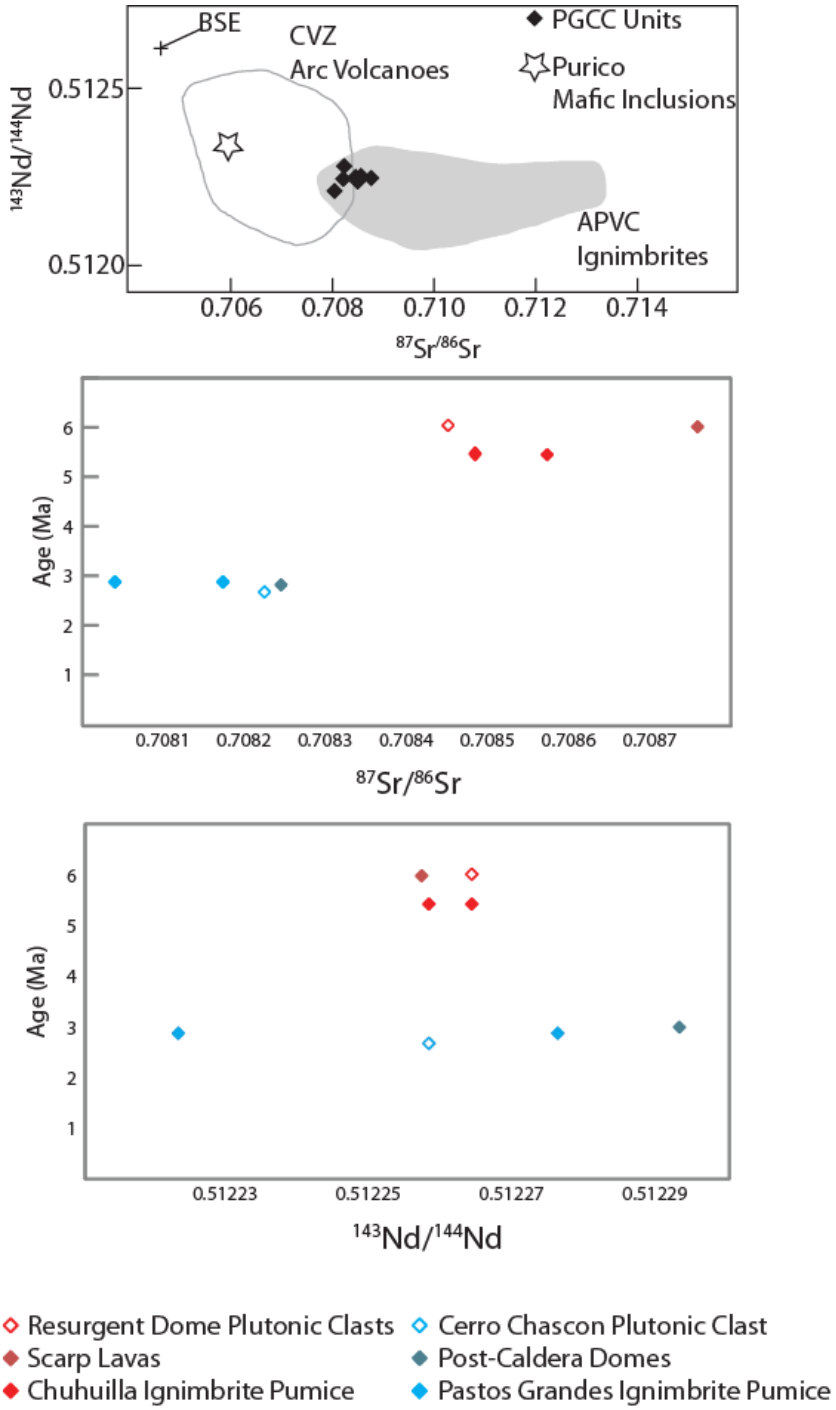

Figure 3.10. Whole rock isotopic variations A) Sr and Nd isotopic ratios fall within the range defined by the APVC. It is generally accepted that these are best reconciled with a model where at least 30-40% mantle-derived magma is mixed-in with crustal melts (e.g. de Silva, 1989; Coira et al., 1993; Ort et al., 1996; Lindsay et al., 2001; Schmitt et al., 2001; de Silva et al., 2006). B) A distinction between the $^{87}Sr/^{86}Sr$ of the Chuhuilla cycle and Pastos Grandes cycle shows a decrease in radiogenic compositions over time.

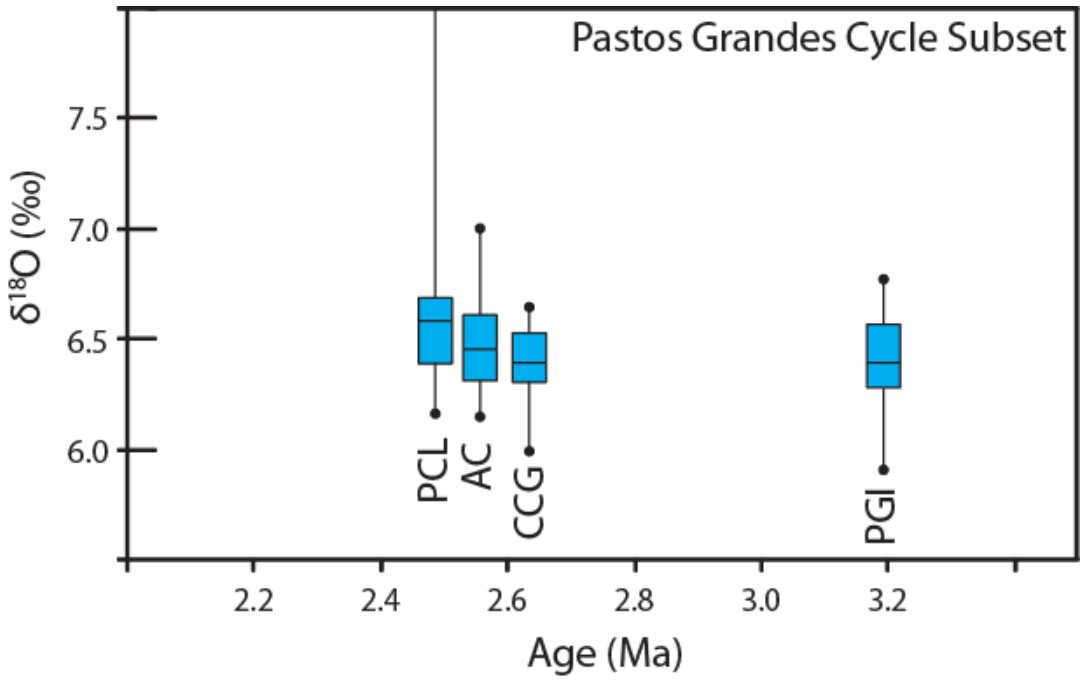

Figure 3.11. The summary of the reconnaissance study of oxygen isotopes in the Pastos Grandes Ignimbrite (PGI), Cerro Aguas Calientes (AC), Cerro Pabellon Cachi Laguna (PCL) and the granodiorite recovered from Cerro Chascon (CCG). The variation in $\delta^{18}O$ shown as a box and whisker plot. The boxes represent the first and third quartile in the data for each sample. The line in the box is the mean. The endpoints on the lines are the minimum and maximum values in each sample population. Note that the maximum for the granodiorite of Cerro Chascon (CCG) is off the scale of the diagram (9.73 ‰)

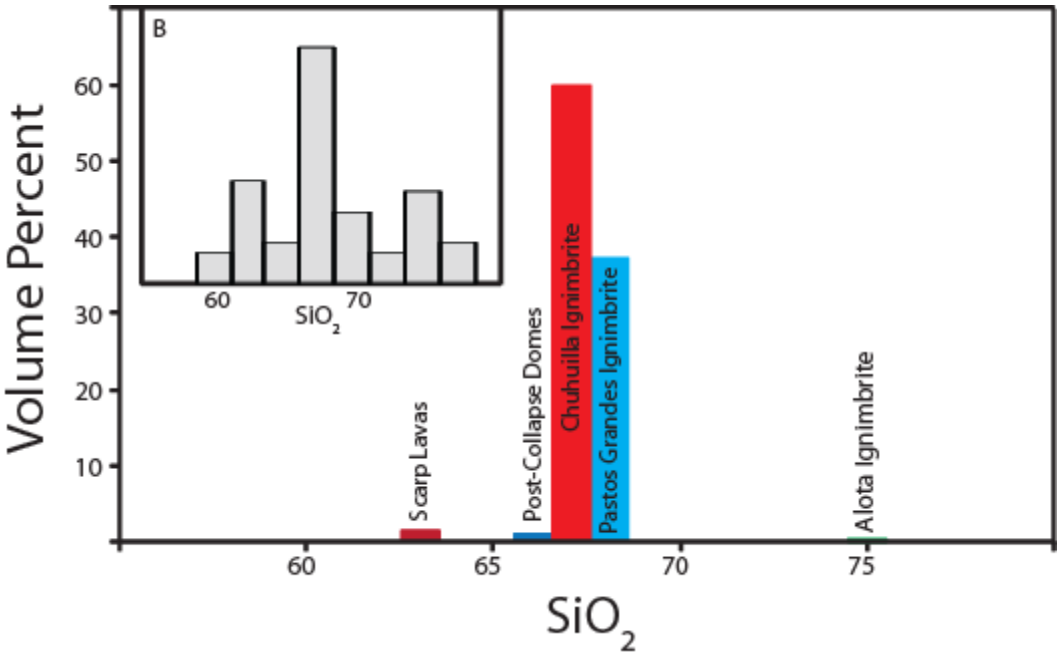

Figure 3.12. The limited compositional variation is shown in two histograms. The first shows the average composition of each major volcanic unit of the PGCC. Each unit is shown as an erupted volume percent of the total volcanic succession. As is shown, the two ignimbrites make up the vast majority of the volume erupted and account for a limited compositional range. Much of the chemical variability in the PGCC comes from the smaller volume deposits. The inset shows a histogram of every whole rock analysis done in the PGCC. In this diagram, the variability is more apparent, yet a distinct peak is at ~68 wt% SiO_2.

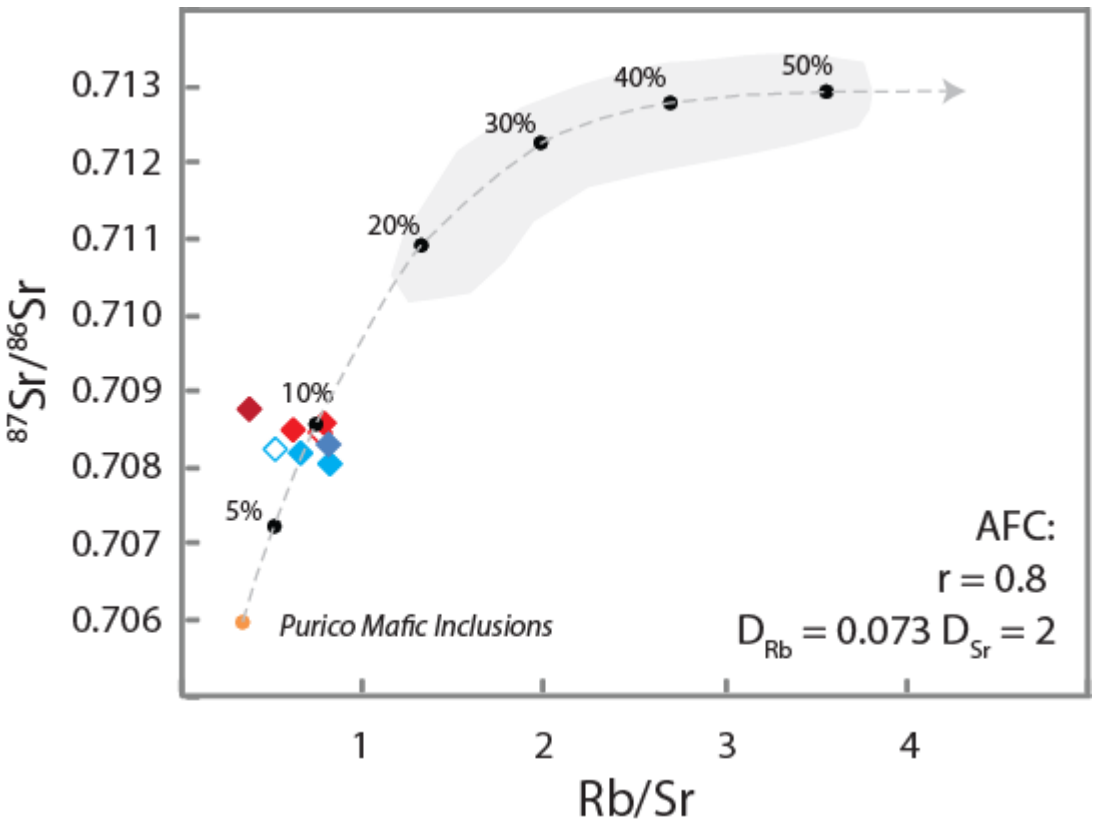

Figure 3.13. AFC, and Rayleigh Models are used to explain the occurrence and chemical relationship of the PGCC volcanics. A) Sr isotopic data and Rb and Sr trace elements for the PGCC magmas. A Simple assimilation-fractional crystallization model shows the derivation of the large-volume dacite magmas from the original, mantle derived parent (Purico mafic inclusions) (Schmitt et al.2001). The assimilant composition is within range of Lucassen et al. (2001).

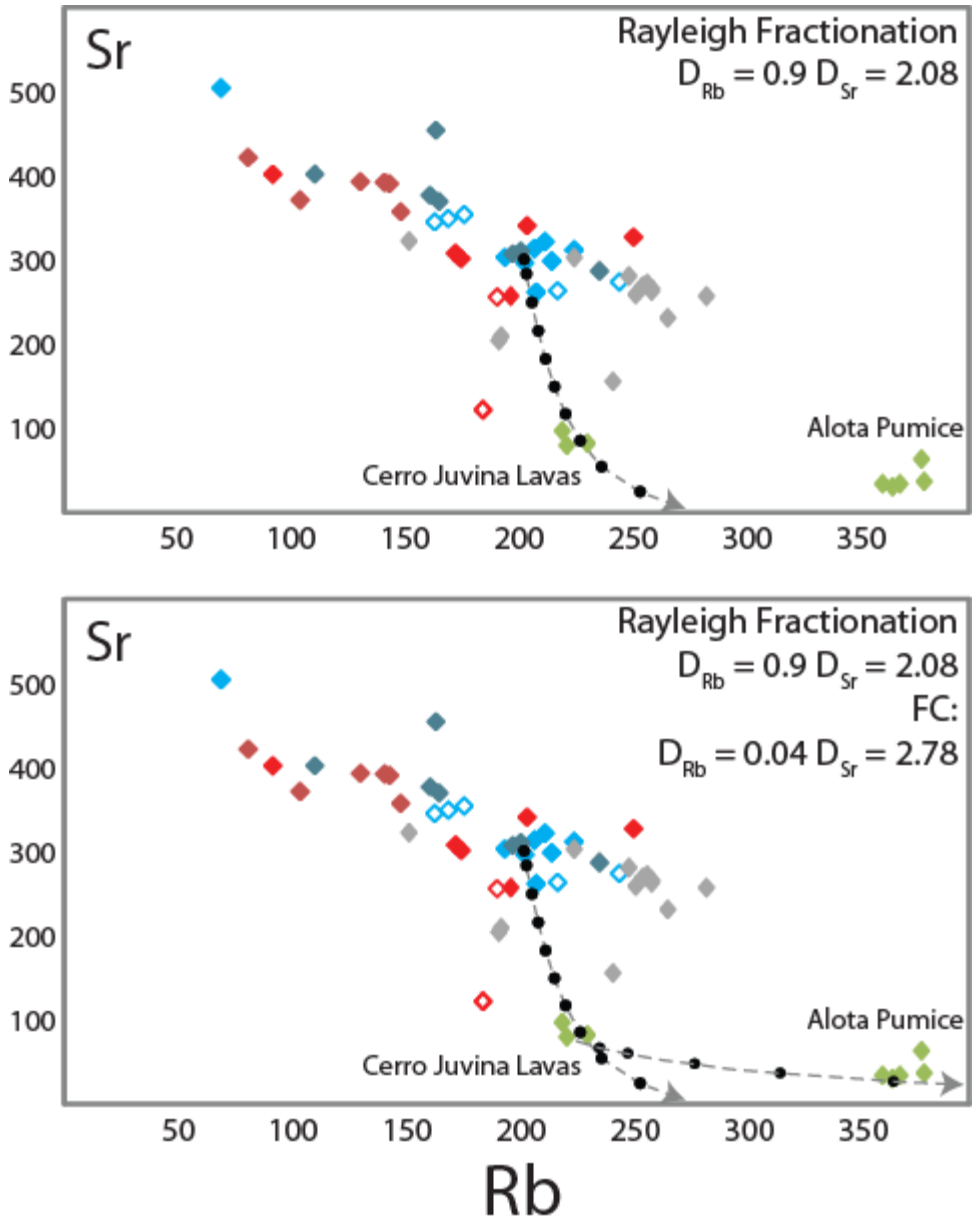

Figure 3.13 Continued. Simple Rayleigh fractionation from the typical caldera-related dacite magma parent results in the Juvina rhyolites with 60-70% fractionation (Top). The same Rayleigh fractionation model is employed again using the Cerro Juvina lavas as the parent to produce the Alota compositions with ~40% fractionation (Bottom).

Table 3.1. Modal Abundances. Crystallinity and modal abundances are based on visual estimates in both hand sample and petrographic thin section.

	Cerro Aguas Calientes	Cerro Pabellon Cachi Laguna	Cerro Arenal	Pastos Grandes Ignimbrite	Juvina Lavas	Alota Ignimbrite	Serrania Khenwal	Cerro Chuhuilla	Chuhuilla Ignimbrite	Resurgent Dome Plutonic Clast	Cerro Chascon Plutonic Clast
Crystallinity	50	50	50	40-45	40	35	50	50	40-45	100	100
Plagioclase	40	40	40	40	40	10	70	70	50	35	35
Sanidine	n.o.	n.o.	5	10	25	35	n.o.	n.o.	10	35	35
Biotite	40	40	40	10	20	10	15	15	15	10	10
Amphibole	5	5	5	<5	n.o.	n.o.	10	10	<5	<5	<5
Quartz	15	15	10	25	10	45	5	5	20	10	10
Zircon	tr.	tr.	tr.	tr.	n.o.	n.o.	tr.	tr.	tr.	tr.	tr.
Apatite	tr.	tr.	tr.	tr.	tr.	tr.	tr.	tr.	tr.	tr.	tr.
Titanite	tr.	tr.	tr.	tr.	tr.	tr.	tr.	tr.	tr.	tr.	tr.
Allanite	tr.	tr.	tr.	tr.	tr.	tr.	tr.	tr.	tr.	tr.	tr.
Fe-Ti Oxides	tr.	tr.	tr.	tr.	tr.	tr.	tr.	tr.	tr.	tr.	tr.

n.o. - non observed tr. - trace amounts

Table 3.2. Whole Rock chemical data. Major element, trace element, and isotope concentrations are shown for each sample of the PGCC. "JFK" samples are new to this study, remaining samples are from Salisbury et al. (2006) or unpublished work. As analyses were performed by a variety of techniques, some samples lack a full suite of trace element analytes.

	Chuhuilla Pumice		Serrania Khenwal/Cerro Chuhuilla									
	JFKBOL 10 -010	CRT 07 - BOL25C	SALB06 - 050	SALB06 - 054	JFKBOL 12 -003	JFKBOL 12 -006	JFKBOL 10-006	JFKBOL 12 -021	JFKBOL 12 -020	JFKBOL 12 -022	JFKBOL 10 -008	JFKBOL 10 -009
SiO2		61.26	67.59	69.13	67.38	66.79	64.10	63.58	64.53	63.59	61.40	61.49
TiO2	0.52	0.95	0.54	0.51	0.55	0.61	0.88	0.85	0.76	0.82	0.94	0.94
Al2O3	15.07	16.78	14.93	15.12	15.28	15.79	15.73	16.04	15.90	15.83	16.22	17.05
FeO*	3.57	6.26	3.50	2.84	3.61	4.05	5.22	5.87	5.42	6.54	6.03	5.95
MnO	0.07	0.10	0.07	0.06	0.06	0.07	0.08	0.08	0.07	0.08	0.10	0.10
MgO	1.65	2.99	1.80	1.72	1.96	1.83	2.67	2.41	2.03	2.00	3.30	2.91
CaO	3.70	5.20	3.47	3.30	3.64	3.93	4.33	4.50	4.36	4.35	5.67	5.10
Na2O	2.57	3.36	3.78	3.01	2.91	2.96	2.98	3.11	3.29	3.17	3.08	3.36
K2O	5.00	2.87	4.17	4.19	4.48	3.81	3.80	3.36	3.47	3.42	3.04	2.90
P2O5	0.50	0.23	0.14	0.13	0.12	0.16	0.21	0.20	0.19	0.20	0.21	0.22
Ba	494.84	745.18	524.00	549.10	510.72	502.88	730.65	682.53	704.25	708.98	675.31	798.65
Th	25.28	13.19	19.80	18.80	20.42	18.51	18.89	17.34	15.68	16.22	12.67	14.99
Nb	12.39	13.35			11.49	11.78	13.63	12.44	13.06	13.77	12.10	14.32
Y	18.55	23.97	16.80	16.70	16.65	16.39	19.09	16.72	17.78	18.68	22.28	24.74
Hf	4.33	5.05			3.84	3.93	5.22	4.73	4.95	4.94	4.76	5.27
Ta	1.57	1.10			1.41	1.36	1.32	1.16	1.13	1.15	1.06	1.21
U	19.59	4.11	10.20	9.50	9.67	9.30	6.86	6.52	5.65	5.80	4.38	4.20
Pb	26.31	14.55			23.37	21.43	21.64	22.59	19.75	20.20	16.01	24.56
Rb	197.21	91.30	174.70	172.20	250.96	203.79	147.91	143.00	130.13	140.73	103.42	80.38
Cs	20.84	3.28			22.15	18.17	10.40	8.56	11.67	14.01	6.92	3.70
Sr	256.15	402.03	300.90	307.30	326.70	340.37	357.04	390.68	393.03	392.36	371.18	422.03
Sc	8.94	15.68			7.98	8.24	11.79	9.93	10.52	10.33	17.11	15.46
Zr	133.83	182.21	132.20	131.20	125.24	131.37	190.65	165.50	180.33	175.76	168.08	189.57
Rb/Sr	0.77	0.23	0.58	0.56	0.77	0.60	0.41	0.37	0.33	0.36	0.28	0.19
Zr/Hf	30.91	36.07			32.60	33.43	36.52	34.96	36.42	35.56	35.28	35.95
Th/U	1.29	3.20	1.94	1.98	2.11	1.99	2.75	2.66	2.77	2.79	2.89	3.57
La	105.34	120.26	83.07	80.56	86.72	95.20	129.32	120.01	121.11	120.40	109.85	132.53
Ce	77.01	90.31	66.96	67.57	67.54	71.93	100.90	90.88	92.24	91.94	83.94	100.76
Pr	60.40	71.93	0.00	0.00	52.36	55.60	80.04	70.66	72.28	72.12	65.04	78.58
Nd	43.67	54.83	40.17	35.33	38.70	41.07	59.61	52.04	54.19	54.44	48.73	58.81
Sm	25.77	32.75			23.65	23.78	34.23	29.80	31.71	30.82	29.65	34.69
Eu	13.50	20.69			14.40	14.04	18.48	17.35	19.34	18.78	19.08	21.40
Gd	15.62	21.14			14.18	14.63	19.97	16.91	18.18	18.27	19.27	22.02
Tb	1.27	1.76			1.17	1.23	1.57	1.35	1.46	1.45	1.63	1.83
Dy	10.81	14.86			9.97	10.13	12.63	10.82	11.62	11.58	13.75	15.05
Ho	9.24	12.88			8.52	8.48	10.13	8.73	9.51	9.53	11.96	13.08
Er	8.52	11.49			7.57	7.67	8.71	7.48	8.29	8.65	10.89	11.62
Yb	8.25	9.98			7.20	7.42	7.62	6.95	7.28	7.38	9.75	10.32
Lu	8.91	10.12			7.42	7.75	7.61	6.70	7.46	7.37	9.84	10.77
Eu/Eu*	0.65	0.77			0.76	0.73	0.68	0.74	0.78	0.77	0.78	0.75
Dy/Yb	1.31	1.49			1.39	1.36	1.66	1.56	1.60	1.57	1.41	1.46
La/Yb	12.77	12.05			12.05	12.82	16.97	17.26	16.63	16.31	11.26	12.85
$^{87}Sr/^{86}Sr$	0.708572					0.708483				0.708757		
	0.000011					0.000011				0.000011		
$^{143}Nd/^{144}Nd$	0.512264					0.512258				0.512257		
	0.000012					0.000010				0.000016		

Table 3.2. Continued.

	Alota/Juwina	Pastos Grandes Ignimbrite										
	SALB06 - 063	CRT 92 - CJ002	CRT 92 - CJ005	CRT 92 - CJ0012	CRT 92 - CJ015	JFKBOL 10-003	SALB06 - 037	CRT 07 - BOL27	JFKBOL 12 -002	JFKBOL 12 -008	JFKBOL 12 -009	JFKBOL 12 -023
SiO2	74.93	75.27	76.37	74.55	75.28	70.05	68.77	68.44	67.83	69.18	69.11	67.81
TiO2	0.061	0.113	0.103	0.077	0.112	0.52	0.50	0.54	0.52	0.50	0.52	0.55
Al2O3	14.68	14.41	13.05	14.63	13.85	14.32	14.83	15.35	15.05	15.17	14.79	15.61
FeO*	0.98	1.20	1.22	0.97	1.20	3.25	3.00	3.41	3.19	3.13	3.33	3.42
MnO	0.125	0.072	0.089	0.113	0.069	0.06	0.06	0.06	0.07	0.06	0.06	0.06
MgO	0.11	0.20	0.23	0.15	0.20	1.43	1.38	1.51	1.45	1.32	1.47	1.63
CaO	0.61	0.84	0.88	1.03	0.84	2.98	3.92	3.35	3.54	3.35	3.45	3.67
Na2O	3.16	3.24	3.28	3.07	2.97	2.71	2.91	2.93	3.81	3.07	3.17	3.04
K2O	5.18	4.58	4.70	5.32	5.33	4.53	4.12	4.25	4.43	4.10	3.98	4.08
P2O5	0.171	0.068	0.064	0.096	0.156	0.15	0.52	0.14	0.12	0.12	0.12	0.13
Ba	53.50	209.19	265.47	55.79	229.06	605.58	316.40	612.34	345.60	432.94	396.85	443.87
Th	8.00	10.02	8.34	8.42	9.69	26.51	26.40	24.90	24.56	25.55	24.78	24.77
Nb		21.68	17.73	35.42	20.73	12.45		12.21	12.16	12.27	12.45	12.58
Y	32.80	38.77	30.92	30.96	36.22	15.49	17.90	15.42	14.88	14.35	14.69	14.89
Hf		2.70	2.42	2.55	2.66	4.49		4.58	3.96	4.20	4.16	4.36
Ta		2.24	1.88	4.99	2.13	1.42		1.36	1.41	1.46	1.45	1.41
U	14.00	6.92	5.27	14.54	6.74	12.80	30.90	11.48	12.28	12.84	13.00	11.71
Pb		27.91	33.10	17.04	18.37	32.00		32.33	20.79	22.70	22.29	28.76
Rb	345.70	207.27	206.57	357.53	216.63	207.94	214.80	207.11	224.69	194.05	202.87	211.76
Cs		10.91	6.85	29.37	10.76	16.97		15.43	20.84	16.69	17.54	17.67
Sr	28.40	66.68	81.63	52.99	68.37	260.76	298.00	313.12	311.31	302.55	295.65	321.22
Sc		6.14	5.26	6.53	5.95	7.49		7.96	6.99	6.53	6.64	7.27
Zr	47.70	62.96	59.51	46.13	64.34	145.97	139.50	153.77	127.15	135.09	136.03	145.04
Rb/Sr	12.17	3.11	2.53	6.75	3.17	0.80	0.72	0.66	0.72	0.64	0.69	0.66
Zr/Hf		23.35	24.59	18.06	24.16	32.49		33.56	32.12	32.15	32.71	33.30
Th/U	0.57	1.45	1.58	0.58	1.44	2.07	0.85	2.17	2.00	1.99	1.91	2.12
La	34.17	64.18	53.69	32.29	60.81	115.98	123.20	121.42	120.09	108.46	101.17	108.43
Ce	26.49	51.34	42.83	28.05	48.87	86.61	85.64	87.81	85.78	79.87	76.18	82.66
Pr		43.52	35.08	24.51	40.33	63.90		68.29	61.38	57.89	56.95	60.92
Nd	16.33	32.04	25.76	18.14	29.39	45.52	39.17	48.99	42.70	40.89	40.69	43.49
Sm		26.77	21.10	19.93	24.32	25.37		26.95	23.44	22.95	22.88	24.47
Eu		7.15	6.73	2.32	6.57	12.55		13.94	12.99	12.83	12.69	13.51
Gd		19.93	15.79	15.92	18.14	14.65		14.72	13.39	13.25	13.20	13.87
Tb		2.25	1.80	1.93	2.06	1.16		1.17	1.09	1.07	1.08	1.10
Dy		21.77	17.13	18.12	20.08	9.45		9.51	8.83	8.73	8.69	9.01
Ho		19.68	15.84	14.96	18.27	7.88		7.85	7.48	7.22	7.31	7.51
Er		19.20	15.17	13.87	17.91	7.02		7.09	6.77	6.55	6.53	7.05
Yb		18.58	14.91	13.57	17.33	6.67		6.50	6.52	6.30	6.41	6.38
Lu		18.17	14.62	12.49	16.81	6.78		6.69	6.95	6.48	6.67	6.47
Eu/Eu*		0.31	0.37	0.13	0.31	0.63		0.67	0.71	0.71	0.70	0.70
Dy/Yb		1.17	1.15	1.34	1.16	1.42		1.46	1.35	1.39	1.36	1.41
La/Yb		3.45	3.60	2.38	3.51	17.38		18.67	18.40	17.21	15.79	17.00
$^{87}Sr/^{86}Sr$						0.708173				0.708040		
						0.000013				0.000010		
$^{143}Nd/^{144}Nd$						0.512276				0.512223		
						0.000009				0.000008		

Table 3.2. Continued.

	Post-Collapse Domes							Granodiorites				
	JFKBOL 10 -011	JFKBOL 10 -013	JFKBOL 10 -014	JFKBOL 10 -015	JFKBOL 12 -015	JFKBOL 12 -016	JFKBOL 10 -016	CCG CC9317	CCG CC9317a	CCG CC9317b	CCG JFKBOL 12 -017B	CCG JFKBOL 12 -017A
SiO2	65.69	66.44	67.71	64.40	69.03	68.62	63.47	68.47	68.73	67.56	71.18	69.90
TiO2	0.67	0.62	0.64	0.81	0.49	0.49	0.58	0.60	0.59	0.61	0.39	0.39
Al2O3	15.91	16.19	15.33	16.37	15.33	15.18	17.01	15.01	14.93	14.99	14.57	15.20
FeO*	4.38	3.89	3.73	4.71	3.43	3.67	4.96	3.43	3.41	3.42	2.55	2.51
MnO	0.08	0.07	0.06	0.07	0.05	0.06	0.11	0.05	0.05	0.05	0.05	0.05
MgO	2.08	1.76	1.63	1.96	1.03	1.32	2.69	1.58	1.54	1.57	1.02	1.01
CaO	3.99	3.95	3.16	4.45	3.14	3.05	5.18	3.51	3.48	3.50	2.62	2.48
Na2O	3.26	3.42	3.24	3.44	3.34	3.42	3.06	3.55	3.49	3.51	3.21	3.24
K2O	3.77	3.51	4.34	3.58	4.04	4.07	2.79	3.67	3.65	3.66	4.32	5.13
P2O5	0.16	0.15	0.15	0.22	0.11	0.12	0.14	0.12	0.12	0.12	0.09	0.10
Ba	652.13	652.94	703.64	765.62	513.82	595.44	548.96	613.00	611.00	609.00	509.13	500.81
Th	20.89	22.48	24.72	19.58	12.08	25.83	26.21	10.00	9.00	9.00	30.79	23.81
Nb	12.27	12.40	15.08	12.02	8.95	13.60	12.70	13.00	14.00	14.00	12.13	11.00
Y	19.88	17.75	15.68	18.60	20.97	16.04	15.40	15.00	15.00	15.00	12.73	12.19
Hf	4.53	4.79	5.74	5.59	3.39	4.40	3.96				4.24	3.67
Ta	1.26	1.33	1.68	1.06	1.03	1.73	1.44				1.49	1.25
U	9.04	9.22	9.32	6.18	5.51	13.80	12.54	5.00	5.00	5.00	10.85	7.65
Pb	23.20	24.51	25.07	21.02	16.58	25.47	25.45	17.00	18.00	21.00	29.91	28.95
Rb	164.93	160.93	236.01	163.84	110.02	197.50	200.72	163.00	176.00	169.00	244.78	217.39
Cs	12.43	13.99	14.66	5.97	6.22	16.95	16.38				13.25	9.72
Sr	366.66	373.80	285.58	455.83	403.15	306.94	310.74	345.00	354.00	349.00	273.11	262.50
Sc	11.61	9.86	8.85	12.34	21.45	7.20	7.19				5.34	5.16
Zr	149.32	155.45	202.15	207.55	114.99	144.78	129.53	126.00	127.00	124.00	132.01	114.97
Rb/Sr	0.45	0.43	0.83	0.36	0.27	0.64	0.65	0.47	0.50	0.48	0.90	0.83
Zr/Hf	32.95	32.47	35.24	37.16	33.92	32.87	32.68				31.17	31.29
Th/U	2.31	2.44	2.65	3.17	2.19	1.87	2.09	2.00	1.80	1.80	2.84	3.11
La	109.98	122.54	146.14	139.55	78.29	112.74	111.81				107.72	95.18
Ce	84.22	93.02	114.67	110.78	57.72	86.05	82.64				78.42	69.75
Pr	63.94	69.62	84.55	85.58	45.02	63.75	60.13				54.98	51.07
Nd	46.80	50.17	59.46	63.35	32.36	45.28	42.78				37.53	35.39
Sm	27.63	28.53	31.31	34.14	19.62	26.48	24.87				20.44	19.62
Eu	15.59	15.59	15.14	17.67	13.25	13.46	13.02				10.96	10.40
Gd	17.14	16.94	17.06	19.00	13.20	14.55	14.41				11.59	11.43
Tb	1.42	1.37	1.32	1.50	1.26	1.19	1.19				0.94	0.92
Dy	11.95	11.08	10.14	11.88	11.89	9.65	9.36				7.50	7.23
Ho	10.35	9.34	8.19	9.94	11.38	8.08	7.84				6.46	6.05
Er	9.24	8.17	7.15	8.57	11.06	7.55	7.29				5.77	5.50
Yb	8.55	7.37	6.43	7.20	10.93	6.79	6.54				5.81	5.21
Lu	8.78	7.60	6.53	7.17	11.56	6.87	6.68				6.08	5.52
Eu/Eu*	0.70	0.69	0.63	0.67	0.81	0.66	0.66				0.68	0.67
Dy/Yb	1.40	1.50	1.58	1.65	1.09	1.42	1.43				1.29	1.39
La/Yb	12.86	16.64	22.71	19.39	7.16	16.60	17.10				18.53	18.26
											0.708224	
											0.000017	
											0.512258	
											0.000009	

Table 3.2. Continued.

	RDG JFKBOL 12 -024A	RDG JFKBOL 12 -024B
SiO2	71.56	74.92
TiO2	0.38	0.21
Al2O3	14.43	13.38
FeO*	2.52	1.68
MnO	0.05	0.02
MgO	0.98	0.42
CaO	2.54	1.37
Na2O	3.22	3.67
K2O	4.23	4.27
P2O5	0.10	0.06
Ba	539.95	355.74
Th	27.26	21.17
Nb	11.64	18.93
Y	14.17	27.13
Hf	3.70	4.16
Ta	1.65	1.95
U	9.87	12.68
Pb	21.82	21.99
Rb	190.62	184.45
Cs	7.31	5.43
Sr	255.02	119.67
Sc	5.11	4.49
Zr	111.73	110.88
Rb/Sr	0.75	1.54
Zr/Hf	30.22	26.68
Th/U	2.76	1.67
La	93.51	91.27
Ce	70.46	74.30
Pr	52.40	57.78
Nd	36.73	41.92
Sm	21.23	29.12
Eu	11.30	8.52
Gd	11.99	19.06
Tb	1.03	1.80
Dy	8.50	15.77
Ho	7.27	13.77
Er	6.80	13.09
Yb	6.43	11.89
Lu	6.63	11.78
Eu/Eu*	0.68	0.35
Dy/Yb	1.32	1.33
La/Yb	14.55	7.68
	0.708450	
	0.000010	
	0.512264	
	0.000010	

Table 3.3. Oxygen Isotope Analyses in Zircon. A subset of samples in the Complex including Pastos Grandes Ignimbrite (PGI), Cerro Aguas Calientes (AC), Cerro Pabellon Cachi Laguna (PCL) and granodiorite from Cerro Chascon (CCG).

Name	I16O	corrected d18O	1 s.e. internal	1 s.e. calibration
PGI @1	3.90E+09	6.51	0.08	0.20
PGI @2	3.91E+09	6.50	0.09	0.20
PGI @3	3.94E+09	6.10	0.07	0.20
PGI @4	3.90E+09	6.05	0.11	0.20
PGI @5	3.87E+09	6.58	0.10	0.20
PGI @6	3.93E+09	6.58	0.08	0.20
PGI @7	3.92E+09	6.71	0.08	0.20
PGI @8	3.87E+09	6.58	0.08	0.20
PGI @9	3.89E+09	6.32	0.11	0.20
PGI @10	3.96E+09	5.92	0.08	0.20
PGI @11	3.95E+09	6.57	0.09	0.20
PGI @12	3.80E+09	6.78	0.11	0.20
PGI @13	3.93E+09	6.30	0.05	0.20
PGI @14	3.93E+09	6.41	0.10	0.20
PGI @15	3.94E+09	6.05	0.12	0.20
PGI @16	3.92E+09	6.55	0.09	0.20
PGI @17	3.91E+09	6.48	0.11	0.20
PGI @18	3.97E+09	6.62	0.09	0.20
PGI @19	3.95E+09	6.28	0.07	0.20
PGI @20	3.93E+09	6.50	0.07	0.20
PGI @21	3.98E+09	6.35	0.11	0.20
CCG @1	3.91E+09	6.40	0.13	0.20
CCG @2	3.90E+09	6.44	0.09	0.20
CCG @3	3.96E+09	6.61	0.07	0.20
CCG @4	3.93E+09	6.31	0.10	0.20
CCG @5	3.93E+09	6.36	0.09	0.20
CCG @6	3.91E+09	6.28	0.13	0.20
CCG @7	3.79E+09	6.56	0.12	0.20
CCG @8	3.89E+09	6.00	0.12	0.20
CCG @9	3.96E+09	6.47	0.10	0.20
CCG @10	3.94E+09	6.53	0.07	0.20
CCG @11	4.00E+09	6.32	0.14	0.20
CCG @12	3.93E+09	6.22	0.09	0.20
CCG @13	3.99E+09	6.17	0.07	0.20

Table 3.3. Continued.

Name	I16O	corrected d18O	1 s.e. internal	1 s.e. calibration
CCG @14	3.92E+09	6.58	0.14	0.20
CCG @15	3.96E+09	6.54	0.05	0.20
CCG @16	3.93E+09	6.46	0.10	0.20
CCG @17	3.96E+09	6.66	0.05	0.20
CCG @18	3.91E+09	6.48	0.12	0.20
PCL @1	3.92E+09	6.43	0.11	0.27
PCL @2	3.91E+09	6.53	0.11	0.27
PCL @3	3.93E+09	6.60	0.11	0.27
PCL @4	3.95E+09	6.63	0.13	0.27
PCL @5	3.94E+09	6.56	0.10	0.27
PCL @6	3.94E+09	6.60	0.08	0.27
PCL @7	3.94E+09	6.59	0.13	0.27
PCL @8	3.94E+09	6.57	0.13	0.27
PCL @9	3.95E+09	6.59	0.10	0.27
PCL @10	3.83E+09	6.33	0.05	0.27
PCL @11	3.86E+09	7.26	0.09	0.27
PCL @12	3.87E+09	6.31	0.09	0.27
PCL @13	3.91E+09	6.50	0.08	0.27
PCL @14	4.05E+09	9.73	0.09	0.27
PCL @15	4.06E+09	6.61	0.06	0.27
PCL @16	4.02E+09	6.38	0.10	0.27
PCL @17	3.98E+09	6.53	0.09	0.27
PCL @18	4.02E+09	6.37	0.11	0.27
PCL @19	3.97E+09	6.18	0.09	0.27
AC @1	4.04E+09	6.61	0.09	0.27
AC @2	4.04E+09	6.41	0.10	0.27
AC @3	4.06E+09	6.39	0.11	0.27
AC @4	3.95E+09	6.39	0.09	0.27
AC @5	3.94E+09	6.32	0.09	0.27
AC @6	4.07E+09	6.35	0.09	0.27
AC @7	4.08E+09	6.16	0.12	0.27
AC @8	4.16E+09	6.73	0.10	0.27
AC @9	4.04E+09	6.73	0.12	0.27
AC @10	4.01E+09	6.33	0.13	0.27
AC @11	4.09E+09	6.52	0.12	0.27
AC @12	4.06E+09	6.32	0.07	0.27
AC @13	4.07E+09	6.36	0.11	0.27
AC @14	4.02E+09	6.53	0.08	0.27
AC @15	4.12E+09	6.26	0.11	0.27
AC @16	4.05E+09	6.35	0.11	0.27
AC @17	4.10E+09	6.48	0.08	0.27
AC @18	3.98E+09	7.02	0.08	0.27
AC @19	4.08E+09	6.69	0.10	0.27
AC @20	4.10E+09	6.64	0.12	0.27

CHAPTER 4

Million-year lifetime of a supereruption magma system revealed by zircon chronochemistry

Jason F. Kaiser

Shanaka de Silva

Axel K. Schmitt

Mayel Sunagua

Abstract

Zircon chronochemistry, the combination of U-Pb ages with indicators for geochemical evolution (e.g., Zr/Hf, Yb/Gd, Eu/Eu*, Th, U) magmatic temperatures (e.g., Ti) in zircon, reveals protracted presence of magma presence before and after the climactic, caldera-forming eruptions of the Pastos Grandes Caldera Complex in southwest Bolivia. Zircons from ignimbrite pumice and associated lava flows and domes define a pre-climactic magmatic stage and a post-climactic magmatic stage. In the initial Chuhuilla caldera cycle, zircon crystallization records pre-climactic magmatic conditions in the Chuhuilla ignimbrite, lava flows and cogenetic granodiorite clasts. In the later, Pastos Grandes caldera cycle, zircon crystallization records both pre- and post-climactic magmatic conditions in the Pastos Grandes ignimbrite, a complex of post-climactic domes, and cogenetic granodiorite clasts. Homogeneity in bulk rock and zircon thermometry and geochemistry indicate that both cycles involved essentially identical dacitic magma, but a trend of increasing textural coarsening of major phases is seen with time in each cycle.

The zircons suggest distinct pulses of magmatism fed each of the caldera cycles. For the younger, Pastos Grandes cycle, where post-climactic volcanism is best exposed, we propose a model in which a single crystal-rich dacite reservoir was maintained above solidus temperature by andesitic recharge that is chemically invisible in the magmatic evolution. The climactic caldera-forming eruption vented the upper portions of the reservoir that were zircon saturated. Subsequently, deeper "remnant" dacite magma previously outside the zone of zircon saturation but crystallizing other major phases, rose to re-establish lithostatic equilibrium, commenced zircon crystallization anew, and drove resurgent volcanism and uplift. This ~1.1 m.y zircon crystallization history records the minimum duration of the lifetime of the PGI supereruption magma from its accumulation to post-climactic solidification. These data support >1 Myr. magma lifetimes and a link between volcanic and plutonic realms in large sub-caldera magma reservoirs in the uppermost crust that feed some supereruptions.

Introduction

It is well known that climactic, caldera-forming eruptions punctuate protracted pre-eruptive magma accumulation over a range of time periods in large silicic magmatic systems (Smith, 1979; Reid et al., 1997; Miller et al., 2004). However, less well understood are details of the full magmatic cycle, including the post-climactic magma history culminating in solidification. Whereas resurgence at the surface (volcanism and uplift) is commonly seen and is understood to be the waning of the supereruption cycle, the full story is hidden at depth. In the rare occasions where confocal volcanic and plutonic rocks are exposed they show striking similarities in geochemistry and petrology but ambiguous age relations. Opposing views are that either plutonic rocks comprise

crystal and liquid residua of volcanic eruptions, and are thus geochemically complementary to volcanic rocks (Hildreth, 2004; Eichelberger et al., 2006; Bachmann et al., 2007; Lipman, 2007; de Silva and Gosnold, 2007), or that plutonic rocks form as unfractionated equivalents of erupted magma (Glazner et al., 2008; Tappa et al., 2011; Zimmerer et al., 2012). This question is particularly relevant for large calderas, where resurgence and post-caldera volcanism suggest a significantly extended magmatic lifetime and attendant hazard of the system (Smith and Bailey, 1968; Marsh, 1984). Herein we apply zircon chronochemistry to volcanic rocks and cogenetic plutonic clasts from the Pastos Grandes caldera in southwest Bolivia. In this system zircon records a quasi-continuous history of thermal, compositional, and textural evolution in a shallow dacitic crustal magma reservoir.

Geologic Background

The Pastos Grandes Caldera Complex (PGCC) in southwestern Bolivia (Figure 4.1) is part of the Altiplano-Puna Volcanic Complex (APVC), an ignimbrite and caldera field formed from ~11 Ma to Recent (de Silva, 1989; de Silva et al., 2006). The earliest PGCC caldera cycle resulted from the 5.45 ± 0.02 Ma (sanidine age) eruption of the 1300 km^3 (DRE) Chuhuilla Ignimbrite. Following the eruption of the Chuhuilla ignimbrite, lavas formed along Serrania Khenwal, an arcuate structure marking the eastern margin of the caldera. A second climactic eruption at 2.89 ± 0.01 Ma (sanidine age) resulted in the ~800 km^3 (DRE) PGI and produced the eponymous ~ 36 x 30 km caldera nested within the larger Chuhuilla caldera (Fig. 1). A distinct ~20 km diameter, 1 km-high resurgent dome and surrounding post-climactic dome complex (Cerro Aguas Calientes, Cerro Pabellon Cachi Laguna, and Cerro Arenal) define the footprint of magmatic and

structural resurgence for the Pastos Grandes supereruption. The final component of both caldera cycles is found as holocrystalline plutonic clasts found in the intracaldera facies o the Pastos Grandes ignimbrite and erupted as ejecta during the much younger (~85 ka) Chascon Runtu-Jarita dome complex episode (Watts et al., 1999).

PGI and Chuhuilla pumice clasts are crystal-rich, calc-alkaline, dacites with SiO_2 between 67 wt% and 70 wt% SiO_2 and ~40% phenocrysts (vesicle free) of 1 – 3 mm plagioclase, quartz, biotite, amphibole, and rare sanidine, set in a vesicular, glassy matrix. Accessory phases include apatite, titanite, Fe-Ti oxides, and zircon. The post-climactic lavas and domes and plutonic clasts have very similar bulk rock compositions to the ignimbrites (as shown in Chapter 3 of Thesis). The post-climactic lavas are denser, similar in mineralogy to the pumice, but are coarser (up to 5 mm for plagioclase and quartz phenocrysts), and with higher phenocryst content (up to 50%). The groundmass of the post-climactic lavas is rich in microlites. The plutonic clasts are granodiorite and have a phaneritic texture with dominant plagioclase, potassium feldspar, biotite, amphibole, and quartz. Thus, the suite shares a general family resemblance in mineralogy and whole rock chemistry with a trend of increasing textural coarseness (maturity) from pumice to lava to granodiorite.

Zircon Preparation and Analytical Procedures

Zircons were recovered by heavy liquid separation from the <250 µm sieved fraction of crushed rock samples. Zircons were mounted in epoxy and polished to intersect crystal interiors. Prior to ion probe analyses, each zircon crystal was examined for internal zoning by cathodoluminescence (CL) imaging using a Leo 1430VP scanning electron

microscope equipped with an Oxford mini-CL detector. CL images were used to target core and rim locations for ion probe analysis with a preference for CL homogenous domains to minimize averaging of multiple growth zones in the zircon crystals. Ion microprobe analyses were performed using the CAMECA ims 1270 ion microprobe at University of California Los Angeles (UCLA). A mass-filtered $^{16}O^-$ primary beam with an intensity of 15-20 nA was focused to a size of 25-30 µm. For U-Pb analyses, secondary ions were extracted at 10 kV, a mass resolution power $m/\Delta m = 4500$ at 10% of the peak height, and an energy bandpass of 50 eV. Replicate analysis of reference zircon AS3 (Paces and Miller, 1993) yielded a $^{206}Pb/^{238}U$ age reproducibility of <3%. Only analyses that yielded greater than 90% radiogenic ^{206}Pb are included in the discussion below.

U-Pb geochronology ion probe craters were subsequently used for trace element analyses after re-imaging the crystals by CL, and repolishing them to remove all but a small vestige of the U-Pb crater. The trace element spot was then placed directly onto the U-Pb spot using an ~15-20 nA $^{16}O^-$ primary ion beam. High energy (+100 eV) secondary ions were analyzed at low mass resolution ($m/\Delta m = 2000$) using energy-filtering to suppress molecular interferences. Trace element relative sensitivity factors were calibrated using NIST610 glass (Pearce et al., 1994). Replicate analyses of zircon standard 91500 agree within <20% with values reported in Liu et al. (2011) for Ti, Zr/Hf and REE with the exceptions of La (0.03 ppm vs. 0.005 ppm) and Lu (16 ppm vs. 12.8 ppm).

Treatment of U-Pb Data

A total of 281 U-Pb zircon analyses were conducted; for individual samples the numbers are as follows: Chuhuilla n = 37, Serrania Khenwal n = 38, Graniodiorite of the resurgent dome (RDG) n = 20, PGI n = 57, Cerro Arenal n = 31, Cerro Pabellon Cachi Laguna n = 22, Cerro Aguas Calientes n = 22 and Granodiorite of Cerro Chascon (CCG) n = 54 (Table 4.1). Populations with mean square of weighted deviate (MSWD) values exceeding the high-95% critical limit for a single population (Mahon, 1996) include: (Chuhuilla Ignimbrite MSWD = 2.53, RDG MSWD = 5.34, PGI MSWD = 5.71; CCG = 4.54; Aguas Calientes = 2.63). Samples below the critical limit are: Serrania Khenwal (MSWD = 1.48), Arenal (MSWD = 1.43) and Pabellon Cachi Laguna (MSWD = 1.55). Probability density functions for individual populations with high MSWD values are skewed towards older ages. We interpret these observations as the result of zircon crystallization over durations which exceed analytical resolution. Because of this, averages do not adequately represent the complexities of the age populations. To refine our interpretation of magma presence through zircon chronology, we applied the age unmixing algorithm of Sambridge and Compston (1994) as implemented in Isoplot Version 3.71 (Ludwig, 2008). PGI, Aguas Calientes, Arenal, and the CCG sample populations were deconvolved assuming two normally-distributed sub-populations in the unmixing algorithm (Figure 4.2); models with more than two populations failed to decrease relative misfit values. The ages of both subpopulations for these samples are shown in Table 4.2. In all cases, the dominant sub-populations yielded younger ages. The older sub-population was generally less abundant, but with a gradual transition. Where statistically significant differences between the dominant and minor sub-

populations were observed (e.g. Figure 4.2c), the older subpopulation was removed from the discussion. While samples of the Chuhuilla cycle yielded high MSWD, those populations fit within the range of normally distributed populations of Serrania Khenwal and thus the algorithm was not used to deconvolve older subpopulations. Because of the nearly identical zircon age distributions in samples PGI and Arenal vs. Pabellon Cachi Laguna, Aguas Calientes, and Granodiorite, we grouped them into two cumulative distributions which were assigned to the pre- and post-climactic magmatic stages, respectively (Figure 4.3). In contrast the populations of the Chuhuilla cycle lie entirely in the pre-climactic magmatic stage.

Zircon Ages and Trace Element Compositions

Probability density curves for populations of both the Chuhuilla and the Pastos Grandes cycle are shown in Figure 4.3. In both examples the crystallization age (associated with the peak of the curve) are reported along with the individual analyses and their errors (1σ). However, the peaks ages only have geological significance if the scatter in the data is purely random analytical noise. The quoted uncertainties on the individual analyses are small and imply that the spread of the chronologic data should be given consideration and has geologic meaning. The overall duration of magmatic zircon crystallization is thus constrained by oldest autocryst ages in the pre-climactic zircon population and the youngest autocryst ages in the post-climactic distribution.

The three peak ages representing each phase of the Chuhuilla cycle are quite similar compared to the peaks of the Pastos Grandes cycle. The Chuhuilla ignimbrite (n = 37) and the RDG (n = 20) have almost identical peak ages of 6.04 ± 0.07 and 6.04 ± 0.11 Ma

respectively. Zircons of the lavas along the collapse scarp of Serrania Khenwal (n = 38) are offset to a slightly older peak age (6.23 ± 0.04 Ma). The probability density curves are overlaid on the ranked order plot of the individual analyses showing approximately 1.3 Myr of zircon crystallization leading up to the eruption of the Chuhuilla ignimbrite. This continuum is represented by 95 analyses from the three phases of the Chuhuilla cycle, none of which sample the post-climactic magma following the eruption of the Chuhuilla ignimbrite.

Peak ages for the two distributions in the Pastos Grandes cycle are 3.17 ± 0.03and 2.69 ± 0.04 respectively, yielding a total crystallization duration of 0.48 ± 0.07 Myr (Figure 4.4). The PGI and Cerro Arenal define a pre-climactic stage with a peak age of 3.14 ± 0.02 Ma for the younger population significantly predating the sanidine $^{40}Ar/^{39}Ar$ climactic eruption age (2.89 ± 0.01 Ma; Salisbury et al., 2011). The older sub-population for these samples averages 3.61 ± 0.02 Ma and extends the pre-eruptive zircon crystallization to a duration of 0.72 ± 0.02 Ma. Cerro Aguas Calientes and Cerro Pabellon Cachi Laguna and the granodiorite define a post-climactic stage with a peak age of 2.51 ± 0.02 Ma representing the age of zircon crystallization following the caldera-forming eruption. Cerro Aguas Calientes and Pabellon Cachi Laguna and granodiorite also contain a minor antecrystic population from the pre-climactic stage. The total duration of zircon crystallization from the oldest significant pre-climactic population at 3.61 ± 0.02 Ma to the post-climactic population at 2.51± 0.02 Ma is 1.10 ± 0.04 Ma. This duration can be seen as a continuum in the individual zircon ages and is supported by the width of the probability density curves of Figure 4.4. The age range could be extended further to include parts of the continuum defined as statistically insignificant (20-30% fractional

abundance of a sample as defined by the unmixing algorithm), but we see this as a statistically ambiguous approach. Clearly xenocrystic ages (i.e. 10.0 ±0.4, 17.2 ± 0.4, and 147 ±6 Ma) are only ~2% of the population, and are exclusively found in crystal interiors (Figure 4.3).

Zircon trace element chemistry shows homogeneity on two different scales. Each of the zircon populations that make of the pre-climactic magma stage of the Chuhuilla cycle show nearly identical trace element signatures (Figure Figure 4.5, Table 4.3). Selected trace element ratios reveal that zircon records the same magma compositional conditions throughout the pre-climactic stage. Similarly, zircons in pre and post-climactic magma populations of the Pastos Grandes cycle independently show nearly identical trace element signatures (Table 4.3). Selected trace element ratios (Figure 4.5) reveal that zircon crystallized under very similar temperature and compositional conditions during pre and post-climactic stages in the shallow crust. Trends of decreasing Zr/Hf with increasing Yb/Gd, implicate co-crystallization of amphibole and titanite with zircon (e.g., Claiborne et al., 2006; Reid et al., 2011) (Figure 4.5c). These trends suggest that crystallization of zircon and titanite is to a first order temperature-dependent (Green and Pearson, 1986; Boehnke et al., 2013) (Figure 4.6). The changes in trace element concentrations reflect melt evolution, following a decreasing temperature trend as crystals grow. The total temperature range for the Ti-in-zircon temperatures is ~200° C (using the calibration of Ferry and Watson, 2007) with no significant differences between pre-climactic and post-climactic zircons - assuming activity of TiO_2 was constant or increased with decreasing temperature when buffered by an equilibrium Fe-Ti oxide

assemblage (Ghiorso and Gualda, 2013). The temperature range agrees with that found in other large silicic systems (e.g. Reid et al., 2011), and are taken as another line of evidence for similar magmatic conditions in the pre and post-climactic stages. The superposition of the temperatures on the trace element diagrams (Figure 4.6) supports the melt evolution trend. The trend in the post-climactic magma stage is more diffuse at the low Yb/Gd end of the spectrum. This diffuse trend is thought to be the result of new zircons crystallizing in the reorganized magma system with variable degrees of amphibole and titanite crystallization. Generally this trend, as with the Th vs U and Zr/Hf vs Eu/Eu* of (Figure 4.5) suggests largely constant chemical and thermal conditions over the million year time span from pre to post-climactic zircon crystallization.

Discussion

Rejuvenation of the Pre-Climactic Chuhuilla Magma System

The zircon age populations of the Chuhuilla cycle support the $^{40}Ar/^{39}Ar$ geochronology described in Chapter 2 of the thesis. The zircon geochronology casts doubt on the validity of the $^{40}Ar/^{39}Ar$ sanidine eruption age of the Chuhuilla ignimbrite. Salisbury et al. (2011) report the $^{40}Ar/^{39}Ar$ sanidine eruption age as 5.45 ± 0.02 Ma and a $^{40}Ar/^{39}Ar$ biotite eruption age of 5.52 ± 0.02 Ma. The sanidine age was preferentially used as the biotite ages had been shown to be unreliable as eruption ages (Hora et al., 2010). The Chuhuilla ignimbrite zircon population contains only one age younger than 5.62 ± 0.22 Ma (5.54 ± 0.21 Ma), which seems to support the $^{40}Ar/^{39}Ar$ biotite eruption age of 5.52 ± 0.02 Ma.

In both the zircon age populations and the $^{40}Ar/^{39}Ar$ eruption ages, the lavas of Serrania Khenwal appear older than the Chuhuilla ignimbrite. Yet field relationships prove undoubtedly that the Chuhuilla ignimbrite is stratigraphically below the lavas and thus older. It was suggested in Chapter 2 that the age discrepancy is the result of a difference in the closer temperatures of biotite and sanidine in the $^{40}Ar/^{39}Ar$ system. A theoretical model was proposed in which the lavas of Serrania Khenwal represent remnant magma with pre-climactic biotite crystallization recording an older age. This same model is supported by the zircon population. Zircon geochronology suggests that the lavas of Serrania Khenwal were sourced from remnant magma left in the sub-caldera system after the eruption of the Chuhuilla ignimbrite. This remnant magma was then extruded along the arcuate line of normal faults created during the collapse of the Chuhuilla caldera.

Longevity of the Pastos Grandes Supervolcanic Magma

Our interpretation is that the zircon data record the transition from pre-climactic magma accumulation (commonly thought of as the magma residence time e.g. Reid et al., 1997; Schmitt et al., 2003; Vazquez and Reid, 2004) to post-climactic resurgence and pluton solidification. Taking the difference between the pre-climactic and post-climactic peak autocryst ages (Figure 4.4) to define the time period from magma accumulation to final pluton solidification, we obtain a time interval of 0.48 ± 0.07 Ma. However, the peak ages only have geological significance if the scatter in the data is purely random analytical noise. The quoted uncertainties on the individual analyses are small and imply that the spread of the chronologic data should be given consideration and has geologic meaning. With this in mind, the statistically resolvable zircon age differences in

individual samples (indicated by the high MSWD values for the population) are best described as a result of quasi-continuous crystallization, with the second, post-climactic, stage of zircon crystallization commencing virtually immediately after the climactic eruption. This continuum of crystallization is supported by the progression of textural maturity seen in the eruptive sequence from ignimbrite through the post-climactic dome complex, to the granodiorite and suggests a single long-lived reservoir. Therefore, we use the age continuum of individual analyses to describe the total minimum crystallization duration of 1.1 Myr from accumulation in the PGI and Cerro Arenal to solidification seen in the post-climactic stage samples. Extended periods of crystallization, rather than single episodes of crystallization, are consistent with gradual variations in Ti-in zircon temperatures and the fractionation histories recorded in trace element compositions of zircons.

The minor antecryst population in the post-climactic population suggests that eruptible volumes of the pre-climactic magma may have been virtually exhausted or that any remnant magma was heated to above zircon saturation temperatures resulting in resorption of pre-existing zircon. The latter scenario presents problems in introducing a thermal excursion while still maintaining the consistent bulk composition of the system, the continuous fractionation trends, and the textural progression that we see. Moreover, cathodoluminescence images indicate a lack of evidence for resorption, and indicate continuous crystallization. Thus, the history sampled by the eruption is best understood in terms of a single magma that was divided into two zones distinguished solely by zircon stability but simultaneously crystallizing major phases. Initially the upper part was

saturated in zircon, whereas temperatures in the lower parts were too high for zircon saturation. After the caldera-forming eruption, the hotter remnant magma and its crystal cargo rose as a result of the lithostatic disequilibrium created by the caldera formation and cooled below zircon saturation. As this "resurgent" intrusion moved into the zircon stability field, new zircons crystallized, and remaining magma from the caldera forming eruption mixed in, explaining the few antecrysts from the pre-climactic population. The Northern Post-Climactic Domes (Cerro Aguas Calientes and Pabellon Cachi Laguna), containing only post-climactic aged zircon, mark effusive leaks from this resurgent intrusion. The distinct zircon populations in otherwise chemically homogeneous magma suggest that the post-climactic zircon population followed the same crystallization sequence as during the pre-climactic magma stage: a corollary of lithostatic, thermal, and bulk chemical environments of the system remaining essentially unchanged. The textural "maturity" of the domes implies a more advanced stage of crystallization than the climactic magma, with final solidification being recorded in the granodiorite clasts. The protracted magmatic lifetime of >1 Myr. from accumulation to solidification, is consistent with the understanding that large-volume silicic caldera systems assemble and evolve over long time scales (Smith, 1979; Reid, 2003; Wotzlaw et al., 2013). In the Central Andes, we see these systems as being open at depth and being maintained by recharge (e.g. de Silva et al., 2006). Moreover, a thermally mature crust, prepared by millions of years of magmatism leads to long thermal lifetimes of these systems (de Silva and Gosnold, 2007). Recharge is a driving force during resurgence at many systems (Marsh, 1984; Kennedy et al., 2012) and is certainly operating, but in the APVC it is "cryptic" in the sense that it does not result in major chemical and thermal excursions in

the upper eruptible parts of the system. At much deeper levels than represented by any of our samples, recharge by andesitic or more mafic parental magmas are the crucial heat engine that keeps the dacitic upper crustal magmas thermally viable. Volumetrically insignificant andesitic and mixed pumices and andesitic enclaves are found in almost every major crystal-rich dacitic ignimbrite in the region, and the final trigger for eruption might come from a recharge event that tips the system over an eruption triggering threshold (Gregg et al., 2012). However, the dominance of crystal-rich dacite of 65 to 68% SiO_2 and temperatures ranging from 750 to 850 °C over almost 10 Ma of activity indicate large magma reservoirs where the upper parts are buffered thermally and compositionally (de Silva et al., 2006). This is the magmatic environment being recorded by zircons in the PGI volcano-plutonic system.

Cyclicity of the PGCC Magmatic System

Though the zircon data support an older Chuhuilla eruption age than previously reported (Salisbury et al., 2011; this Thesis), the entire U-Pb zircon age range is older than the climactic eruption of the Chuhuilla ignimbrite. This age distribution is in stark contrast to that of the Pastos Grandes cycle. Instead of being distributed around the climactic eruption age, the ignimbrite, the lavas of Serrania Khenwal (post-climactic lavas), and the granodiorite clasts all represent pre-climactic magma. We propose that, instead of the granodiorite clasts representing late-stage remnant magma crystallization, they were part of a carapace of the plutonic system that crystallized prior to the eruption of the Chuhuilla ignimbrite. These clasts represent the side or the roof of the magma reservoir that got recycled as accidental clasts during the Pastos Grandes cycle, getting entrained in the intracaldera facies of the resurgent dome. Any post-climactic magmatism following

the Chuhuilla cycle likely would have been recorded in zircons as was the case for the Pastos Grandes cycle; however, the zircons would have been resorbed during the prolonged pre-climactic magma stage of the Pastos Grandes cycle. The result is a zircon geochronology record with two distinct pulses of activity coinciding with each cycle of caldera-forming volcanism (Figure S4.3).

The trace trends suggest constant chemical conditions in the 1.3 Myr leading up to the ChI eruption. When combined with the zircon chronochemistry of the Pastos Grandes cycle, it becomes apparent that volcanism in the PGCC reflects discrete pulses of magmatism in the shallow crust. Though separated by nearly 2 Myr, each of these magmatic cycles experienced the same chemical and thermal conditions. This prolonged homogeneity is a reflection of the storage and processing conditions of the regional magmatic system under the APVC.

Conclusions

Zircon chronochemistry reveals protracted episodes of homogenous magmatism punctuated by climactic, caldera-forming eruptions. The zircon record associated with each caldera cycle is on the order of 1 Myr, however only the pre-climactic record is preserved for the older, Chuhuilla cycle. Zircon crystallization ages and chemistry from pumice, lava, and plutonic clasts associated with the 2.89 Ma PGI supereruption reveal ~1.1 Myr. of continuous magmatic evolution. These data connote a single, long-lived dacite magma reservoir that was chemically-buffered but partitioned by zircon stability that produced two successive populations of zircons during pre- and post-climactic evolution. This model is supported by the chemical homogeneity and progressive textural maturity from the ignimbrite, through the Post-Climactic Domes, to the cogenetic

granodiorite clasts. Together, these magmatic stages account not only for the accumulation stage of magma that was interrupted by climactic eruption, but also for an equally long post-climactic stage of resurgence to pluton solidification. Therefore we define "magma residence" for the PGI supereruption magma as extending from accumulation to solidification.

Acknowledgements

This work was enabled by support from National Science Foundation grant EAR 0838536 and 0908324. The ion microprobe facility at the University of California– Los Angeles (UCLA) is partly supported by a grant from the Instrumentation and Facilities Program, Division of Earth Sciences, National Science Foundation.

References

Bachmann, O., Miller, C. F., & de Silva, S. L. (2007). The volcanic–plutonic connection as a stage for understanding crustal magmatism. *Journal of Volcanology and Geothermal Research*, *167*(1), 1-23.

Boehnke, P., Watson, E. B., Trail, D., Harrison, T. M., & Schmitt, A. K. (2013). Zircon saturation re-revisited. *Chemical Geology*, *351*, 324-334.

Claiborne, L. L., Miller, C. F., Walker, B. A., Wooden, J. L., Mazdab, F. K., & Bea, F. (2006). Tracking magmatic processes through Zr/Hf ratios in rocks and Hf and Ti zoning in zircons: an example from the Spirit Mountain batholith, Nevada. *Mineralogical Magazine*, *70*(5), 517-543.

de Silva, S. L. (1989). Altiplano-Puna volcanic complex of the central Andes. *Geology*, *17*(12), 1102-1106.

de Silva, S., Zandt, G., Trumbull, R., Viramonte, J. G., Salas, G., & Jiménez, N. (2006). Large ignimbrite eruptions and volcano-tectonic depressions in the Central Andes: a thermomechanical perspective. *Geological Society, London, Special Publications*, *269*(1), 47-63.

de Silva, S. L., & Gosnold, W. D. (2007). Episodic construction of batholiths: Insights from the spatiotemporal development of an ignimbrite flare-up. *Journal of Volcanology and Geothermal Research*, *167*(1), 320-335.

Eichelberger, J. C., Izbekov, P. E., & Browne, B. L. (2006). Bulk chemical trends at arc volcanoes are not liquid lines of descent. *Lithos*, *87*(1), 135-154.

Ghiorso, M. S., & Gualda, G. A. (2013). A method for estimating the activity of titania in magmatic liquids from the compositions of coexisting rhombohedral and cubic iron–titanium oxides. *Contributions to Mineralogy and Petrology*,*165*(1), 73-81.

Glazner, A. F., Bartley, J. M., Coleman, D. S., Gray, W., & Taylor, R. Z. (2004). Are plutons assembled over millions of years by amalgamation from small magma chambers?. *GSA today*, *14*(4/5), 4-12.

Glazner, A. F., Coleman, D. S., & Bartley, J. M. (2008). The tenuous connection between high-silica rhyolites and granodiorite plutons. *Geology*,*36*(2), 183-186.

Green, T. H., & Pearson, N. J. (1986). Ti-rich accessory phase saturation in hydrous mafic-felsic compositions at high P, T. *Chemical Geology*, *54*(3), 185-201.

Gregg, P. M., De Silva, S. L., Grosfils, E. B., & Parmigiani, J. P. (2012). Catastrophic caldera-forming eruptions: Thermomechanics and implications for eruption triggering and maximum caldera dimensions on Earth. *Journal of Volcanology and Geothermal Research*, *241*, 1-12.

Hildreth, W. (2004). Volcanological perspectives on Long Valley, Mammoth Mountain, and Mono Craters: several contiguous but discrete systems. *Journal of Volcanology and Geothermal Research*, *136*(3), 169-198.

Kennedy, B., Wilcock, J., & Stix, J. (2012). Caldera resurgence during magma replenishment and rejuvenation at Valles and Lake City calderas. *Bulletin of volcanology*, *74*(8), 1833-1847.

Lipman, P. W. (2007). Incremental assembly and prolonged consolidation of Cordilleran magma chambers: Evidence from the Southern Rocky Mountain volcanic field. *Geosphere*, *3*(1), 42-70.

Liu, Y., Hu, Z., Zong, K., Gao, C., Gao, S., Xu, J., & Chen, H. (2010). Reappraisement and refinement of zircon U-Pb isotope and trace element analyses by LA-ICP-MS. *Chinese Science Bulletin*, *55*(15), 1535-1546.

Ludwig, K. R. (2008). *User's manual for Isoplot 3.17: a geochronological toolkit for Microsoft Excel* (No. 4). Kenneth R. Ludwig.

Mahon, K. I. (1996). The New "York" regression: Application of an improved statistical method to geochemistry. *International Geology Review*, *38*(4), 293-303.

Marsh, B. D. (1984). On the mechanics of caldera resurgence. *Journal of Geophysical Research: Solid Earth (1978–2012)*, *89*(B10), 8245-8251.

Miller, J. S., & Wooden, J. L. (2004). Residence, resorption and recycling of zircons in Devils Kitchen rhyolite, Coso Volcanic field, California. *Journal of Petrology*, *45*(11), 2155-2170.

Paces, J. B., & Miller, J. D. (1993). Precise U-Pb ages of Duluth Complex and related mafic intrusions, northeastern Minnesota: Geochronological insights to physical, petrogenetic, paleomagnetic, and tectonomagmatic processes associated with the 1.1 Ga Midcontinent Rift System. *Journal of Geophysical Research: Solid Earth (1978–2012)*, *98*(B8), 13997-14013.

Reid, M. R. (2003). Timescales of magma transfer and storage in the crust.*Treatise on geochemistry*, *3*, 167-193.

Reid, M. R., Coath, C. D., Mark Harrison, T., & McKeegan, K. D. (1997). Prolonged residence times for the youngest rhyolites associated with Long Valley Caldera: ^{230}Th—^{238}U ion microprobe dating of young zircons. *Earth and Planetary Science Letters*, *150*(1), 27-39.

Reid, M. R., Vazquez, J. A., & Schmitt, A. K. (2011). Zircon-scale insights into the history of a Supervolcano, Bishop Tuff, Long Valley, California, with

implications for the Ti-in-zircon geothermometer. *Contributions to Mineralogy and Petrology*, *161*(2), 293-311.

Salisbury, M. J., Jicha, B. R., de Silva, S. L., Singer, B. S., Jiménez, N. C., & Ort, M. H. (2011). $^{40}Ar/^{39}Ar$ chronostratigraphy of Altiplano-Puna volcanic complex ignimbrites reveals the development of a major magmatic province. *Geological Society of America Bulletin*, *123*(5-6), 821-840.

Sambridge, M. S., & Compston, W. (1994). Mixture modeling of multi-component data sets with application to ion-probe zircon ages. *Earth and Planetary Science Letters*, *128*(3), 373-390.

Smith, R. L., & Bailey, R. A. (1968). Resurgent cauldrons. *Geological Society of America Memoirs*, *116*, 613-662.

Tappa, M. J., Coleman, D. S., Mills, R. D., & Samperton, K. M. (2011). The plutonic record of a silicic ignimbrite from the Latir volcanic field, New Mexico.*Geochemistry, Geophysics, Geosystems*, *12*(10).

Watson, E. B. (1996). Dissolution, growth and survival of zircons during crustal fusion: kinetic principals, geological models and implications for isotopic inheritance. *Transactions of the Royal Society of Edinburgh: Earth Sciences*,*87*(1-2), 43-56.

Watson, E. B., Wark, D. A., & Thomas, J. B. (2006). Crystallization thermometers for zircon and rutile. *Contributions to Mineralogy and Petrology*,*151*(4), 413-433.

Watts, R. B., de Silva, S. L., de Rios, G. J., & Croudace, I. (1999). Effusive eruption of viscous silicic magma triggered and driven by recharge: a case study of the Cerro Chascon-Runtu Jarita Dome Complex in Southwest Bolivia.*Bulletin of volcanology*, *61*(4), 241-264.

Wotzlaw, J. F., Schaltegger, U., Frick, D. A., Dungan, M. A., Gerdes, A., & Günther, D. (2013). Tracking the evolution of large-volume silicic magma reservoirs from assembly to supereruption. *Geology*, *41*(8), 867-870.

Zimmerer, M. J., & McIntosh, W. C. (2012). The geochronology of volcanic and plutonic rocks at the Questa caldera: Constraints on the origin of caldera-related silicic magmas. *Geological Society of America Bulletin*, *124*(7-8), 1394-1408.

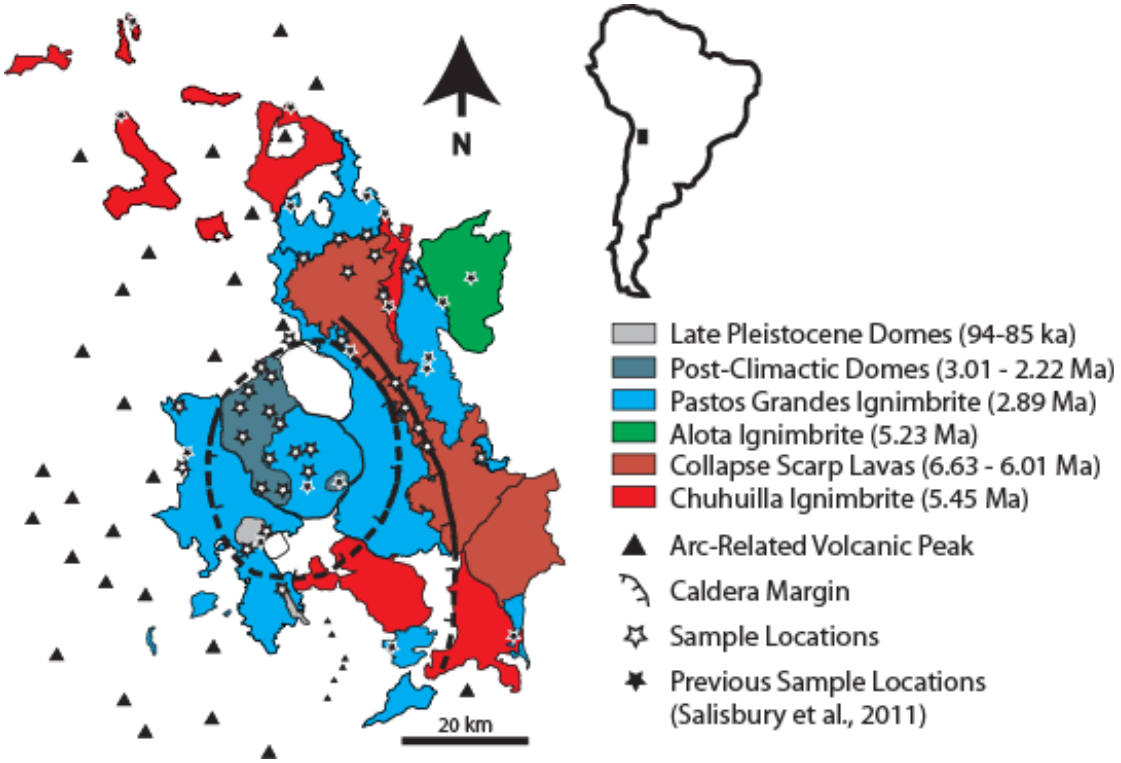

Figure 4.1. Geologic Map of the Pastos Grandes Caldera Complex highlighting the deposits of the caldera-forming eruptions. The deposits include both the large-volume ignimbrites as well as the post-climactic lavas and domes such as the suite along Serrania Khenwal, and the Post-Climactic Dome Complex in the Pastos Grandes Calddera (Cerro Aguas Calientes to the North, Cerro Pabellon Cachi Laguna in the middle, and Cerro Arenal to the South). The resurgent dome and Cerro Chascon, both of which are located in the Pastos Grandes caldera, host granodiorite clasts (RDG and CCG respectively).

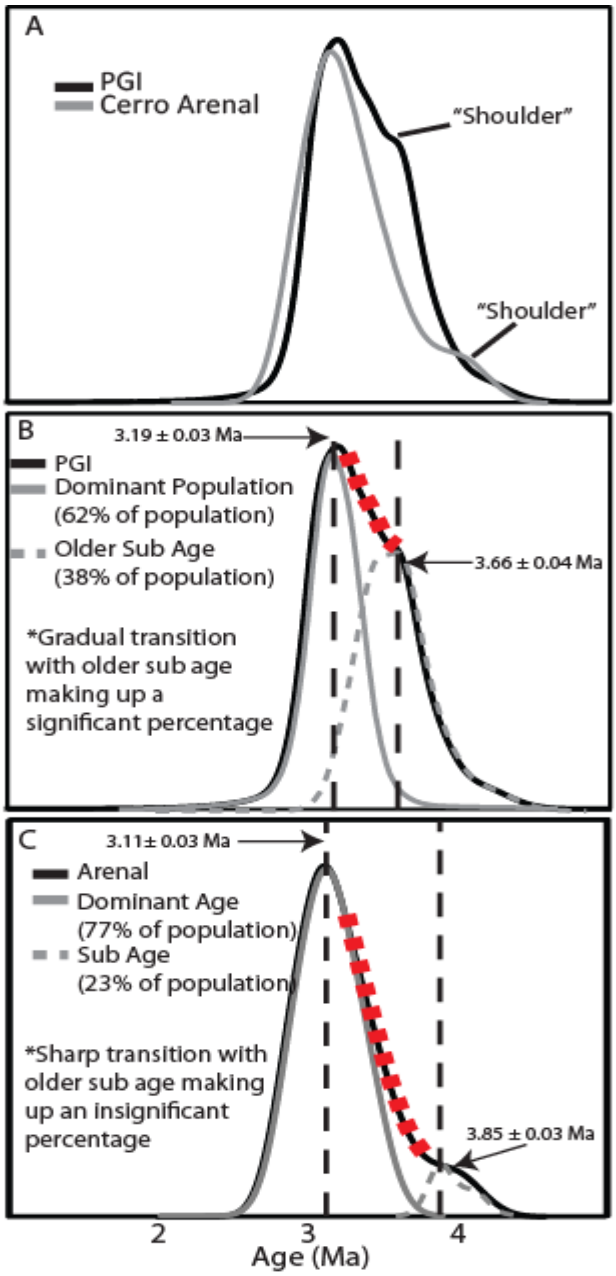

Figure 4.2. Examples of probability density curves for the PGI and SPCD. A) The composite curves for both the PGI and the SPCD. "Shoulders" on the older extent of the population represent subsets in the data identified by the unmixing algorithm. B) The probability density curves for the two sub populations identified in the PGI by the unmixing algorithm. In this example the transition (red dashed line) from the dominant young population and the older subpopulation is gradual as the old sub-population makes up a statistically significant percentage (38%) of the PGI analyses. C) The probability density curves for the two sub populations identified in the SPCD by the unmixing algorithm. In this example the transition (red dashed line) from the dominant young population and the older sub-population is sharp as the old sub population makes up only 23% of the SPCD analyses. This sub-population is the oldest of the study and is considered here as statistically insignificant.

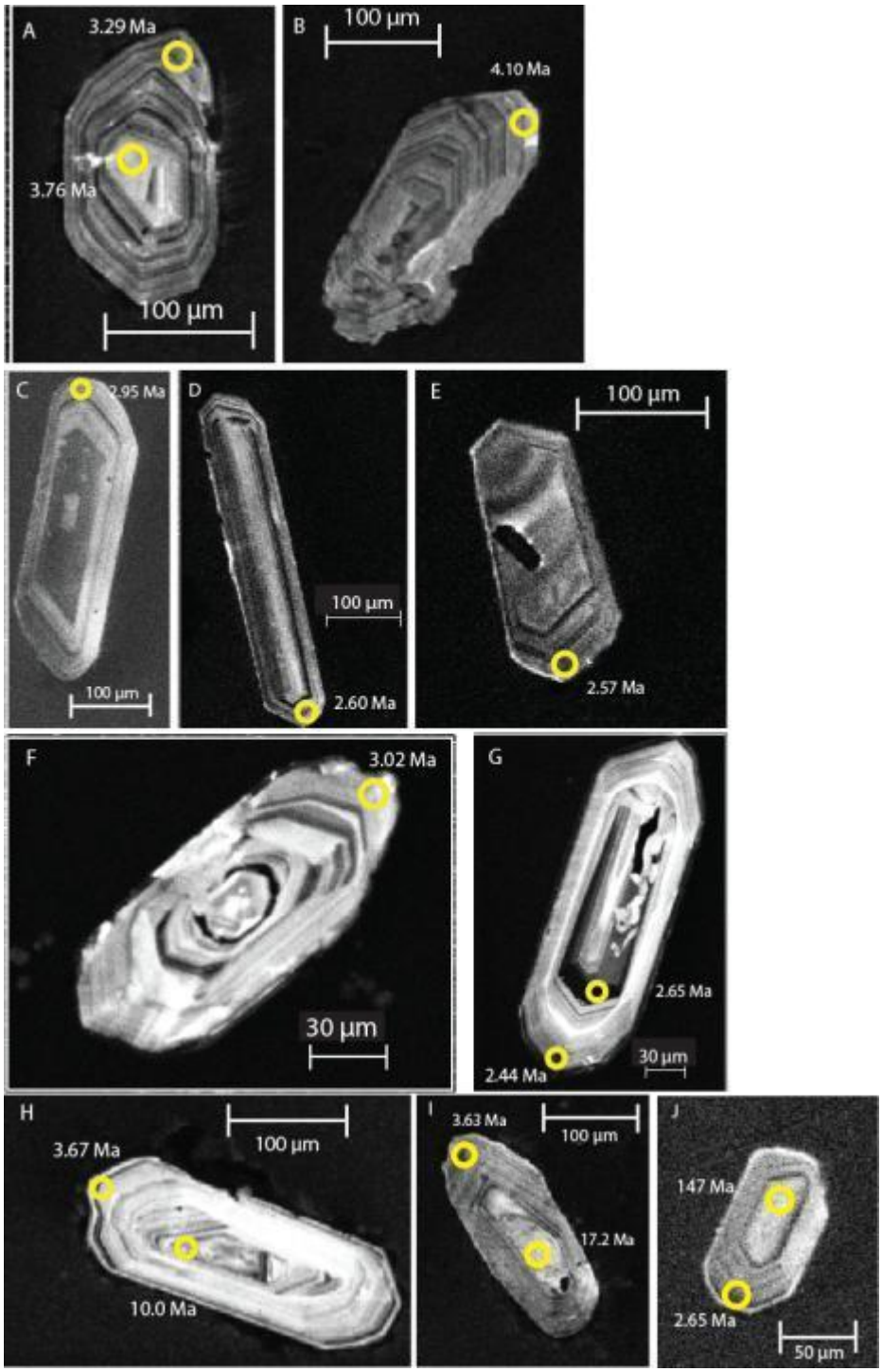

Figure 4.3. Representative cathodoluminescence 93 images of zircon crystals from each of the samples. A & B from the Pastos Grandes Ignimbrite. While most analyses represent rim ages, core/rim pairs were compared in selected crystals. C, D, & E from the South, Middle and North Post-Climactic Dome resepectively. F & G from the plutonic clasts. H, I, & J Illustrate the xenocrystic cores that make up roughly 2% of the total population.

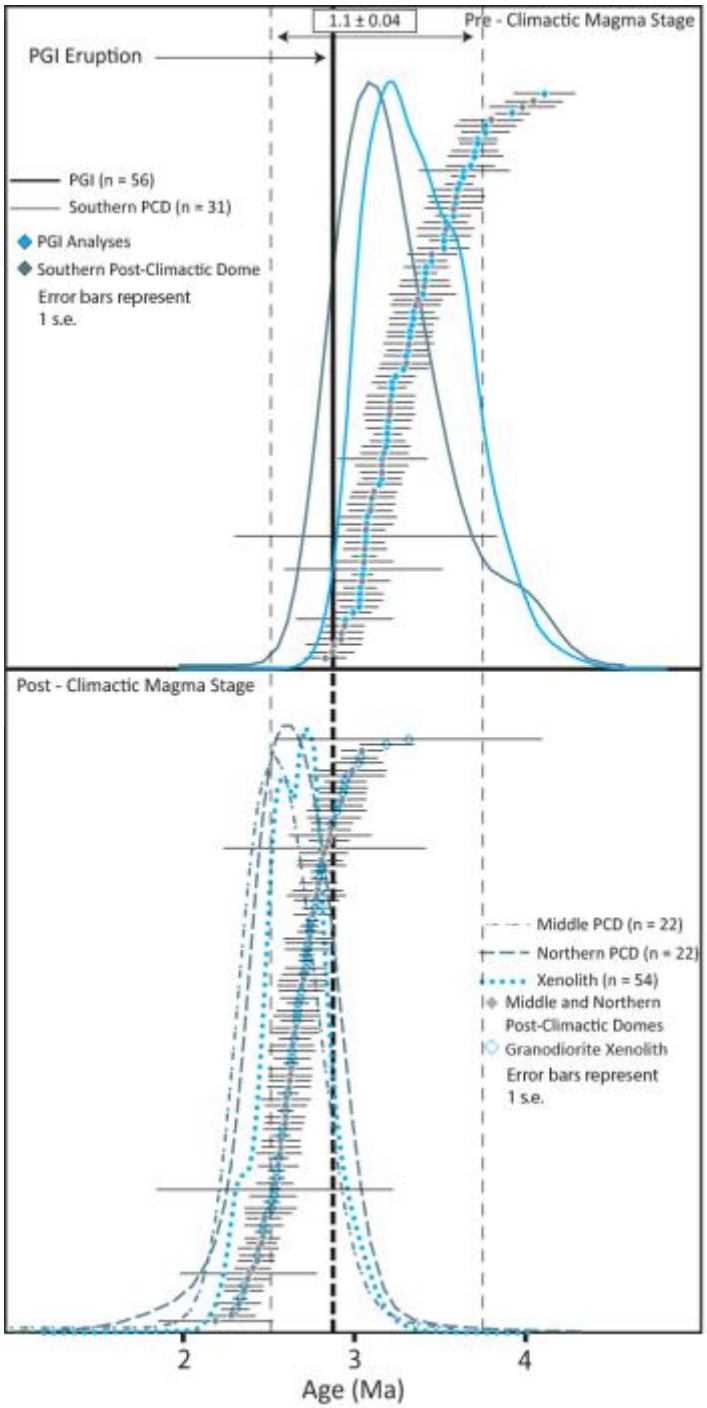

Figure 4.4. Probability density curves and ranked order plot for PGI, three Post-Climactic Domes, and granodiorite clasts zircons (n = 186). The PGI (Zircon age: 3.19 ± 0.04 Ma) and the South Post-Climactic Dome (Zircon age: 3.11 ± 0.03 Ma) make up the pre-climactic magma stage. The Middle (Zircon age: 2.51± 0.04 Ma) and Northern (2.54 ± 0.05 Ma) Post-Climactic Domes as well as the granodiorite (2.63 ± 0.01 Ma) contain similar zircon age populations in the post-climactic magma stage. All errors are 1 sigma.

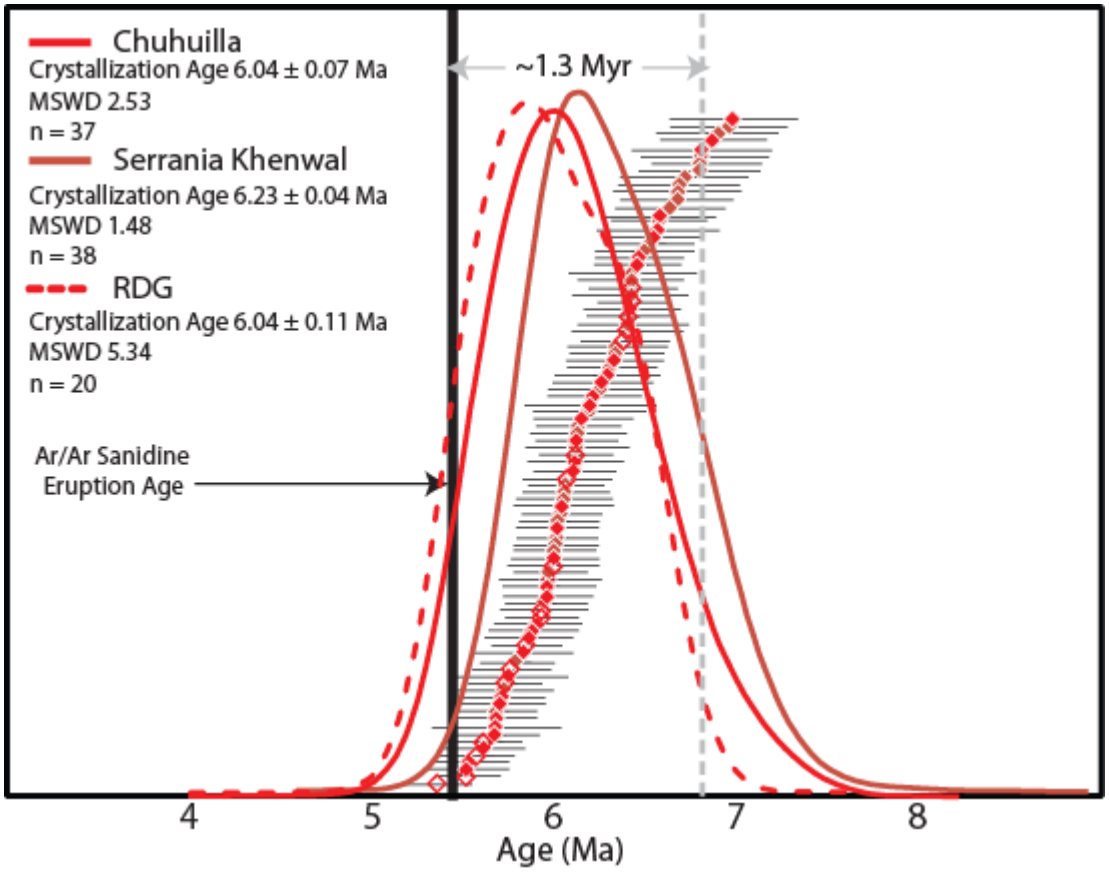

Figure 4.4 Continued. Probability density curves and ranked order plot for the Chuhuilla ignimbrite, Serrania Khenwal Lavas, and granodiorite recovered from the resurgent dome of the Pastos Grandes Caldera. In contrast to the Pastos Grandes cycle all samples yielded zircons with pre-climactic populations ages (6.04 – 6.23 Ma) and a total zircon crystallization of ~1.3 Myr.

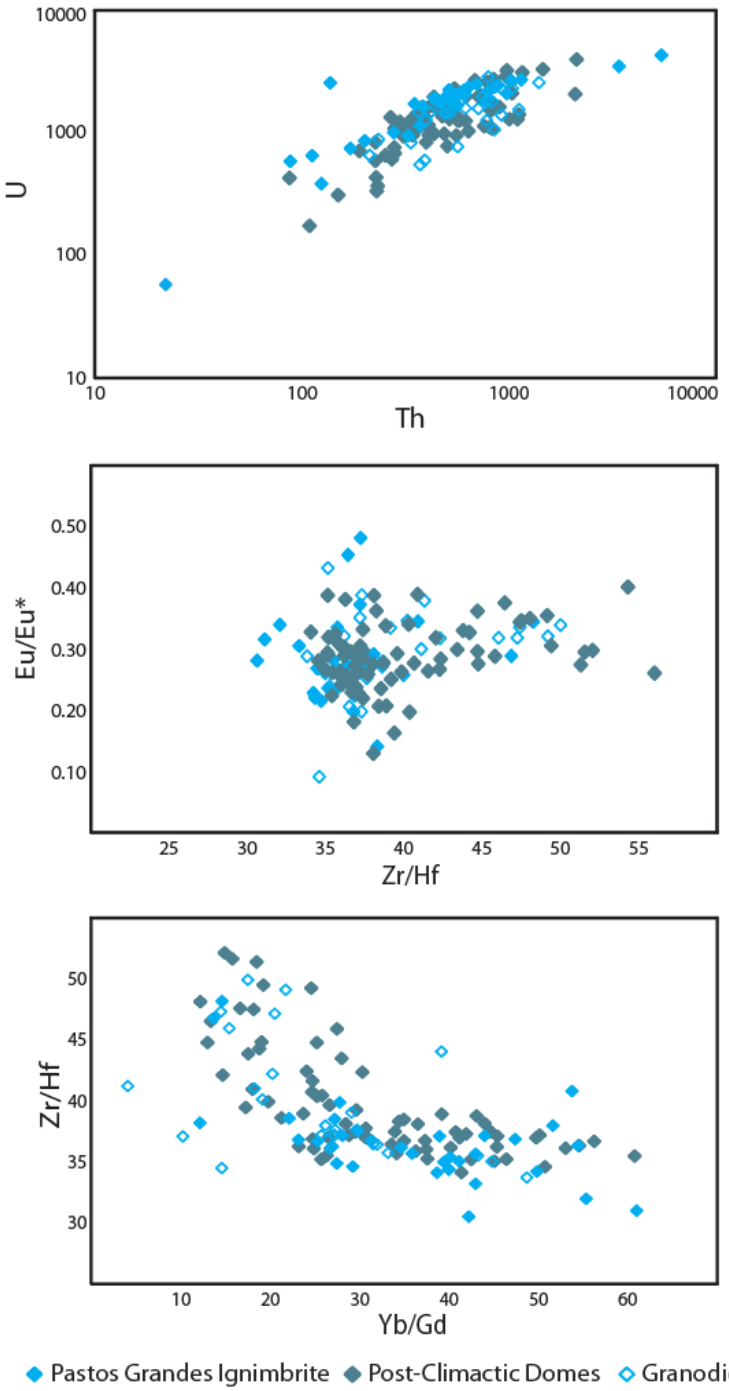

Figure 4.5. Zircon trace element variation diagrams for pre- and post- climactic rocks. Log scale Th vs U diagram. Zircons from samples representing both pre and post-climactic activity overlap. Zr/Hf vs Eu/Eu* shows the same diffuse pattern in pre and post-climactic samples. The measure of the Eu anomaly reflects the affects of plagioclase fractionation as being nearly identical in the two magmatic stages. Decreasing Zr/Hf with increasing Yb/Gd suggests co-crystallization of amphibole and to a lesser extent titanite controlling MREE as zircon crystallizes.

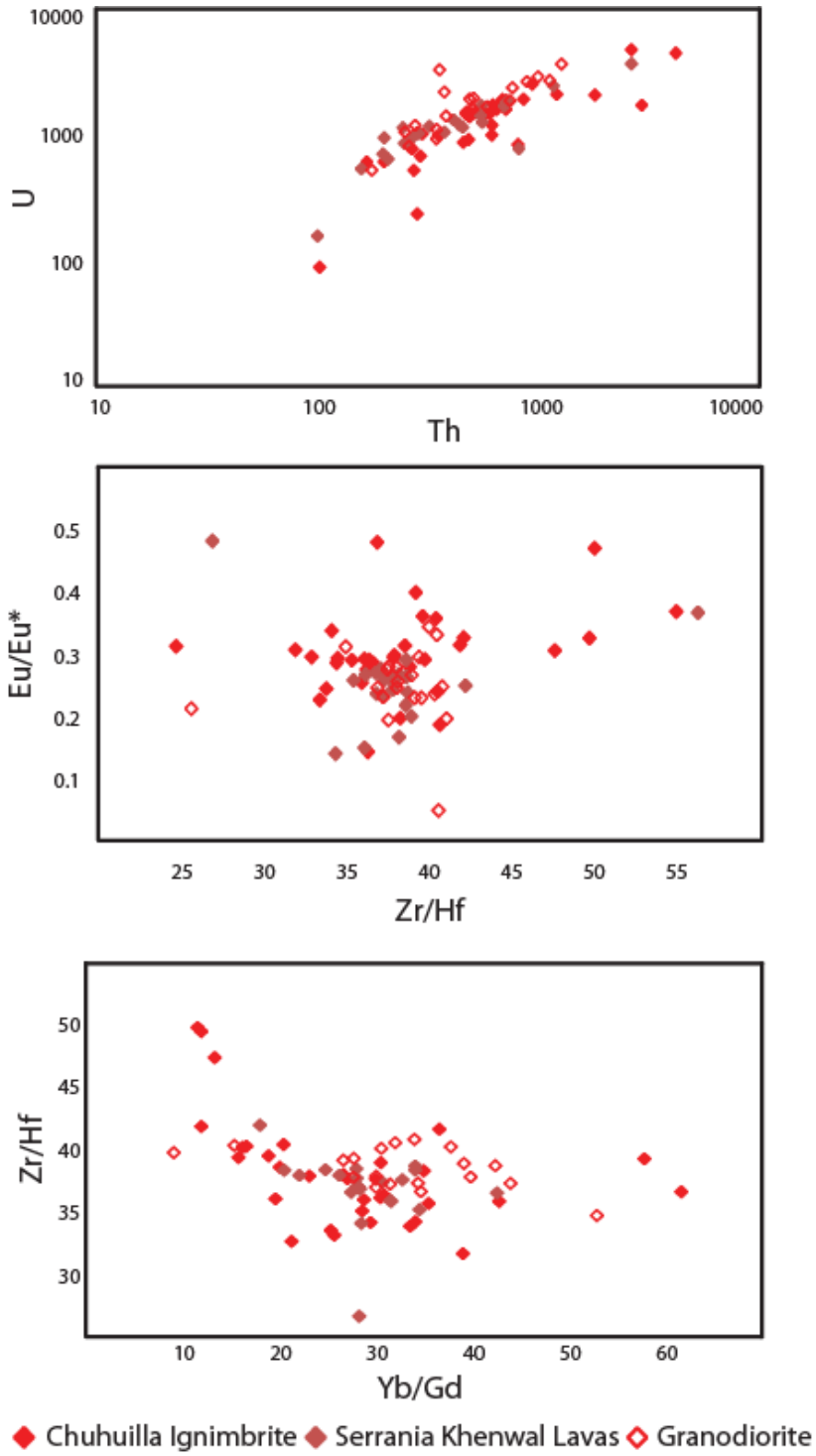

Figure 4.5 Continued. Zircon trace element variation diagrams for samples of the Chuhuilla caldera cycle. Zircons from all samples overlap with each other and with the samples of the Pastos Grandes cycle.

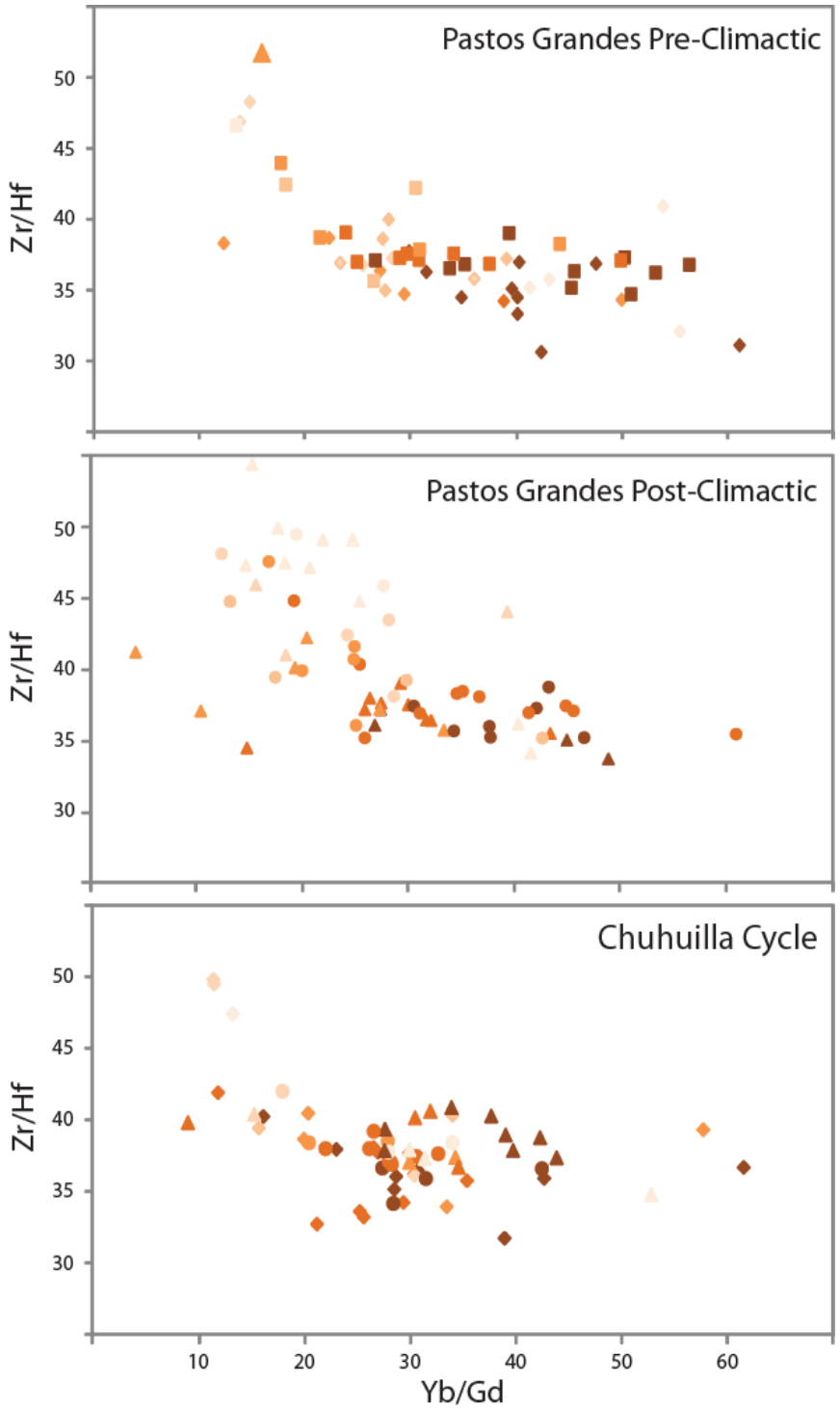

Figure 4.6. The same Yb/Gd vs Zr/Hf diagrams of Figure 4.5 now coded by modeled temperature. Lighter shades refer to higher temperature, darker shades refer to cooler temperatures. These trends corroborate the notion that the zircon compositions represent a continuum of crystallization in each magma stage.

Table 4.1. Zircon Geochronology. Samples from the PGI, C. Aguas Calientes, C. Pabellon Cachi Laguna, C. Arenal, CCG, Chuhuilla, Serrania Khenwal, and RDG are represented. Analyses with less than 90% radiogenic ^{206}Pb are not considered in the discussion of the data.

Sample/ Analysis	206Pb/ 238U Age	±1σ	238U/ 206Pb	±1σ	207Pb/ 206Pb	±1σ	% 206Pb*
PGI @1	3.29	0.14	2017	90.35	0.05	0.003	99.90
PGI @2	3.76	0.18	1729	81.87	0.06	0.006	98.26
PGI @3	3.03	0.12	2157	82.82	0.06	0.004	98.70
PGI @4	3.15	0.13	1871	70.71	0.13	0.007	88.89
PGI @5	3.16	0.11	2064	73.70	0.06	0.004	98.02
PGI @6	4.10	0.18	1594	70.60	0.05	0.003	99.01
PGI @7	3.10	0.14	2085	89.99	0.07	0.008	97.16
PGI @8	3.03	0.13	2163	93.11	0.06	0.006	98.56
PGI @9	7.55	0.32	855	36.52	0.05	0.003	99.03
PGI @10	3.19	0.14	2061	89.20	0.05	0.005	98.88
PGI @11	3.16	0.26	1189	49.66	0.39	0.010	56.58
PGI @13	3.08	0.17	1780	81.40	0.18	0.006	82.46
PGI @14	3.41	0.14	1948	80.81	0.05	0.004	100.13
PGI @15	3.59	0.16	1816	78.84	0.06	0.004	98.29
PGI @16	3.35	0.15	1948	86.54	0.06	0.003	98.37
PGI @17	3.07	0.75	444	17.67	0.67	0.011	20.46
PGI @18	3.53	0.13	1873	70.16	0.05	0.004	99.89
PGI @19	3.22	0.14	2037	89.25	0.06	0.004	98.71
PGI @20	3.52	0.15	1844	79.23	0.06	0.004	98.01
PGI @21	3.20	0.14	2044	90.22	0.06	0.004	98.54
PGI @22	3.52	0.16	1856	83.33	0.06	0.003	98.81
PGI @23	3.22	0.15	2025	56.16	0.06	0.004	93.94
PGI @24	3.05	0.06	2106	41.65	0.07	0.005	96.68
PGI @25	3.57	0.10	1814	52.33	0.06	0.004	97.78
PGI @26	3.71	0.11	1733	50.48	0.07	0.007	97.19
PGI @28	3.91	0.10	1667	43.63	0.06	0.004	98.69
PGI @29	3.00	0.10	2135	70.68	0.08	0.008	96.05
PGI @30	3.61	0.08	1797	40.05	0.06	0.003	98.47

Table 4.1. (Continued)

Sample/ Analysis	206Pb/ 238U Age	±1σ	238U/ 206Pb	±1σ	207Pb/ 206Pb	±1σ	% 206Pb*
PGI @32	3.63	0.07	1786	36.05	0.06	0.003	98.04
PGI @33	3.19	0.08	2025	49.62	0.07	0.005	97.22
PGI @34	3.06	0.08	2135	52.42	0.06	0.003	98.17
PGI @35	3.45	0.09	1894	50.92	0.06	0.004	98.57
PGI @36	3.04	0.10	2095	58.79	0.08	0.012	95.62
PGI @37	3.41	0.07	1911	39.42	0.06	0.005	98.25
PGI @38	3.52	0.09	1868	47.13	0.05	0.004	99.18
PGI @39	3.32	0.14	1938	79.62	0.07	0.005	96.93
PGI @40	3.40	0.19	1572	67.47	0.20	0.012	80.39
PGI @41	3.06	0.46	799	37.07	0.54	0.010	36.66
PGI @42	3.20	0.13	2054	82.68	0.06	0.004	98.76
PGI @43	3.35	0.12	1962	69.67	0.06	0.002	98.76
PGI @44	3.41	0.13	1894	72.07	0.07	0.003	97.37
PGI @45	3.22	0.12	2004	73.92	0.07	0.004	97.58
PGI @46	3.76	0.14	1667	60.32	0.08	0.004	95.34
PGI @47	3.19	0.10	2042	66.69	0.06	0.002	97.96
PGI @48	3.70	0.13	1764	64.1	0.05	0.002	99.22
PGI @49	3.60	0.13	1822	68.09	0.06	0.004	98.85
PGI @50	3.32	0.13	1950	74.94	0.07	0.004	97.52
PGI @51	3.06	0.12	2156	83.68	0.05	0.003	99.25
PGI @52	3.70	0.16	1746	74.72	0.07	0.005	97.43
PGI @53	3.33	0.13	1970	78.04	0.06	0.006	98.82
PGI @54	3.63	0.26	1183	51.64	0.32	0.007	64.82
PGI @55	3.24	0.12	2000	72.4	0.07	0.006	97.51
PGI @56	3.31	0.12	1966	73.45	0.06	0.004	98.02
PGI @57	3.30	0.13	1961	77.31	0.07	0.004	97.45
PGI @58	3.67	0.14	1689	61.63	0.09	0.006	94.11
PGI @59	3.22	0.09	2025	56.16	0.06	0.004	98.52

Table 4.1. (Continued)

Sample/ Analysis	206Pb/ 238U Age	±1σ	238U/ 206Pb	±1σ	207Pb/ 206Pb	±1σ	% 206Pb*
PGI @60	2.95	0.28	703	18.3	0.58	0.009	31.23
CCG @1	2.47	0.11	2641	118.54	0.07	0.007	97.53
CCG @2	2.36	0.11	2660	111.11	0.09	0.012	94.64
CCG @3	2.94	0.14	2224	106.81	0.06	0.009	98.17
CCG @4	3.51	0.14	1867	77.74	0.05	0.004	98.87
CCG @5	2.67	0.12	2407	106.00	0.08	0.008	96.20
CCG @6	2.90	0.15	2256	117.09	0.06	0.005	98.54
CCG @7	2.78	0.13	2335	110.17	0.07	0.009	97.07
CCG @8	2.58	0.11	2532	111.52	0.06	0.005	97.75
CCG @9	2.64	0.14	2451	124.35	0.07	0.007	96.61
CCG @10	2.72	0.12	2407	108.37	0.06	0.005	98.10
CCG @11	2.70	0.12	2427	111.34	0.06	0.005	98.50
CCG @12	2.44	0.10	2694	113.22	0.06	0.006	98.19
CCG @13	2.65	0.09	2447	80.86	0.05	0.003	99.11
CCG @14	2.50	0.14	2530	129.91	0.08	0.012	95.56
CCG @15	3.02	0.14	2186	103.68	0.05	0.005	98.96
CCG @16	2.89	0.17	2106	109.96	0.11	0.013	91.76
CCG @17	2.68	0.11	2436	100.29	0.06	0.004	97.87
CCG @18	2.67	0.14	2470	126.87	0.06	0.005	98.74
CCG @19	2.93	0.14	2237	104.55	0.06	0.008	98.52
CCG @20	2.80	0.14	2339	117.04	0.06	0.006	98.51
CCG @21	2.53	0.14	2530	130.55	0.07	0.011	96.40
CCG @22	2.72	0.12	2396	109.68	0.06	0.006	98.26
CCG @23	2.73	0.13	2374	109.30	0.07	0.006	97.52
CCG @24	2.69	0.13	2422	116.72	0.07	0.007	97.42
CCG @25	2.94	0.12	2228	90.81	0.06	0.005	98.31
CCG @26	2.66	0.10	2445	88.47	0.07	0.005	97.51
CCG @27	2.31	0.08	2773	93.05	0.08	0.006	95.58

Table 4.1. (Continued)

Sample/ Analysis	206Pb/ 238U Age	±1σ	238U/ 206Pb	±1σ	207Pb/ 206Pb	±1σ	% 206Pb*
CCG @28	3.03	0.11	2093	68.36	0.07	0.009	96.74
CCG @29	2.61	0.06	2458	56.92	0.08	0.008	96.01
CCG @30	3.31	0.75	255	5.35	0.73	0.011	12.82
CCG @31	2.96	0.21	1066	32.40	0.46	0.011	47.72
CCG @32	2.52	0.15	1909	71.83	0.26	0.022	72.36
CCG @33	2.86	0.12	1705	43.91	0.25	0.011	74.57
CCG @34	2.63	0.11	2388	87.80	0.09	0.011	94.82
AC @1	2.92	0.14	2229	104.80	0.06	0.005	98.44
AC @2	2.88	0.16	2181	113.16	0.09	0.009	94.90
AC @3	2.80	0.13	2322	106.20	0.06	0.006	97.88
AC @4	2.54	0.11	2617	111.64	0.05	0.005	99.63
AC @5	2.63	0.13	2444	118.31	0.08	0.007	96.06
AC @6	2.57	0.11	2549	112.41	0.06	0.005	98.32
AC @7	2.85	0.12	2306	94.68	0.06	0.003	98.54
AC @8	2.39	0.39	2787	468.40	0.05	0.011	99.26
AC @9	2.20	0.33	3018	465.56	0.06	0.004	98.81
AC @10	2.62	0.12	2469	108.52	0.07	0.007	96.89
AC @11	2.78	0.15	2285	112.22	0.08	0.013	95.50
AC @12	2.76	0.11	2404	100.59	0.05	0.004	99.56
AC @13	2.66	0.13	2375	112.84	0.09	0.009	94.91
AC @14	2.46	0.08	2630	87.17	0.07	0.006	97.46
AC @15	2.78	0.17	1695	70.41	0.28	0.004	70.68
AC @16	2.33	0.14	2626	139.99	0.12	0.013	90.99
AC @17	2.74	0.14	2290	112.21	0.09	0.013	94.41
AC @18	2.83	0.58	1329	118.06	0.39	0.034	56.43
AC @19	2.57	0.11	2513	106.11	0.07	0.009	96.98
AC @20	2.44	0.11	2643	122.28	0.07	0.007	96.41
AC @21	2.86	0.24	1473	73.38	0.33	0.012	63.17

Table 4.1. (Continued)

Sample/ Analysis	206Pb/ 238U Age	±1σ	238U/ 206Pb	±1σ	207Pb/ 206Pb	±1σ	% 206Pb*
AC @22	2.60	0.12	2516	114.61	0.06	0.008	98.21
PCL @1	2.70	0.14	2406	123.32	0.06	0.008	97.85
PCL @2	2.86	0.12	2293	95.13	0.06	0.005	98.26
PCL @3	2.43	0.11	2643	116.69	0.08	0.006	96.10
PCL @4	2.64	0.12	2430	108.02	0.08	0.008	95.87
PCL @5	2.69	0.14	2350	117.09	0.08	0.008	95.19
PCL @6	2.82	0.14	2288	114.15	0.07	0.009	96.95
PCL @7	2.79	0.11	2358	91.78	0.06	0.008	98.74
PCL @8	2.62	0.13	2455	116.34	0.07	0.007	96.47
PCL @9	2.60	0.14	2380	112.19	0.10	0.017	93.12
PCL @10	2.29	0.14	2771	162.00	0.09	0.011	94.41
PCL @11	2.48	0.10	2690	110.02	0.05	0.005	99.76
PCL @12	2.36	0.11	2401	95.12	0.17	0.009	84.69
PCL @13	2.63	0.12	2473	116.79	0.07	0.005	97.32
PCL @14	2.57	0.13	2477	116.58	0.09	0.013	94.94
PCL @15	2.41	0.10	2690	113.57	0.07	0.007	96.75
PCL @16	2.60	0.11	2509	107.00	0.07	0.005	97.43
PCL @17	2.60	0.12	2484	111.67	0.07	0.006	96.55
PCL @18	2.65	0.14	2362	121.66	0.10	0.008	93.65
PCL @19	2.38	0.13	2651	127.21	0.08	0.018	95.18
PCL @20	2.98	0.20	2157	140.11	0.07	0.007	96.62
PCL @21	2.47	0.10	2608	104.03	0.07	0.007	96.42
PCL @22	2.56	0.11	2528	108.68	0.07	0.010	96.96
Arenal @1	3.06	0.17	2120	111.46	0.07	0.018	97.31
Arenal @2	3.37	0.14	1952	81.16	0.05	0.003	99.12
Arenal @3	3.36	0.14	1926	81.58	0.07	0.005	97.31
Arenal @4	3.41	0.15	1928	85.45	0.05	0.004	99.02
Arenal @5	3.45	0.14	1858	76.67	0.07	0.005	96.68

Table 4.1. (Continued)

Sample/ Analysis	206Pb/ 238U Age	±1σ	238U/ 206Pb	±1σ	207Pb/ 206Pb	±1σ	% 206Pb*
Arenal @6	2.88	0.16	1802	72.45	0.21	0.014	78.84
Arenal @7	3.97	0.19	1658	81.63	0.05	0.003	99.77
Arenal @8	3.17	0.14	2010	86.46	0.08	0.005	96.10
Arenal @9	2.88	0.13	2291	105.54	0.05	0.006	99.07
Arenal @10	3.10	0.13	2132	89.56	0.05	0.004	99.21
Arenal @11	3.30	0.15	1996	94.42	0.05	0.005	99.16
Arenal @12	3.06	0.12	2156	88.33	0.05	0.004	99.29
Arenal @13	3.21	0.15	2069	98.04	0.05	0.005	99.83
Arenal @14	3.57	0.17	1828	84.92	0.06	0.005	98.59
Arenal @15	2.84	0.12	2225	90.08	0.09	0.007	94.57
Arenal @16	3.21	0.14	2048	89.37	0.05	0.005	98.98
Arenal @17	3.21	0.14	2028	88.39	0.06	0.005	97.94
Arenal @18	3.16	0.15	2036	96.15	0.07	0.005	97.58
Arenal @19	3.32	0.14	1970	85.38	0.06	0.004	98.52
Arenal @20	3.16	0.13	2085	85.65	0.05	0.004	99.18
Arenal @21	3.79	0.19	1577	70.16	0.12	0.007	90.74
Arenal @22	4.04	0.16	1628	66.80	0.05	0.005	99.59
Arenal @23	3.59	0.16	1848	87.06	0.04	0.003	100.17
Arenal @24	3.05	0.16	2059	100.93	0.08	0.006	95.65
Arenal @25	2.93	0.13	2240	97.86	0.06	0.004	98.46
Arenal @26	3.53	0.17	1863	89.92	0.05	0.004	99.11
Arenal @27	3.07	0.11	2157	81.39	0.05	0.003	99.56
Arenal @28	3.12	0.13	2066	87.05	0.07	0.005	96.93
Arenal @29	2.95	0.11	2241	86.85	0.05	0.004	99.31
Arenal @30	3.10	0.13	2128	90.99	0.05	0.004	99.25
Arenal @31	2.93	0.13	2242	101.05	0.06	0.006	98.50
Chu @1	6.47	0.23	1000	36	0.0523	0.002	99.2
Chu @2	6.47	0.24	996	37	0.0548	0.003	98.9

Table 4.1. (Continued)

Sample/ Analysis	206Pb/ 238U Age	±1σ	238U/ 206Pb	±1σ	207Pb/ 206Pb	±1σ	% 206Pb*
Chu @3	~~7.21~~	~~1.13~~	~~332~~	~~16~~	~~0.5418~~	~~0.008~~	~~36.6~~
Chu @4	6.82	0.39	934	51	0.0661	0.012	97.5
Chu @5	5.53	0.22	1175	46	0.0536	0.004	99.0
Chu @6	5.97	0.28	1086	51	0.0534	0.004	99.1
Chu @7	6.30	0.29	1032	47	0.0505	0.004	99.4
Chu @8	5.91	0.24	1104	45	0.0484	0.003	99.7
Chu @9	5.68	0.23	1137	47	0.0571	0.003	98.6
Chu @10	5.54	0.21	1166	43	0.0584	0.008	98.4
Chu @11	6.16	0.26	1042	44	0.0615	0.004	98.0
Chu @12	6.27	0.28	1042	46	0.0476	0.003	99.8
Chu @13	5.97	0.25	1082	45	0.0564	0.003	98.7
Chu @14	6.22	0.25	1034	41	0.0591	0.006	98.4
Chu @15	5.89	0.25	1095	46	0.0585	0.004	98.4
Chu @16	~~6.20~~	~~0.36~~	~~891~~	~~41~~	~~0.1665~~	~~0.014~~	~~84.6~~
Chu @17	6.01	0.24	1073	42	0.0591	0.003	98.4
Chu @18	6.05	0.27	1053	45	0.0676	0.003	97.3
Chu @19	~~7.24~~	~~1.77~~	~~444~~	~~40~~	~~0.4431~~	~~0.031~~	~~49.3~~
Chu @20	6.99	0.35	929	46	0.0475	0.004	99.8
Chu @21	6.59	0.30	978	45	0.0553	0.004	98.8
Chu @22	5.69	0.36	1101	66	0.0773	0.011	96.0
Chu @23	5.97	0.26	1088	47	0.0519	0.003	99.3
Chu @24	5.69	0.22	1131	44	0.0609	0.002	98.1
Chu @25	6.11	0.22	1062	39	0.0526	0.002	99.2
Chu @26	6.56	0.26	984	39	0.0566	0.004	98.7
Chu @27	5.71	0.24	1141	49	0.0516	0.004	99.3
Chu @28	6.13	0.23	1056	39	0.0534	0.004	99.1
Chu @29	6.43	0.26	1002	41	0.0581	0.002	98.5
Chu @30	6.34	0.27	1009	42	0.0641	0.003	97.7

Table 4.1. (Continued)

Sample/ Analysis	206Pb/ 238U Age	±1σ	238U/ 206Pb	±1σ	207Pb/ 206Pb	±1σ	% 206Pb*
Chu @31	5.72	0.22	1133	44	0.0542	0.003	99.0
Chu @32	6.88	0.29	943	40	0.0513	0.002	99.3
Chu @33	5.87	0.24	1099	44	0.0583	0.004	98.5
Chu @34	6.12	0.26	1044	44	0.0653	0.005	97.5
Chu @35	6.58	0.33	970	48	0.0632	0.008	97.8
Chu @36	5.62	0.22	1156	46	0.0526	0.004	99.2
Chu @37	~~5.75~~	~~0.32~~	~~842~~	~~33~~	~~0.2505~~	~~0.007~~	~~73.9~~
Chu @38	5.83	0.27	1011	42	0.1241	0.006	90.0
Chu @39	5.24	0.22	1229	51	0.0554	0.004	98.8
Chu @40	6.02	0.23	1050	39	0.0717	0.004	96.7
SK @1	6.35	0.25	1027	40	0.0493	0.003	99.6
SK @2	5.69	0.21	1143	43	0.0521	0.003	99.2
SK @3	6.07	0.24	1073	43	0.0507	0.003	99.4
SK @4	6.01	0.22	1077	39	0.0549	0.004	98.9
SK @5	7.18	0.29	854	31	0.0942	0.009	93.9
SK @6	6.14	0.26	1055	44	0.0542	0.003	99.0
SK @7	6.54	0.26	988	40	0.0553	0.004	98.8
SK @8	6.20	0.31	961	42	0.1163	0.009	91.0
SK @9	6.14	0.24	984	34	0.1070	0.007	92.2
SK @10	6.13	0.28	1029	45	0.0747	0.006	96.3
SK @11	6.69	0.31	974	46	0.0486	0.004	99.7
SK @12	6.81	0.34	933	45	0.0675	0.005	97.3
SK @13	6.51	0.28	978	41	0.0670	0.005	97.3
SK @14	6.66	0.29	970	42	0.0527	0.003	99.2
SK @15	5.95	0.23	1094	42	0.0499	0.003	99.5
SK @16	6.02	0.23	1082	41	0.0495	0.004	99.6
SK @17	6.44	0.30	996	46	0.0609	0.004	98.1
SK @18	6.44	0.27	951	37	0.0950	0.005	93.8

Table 4.1. (Continued)

Sample/ Analysis	206Pb/ 238U Age	±1σ	238U/ 206Pb	±1σ	207Pb/ 206Pb	±1σ	% 206Pb*
SK @19	7.85	0.39	742	30	0.1297	0.014	89.3
SK @20	6.97	0.32	859	35	0.1106	0.009	91.8
SK @21	5.73	0.26	1053	42	0.1091	0.011	92.0
SK @22	6.04	0.22	1062	38	0.0618	0.004	98.0
SK @23	~~6.92~~	~~0.80~~	~~532~~	~~26~~	~~0.3887~~	~~0.023~~	~~56.2~~
SK @24	6.41	0.28	974	40	0.0824	0.007	95.4
SK @25	6.81	0.27	907	33	0.0891	0.008	94.5
SK @26	6.02	0.23	1023	37	0.0931	0.007	94.0
SK @27	5.98	0.20	1048	32	0.0813	0.009	95.5
SK @28	6.59	0.23	950	31	0.0804	0.008	95.6
SK @29	~~6.70~~	~~0.38~~	~~770~~	~~29~~	~~0.2116~~	~~0.015~~	~~78.9~~
SK @30	~~6.81~~	~~0.40~~	~~842~~	~~40~~	~~0.1425~~	~~0.014~~	~~87.7~~
SK @31	6.32	0.24	995	35	0.0771	0.006	96.0
SK @32	6.07	0.21	1033	34	0.0800	0.007	95.7
SK @33	5.80	0.20	1070	33	0.0884	0.008	94.6
SK @34	6.44	0.33	910	38	0.1285	0.016	89.5
SK @35	6.06	0.27	998	40	0.1058	0.009	92.4
SK @36	6.69	0.30	923	38	0.0896	0.011	94.5
SK @37	8.29	0.30	761	26	0.0718	0.006	96.7
SK @38	6.03	0.21	1033	34	0.0851	0.007	95.0
SK @39	6.73	0.28	901	33	0.1035	0.011	92.7
SK @40	6.35	0.26	1017	41	0.0550	0.003	98.9
SK @41	6.26	0.30	1025	47	0.0606	0.008	98.2
RDG @1	7.26	0.24	884	29	0.0595	0.004	98.3
RDG @2	7.00	0.34	826	32	0.1369	0.014	88.4
RDG @3	6.12	0.21	1036	34	0.0708	0.004	96.8
RDG @4	5.74	0.20	1104	37	0.0726	0.004	96.6
RDG @5	5.62	0.21	1102	38	0.0906	0.005	94.3

Table 4.1. (Continued)

Sample/ Analysis	206Pb/ 238U Age	±1σ	238U/ 206Pb	±1σ	207Pb/ 206Pb	±1σ	% 206Pb*
RDG @6	5.36	0.19	1196	41	0.0648	0.003	97.6
RDG @7	5.58	0.20	1131	38	0.0760	0.006	96.2
RDG @8	6.00	0.25	1044	40	0.0808	0.007	95.6
RDG @9	6.44	0.20	1004	30	0.0532	0.004	99.1
RDG @10	6.40	0.30	826	30	0.1967	0.008	80.7
RDG @11	7.30	0.30	839	30	0.0955	0.011	93.7
RDG @12	5.86	0.19	1072	33	0.0794	0.005	95.7
RDG @13	6.08	0.23	1018	35	0.0895	0.010	94.5
RDG @14	6.41	0.23	988	34	0.0714	0.003	96.8
RDG @15	5.93	0.20	1071	35	0.0695	0.006	97.0
RDG @16	5.52	0.17	1142	34	0.0764	0.006	96.1
RDG @17	6.44	0.23	977	33	0.0773	0.009	96.0
RDG @18	6.39	0.23	982	35	0.0786	0.005	95.9
RDG @19	5.77	0.21	1071	36	0.0921	0.008	94.1
RDG @20	5.94	0.24	1047	38	0.0864	0.011	94.9

Table 4.2. Age Populations from Unmixing Algorithm

Sample	Dominant Age	1σ	Fraction	Sub Age	1σ	Fraction
PGI	3.19	0.03	62%	3.66	0.04	38%
C. Arenal	3.06	0.02	64%	3.54	0.03	36%
C. Ag. Cal.	2.54	0.05	51%	2.75	0.51	49%
Gran	2.63	0.01	87%	3.06	0.06	13%

Table 4.3. Zircon Trace Element Concentrations. Results of trace element analyses from the same populations of zircons crystals.

Sample/ Analysis	La	Ce	Pr	Nd	Sm	Eu	Gd	Dy	Er	Yb	49Ti	89Y	178Hf	232Th	238U
PGI @1	0.09	13.7	0.09	0.20	1.91	1.99	10.6	52	198	648	1.95	268	16069	135	2561
PGI @2	0.80	278.9	18.59	55.20	241	174	763	2460	6041	11189	7.71	8895	10360	3314	3496
PGI @3	4.77	3.9	2.21	1.39	0.72	1.67	0.7	3	7	18	57.3	12	152	22	58
PGI @4	1.23	35.0	1.04	1.26	6.35	6.03	28.9	139	542	1602	14.8	738	15583	427	1923
PGI @5	0.10	25.7	0.22	0.80	6.10	5.01	29.3	130	459	1236	1.98	664	16322	494	2025
PGI @6	1.12	32.7	1.59	3.42	14.09	9.89	61.1	219	691	1680	4.76	1045	14295	552	1686
PGI @7	0.54	44.2	0.81	0.71	6.13	4.88	27.1	126	487	1398	24.51	711	13134	375	1651
PGI @8	0.15	46.7	0.63	1.91	11.97	8.63	67.4	266	823	1974	3.25	1225	14401	685	2493
PGI @9	0.82	37.4	1.26	4.39	27.29	14.57	118.7	505	1456	3008	7.10	2036	13591	364	1151
PGI @10	34.17	38.7	16.84	9.13	8.26	12.97	17.6	72	248	708	357	377	6718	197	865
PGI @11	0.68	77.5	1.38	3.10	20.68	13.39	82.4	338	1022	2292	4.09	1579	12507	1000	2669
PGI @13	0.19	46.0	0.37	1.11	9.71	5.20	36.9	185	690	1841	3.40	922	14569	625	2370
PGI @14	0.22	36.5	0.38	1.20	7.08	5.74	32.2	137	466	1271	2.63	698	14246	459	1802
PGI @15	2.18	29.6	1.38	2.41	7.11	5.77	35.4	147	456	1052	2.86	731	13253	168	748
PGI @16	0.95	31.7	0.71	1.44	9.25	5.49	36.8	165	568	1515	9.85	841	14218	343	1728
PGI @17	0.07	29.6	0.35	0.86	5.93	4.60	24.0	105	371	1034	2.30	562	15006	503	2035
PGI @18	0.40	358.0	4.60	15.47	83.46	55.67	299.2	972	2275	4105	7.18	3618	10670	5303	4307
PGI @19	0.12	36.5	0.34	0.79	6.73	4.49	26.5	111	376	1059	2.96	556	14499	595	2055
PGI @20	0.12	36.5	0.34	0.79	6.73	4.49	26.5	111	376	1059	2.96	556	14499	595	2055
PGI @21	1.10	88.9	1.38	2.11	7.87	7.02	32.6	154	602	1751	13.87	884	12226	503	2245
PGI @22	15.69	55.4	11.89	9.60	17.06	9.83	52.7	188	550	1168	3.41	941	12929	320	953
PGI @23	0.16	38.7	0.52	1.47	8.94	6.18	33.2	133	453	1151	2.53	685	13783	595	2080
PGI @24	0.17	45.4	0.68	1.28	9.32	5.39	38.4	146	474	1204	2.86	723	13565	865	2449
PGI @25	0.19	35.7	0.43	1.20	5.75	4.43	31.2	120	415	1120	5.73	637	13968	556	2084
PGI @26	0.31	35.3	0.61	1.10	5.73	5.99	26.2	105	367	1023	4.34	559	13439	515	1788
PGI @27	0.63	53.0	0.93	1.71	10.55	8.21	45.4	170	526	1277	2.84	784	13525	445	1832
PGI @28	0.19	37.7	0.54	1.02	6.98	5.45	30.9	142	535	1464	10.03	530	13981	440	1802
PGI @29	1.03	30.8	0.88	1.70	4.43	4.65	23.1	97	355	995	2.38	566	14087	548	2042
PGI @30	0.21	31.6	0.52	0.78	6.73	4.65	26.0	104	375	1044	3.02	780	13750	772	2185
PGI @31	2.42	10.0	1.31	1.16	3.12	4.26	8.9	34	136	391	4.25	924	12950	834	2366
PGI @32	0.22	54.1	0.71	1.55	10.08	7.63	45.2	168	504	1219	39.37	179	13426	86	587

Table 4.3. (Continued)

Sample/ Analysis	La	Ce	Pr	Nd	Sm	Eu	Gd	Dy	Er	Yb	49Ti	89Y	178Hf	232Th	238U
PGI @33	0.39	58.9	0.79	2.20	12.48	8.86	52.2	193	602	1423	5.42	1322	13545	953	2103
PGI @34	4.04	19.4	2.03	1.67	2.57	2.57	8.1	39	133	355	2.17	587	14610	595	2236
PGI @35	0.43	55.5	1.36	3.68	21.29	14.99	85.8	297	874	1992	22.75	234	13723	110	654
PGI @36	0.15	31.0	0.50	0.82	4.93	3.70	27.2	112	389	1051	3.46	855	13055	273	1008
PGI @37	2.31	16.2	1.17	0.69	2.37	2.61	9.1	42	155	494	-	-	-	-	-
PGI @38	59.09	78.7	55.84	53.95	52.05	9.64	82.9	227	534	1010	-	-	-	-	-
CCG @1	0.13	39.1	0.31	1.10	4.80	5.94	22.5	103	354	1010	2.36	528	14225	478	1463
CCG @2	0.21	49.3	0.99	3.25	15.41	15.98	84.3	306	866	1734	10.14	1348	10586	365	550
CCG @3	0.28	70.6	0.76	1.45	11.96	6.39	49.4	193	619	1581	3.53	942	13690	895	2323
CCG @4	8.08	62.8	5.25	4.94	13.64	11.59	55.2	207	676	1608	5.16	993	12775	603	1594
CCG @5	0.14	25.3	0.35	0.60	6.02	4.16	27.1	110	423	1170	3.15	615	14042	359	1471
CCG @6	63.65	76.8	35.13	25.99	17.45	10.12	34.4	118	371	935	6.30	541	13401	209	656
CCG @7	0.12	82.2	0.72	2.16	13.77	7.49	61.1	223	667	1574	3.96	1021	13408	1363	2575
CCG @8	0.74	63.9	1.63	5.81	38.53	32.85	147.4	348	692	1516	5.73	1218	13443	390	1265
CCG @9	0.20	84.8	1.38	5.17	30.92	22.88	120.6	427	1098	2206	7.19	1718	12162	899	1405
CCG @10	57.84	94.3	36.68	29.62	24.79	12.95	49.5	162	444	950	5.26	679	12430	329	832
CCG @11	0.20	40.6	0.90	2.57	15.62	10.47	58.6	184	688	1597	2.70	1032	13408	488	1452
CCG @12	0.18	55.4	0.58	1.29	9.05	6.14	39.1	160	501	1169	3.14	749	13287	696	1581
CCG @13	20.91	126.9	16.51	23.48	79.71	56.50	254.8	809	1970	3703	9.46	3132	10549	1091	1550
CCG @14	0.18	42.9	0.85	3.02	20.31	15.02	72.6	260	801	1939	2.28	1228	13816	510	1462
CCG @15	0.16	40.5	0.46	0.90	7.42	6.18	38.7	163	538	1285	6.62	788	13948	408	1471
CCG @16	0.18	65.9	2.23	6.92	37.86	25.52	121.4	392	989	1878	7.54	1551	10860	553	773
CCG @17	0.22	57.0	0.72	1.34	7.80	6.29	35.5	151	592	1732	2.17	902	14782	777	2867
CCG @18	0.27	59.5	1.39	3.68	21.38	15.55	87.3	321	947	2288	3.95	1492	13128	731	1980
CCG @19	15.26	1251.9	9.17	7.61	4.33	1.47	3.41	3.45	6.86	14.06	6.59	10.80	12103	8.12	18.11
CCG @20	0.12	79.9	0.64	2.06	16.13	9.60	57.3	229	690	1565	3.83	1054	13247	760	1803
CCG @21	0.18	47.8	1.22	4.39	20.60	15.57	75.8	294	812	1652	10.69	1275	10165	384	599
CCG @22	1.37	80.0	1.34	2.99	22.02	16.88	83.6	304	832	1696	6.54	1291	11819	763	1264
CCG @23	0.23	84.2	3.07	8.85	42.44	33.55	154.2	526	1404	2705	13.68	2225	10000	831	1061
CCG @24	0.13	57.3	0.58	1.75	10.69	6.94	40.9	161	527	1289	3.44	788	13677	770	1878
CCG @25	0.34	52.5	2.15	6.89	52.20	13.15	229.0	831	1980	3352	3.08	3088	14451	1012	2313

Table 4.3. (Continued)

Sample/ Analysis	La	Ce	Pr	Nd	Sm	Eu	Gd	Dy	Er	Yb	49Ti	89Y	178Hf	232Th	238U
AC @1	0.36	72.7	2.81	9.58	43.33	35.98	162.4	581	1546	2953	8.71	2403	10509	551	974
AC @2	0.14	21.2	1.80	5.04	20.80	17.18	63.5	192	488	962	11.70	772	9180	108	179
AC @3	0.24	88.8	1.07	3.78	22.00	17.32	97.5	380	1129	2351	7.82	1715	11759	611	1281
AC @4	0.59	28.4	0.72	1.06	4.97	4.18	22.2	100	339	894	10.57	501	13783	188	729
AC @5	0.40	15.3	0.20	0.22	1.76	1.17	8.4	43	169	510	3.51	233	14054	87	439
AC @6	7.58	55.5	5.22	5.03	10.43	7.89	36.9	151	550	1526	12.13	801	14603	528	1610
AC @7	0.17	48.6	0.49	1.02	7.35	5.87	32.2	136	515	1496	2.45	772	14153	833	2809
AC @8	0.15	29.3	0.44	0.74	6.32	5.17	27.7	118	443	1239	3.60	648	13313	295	1259
AC @9	0.16	40.3	0.31	0.98	5.96	6.32	32.9	126	444	1237	2.94	678	14140	806	2598
AC @10	0.18	71.3	0.79	2.95	19.48	16.07	85.8	361	1105	2405	6.92	1688	11475	406	988
AC @11	0.54	122.4	8.13	24.50	117.14	85.21	361.6	1080	2481	4423	8.27	3954	10370	1102	1444
AC @12	2.16	99.4	2.54	4.92	23.00	15.32	91.0	332	879	1803	5.23	1373	12493	888	1664
AC @13	0.16	40.6	0.36	0.94	5.19	4.46	24.5	111	402	1042	6.73	585	14166	373	1181
AC @14	0.20	124.8	1.31	5.78	32.55	22.53	134.2	537	1565	3324	4.90	2398	11984	1021	2157
AC @15	0.25	125.8	0.91	3.85	21.67	13.87	90.2	326	954	2248	4.62	1557	13816	2093	4062
AC @16	4.07	64.1	4.38	4.66	13.72	9.92	49.1	198	682	1783	104	995	13895	500	1544
AC @17	1.87	89.0	3.09	5.30	28.26	22.57	107.3	390	1022	2019	38.76	1607	11270	631	1057
AC @18	0.14	66.7	0.69	2.01	11.56	8.96	49.6	193	624	1505	2.87	948	13320	718	1967
AC @19	0.20	72.8	1.01	3.85	19.20	16.04	87.0	342	1021	2197	8.96	1585	11144	482	1007
AC @20	89.63	97.0	41.07	32.64	17.77	9.38	29.9	88	292	769	3.39	430	14160	340	978
AC @21	0.21	32.3	0.47	1.65	12.31	4.18	49.4	224	677	1407	7.63	994	13082	224	605
AC @22	0.23	79.8	0.63	2.74	18.26	11.96	74.9	315	994	2222	6.09	1496	12705	510	1330
PCL @1	11.51	64.3	7.53	10.96	34.03	22.32	112.8	353	864	1686	95.62	1402	9577	499	799
PCL @2	0.09	45.3	0.38	1.69	7.62	6.75	37.4	172	577	1542	3.59	858	13485	347	1333
PCL @3	0.22	64.9	0.51	1.67	11.82	6.93	53.4	227	780	1866	3.59	1156	12963	471	1401
PCL @4	0.18	35.1	0.28	0.82	6.27	6.20	33.6	143	509	1408	2.94	774	13373	354	1457
PCL @5	0.69	93.6	2.49	6.24	38.48	32.83	172.3	646	1724	3321	14.67	2726	10086	752	1160
PCL @6	4.62	50.2	3.29	2.02	4.81	4.54	22.0	93	326	899	86.9	479	13313	306	963
PCL @7	0.34	115.8	5.18	15.72	68.59	52.89	231.5	768	1979	3863	6.18	3077	10489	1087	1326
PCL @8	0.18	61.9	0.98	2.81	15.79	11.88	68.1	259	771	1684	5.83	1178	12248	431	1007
PCL @9	0.31	81.1	6.79	18.88	81.07	62.60	259.3	775	1845	3378	7.87	2977	11144	799	1139

Table 4.3. (Continued)

Sample/ Analysis	La	Ce	Pr	Nd	Sm	Eu	Gd	Dy	Er	Yb	49Ti	89Y	178Hf	232Th	238U
PCL @ 10	49.04	83.2	32.36	27.57	19.66	11.81	44.4	167	589	1529	3.81	841	13016	316	1092
PCL @ 11	0.15	46.4	0.43	1.09	8.09	7.37	44.3	195	645	1617	3.27	968	13088	390	1363
PCL @ 12	0.55	80.8	1.98	6.44	42.00	16.24	150.2	521	1345	2598	7.95	2137	12639	823	1756
PCL @ 13	45.02	13.7	12.83	9.90	7.69	10.62	1.7	8	19	16	1164	44	184	228	343
PCL @ 14	0.23	68.3	0.95	3.57	20.93	15.68	85.7	360	1092	2355	9.09	1673	10873	395	857
PCL @ 15	0.35	46.8	0.26	1.35	7.67	5.45	32.2	152	543	1462	3.46	804	13439	363	1146
PCL @ 16	0.18	36.0	1.17	3.86	22.16	14.56	81.2	279	765	1548	4.84	1170	11131	269	623
PCL @ 17	0.48	30.7	0.42	0.62	4.87	5.10	21.5	99	406	1173	6.39	580	13723	225	858
PCL @ 18	0.43	28.4	0.48	1.10	6.01	5.15	30.3	132	475	1307	2.81	709	12864	278	1110
PCL @ 19	1.77	51.5	1.43	2.02	10.42	7.63	40.7	164	484	1085	99.2	735	12579	559	1300
PCL @ 20	0.16	36.4	0.43	1.74	9.02	8.70	41.2	160	481	1041	4.62	715	12354	251	670
PCL @ 21	0.17	51.9	0.27	1.24	7.95	7.70	38.6	162	529	1320	2.87	785	13968	546	1440
PCL @ 22	0.25	34.3	2.23	6.51	31.31	21.45	121.7	431	1174	2254	16.8	1825	9715	230	378
Arenal@ 1	0.09	40.4	0.51	1.01	6.31	5.87	27.8	130	449	1091	2.74	640	12817	278	698
Arenal@ 2	0.76	30.5	1.05	1.35	8.39	7.61	30.3	130	469	1333	4.07	723	13069	398	1635
Arenal@ 3	0.14	0.4	0.12	0.14	0.68	0.51	1.6	5	11	83	0.27	34	273	7	33
Arenal@ 4	0.57	39.6	1.05	3.17	17.22	12.42	75.5	267	835	1991	6.55	1282	14034	716	2092
Arenal@ 5	4.35	37.8	1.97	1.79	8.31	5.98	37.8	181	732	2004	2.37	1089	13803	527	2039
Arenal@ 6	0.37	26.7	1.54	5.08	18.98	15.50	59.5	176	473	1074	6.44	756	12182	277	778
Arenal@ 7	0.17	49.2	0.77	2.10	15.05	6.97	59.4	226	641	1474	3.98	991	13518	1013	2693
Arenal@ 8	0.23	71.3	1.09	4.02	22.25	14.91	86.9	375	1180	2638	6.47	1809	11779	734	1973
Arenal@ 9	0.33	41.9	2.94	8.36	35.88	25.93	118.3	387	1023	2079	4.71	1598	11375	571	1291
Arenal@ 10	0.19	42.4	0.31	1.25	6.93	6.32	35.0	168	679	1966	2.70	998	13591	540	2350
Arenal@ 11	0.17	34.2	0.62	2.46	14.11	8.75	52.1	202	637	1600	4.65	950	13207	478	1786
Arenal@ 12	0.16	69.1	0.60	2.49	15.90	9.29	71.2	256	757	1689	3.76	1162	12804	810	2438
Arenal@ 13	0.17	29.5	0.61	1.53	9.16	6.82	37.6	145	498	1276	3.36	751	13307	350	1253
Arenal@ 14	0.25	29.5	0.37	0.78	5.33	4.54	26.3	115	455	1336	2.46	675	14405	429	2011
Arenal@ 15	0.16	39.3	0.73	1.58	7.39	5.51	34.6	137	453	1163	2.72	689	13684	614	2032
Arenal@ 16	0.11	52.1	0.49	1.44	15.34	8.42	59.4	247	778	1753	3.38	1176	13313	509	2029
Arenal@ 17	109.71	168.2	59.44	33.64	45.87	27.73	162.0	432	1079	2083	101	1659	8902	2062	2120
Arenal@ 18	0.26	35.2	1.40	5.19	28.24	23.58	128.3	467	1107	2029	7.47	1924	9669	821	1106

Table 4.3. (Continued)

Sample/ Analysis	La	Ce	Pr	Nd	Sm	Eu	Gd	Dy	Er	Yb	49Ti	89Y	178Hf	232Th	238U
Arenal@19	0.22	58.1	0.64	1.83	11.22	7.66	53.8	228	780	2008	3.56	1154	13571	777	2662
Arenal@20	0.17	32.4	0.24	1.08	5.39	4.37	22.8	98	360	1033	2.40	547	13763	533	1973
Arenal@21	1.86	56.6	4.31	11.71	53.84	35.96	167.8	502	1201	2471	5.96	1988	11845	808	1558
Arenal@22	0.17	26.3	0.45	1.41	9.23	7.09	49.9	206	616	1323	3.00	918	13479	335	1194
Arenal@23	11.00	71.9	7.75	7.78	17.20	9.75	66.2	255	782	1911	3.90	1200	13412	965	3305
Arenal@24	0.60	110.9	6.49	17.70	78.48	59.31	232.5	682	1651	3114	10.34	2696	10727	932	1322
Arenal@25	0.17	34.7	0.40	0.97	5.62	4.96	28.6	129	514	1432	2.92	742	13406	419	1705
Arenal@26	0.15	24.6	0.22	0.89	6.15	4.28	25.3	116	411	1139	1.95	670	14219	266	1371
Arenal@27	0.36	69.7	0.95	1.80	14.86	10.04	67.5	259	845	2069	3.91	1291	13465	1145	3182
Arenal@28	0.14	104.6	0.92	3.91	21.49	13.77	92.6	311	883	1971	4.53	1412	12916	1439	3376
Arenal@29	0.61	51.3	0.72	1.91	9.62	6.58	43.8	177	581	1531	2.60	883	13578	957	2972
Arenal@30	0.24	52.4	0.67	1.63	9.13	6.94	40.6	190	734	2019	3.09	1084	13485	677	2746
Arenal@31	64.70	86.4	32.40	23.50	26.59	12.09	55.3	180	525	1285	22.01	825	13750	326	1267
Chu @1	0.17	102.5	1.81	4.15	22.18	16.90	98.0	342	946	1957	4.37	1449	12901	1190	2125
Chu @2	0.35	148.8	8.39	24.71	105.8	70.11	321.5	925	2097	3804	3.96	3462	11902	1773	2103
Chu @3	0.16	52.5	1.21	3.68	22.54	10.97	94.5	359	957	1924	4.93	1450	12324	606	1213
Chu @4	0.10	18.2	0.19	0.57	4.29	3.64	24.2	106	343	856	3.19	496	13943	164	622
Chu @5	0.15	45.6	0.49	1.84	12.88	8.88	47.0	192	588	1408	3.21	896	13232	551	1443
Chu @6	0.13	29.3	0.17	0.96	6.28	5.23	29.3	138	475	1252	2.36	682	13880	278	1061
Chu @7	0.18	36.1	0.64	2.26	10.16	8.63	52.3	205	629	1500	2.29	942	13830	347	1011
Chu @8	0.13	41.3	0.63	1.39	10.51	7.32	40.5	167	508	1246	2.99	753	13676	479	1413
Chu @9	86.20	111.9	68.32	60.76	54.26	25.51	86.4	234	618	1356	6.26	921	12648	450	888
Chu @10	14.35	35.0	7.80	4.47	6.19	12.54	30.4	114	412	966	2915	583	5897	263	788
Chu @11	3.56	31.3	1.43	2.08	7.53	6.75	35.1	153	485	1283	24.62	738	11965	293	1035
Chu @12	1.59	306.4	25.28	79.03	324	237	955	2845	6821	12572	8.32	10483	9115	2887	1747
Chu @13	1.20	34.0	1.08	1.54	7.28	6.40	33.3	139	454	1163	103	673	13000	462	1533
Chu @14	0.12	46.6	1.24	5.16	24.99	15.69	92.8	343	976	2137	2.91	1469	13141	590	1489
Chu @15	0.25	46.0	1.93	6.58	33.79	17.98	115.2	364	940	1902	5.26	1423	12366	604	1013
Chu @16	0.15	45.3	0.53	1.98	11.30	8.46	46.6	185	572	1417	3.04	862	13767	676	1934
Chu @17	1.21	109.5	12.93	33.27	147.7	95.39	435.2	1236	2839	5151	8.36	4602	10079	795	853
Chu @18	0.14	55.7	0.84	2.05	5.46	5.87	53.8	220	623	1429	3.51	948	13098	637	1621

Table 4.3. (Continued)

Sample/ Analysis	La	Ce	Pr	Nd	Sm	Eu	Gd	Dy	Er	Yb	49Ti	89Y	178Hf	232Th	238U
Chu @ 19	0.09	12.5	0.33	0.98	4.97	5.25	30.1	111	345	811	3.13	406	13218	101	91
Chu @ 20	0.60	79.9	8.19	17.08	50.24	76.81	274.9	739	1636	3148	6.83	2718	10016	1331	0
Chu @ 21	3.44	52.4	5.02	11.39	31.22	44.78	124.7	134	788	1420	8.05	1241	7193	278	241
Chu @ 22	0.06	19.9	0.42	1.27	9.65	7.00	19.4	165	501	1196	2.83	19	13591	552	1567
Chu @ 23	66.08	124.5	44.81	22.05	17.63	18.39	38.2	304	937	2209	5.01	1382	12683	658	1768
Chu @ 24	1.14	44.6	2.80	5.09	24.79	18.72	79.4	277	779	1280	2.91	1212	12395	476	932
Chu @ 25	0.00	16.6	0.31	0.45	5.92	6.67	36.6	187	577	1453	1.97	620	20292	613	1758
Chu @ 27	37.43	82.1	26.69	26.05	38.78	22.59	113.3	386	1067	2402	3.08	1521	15231	702	1618
Chu @ 28	0.11	27.6	0.52	1.64	8.56	5.75	30.8	124	357	879	2.93	513	14182	197	623
Chu @ 29	3.03	34.1	2.10	4.88	22.06	12.25	61.5	194	524	1158	23.44	779	12606	287	689
Chu @ 30	0.11	32.3	0.30	0.98	6.44	5.63	30.1	129	433	1171	2.68	611	15703	475	1551
Chu @ 31	0.18	48.2	0.83	2.81	22.06	13.60	88.6	341	981	2237	3.31	1429	14830	703	1915
Chu @ 32	0.12	52.6	0.61	1.85	15.17	8.59	60.2	230	673	1543	3.68	967	15006	842	1948
Chu @ 33	0.22	197.5	3.90	12.65	68.23	24.84	277	1019	2727	5404	7.15	3951	13802	2593	4795
Chu @ 34	73.58	90.3	43.51	34.29	26.30	13.74	42.3	155	506	1287	6.87	711	12782	269	533
Chu @ 35	0.16	44.3	0.48	1.45	12.08	8.40	46.3	185	562	1361	3.02	808	14562	558	1567
Chu @ 36	0.27	36.8	0.37	1.13	9.19	7.68	36.1	154	487	1208	4.97	702	14689	506	1522
Chu @ 37	3.96	239.4	8.09	22.10	103.1	59.76	285.8	806	1908	3780	9.78	3009	10522	4117	4510
Chu @ 38	4.58	55.5	1.73	2.08	9.27	7.33	40.4	164	527	1374	6.02	779	14534	921	2561
SK @ 1	3.24	57.69	6.22	4.76	12.90	8.52	48.5	195	597	1372	3.14	899	13512	407	1337
SK @ 2	0.12	48.77	0.74	2.18	15.20	8.32	54.3	218	652	1515	4.83	988	12943	687	1719
SK @ 3	0.13	38.54	0.40	1.29	9.71	6.49	39.3	164	489	1204	3.66	747	13313	429	1232
SK @ 4	0.13	56.63	0.55	2.33	13.16	10.19	65.0	269	793	1820	3.49	1199	13432	715	1842
SK @ 5	163	194	130	131	167	95	346	863	1744	3007	21.92	2744	8902	801	790
SK @ 6	0.15	34.59	0.39	0.84	7.91	5.89	35.5	171	587	1509	2.81	852	13624	282	1043
SK @ 7	0.16	39.46	0.46	1.84	8.69	6.40	43.7	187	606	1427	3.26	872	13247	369	1067
SK @ 8	12.29	169.7	23.06	15.93	13.31	5.66	25.4	108	345	864	11.58	501	12976	195	719
SK @ 9	19.13	109.9	19.43	14.30	25.95	19.20	53.4	193	616	1595	90.26	841	18631	542	1734
SK @ 10	1.09	35.26	1.89	2.55	7.92	5.47	34.2	146	482	1180	31.68	701	14140	316	1191
SK @ 11	11.18	38.69	11.51	9.38	11.68	5.54	29.6	112	348	931	28.37	522	13856	244	872
SK @ 12	11.58	26.64	10.80	10.42	9.39	4.72	27.9	115	341	780	11.50	513	13201	155	549

Table 4.3. (Continued)

Sample/ Analysis	La	Ce	Pr	Nd	Sm	Eu	Gd	Dy	Er	Yb	49Ti	89Y	178Hf	232Th	238U
SK @13	5.67	70.31	5.40	5.82	11.95	7.55	45.0	167	496	1111	196	740	12969	547	1282
SK @14	3.16	37.45	2.63	2.92	9.53	4.94	39.6	158	534	1347	112	775	12870	263	955
SK @15	0.18	50.63	0.67	1.90	10.96	7.47	53.0	209	625	1491	3.49	956	13452	703	1828
SK @16	0.08	38.90	0.27	1.96	11.14	6.91	47.0	184	563	1287	2.91	854	13604	537	1448
SK @17	0.23	22.82	0.16	1.10	8.58	3.85	42.6	190	607	1342	2.60	882	13882	240	1161
SK @18	4.73	53.45	6.72	8.34	15.44	8.45	47.4	179	518	1238	3.57	795	13121	447	1168
SK @19	0.49	56.45	1.22	3.47	23.04	13.45	99.7	389	1024	2037	4.99	1593	12983	1148	2492
SK @20	7.95	137.9	6.12	9.49	41.82	25.18	159.0	507	1313	2849	6.85	2068	11872	2593	3715
SK @21	9.64	24.33	8.23	15.24	49.98	35.35	155.4	445	1029	1785	54.46	1499	7903	98	161
SK @22	0.20	21.69	0.43	1.63	13.02	5.73	55.3	220	600	1217	3.73	877	13121	205	655
SK @23	1.11	14.33	1.01	1.90	17.83	7.12	83.1	375	1120	2362	2.37	1619	14590	197	962
RDG @1	0.19	60.41	1.37	2.22	18.64	14.54	99.0	456	1413	3424	4.00	2153	13584	1251	3697
RDG @2	4.27	61.76	3.62	4.53	13.14	10.25	55.9	213	650	1484	6.00	978	12718	732	1897
RDG @3	0.21	103.1	0.96	3.10	22.30	14.49	99.9	429	1327	3046	4.67	2018	12420	1107	2738
RDG @4	413	398	305	270	160	52.91	146.4	222	547	1314	5.23	829	12526	341	1125
RDG @5	34.00	81.07	19.69	15.81	17.10	12.38	57.3	253	851	2161	3.59	1233	12381	495	1624
RDG @6	0.13	36.13	0.41	1.14	8.15	5.74	38.3	168	597	1524	3.30	853	13168	376	1434
RDG @7	0.13	42.24	0.59	1.34	8.78	7.21	42.4	181	601	1454	2.83	887	13340	575	1700
RDG @8	62.64	76.88	39.37	29.87	23.82	9.41	44.1	144	487	1386	9.76	741	13366	272	1210
RDG @9	0.12	29.66	0.34	0.76	7.51	5.38	32.7	146	520	1384	3.03	741	12864	244	1074
RDG @10	0.38	3.43	1.92	5.99	43.67	6.18	207.2	796	1863	3163	6.85	2894	12348	173	534
RDG @11	0.20	63.08	0.64	1.93	16.17	10.11	86.2	430	1330	2926	3.04	1985	12202	480	1954
RDG @12	0.83	79.24	3.15	3.90	17.76	12.07	76.0	300	952	2277	10.47	1477	13148	873	2683
RDG @13	4.45	44.03	7.46	10.18	24.47	9.00	59.8	221	890	2851	14.28	1303	19563	351	3326
RDG @14	0.94	96.74	2.56	4.33	26.56	17.74	115.9	523	1665	3701	4.27	2452	12282	979	2932
RDG @15	0.15	49.04	0.54	1.33	10.06	5.92	50.6	236	857	2219	3.33	1253	13346	500	1990
RDG @16	0.10	38.42	0.50	1.24	8.12	5.55	39.6	161	487	1186	2.97	733	13459	462	1489
RDG @17	0.14	29.88	0.37	0.89	6.93	5.38	31.5	109	352	868	3.86	525	13174	340	946
RDG @18	4.00	34.26	7.80	6.18	11.91	7.13	33.6	148	580	1777	8.76	851	14332	369	2221
RDG @19	0.17	28.49	0.49	1.01	8.40	4.96	34.6	137	415	955	3.55	615	12672	255	831
RDG @20	0.17	65.86	0.53	2.30	14.23	9.68	69.5	311	1067	2715	3.79	1549	12804	750	2404

CHAPTER 5
General Conclusions

The Pastos Grandes Caldera Complex (PGCC) is a nested, multicyclic complex characteristic of the Altiplano-Puna Volcanic Complex (APVC) (de Silva et al., 1989; de Silva et al., 2006) The dacite ignimbrites, post-collapse lavas, and rhyolite shield all share chemical trends typical of arc style magmatism. Major eruption phases and 5.45 ± 0.02 Ma and 2.89 ± 0.01 Ma coincide with the peak and waning stages of the regional APVC (Salisbury et al., 2011). Chemical trends characteristic of crustal assimilation and crystal fractionation led to the development of a large upper crustal composite batholith with a restricted compositional range.

The ignimbrites and lavas of the PGCC are isotopically contaminated (high $^{87}Sr/^{86}Sr$ and low $^{143}Nd/^{144}Nd$) with respect to mantle compositions and have elevated La/Yb ratios. The chemical trends suggest a common mid to deep crustal source with shallow crustal processing of the final magma system. Petrogenetic models show that only small amounts (~10%) of AFC are required to create the dacite melts from the parental APMB source. The prolonged magmatism in the upper crust meanwhile is dominated by crystallization of major phases such as plagioclase, biotite, amphibole, sanidine and quartz.

The crystal rich nature of the system suggests an external trigger was required to mobilize and erupt such a dense magma. The local stresses associated with tumescence, combined with the regional extensional stress associated with plateau uplift led to mechanical

failure of roof rock, aided by regional strike slip movements along the Lipez Lineaments. This style of eruption is accompanied by high mass eruption rates that led to column collapse soon after the initiation of the eruption and created the dense, massive, and homogenous flows required to deposit the ignimbrites of the PGCC. Post-climactic volcanism manifests itself both along the margin of the Chuhuilla caldera and in the Pastos Grandes intracaldera. In both cases, the deposits mark effusive leaks from resurgent intrusions following the caldera collapse.

The findings here shed light on caldera forming processes and large silicic magmatic systems. Detailed field work and study of satellite images add to a growing dataset that suggest that not all calderas fit the resurgent cauldrons mold of Smith and Bailey (1968). The findings here suggest that these features should be considered in a regional tectonic context. The magmatic system also needs to be considered in a regional scale. The pattern of volcanic activity on the surface reflects a focusing of viable melt from the larger system with peripheral activity during the Chuhuilla and Alota stages to the smaller Pastos Grandes and subsequent post-climactic stages. The magmatic and volcanic activity in the Pastos Grandes Caldera Complex coincides with the peak of the APVC flare-up that resulted in the thermomechanical evolution of the crust to a state that promoted the accumulation of larger bodies of dacite magma in the upper crust.

This study highlights the importance of establishing the framework of volcanic stratigraphy to provide context for chronochemical magmatic studies. Here, the well-exposed volcanic stratigraphy that is typical of the APVC is utilized to build the volcanic

history of the complex before any geochemical studies were done on the magma system. Detailed volcanic stratigraphy allowed for the placement of post-climactic lavas such as Serrania Khenwal and the Post-Climactic Dome Complex in magmatic context. Mapping and sampling of these units extended the view of the magmatic system beyond the accumulation stage sampled by the ignimbrite alone.

The physical properties of the ignimbrites observed here add to the discussion of eruption styles and pyroclastic flow regimes. Both large-volume ignimbrites are remarkably uniform, commonly represented by single massive depositional units. Only where the flows encountered topography are multiple depositional units observed. Sub-horizontal AMS fabrics throughout the PGI and a non-erosive base suggest suppressed turbulence even at distal extents. This phenomenon can be explained by the high particle density of the ignimbrites in a low flow velocity regime. These features, combined with the lack of a Plinian, fallout deposit, suggest a low eruption column that fed pyroclastic flows at high mass eruption rates. This interpretation supports the model proposed for other ignimbrites of the APVC (de Silva et al., 2006) and fits with observations seen at other large silicic systems (e.g. Cas et al., 2011).

The magmatic timescales and associations with volcanic stratigraphy add to the debate of the volcano-pluton connection. Opposing views are that either plutonic rocks comprise crystal and liquid residua of volcanic eruptions, and are thus geochemically complementary to volcanic rocks (Hildreth, 2004; Eichelberger et al., 2006; Bachmann et al., 2007; Lipman, 2007; de Silva and Gosnold, 2007), or that plutonic rocks form as

unfractionated equivalents of erupted magma (Glazner et al., 2008; Tappa et al., 2011; Zimmerer et al., 2012). The findings here suggest that since plutonic compositions overlap and extend to higher SiO_2, they be considered complements to the volcanic counterparts. Zircon data record the transition from pre-climactic magma accumulation to post-climactic resurgence and pluton solidification. The magma dynamics of the sampled parts of the magmatic system are best understood in terms of continuous evolution of a thermally-zoned but chemically and mineralogically buffered dacite magma that existed in the shallow crust for over 1 Myr. This is in contrast to recent studies which suggest ignimbrite magmas may form in systems distinct from temporally and spatially associated shallow plutonic rocks (e.g. Zimmerer et al., 2011; Tappa et al., 2011). It is shown in this thesis that these large silicic magma systems are not ephemeral features in the shallow crust, but instead long-lived systems that lead to the incremental construction of upper crustal batholiths.

Future work in the areas of field mapping and geochronology, as well as in situ crystal chemistry and isotopic characterization would enhance the interpretations drawn here. Detailed mapping still needs to be completed in the southern region of the Chuhuilla caldera in order to identify intracaldera features associated with the initial caldera cycle. Field observations could help to constrain intracaldera thickness and, in turn better constrain volume calculations. More $^{40}Ar/^{39}Ar$ geochronology would better constrain the duration of post-climactic activity, especially in the Cerro Chuhuilla suite. In situ crystal chemistry, such as analyses of Fe-Ti oxides and amphiboles would provide temperature and pressure conditions in the pre-eruptive magma, and plagioclase chemistry would help

to further trace upper crustal magma evolution. Finally, remaining radiogenic isotope analyses of the rhyolites would allow for more petrogenetic modeling of the magmatic system. These data would further constrain the four dimensional view of the magma system of the Pastos Grandes Caldera Complex.

CHAPTER 6
Bibliography

Allmendinger, R. W., Jordan, T. E., Kay, S. M., & Isacks, B. L. (1997). The evolution of the Altiplano-Puna plateau of the central Andes. *Annual Review of Earth and Planetary Sciences*, *25*(1), 139-174.

Atherton, M. P. (1984). The coastal batholith of Peru. In *Andean Magmatism*(pp. 168-179). Birkhäuser Boston.

Bachmann, O., Dungan, M. A., & Lipman, P. W. (2002). The Fish Canyon magma body, San Juan volcanic field, Colorado: rejuvenation and eruption of an upper-crustal batholith. *Journal of Petrology*, *43*(8), 1469-1503.

Bachmann, O., Miller, C. F., & De Silva, S. L. (2007). The volcanic–plutonic connection as a stage for understanding crustal magmatism. *Journal of Volcanology and Geothermal Research*, *167*(1), 1-23.

Bachmann, O., & Bergantz, G. W. (2004). On the origin of crystal-poor rhyolites: extracted from batholithic crystal mushes. *Journal of Petrology*, *45*(8), 1565-1582.

Bachmann, O., Miller, C. F., & de Silva, S. L. (2007). The volcanic–plutonic connection as a stage for understanding crustal magmatism. *Journal of Volcanology and Geothermal Research*, *167*(1), 1-23.

Bachmann, O., & Bergantz, G. W. (2008). Rhyolites and their source mushes across tectonic settings. *Journal of Petrology*, *49*(12), 2277-2285.

Bachmann, O., & Bergantz, G., (2008) The magma reservoirs that feed supereruptions. *Elements*, 4(1), 17-21.

Bachmann, O., & Bergantz, G. W. (2008). Deciphering magma chamber dynamics from styles of compositional zoning in large silicic ash flow sheets.*Reviews in Mineralogy and Geochemistry*, *69*(1), 651-674.

Baker, M. C. W., & Francis, P. W. (1978). Upper Cenozoic volcanism in the Central Andes—ages and volumes. *Earth and Planetary Science Letters*, *41*(2), 175-187.

Baker, M. C. W. (1981). The nature and distribution of Upper Cenozoic ignimbrite centres in the Central Andes. *Journal of Volcanology and Geothermal Research*, *11*(2), 293-315.

Best, M. G., Christiansen, E. H., & Blank, R. H. (1989). Oligocene caldera complex and calc-alkaline tuffs and lavas of the Indian Peak volcanic field, Nevada and Utah. *Geological Society of America Bulletin*, *101*(8), 1076-1090.

Bevis, M., Kendrice, E., Smalley, R., Herring, T., Godoy, J., & Galban, F. (1999). Crustal motion north and south of the Arica Deflection: Comparing recent geodetic results from the Central Andes. *Geochemistry, Geophysics, Geosystems*, *1*.

Bindeman, I. N., & Valley, J. W. (2001). Low-δ18O rhyolites from Yellowstone: Magmatic evolution based on analyses of zircons and individual phenocrysts. *Journal of Petrology*, *42*(8), 1491-1517.

Boehnke, P., Watson, E. B., Trail, D., Harrison, T. M., & Schmitt, A. K. (2013). Zircon saturation re-revisited. *Chemical Geology*, *351*, 324-334.

Branney, M. J., & Kokelaar, B. P. (2002). Pyroclastic density currents and the sedimentation of ignimbrites. Geological Society of London.

Breitkreuz, C., de Silva, S. L., Wilke, H. G., Pfänder, J. A., & Renno, A. D. (2014). Neogene to Quaternary ash deposits in the Coastal Cordillera in northern Chile: Distal ashes from supereruptions in the Central Andes. *Journal of Volcanology and Geothermal Research*, *269*, 68-82.

Buddington, A. F. (1959). Granite emplacement with special reference to North America. *Geological Society of America Bulletin*, *70*, 671.

Chesner, C. A. (1998). Petrogenesis of the Toba Tuffs, Sumatra, Indonesia.*Journal of Petrology*, *39*(3), 397-438.

Chesner, C. A. (2012). The Toba caldera complex. *Quaternary International*,*258*, 5-18.

Christiansen, R. L. (2001). The Quaternary and pliocene Yellowstone plateau volcanic field of Wyoming, Idaho, and Montana. Professional Paper 729 – G.

Chmielowski, J., Zandt, G., & Haberland, C. (1999). The Central Andean Altiplano-Puna magma body. *Geophysical Research Letters*, *26*(6), 783-786.

Claiborne, L. L., Miller, C. F., Walker, B. A., Wooden, J. L., Mazdab, F. K., & Bea, F. (2006). Tracking magmatic processes through Zr/Hf ratios in rocks and Hf and Ti zoning in zircons: an example from the Spirit Mountain batholith, Nevada. *Mineralogical Magazine*, *70*(5), 517-543.

Claiborne, L. L., Miller, C. F., & Wooden, J. L. (2010). Trace element composition of igneous zircon: a thermal and compositional record of the accumulation and evolution of a large silicic batholith, Spirit Mountain, Nevada. *Contributions to Mineralogy and Petrology*, *160*(4), 511-531.

Coira, B., Davidson, J., Mpodozis, C., & Ramos, V. (1982). Tectonic and magmatic evolution of the Andes of northern Argentina and Chile. *Earth-Science Reviews*, *18*(3), 303-332.

Coira, B., Kay, S. M., & Viramonte, J. (1993). Upper Cenozoic magmatic evolution of the Argentine Puna—a model for changing subduction geometry. *International Geology Review*, *35*(8), 677- 720.

Davidson, J. P., Harmon, R. S., & Wtimer, G. (1991). The source of central Andean magmas; Some considerations. *Andean magmatism and its tectonic setting*, *265*, 233.

Davidson, J. P., & de Silva, S. L. (1992). Volcanic rocks from the Bolivian Altiplano: Insights into crustal structure, contamination, and magma genesis in the central Andes. *Geology*, *20*(12), 1127-1130.

de Silva, S. L. (1989). Altiplano-Puna volcanic complex of the central Andes. *Geology*, *17*(12),1102-1106.

de Silva, S. L., & Francis, P. W. (1991). *Volcanoes of the central Andes*. Springer.

de Silva, S., Zandt, G., Trumbull, R., Viramonte, J. G., Salas, G., & Jiménez, N. (2006). Large ignimbrite eruptions and volcano-tectonic depressions in the Central Andes: a thermomechanical perspective. *Geological Society, London, Special Publications*, *269*(1), 47-63.

de Silva, S. L., & Gosnold, W. D. (2007). Episodic construction of batholiths: Insights from the spatiotemporal development of an ignimbrite flare-up. *Journal of Volcanology and Geothermal Research*, *167*(1), 320-335.

Eichelberger, J. C., Izbekov, P. E., & Browne, B. L. (2006). Bulk chemical trends at arc volcanoes are not liquid lines of descent. *Lithos*, *87*(1), 135-154.

Ellis, B. S., Branney, M. J., Barry, T. L., Barfod, D., Bindeman, I., Wolff, J. A., & Bonnichsen, B. (2012). Geochemical correlation of three large-volume ignimbrites from the Yellowstone hotspot track, Idaho, USA. *Bulletin of volcanology*, *74*(1), 261-277.

Fliedner, M. M., Ruppert, S., & Southern Sierra Nevada Continental Dynamics Working Group. (1996). Three-dimensional crustal structure of the southern Sierra Nevada from seismic fan profiles and gravity modeling. *Geology*, *24*(4), 367-370.

Folkes, C. B., Wright, H. M., Cas, R. A., de Silva, S. L., Lesti, C., & Viramonte, J. G. (2011). A re-appraisal of the stratigraphy and volcanology of the Cerro Galán volcanic system, NW Argentina. *Bulletin of volcanology*, *73*(10), 1427-1454.

Folkes, C. B., de Silva, S. L., Wright, H. M., & Cas, R. A. (2011). Geochemical homogeneity of a long-lived, large silicic system; evidence from the Cerro Galán caldera, NW Argentina. *Bulletin of volcanology*, *73*(10), 1455-1486.

Gaupp, R., Kött, A., & Wörner, G. (1999). Palaeoclimatic implications of Mio–Pliocene sedimentation in the high-altitude intra-arc Lauca Basin of northern Chile. *Palaeogeography, Palaeoclimatology, Palaeoecology*, *151*(1), 79-100.

Ghiorso, M. S., & Gualda, G. A. (2013). A method for estimating the activity of titania in magmatic liquids from the compositions of coexisting rhombohedral and cubic iron–titanium oxides. *Contributions to Mineralogy and Petrology*,*165*(1), 73-81.

Glazner, A. F., Bartley, J. M., Coleman, D. S., Gray, W., & Taylor, R. Z. (2004). Are plutons assembled over millions of years by amalgamation from small magma chambers?. *GSA today*, *14*(4/5), 4-12.

Glazner, A. F., Coleman, D. S., & Bartley, J. M. (2008). The tenuous connection between high-silica rhyolites and granodiorite plutons. *Geology*,*36*(2), 183-186.

Green, T. H., & Pearson, N. J. (1986). Ti-rich accessory phase saturation in hydrous mafic-felsic compositions at high P, T. *Chemical Geology*, *54*(3), 185-201.

Gregg, P. M., De Silva, S. L., Grosfils, E. B., & Parmigiani, J. P. (2012). Catastrophic caldera-forming eruptions: Thermomechanics and implications for eruption triggering and maximum caldera dimensions on Earth. *Journal of Volcanology and Geothermal Research*, *241*, 1-12.

Grocke, S. B; de Silva, S. L; Lindsay, J. M., Iriarte, R., Cottrell, E; Andrews, B. J., Magma Evolution and Dynamics of the 3.49 Ma Tara Supereruption, Guacha Caldera, SW Bolivia. Manuscript Submitted for Publication.

Grunder, A. L., Klemetti, E. W., Feeley, T. C., & McKee, C. M. (2006). Eleven million years of arc volcanism at the Aucanquilcha Volcanic Cluster, northern Chilean Andes: implications for the life span and emplacement of plutons. *Earth Sciences*, *97*, 415-436.

Hildreth, W. (1981). Gradients in silicic magma chambers: implications for lithospheric magmatism. *Journal of Geophysical Research: Solid Earth (1978–2012)*, *86*(B11), 10153-10192.

Hildreth, W., & Mahood, G. A. (1986). Ring-fracture eruption of the Bishop Tuff.*Geological Society of America Bulletin*, *97*(4), 396-403.

Hildreth, W., & Moorbath, S. (1988). Crustal contributions to arc magmatism in the Andes of central Chile. *Contributions to Mineralogy and Petrology*, *98*(4), 455 -489.

Hildreth, W. E. S., Halliday, A. N., & Christiansen, R. L. (1991). Isotopic and chemical evidence concerning the genesis and contamination of basaltic and rhyolitic magma beneath the Yellowstone Plateau volcanic field. *Journal of Petrology*, *32*(1), 63-138.

Hildreth, W. (2004). Volcanological perspectives on Long Valley, Mammoth Mountain, and Mono Craters: several contiguous but discrete systems. *Journal of Volcanology and Geothermal Research*, *136*(3), 169-198.

Hoke, L., & Lamb, S. (2007). Cenozoic behind-arc volcanism in the Bolivian Andes, South America: implications for mantle melt generation and lithospheric structure. *Journal of the Geological Society*, *164*(4), 795-814.

Hora, J. M., Singer, B. S., Jicha, B. R., Beard, B. L., Johnson, C. M., de Silva, S., & Salisbury, M. (2010). Volcanic biotite-sanidine 40Ar/39Ar age discordances reflect Ar partitioning and pre-eruption closure in biotite. *Geology*,*38*(10), 923-926.

Isacks, B. L. (1988). Uplift of the central Andean plateau and bending of the Bolivian orocline. *Journal of Geophysical Research: Solid Earth (1978–2012)*,*93*(B4), 3211-3231.

James, D. E., & Sacks, I. S. (1999). Cenozoic formation of the Central Andes: A geophysical perspective. *Geology and Ore Deposits of the Central Andes (Skinner, BJ; editor). Society of Economic Geology, Special Publication*, *7*, 1-26.

Jellinek, A. M., & DePaolo, D. J. (2003). A model for the origin of large silicic magma chambers: precursors of caldera-forming eruptions. *Bulletin of Volcanology*, *65*(5), 363-381.

Johnson, C. M., Lipman, P. W., & Czamanske, G. K. (1990). H, O, Sr, Nd, and Pb isotope geochemistry of the Latir volcanic field and cogenetic intrusions, New Mexico, and relations between evolution of a continental magmatic center and modifications of the lithosphere. *Contributions to Mineralogy and Petrology*,*104*(1), 99-124.

Johnson, D. M., Hooper, P. R., & Conrey, R. M. (1999). XRF analysis of rocks and minerals for major and trace elements on a single low dilution Li-tetraborate fused bead. *Advances in X-ray Analysis*, *41*, 843-867.

Kay, S. M., Coira, B., & Viramonte, J. (1994). Young mafic back arc volcanic rocks as indicators of continental lithospheric delamination beneath the Argentine Puna plateau, central Andes. *Journal of Geophysical Research: Solid Earth (1978–2012)*, *99*(B12), 24323-24339.

Kay, S. M., Mpodozis, C., & Coira, B. (1999). Neogene magmatism, tectonism, and mineral deposits of the Central Andes (22 to 33 S latitude). *Geology and Ore Deposits of theCentral Andes (Skinner, BJ; editor). Society of Economic Geologists, Special Publication*, *7*, 27-59.

Kay, S. M., & Coira, B. L. (2009). Shallowing and steepening subduction zones, continental lithospheric loss, magmatism, and crustalflow under the Central Andean Altiplano-PunaPlateau. *Backbone of the Americas: shallow subduction, plateau uplift, and ridge and terrane collision*, *204*, 229.

Kendrick, E., Bevis, M., Smalley, R., & Brooks, B. (2001). An integrated crustal velocity field for the central Andes. *Geochemistry, Geophysics, Geosystems*,*2*(11).

Kennedy, B., Wilcock, J., & Stix, J. (2012). Caldera resurgence during magma replenishment and rejuvenation at Valles and Lake City calderas. *Bulletin of volcanology*, *74*(8), 1833-1847.

Koppers, A. A. (2002). ArArCALC—software for $^{40}Ar/^{39}Ar$ age calculations. *Computers & Geosciences*, *28*(5), 605-619.

Lanphere, M. A., & Dalrymple, G.B. (1976). Identification of excess ^{40}Ar by the $^{40}Ar/^{39}Ar$ age spectrum technique. *Earth and Planetary Science Letters*, *32*(2), 141-148.

Lindsay, J. M., De Silva, S., Trumbull, R., Emmermann, R., & Wemmer, K. (2001). La Pacana caldera, N. Chile: a re-evaluation of the stratigraphy and volcanology of one of the world's largest resurgent calderas. *Journal of Volcanology and Geothermal Research*, *106*(1), 145-173.

Lindsay, J. M., Schmitt, A. K., Trumbull, R. B., De Silva, S. L., Siebel, W., & Emmermann, R. (2001). Magmatic evolution of the La Pacana caldera system, Central Andes, Chile: compositional variation of two cogenetic, large-volume felsic ignimbrites. *Journal of Petrology*, *42*(3), 459-486.

Lipman, P. W. (1983). The Miocene Questa caldera, northern New Mexico: relation to batholith emplacement and associated molybdenum mineralization. In *The genesis of Rocky Mountain ore deposits: changes with time and tectonics. Proc Denver Region Explor Geol Soc Symp* (pp. 133-147).

Lipman, P. W. (1984). The roots of ash flow calderas in western North America: Windows into the tops of granitic batholiths. *Journal of Geophysical Research: Solid Earth (1978–2012)*, *89*(B10), 8801-8841.

Lipman, P. W. (2007). Incremental assembly and prolonged consolidation of Cordilleran magmachambers: Evidence from the Southern Rocky Mountain volcanic field. *Geosphere*, *3*(1), 42-70.

Liu, Y., Hu, Z., Zong, K., Gao, C., Gao, S., Xu, J., & Chen, H. (2010). Reappraisement and refinement of zircon U-Pb isotope and trace element analyses by LA-ICP-MS. *Chinese Science Bulletin*, *55*(15), 1535-1546.

Loewy, S. L., Connelly, J. N., & Dalziel, I. W. (2004). An orphaned basement block: The Arequipa-Antofalla Basement of the central Andean margin of South America. *Geological Society of America Bulletin*, *116*(1-2), 171-187.

Lucassen, F., Becchio, R., Harmon, R., Kasemann, S., Franz, G., Trumbull, R., & Dulski, P. (2001). Composition and density model of the continental crust at an active continental margin—the Central Andes between 21 and 27 S.*Tectonophysics*, *341*(1), 195-223.

Ludwig, K. R. (2008). *User's manual for Isoplot 3.17: a geochronological toolkit for Microsoft Excel* (No. 4). Kenneth R. Ludwig.

Macfarlane, A. W., Marcet, P., LeHuray, A. P., & Petersen, U. (1990). Lead isotope provinces of the Central Andes inferred from ores and crustal rocks. *Economic Geology*, *85*(8), 1857-1880.

Mahon, K. I. (1996). The New "York" regression: Application of an improved statistical method to geochemistry. *International Geology Review*, *38*(4), 293-303.

Mamani, M., Wörner, G., & Sempere, T. (2010). Geochemical variations in igneous rocks of the Central Andean orocline (13 S to 18 S): tracing crustal thickening and

magma generation through time and space. *Geological Society of America Bulletin*, *122*(1-2), 162-182.

Marsh, B. D. (1984). On the mechanics of caldera resurgence. *Journal of Geophysical Research: Solid Earth (1978–2012)*, *89*(B10), 8245-8251.

Mason, B. G., Pyle, D. M., & Oppenheimer, C. (2004). The size and frequency of the largest explosive eruptions on Earth. *Bulletin of Volcanology*, *66*(8), 735-748.

McGlashan, N., Brown, L., & Kay, S. (2008). Crustal thickness in the central Andes from teleseismically recorded depth phase precursors. *Geophysical Journal International*, *175*(3), 1013-1022.

McNulty, B. A., Tobisch, O. T., Cruden, A. R., & Gilder, S. (2000). Multistage emplacement of the Mount Givens pluton, central Sierra Nevada batholith, California. *Geological Society of America Bulletin*, *112*(1), 119-135.

Miller, J. F. (1988). *Granite petrogenesis in the Cordillera Real, Bolivia and crustal evolution in the Central Andes* (Doctoral dissertation, Open University).

Miller, J. F., & Harris, N. B. W. (1989). Evolution of continental crust in the Central Andes; constraints from Nd isotope systematics. *Geology*, *17*(7), 615-617.

Miller, J. S., & Wooden, J. L. (2004). Residence, resorption and recycling of zircons in Devils Kitchen rhyolite, Coso Volcanic field, California. *Journal of Petrology*, *45*(11), 2155-2170.

Muir, D. D., Blundy, J. D., Rust, A. C., & Hickey, J. (2014). Experimental constraints on dacite pre-eruptive magma storage conditions beneath Uturuncu volcano. *Journal of Petrology*, *55*(4), 749-767.

Ninkovich, D., Sparks, R. S. J., & Ledbetter, M. T. (1978). The exceptional magnitude and intensity of the Toba eruption, Sumatra: an example of the use of deep-sea tephra layers as a geological tool. *Bulletin Volcanologique*, *41*(3), 286-298.

Ort, M. H. (1993). Eruptive processes and caldera formation in a nested downsag collapse caldera: Cerro Panizos, central Andes Mountains. *Journal of Volcanology and Geothermal Research*, *56*(3), 221-252.

Ort, M. H., Coira, B. L., & Mazzoni, M. M. (1996). Generation of a crust-mantle magma mixture: magma sources and contamination at Cerro Panizos, central Andes. *Contributions to Mineralogy and Petrology*, *123*(3), 308-322.

Ort, M. H., Silva, S. L., Jiménez, C., Jicha, B. R., & Singer, B. S. (2013). Correlation of ignimbrites using characteristic remanent magnetization and anisotropy of magnetic susceptibility, Central Andes, Bolivia. *Geochemistry, Geophysics, Geosystems*, *14*(1), 141-157.

Paces, J. B., & Miller, J. D. (1993). Precise U-Pb ages of Duluth Complex and related mafic intrusions, northeastern Minnesota: Geochronological insights to physical, petrogenetic, paleomagnetic, and tectonomagmatic processes associated with the 1.1 Ga Midcontinent Rift System. *Journal of Geophysical Research: Solid Earth (1978–2012)*, *98*(B8), 13997-14013.

Pacheco, J., and Ramírez, V., 1997a, Hoja Geológica Cañapa/ Alota 5929/6029: Servicio Nacional de Geológica y Mineria Carta Geológica de Bolivia Publicacíon SGM Serie I–CGB-45, scale 1:100,000, 1 sheet.

Paine, J. H., Nomade, S., & Renne, P. R. (2006). Quantification of ^{39}Ar recoil ejection from GA1550 biotite during neutron irradiation as a function of grain dimensions. *Geochimica et Cosmochimica Acta*, *70*(6), 1507-1517.

Petrinovic, I. A. (1994). *Volcanismo Cenozoico asociado al lineamiento Calama–Olacapato–El Toro en el tramo comprendido entre San Antonio de los Cobres y Olacapato, provincial de Salta, Argentina* (Doctoral dissertation, Phd Thesis Universidad Nacional de Salta, Argentina. 234 p.Unpublished).

Reid, M. R. (2003). Timescales of magma transfer and storage in the crust.*Treatise on geochemistry*, *3*, 167-193.

Reid, M. R., Coath, C. D., Mark Harrison, T., & McKeegan, K. D. (1997). Prolonged residence times for the youngest rhyolites associated with Long Valley Caldera: ^{230}Th—^{238}U ion microprobe dating of young zircons. *Earth and Planetary Science Letters*, *150*(1), 27-39.

Reid, M. R., Vazquez, J. A., & Schmitt, A. K. (2011). Zircon-scale insights into the history of a Supervolcano, Bishop Tuff, Long Valley, California, with implications for the Ti-in-zircon geothermometer. *Contributions to Mineralogy and Petrology*, *161*(2), 293-311.

Richards, J. P., & Villeneuve, M. (2002). Characteristics of late Cenozoic volcanism along the Archibarca lineament from Cerro Llullaillaco to Corrida de Cori, northwest Argentina. *Journal of Volcanology and Geothermal Research*,*116*(3), 161-200.

Riller, U., Petrinovic, I., Ramelow, J., Strecker, M., & Oncken, O. (2001). Late Cenozoic tectonism, collapse caldera and plateau formation in the central Andes. *Earth and Planetary Science Letters*, *188*(3), 299-311.

Riller, U., Oncken, O. (2003) Growth of the Central Andean Plateau by tectonic segmentation is controlled by the gradient in crustal shortening. *Journal of Geology* 111, 367-384.

Roberts, H. J., Kelley, S. P., & Dahl, P. S. (2001). Obtaining geologically meaningful ^{40}Ar/^{39}Ar ages from altered biotite.*Chemical Geology*, *172*(3), 277-290.

Rose, W. I., & Chesner, C. A. (1987). Dispersal of ash in the great Toba eruption, 75 ka. *Geology*, *15*(10), 913-917.

Salisbury, M. J., Jicha, B. R., de Silva, S. L., Singer, B. S., Jiménez, N. C., & Ort, M. H. (2011). ^{40}Ar/^{39}Ar chronostratigraphy of Altiplano-Puna volcanic complex ignimbrites reveals the development of a major magmatic province. *Geological Society of America Bulletin*, *123*(5-6), 821-840.

Sambridge, M. S., & Compston, W. (1994). Mixture modeling of multi-component data sets with application to ion-probe zircon ages. *Earth and Planetary Science Letters*, *128*(3), 373-390.

Schmitt, A., de Silva, S., Trumbull, R., & Emmermann, R. (2001). Magma evolution in the Purico ignimbrite complex, northern Chile: evidence for zoning of a dacitic magma by injection of rhyolitic melts following mafic recharge.*Contributions to Mineralogy and Petrology*, *140*(6), 680-700.

Sempere, T., Hérail, G., Oller, J., & Bonhomme, M. G. (1990). Late Oligocene-early Miocene major tectonic crisis and related basins in Bolivia. *Geology*,*18*(10), 946-949.

Sigurdsson, H., & Carey, S. (1989). Plinian and co-ignimbrite tephra fall from the 1815 eruption of Tambora volacano. *Bulletin of Volcanology*, *51*(4), 243-270.

Smith, R. L. (1960). Ash flows. *Geological Society of America Bulletin*, *71*(6), 795-841.

Smith, R. L., & Bailey, R. A. (1968). Resurgent cauldrons. *Geological Society of America Memoirs*, *116*, 613-662.

Smith, R. L. (1979). Ash-flow magmatism. *Ash-flow tuffs: Geological Society of America Special Paper*, *180*, 5-27.

Smith, M. E., Singer, B. S., Carroll, A. R., & Fournelle, J. H. (2008). Precise dating of biotite in distal volcanic ash: Isolating subtle alteration using $^{40}Ar/^{39}Ar$ laser incremental heating and electron microprobe techniques. *American Mineralogist*, *93*(5-6), 784-795.

Soler, M. M., Caffe, P. J., Coira, B. L., Onoe, A. T., & Kay, S. M. (2007). Geology of the Vilama caldera: a new interpretation of a large-scale explosive event in the Central Andean plateau during the Upper Miocene. *Journal of volcanology and geothermal research*, *164*(1), 27-53.

Somoza, R. (1998). Updated azca (Farallon)—South America relative motions during the last 40 My: implications for mountain building in the central Andean region. *Journal of South American Earth Sciences*, *11*(3), 211-215.

Sparks, R. S. J., Francis, P. W., Hamer, R. D., Pankhurst, R. J., O'callaghan, L. O., Thorpe, R. S., & Page, R. (1985). Ignimbrites of the Cerro Galan Caldera, NW Argentina. *Journal of Volcanology and Geothermal Research*, *24*(3), 205-248.

Sparks, R. S. J., Bursik, M. I., Carey, S. N., Gilbert, J., Glaze, L. S., Sigurdsson, H., & Woods, A. W. (1997). *Volcanic plumes*. Wiley.

Spinks, K. D., Acocella, V., Cole, J. W., & Bassett, K. N. (2005). Structural control of volcanism and caldera development in the transtensional Taupo Volcanic Zone, New Zealand. *Journal of Volcanology and Geothermal Research*, *144*(1), 7-22.

Stern, C. R. (2004). Active Andean volcanism: its geologic and tectonic setting. *Revista geológica de Chile*, *31*(2), 161-206.

Strecker, M. R., Alonso, R. N., Bookhagen, B., Carrapa, B., Hilley, G. E., Sobel, E. R., & Trauth, M. H. (2007). Tectonics and climate of the southern central Andes. *Annu. Rev. Earth Planet. Sci.*, *35*, 747-787.

Tappa, M. J., Coleman, D. S., Mills, R. D., & Samperton, K. M. (2011). The plutonic record of a silicic ignimbrite from the Latir volcanic field, New Mexico. *Geochemistry, Geophysics, Geosystems*, *12*(10).

Tierney, C.R., (2011) Timescales of large silicic magma systems: implications from accessory minerals in Pleistocene lavas of the Altiplano-Puna Volcanic Complex, central Andes (Master's Thesis) Oregon State University, Corvallis OR.

Valley, J. W. (2003). Oxygen isotopes in zircon. *Reviews in mineralogy and geochemistry*, *53*(1), 343-385.

Van Bemmelen, R. V. (1939). The volcano-tectonic origin of Lake Toba (North Sumatra). *Ing. Ned. Ind*, *6*(9), 126-140.

Viramonte, J. G., Galliski, M. A., Saavedra, V. A., Aparicio, A., García-Cacho, G. L., & Escorza, C. M. (1984). El finivulcanismo básico de la depresión de Arizaro, provincia de Salta. *IX Cong. Geol. Arg, Actas*, *3*, 234-251.

Watanabe, K., Ono, K., Sakaguchi, K., Takada, A., & Hoshizumi, H. (1999). Co -ignimbrite ash-fall deposits of the 1991 eruptions of Fugen-dake, Unzen Volcano, Japan. *Journal of volcanology and geothermal research*, *89*(1), 95-112.

Watson, E. B. (1996). Dissolution, growth and survival of zircons during crustal fusion: kinetic principals, geological models and implications for isotopic

inheritance. *Transactions of the Royal Society of Edinburgh: Earth Sciences*,*87*(1-2), 43-56.

Watson, E. B., Wark, D. A., & Thomas, J. B. (2006). Crystallization thermometers for zircon and rutile. *Contributions to Mineralogy and Petrology*,*151*(4), 413-433.

Watts, R. B., de Silva, S. L., de Rios, G. J., & Croudace, I. (1999). Effusive eruption of viscous silicic magma triggered and driven by recharge: a case study of the Cerro Chascon-Runtu Jarita Dome Complex in Southwest Bolivia.*Bulletin of volcanology*, *61*(4), 241-264.

Whitman, D., Isacks, B. L., & Kay, S. M. (1996). Lithospheric structure and along-strike segmentation of the Central Andean Plateau: seismic Q, magmatism, flexure, topography and tectonics. *Tectonophysics*, *259*(1), 29-40.

Wilson, C. J. N. (2001). The 26.5 ka Oruanui eruption, New Zealand: an introduction and overview. *Journal of Volcanology and Geothermal Research*, *112*(1), 133-174.

Wörner, G., Moorbath, S., & Harmon, R. S. (1992). Andean Cenozoic volcanic centers reflect basement isotopic domains. *Geology*, *20*(12), 1103-1106.

Wotzlaw, J. F., Schaltegger, U., Frick, D. A., Dungan, M. A., Gerdes, A., & Günther, D. (2013). Tracking the evolution of large-volume silicic magma reservoirs from assembly to supereruption. *Geology*, *41*(8), 867-870.

Zandt, G., Leidig, M., Chmielowski, J., Baumont, D., & Yuan, X. (2003). Seismic detection and characterization of the Altiplano-Puna magma body, central Andes. *Pure and Applied Geophysics*, *160*(3-4), 789-807.

Zimmerer, M. J., & McIntosh, W. C. (2012). The geochronology of volcanic and plutonic rocks atthe Questa caldera: Constraints on the origin of caldera-related silicic magmas. *Geological Society of America Bulletin*, *124*(7-8), 1394-1408.